Julia Schmid

Searches for High-Energy Neutrinos from Gamma-Ray Bursts with the Antares Neutrino Telescope

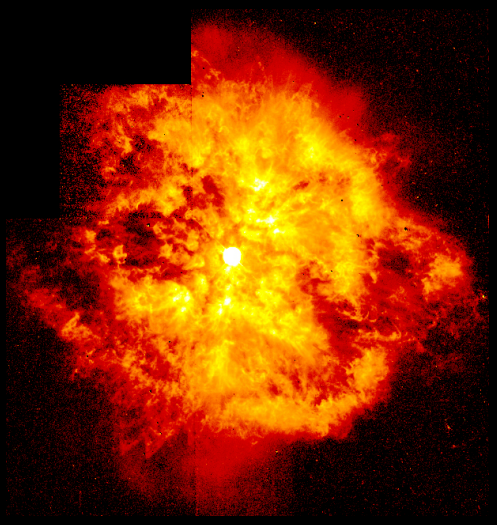

Searches for High-Energy Neutrinos from Gamma-Ray Bursts with the Antares Neutrino Telescope

Suche nach hochenergetischer Neutrinoemission von Gammablitzen mit dem Neutrinoteleskop Antares

Der Naturwissenschaftlichen Fakultät
der Friedrich-Alexander-Universität Erlangen-Nürnberg
zur Erlangung des Doktorgrades Dr. rer. nat.
vorgelegt von
Julia Schmid
aus Darmstadt

Image on front page: Hubble Space Telescope image of Wolf-Rayet star WR 124 and its surrounding nebula. Wolf-Rayet stars are candidates for being progenitors of long-duration gamma-ray bursts. Credit: Yves Grosdidier (Université de Montréal & Observatoire de Strasbourg), Anthony Moffat (Université de Montréal), Gilles Joncas (Université Laval), Agnes Acker (Observatoire de Strasbourg), and NASA

Als Dissertation genehmigt
von der Naturwissenschaftlichen Fakultät
der Friedrich-Alexander-Universität Erlangen-Nürnberg

Tag der mündlichen Prüfung: 19.12.2014
Vorsitzender des Promotionsorgans: Prof. Dr. Jörn Wilms
Gutachter:

Prof. Dr. Gisela Anton (ECAP, Erlangen)
Prof. Dr. Antoine Kouchner (APC, Paris, Frankreich)
Prof. Dr. Albrecht Karle (WIPAC, Madison, USA)

Human beings, who are almost unique in having the ability to learn from the experience of others, are also remarkable for their apparent disinclination to do so.

— Douglas Adams —

ZUSAMMENFASSUNG

In dieser Arbeit wurde erforscht, wie mit dem Neutrinoteleskop ANTARES ein Neutrinosignal von Gamma-Ray Bursts, zu deutsch Gammablitzen, gefunden werden kann. Dies sind Quellen hochenergetischer Gammastrahlung, die unvorhersagbar und gleichmäßig am Himmel verteilt auftreten und innerhalb von Sekunden vergleichbar viel Energie freisetzen, wie zum Beispiel der Sonne im Laufe ihrer gesamten Lebenszeit zur Verfügung steht. Man bringt sie mit Explosionen sehr massiver Sterne oder dem Verschmelzen zweier kompakter Objekte in Verbindung, in deren Endstadium aller Wahrscheinlichkeit nach ein schwarzes Loch gebildet wird. Die beobachtete elektromagnetische Strahlung kann mit hochrelativistischer Materie erklärt werden, die entlang der Blickrichtung von der Quelle ausgestoßen wird, wobei Elektronen aufgrund des Fermi-Prozesses beschleunigt werden.

Es wird indes vermutet, dass der relativistische Ausstoß nicht ausschließlich aus Leptonen besteht, sondern auch einen Anteil hadronischer Materie enthält. Sämtliche geladenen Teilchen würden damit gleichermaßen mit den Elektronen beschleunigt werden. Protonen könnten auf diese Weise Energien von bis zu 10^{20} Elektronenvolt erreichen. Bei deren Wechselwirkung mit den ausgestrahlten Photonen würden unausweichlich hochenergetische Neutrinos entstehen, die zusammen mit dem elektromagnetischen Signal ausgestrahlt würden.

Schon 1997 sagten Waxman und Bahcall ein solches Neutrinosignal vorher, es ist aber trotz zahlreicher Detektionsversuche bis heute unentdeckt geblieben. Die eindeutige Zuordnung eines solchen Signals zu einer astrophysikalischen Quelle würde zum ersten Mal zweifelsfrei die Beschleunigung von Hadronen beweisen, die durch Beobachtungen im rein elektromagnetischen Spektrum nicht zugänglich ist. Um aber den bis dato unbekannten Ursprung der kosmischen Strahlung besonders in den höchsten Energien zu erklären ist es unabdingbar, jene Prozesse im Universum zu identifizieren, in denen Baryonen auf eben diese Energien beschleunigt werden können.

In dieser Arbeit untersuchte ich zunächst, ob die Rekonstruktion von Teilchenspuren im ANTARES-Detektor verbessert werden kann, indem Parameterkonstellationen ausgemacht werden, die systematische Verschiebungen in der Richtungsrekonstruktion der Daten hervorrufen. Wenn solche Effekte nachgewiesen und quantifiziert werden können, kann man diese Information auch in der zu entwickelnden Suche nach einem Neutrinosignal nutzen, um die Rekonstruktion der Ursprungsrichtung zu korrigieren. Ich konnte mithilfe einer systematischen Durchleuchtung des Detektorvolumens mit simulierten relativistischen Myonen zeigen, dass in circa 1% aller Fälle tatsächlich ein Großteil der rekonstruierten Richtungen um mehr als die Punktauflösung des Detektors von der ursprünglich simulierten Richtung abweicht. Mit diesem Wissen kann man die Rekonstruktion einzelner Ereignisse in den Daten verbessern und somit möglicherweise einen Gammablitz als Quelle eines potentiellen Neutrinosignals bekräftigen.

Es wurden außerdem verschiedene Möglichkeiten untersucht, wie ein mit Gammablitzen assoziiertes Neutrinosignal in den ANTARES-Daten gefunden werden kann, wenn dieses einerseits gleichzeitig mit dem elektromagnetischen Signal erwartet wird, aber möglicherweise andererseits auch mit einem gewissen zeitlichen Versatz ankommt. Es wurden hierbei Daten von unterschiedlichen Satellitenmissionen wie zum Beispiel *Swift* und *Fermi* sowie erdgebundenen Teleskopen herangezogen, um nach Korrelationen mit den Daten

des Neutrinoexperiments zu suchen.

Ausgehend von einer sehr simplen, sogenannten gebinnten Analysemethode, die ich beispielhaft anhand des Gammablitzes GRB091026 aufzeige, wurde ein aufwändigeres Verfahren entwickelt, dass das Entdeckungspotential signifikant um bis zu 200% verbessern kann. In dieser werden Signal- und Untergrundverteilungen durch kontinuierliche Funktionen beschrieben und ein Algorithmus kann auf deren Basis eine Signalhypothese von Untergrund unterscheiden. Zum ersten Mal wurde dabei eine solche Suche hinsichlich eines neuartigen numerischen Modells optimiert, das den Neutrinofluss von Gammablitzen mit beispielhafter Genauigkeit vorhersagt. Nachdem ältere und optimistischere Modelle bereits dadurch ausgeschlossen wurden, dass das IceCube-Experiment keinerlei Neutrino finden konnte, zeigen die neuen Vorhersagen jedoch, dass deutlich weniger Ereignisse in den laufenden Neutrinoteleskopen Antares und IceCube zu erwarten sind, als zunächst angenommen. Mit der ausgearbeiteten Methode wurde dann nach einem Neutrinosignal von Gammablitzen in den Antares-Daten, die zwischen Dezember 2007 und 2011 genommen worden waren, gesucht. Ein ähnliches Verfahren wurde angewendet, um eine möglichst zeitnahe Analyse eines potentiellen Neutrinosignals von GRB130427A, einem außergewöhnlich hellen Gammablitz im Frühjahr des Jahres 2013, zu ermöglichen. Ebenso wie in vorangegangenen Untersuchungen wurden auch in diesen beiden Analysen keine Neutrinoereignisse in direktem Zusammenhang mit den ausgewählten Gammablitzen gefunden, so dass letztendlich nur Obergrenzen auf den tatsächlichen Neutrinofluß angegeben werden können, die um den Faktor 38 über den Vorhersagen liegen. Dies sind die Ersten ihrer Art, die ausgehend von zeitgemäßen numerischen Modellen abgeleitet wurden. Sie sind in gewissem Umfang komplementär zu vorherigen Grenzen anderer Experimente, sowohl hinsichtlich des jeweils gültigen Energiebereichs, der Himmelsabdeckung als auch der Zeitspanne der Datennahme.

Nachdem das Detektionspotenzial des Antares-Detektors detailliert untersucht wurde, zeige ich, wie man daraus das Potential des zukünftigen Experiments KM3NeT ableiten kann, ein ähnlich geartetes Neutrinosignal von Gammablitzen zu identifizieren. Ich werde darlegen, dass das geplante Teleskop mit bislang noch nicht gekannter Präzision das vorherrschende Modell entweder bestätigen oder massiv einschränken können wird.

Außerdem wird gezeigt, wie man die Suche nach gleichzeitig mit der Gammastrahlung auftreffenden Neutrinosignalen ausdehnen kann, um einen möglichen Zeitversatz zwischen diesen beiden zuzulassen. Mehrere Modelle sagen zum Beispiel eine zeitlich verschobene Emission von Neutrinos innerhalb der Quelle vorher, die bis zu einen Tag ausmachen kann. In Anderen wiederum wirkt sich die Symmetriebrechung der Lorentzinvarianz bei hohen Energieskalen auf die Ankunftszeiten der beiden Signale aus. Gammablitze sind dank ihrer kosmologischen Entfernung und ihrer transienten Natur ein ideales und einzigartiges Testumfeld, um derartige Effekte nachzuweisen. Die vorgestellte Methode ist in der Lage, um bis zu vierzig Tage zeitversetzte Neutrinosignale nachzuweisen, jedoch gleichzeitig kaum Modellannahmen über die Natur eines solchen Versatzes zu treffen. Mithilfe fingierter Testsignale kann ich zeigen, dass das entwickelte Verfahren ein solches zeitlich verschobenes Signal von Gammablitzen zuverlässig aufspüren kann, wenn nur etwa jeder Hundertste ein einzelnes Neutrinoereignis in den Antares-Daten hervorruft. Letztendlich wurden potentiell astrophysikalische Neutrinokandidaten aus sechs Jahren Datennahme von 2007 bis 2012 mit dem Antares-Detektor auf ein derartiges Signal durch-

sucht; es fiel jedoch kein einziges Ereignis in eines der definierten Suchfenster um die Gammablitze. Da allein aus zufallsverteilten Daten schon über vier Übereinstimmungen vorhergesagt worden waren, stellt dies eine erhebliche Unterfluktuation gegenüber den Erwartungen selbst ohne Signalannahme dar. Zusätzlich durchmusterte ich auch einen öffentlich zugänglichen Datensatz des IceCube-Experiments aus einem Jahr Laufzeit, in dem ein leichter Überschuss an Koinzidenzen gegenüber der Untergrunderwartung ausgemacht werden konnte. Dieser ist jedoch immer noch mit fünfprozentiger Wahrscheinlichkeit mit dem Untergrund verträglich und somit nicht signifikant.

Auch diese Arbeit konnte also bedauerlicherweise nur vorherige Analysen bestätigen, die keinerlei Neutrinosignal von Gammablitzen nachweisen konnten. Es wurden jedoch neuartige Methoden aufgezeigt, die die Detektionswahrscheinlichkeit erheblich verbessern und es in den nächsten Jahren mit den laufenden Experimenten und insbesondere mit dem geplanten Großprojekt KM3NeT ermöglichen sollten, die ersten mit Gammablitzen assoziierten Neutrinos nachzuweisen. Außerdem wurden zum ersten Mal Daten von Neutrinoteleskopen auf der Suche nach Signalen von Gammablitzen mit bis zu 40 Tagen Zeitverschiebung analysiert.

ABSTRACT

In this work, I investigated how a presumable neutrino signal associated with gamma-ray bursts can be identified using data from the ANTARES neutrino telescope. Gamma-ray bursts (GRBs) are cataclysmic events most likely connected to the collapse of an extremely massive star or a binary system into a black hole. In the order of seconds, they emit high-energy gamma rays that can outshine the rest of the universe, making them the most powerful processes known. The observations are commonly explained by highly relativistic outflows of material pointed towards Earth, in which electrons are accelerated and give rise to a photon signal due to synchrotron and inverse Compton processes. If in addition to the leptonic matter, protons are also present in the ejecta, they would be similarly accelerated to energies up to 10^{20} electron volts. Their interactions with the present photon field would inevitably yield the simultaneous emission of neutrinos of $\sim 10^{15}$ electron volts. This flux was first predicted in 1997 by Waxman and Bahcall, but despite numerous experiments, no conclusive evidence for neutrino signals from GRBs has yet been found.

The compelling evidence of a high-energy cosmic neutrino signal correlated with astrophysical sources would, for the first time, prove the acceleration of hadrons beyond any doubt, a hypothesis that cannot be tested by pure electromagnetic observation. However, to explain the origin of cosmic rays at ultra-high energies, it is absolutely crucial to identify those processes in the universe that are capable of accelerating baryons to such energies.

As a first step, I investigated whether or not the reconstruction of particle trajectories in the ANTARES data can be improved by identifying parameter configurations that give rise to systematic deviations in the directional reconstruction. If such effects can be detected and quantified, this knowledge can be used to correct the reconstruction on an event-by-event basis and narrow down the most probable source of emission. Having scanned the instrumented volume with simulated muons, I showed that overall shifts in the reconstructed directions by more than the detector's resolution occur in 1% of the sample. Hence, with a non-negligible chance the reconstruction of individual data events can be refined and thereby reinforce a gamma-ray burst as the source of emission of a presumable neutrino signal.

Several techniques to single out a neutrino signal from GRBs in the ANTARES data were developed, both in the search for simultaneous as well as a possibly time-shifted neutrino emission with respect to the photon signal. I made use of data from multiple spacecraft and Earth-bound telescopes within the Gamma-ray burst Coordinates Network such as the *Swift* and *Fermi* satellites to search for correlated neutrinos in the data from the ANTARES telescope.

Starting from a simple counting method demonstrated on the showcase burst GRB091026, I showed how the use of an un-binned likelihood can improve the detection prospects by up to a factor of two. The developed technique was optimized in terms of maximal detection power to search for coincident neutrinos with gamma-ray bursts occurring between December 2007 and 2011, after the completion of the ANTARES detector. The presented work has been the first of this kind being optimized for a second-generation neutrino-emission model. The early and more optimistic models had previously been excluded by the non-observation of any neutrino signal from GRBs with ICECUBE. However, the recent models predict considerably less neutrino events from these sources, so that the present limits do

not constrain the hadronic acceleration in the internal shock scenario of gamma-ray bursts yet. Similar methods were employed during a search for a neutrino signal from a particularly bright gamma-ray burst in 2013, GRB130427A, in the ANTARES data. Unfortunately, none of these analyses could identify any data events simultaneously with the selected bursts. Hence, only upper limits on the neutrino flux could be derived which lie a factor of 38 above the model predictions. These are compatible with previous limits set by other experiments, but complementary in sky coverage, energy range or data livetime.

Having studied the capability of the ANTARES detector to identify neutrino signals from gamma-ray bursts, I made use of this knowledge to infer the detection potential of the future KM3NET experiment to distinguish a similar signal over background. I demonstrated that the planned detector will be capable of probing the prevailing models and the parameter space upon which they are based with unprecedented precision, allowing to either detect or severely constrain the fireball paradigm in the next decades.

Moreover, I investigated the capabilities to detect a neutrino signal associated with gamma-ray-burst alerts if it was shifted in time with respect to the electromagnetic signal. Numerous models predict, for instance, the delayed emission of neutrinos at the sources up to one day, while others derive different arrival times for neutrinos and photons due to symmetry breaking of Lorentz invariance. Thanks to their cosmic distances and transient nature, gamma-ray bursts provide unique test environments to study and verify such effects. A completely novel technique was developed to distinguish such a signal from the expected background, which allows even faint signals to be detected as a cumulative effect in a large sample of GRBs. Such an approach is completely unprecedented in its capabilities to identify neutrino signals which might be delayed with respect to the photon detections by up to 40 days, while at the same time imposing as few assumptions on any model as possible. Mimicking a test signal in only a fraction of gamma-ray bursts, I showed that the method robustly detects an associated neutrino flux if only around 1% of all GRBs gave rise to an associated signal event in the ANTARES data. Six years of data from the ANTARES telescope were examined in the search for a GRB-associated neutrino excess, yet not a single potential astrophysical neutrino candidates could be found in the defined search windows. Since more than four spatial coincidences would have been expected from mere randomized data, this represents a substantial under-fluctuation with respect to the expectations from pure background. In addition, one year of public ICECUBE data were scanned for such an excess. Slightly more neutrino candidates coincided spatially with the gamma-ray bursts than derived from background only. Yet, the excess is still compatible with mere background with a five per cent probability and consequently not significant.

This work can therefore only confirm previous analyses that could not identify any significant neutrino excess associated with gamma-ray bursts. Nevertheless, novel techniques are presented that can considerably enhance the detection potential for such signals and will certainly allow the operating experiments and, in particular, the planned KM3NET detector to put the prevailing models of hadronic acceleration in gamma-ray bursts to the proof in the near future. For the first time, neutrino emission from gamma-ray bursts has been searched for in the data from the current neutrino telescopes considering a time delay of up to forty days.

CONTENTS

1. Introduction

Men have always gazed at the stars above, wondering about their origin and the different phenomena that caused their light. They have learned to analyze and utilize the changing star positions over time, for example for navigation. For a long time, humans have relied only on the visible starlight to study the phenomena of the universe. At the turn of the 19th Century, Johann Ritter and Wilhelm Herschel discovered ultra-violet and infra-red light (Ritter, 1810; Herschel, 1801). Together with the detection of radio waves near the close of the Century by Heinrich Hertz (Hertz, 1887), they showed that the light spectrum extends to lower and higher energies outside the human visibility region. However, it was only after the accidental discovery of radio waves from our galaxy by Jansky in 1932 (Jansky, 1933), that new experimental techniques were developed that subsequently extended astronomy to energy bands above and below the optical wavelength range, proving that there is quite literally more to discover in the universe than 'meets the eye'. Meanwhile, investigations of the mysterious flux from the universe – the so-called cosmic rays – discovered by Victor Hess in 1912 (Hess, 1912) had shown that the radiation from space not only extends to a much larger energy ranges than previously thought, but also comprises particle components in addition to the electromagnetic emission. Nowadays, astronomy exploits the entire electromagnetic wavelength range, from low-energy radio waves, optical and X-rays up to high-energy gamma-ray photons. At the same time, attempts are made to identify the different cosmic ray components even at the highest energies and to probe the universe in the light of other astrophysical messengers, such as gravitational waves or neutrinos.

The first compelling evidence for a neutrino signal from space was found in 1987, when more than twenty neutrinos of $\sim$ MeV energies were detected in several instruments coincident with supernova SN1987 (Hirata et al., 1988; Aglietta et al., 1987; Bionta et al., 1987; Alekseev et al., 1987). This discovery demonstrated that it is in principle feasible, even if highly challenging, to detect cosmic neutrinos. There are numerous additional motivations to continue this search, in particular the quest of finally identifying the sources of the most energetic cosmic rays. Despite their detection as long as 100 years ago, the origin of cosmic rays in particular at ultra-high energies above 10^{18} eV remains completely unknown and prevails as one of the main unsolved questions in today's physics. Due to their electric charge, these particles are deflected by magnetic fields in the universe, hence their directions are completely randomized when reaching Earth. However, the interaction of cosmic rays with photons or matter in their emission or acceleration region would inevitably yield the simultaneous production of neutrinos. Since these particles carry no charge, they are not perturbed by magnetic fields and point directly back to their point of emission. Furthermore, neutrinos can escape the innermost dense regions of astrophysical objects long before they become optically thin and release photons. In contrast to electromagnetic emission that traces the acceleration of electrons (through synchrotron emission) as well as cosmic rays, the detection of neutrinos alone could unambiguously prove the acceleration

of hadronic particles in an astrophysical process. Thus the observation of high-energy neutrinos could bring the only conclusive identification of sources of the most energetic cosmic rays.

In addition, cosmic neutrinos of the highest energies are of particular interest since the photon range above a certain energy is significantly reduced due to the interaction with the omnipresent low-energy cosmic microwave background. Photons of $\sim 10\,\mathrm{TeV}$, for example, can only travel as far as the nearest active galaxy, which significantly limits the possibilities for astronomy at the highest energies (Learned & Mannheim, 2000). Neutrinos of the same and higher energies, on the other hand, do not suffer from these interactions and can consequently traverse cosmological distances without being deflected[1]. Moreover, the neutrino cross-section with a potential detection medium increases significantly with energy, and secondary particles produced in the interactions are mostly aligned, so that the directional information about the neutrino's origin is well conserved. Hence, high-energy neutrinos provide an unique messenger to extend astronomy to the highest energies and largest distances, beyond the scope of electromagnetic radiation.

Due to the relatively low cross-section of neutrinos with matter, high-energy neutrino detectors require large amounts of detection material – current very-large-volume neutrino telescopes like IceCube and Antares make use of natural seawater or ice (see, e.g., Katz & Spiering, 2012, and references therein). For sufficiently high primary neutrino energies, the velocity of the secondary particles exceeds that of light in the ambient medium, inducing the emission of Cherenkov photons. Three-dimensional arrays of photodetectors record this light, and the directional information of the parent cosmic neutrino can be inferred from the photon arrival times and positions. The neutrino experiments can simultaneously observe at least half of the sky. Due to its location at the South Pole, the IceCube detector has its maximum sensitivity for Northern Hemisphere sources, whereas the Antares detector, being situated at a latitude of 43°, has its maximum sensitivity for the Southern Hemisphere.

Cosmic neutrinos of the highest energies are naturally assumed to be produced in the most powerful processes known in the universe, where observed non-thermal electromagnetic spectra hint at the acceleration of particles. Among the most promising candidate sources are accreting super-massive black holes in the centers of galaxies, active galactic nuclei, where material is expelled in relativistic jets. Associated shock fronts within these jets may accelerate electrons but also protons to very high energies via the Fermi mechanism (Gaisser et al., 1995). Particularly, if the jet is pointed towards Earth, the emission in the rest frame is relativistically boosted and might enhance the observed fluxes. On smaller scales, accreting stellar-mass black holes in binary systems that emit jets might also be capable of producing high-energy neutrinos (Levinson & Waxman, 2001).

The recently discovered emission from the so-called Fermi bubbles, two large lobes of gamma radiation extending perpendicular to the galactic plane (Carretti et al., 2013), has been associated with hadronic models (Crocker & Aharonian, 2011; Lacki, 2014; Thoudam, 2013), which could be put to the proof by the observation of a spatially correlated neutrino signal. Additionally, the galactic disc itself is a bright source of diffuse gamma-ray emission

[1] A similar effect has been proposed to arise for high-energy neutrinos interacting with the low-energy relic neutrino background (Waxman, 1998). However, this cut-off occurs at energies $\gtrsim 10^{12}\,\mathrm{GeV}$, which is some orders of magnitude higher than the energies relevant in this work.

(Ackermann et al., 2012), which can be explained by the interaction of cosmic rays with the interstellar medium and the subsequent decay of the secondary neutral pions. The decay of simultaneously produced charged pions would result in a flux of cosmic neutrinos from the galactic disc (Stecker, 1979). A quasi-guaranteed diffuse signal of neutrinos was predicted by Greisen (1966); Zatsepin & Kuz'min (1966) from the interaction of the highest-energy cosmic rays with the omnipresent cosmic microwave background photons. Again, these would produce charged and neutral pions that would give rise to a flux of cosmogenic neutrinos and photons from their subsequent decay (see Ahlers et al., 2010, for recent predictions of the neutrino flux).

Moreover, attempts are made to test scenarios beyond the Standard Model for particle physics by means of high-energy neutrinos, such as certain models for non-baryonic dark matter. Some theories explain the dark matter content of the universe by a weakly interacting massive particle, that is, a stable particle that interacts only gravitationally and via the electroweak force. Such particles would accumulate in dense regions like the Sun or the Earth, giving rise to an increased self-annihilation rate in the core of these objects (see, e.g., Gould, 1988). These scenarios can be put to the test by the observation of the resulting interaction products – in particular neutrinos, since they alone can escape the core of the dense objects. Consequently, neutrinos represent an ideal messenger to probe the dark-matter density profile in the universe.

Gamma-ray bursts (GRBs), intense short-term outbursts of gamma rays (see Gehrels & Mészáros, 2012, for a recent review), are among the most powerful cataclysmic processes in the universe and thus highly suitable candidates for the acceleration of the most energetic cosmic rays (Waxman, 1995a). The gamma-ray emission lasts only in the order of seconds to minutes, whereas the so-called afterglow can be observed in lower energy bands up to several days. The bursts seem to be correlated with the formation of a black hole and the ejection of material in relativistic jets pointed towards the observer. The electromagnetic signal can be explained by the acceleration of electrons in shock fronts within these jets, followed by inverse Compton scattering of the emitted photons. The relativistic beaming of the jet towards Earth serves to explain the highly energetic photon signal with variability on time scales of only milliseconds. We naturally assume that the jet outflow is not exclusively leptonic, but contains a fraction of hadronic material. Charged hadrons would be accelerated in the shock fronts similarly to the electrons. Again, the only unambiguous test for these scenarios can be provided by the discovery of simultaneously produced neutrinos from the photohadronic interactions with the local photon field in these environments. This work will be mainly dedicated to the development of detection techniques for neutrino signals from GRBs.

Up until recently, no compelling evidence of high-energy cosmic neutrinos had been reported by any experiment, and only upper limits on the flux had been derived. Then, in 2013, the IceCube collaboration announced their first detection of a high-energy cosmic neutrino signal (Aartsen et al., 2013a, 2014) – a tremendous breakthrough, demonstrating that the field is drawing closer and closer to the goal of finally probing the universe in the 'light' of neutrinos. In a 3–year data set from 2010 to 2013, 37 neutrino candidates with energies up to 2 PeV could be identified, an observation which is incompatible with the pure background hypothesis at a significance level of 5.7σ. The arrival directions of the reconstructed data events in equatorial coordinates are shown in Figure 1.1, showing no

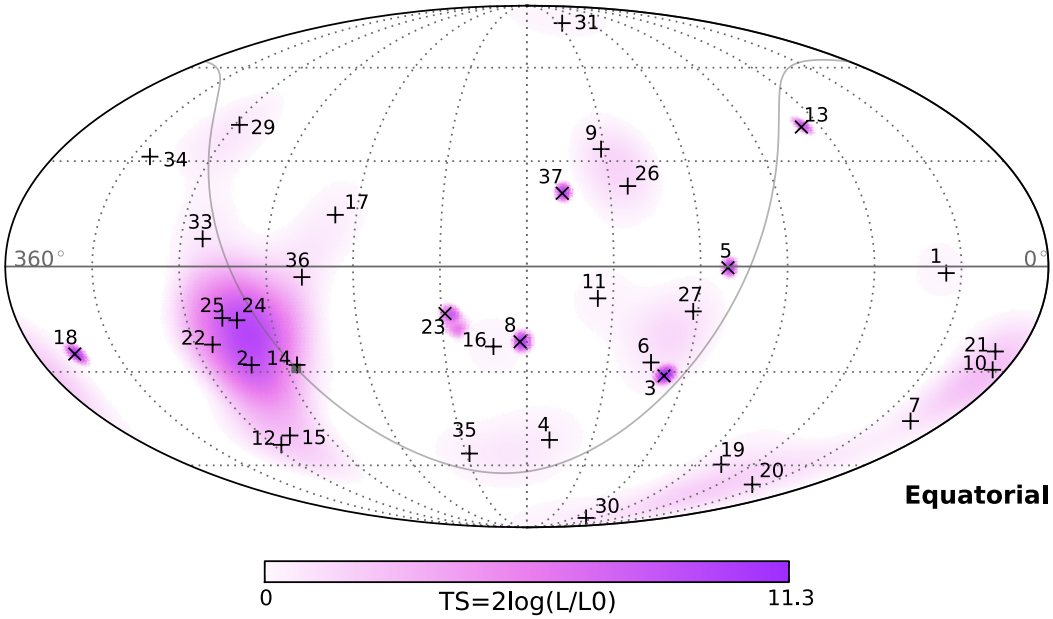

FIGURE 1.1.: Sky map in equatorial coordinates RA and δ of the first significant evidence for a cosmic neutrino signal in the ICECUBE data from the years 2010 to 2013. Cascade–like event signatures are marked with $+$, muon events are marked with $\times$. The probability for a point source at each of the locations is color-coded. No indication for significant clustering could be found. (Figure from Aartsen et al., 2014)

conclusive evidence for a significant clustering in any area in the sky. Some attempts have been made to associate part of the neutrino flux with the galactic center (Razzaque, 2013a; Gonzalez-Garcia et al., 2014) or the galactic halo (Taylor et al., 2014). However, hypotheses of neutrino point source in the direction of the center of the Milky Way inferred from the first 2 years of the ICECUBE data could be rejected given the non-observation of the claimed flux with the ANTARES neutrino telescope (Adrián-Martínez et al., 2014). Up to now, the observed signal is still consistent with the assumption of isotropic sky distribution.

Outline of This Work

In the following work, I will present analyses of data from the Antares neutrino telescope in the search for neutrino signals associated with gamma-ray bursts. The main incentive is to discover correlations of the electromagnetic emission with high-energy neutrinos, which could for the first time unambiguously prove the acceleration of hadrons in the sources and help to demystify the origin of the observed ultra-high-energy cosmic ray flux. I will introduce the sources in detail in Section 2, where their discovery, the presumable emission mechanisms and recent observations will be discussed. The Antares detector will be presented in Section 3. In Section 4, prospects will be investigated to refine the directional reconstruction of particle trajectories in the instrument by identifying presumable systematic effects in the data reconstruction algorithms (Section 4).

I will examine a simple counting technique and its capabilities to identify a signal over background in the data of a showcase burst in Section 5. Three parameters will be studied, upon which the data selection criteria can be optimized, and their performances and limitations will be discussed. Elaborating on this basic approach, a more sophisticated method will be developed in Section 6 that will take into account the different characteristics of expected signal and background distributions to efficiently distinguish between the two. This technique will be optimized in terms of maximal detection probability, and data from the telescope from the period between the end of 2007 and 2011 will be subsequently scanned in the search for a high-energy neutrino signal associated with gamma-ray bursts. I published the results in the article Adrián-Martínez et al. (2013d), hence Section 6 and, in parts, Sections 2 & 3, reproduce and extend this publication. A similar method will also be employed to search for a signal from the exceptionally bright burst GRB130427A that occurred in 2013 (Section 7). In Section 8, I will also discuss the estimated performances of the future KM3NeT telescope to distinguish a GRB neutrino signal from the background.

With most previous searches focused on coincident neutrino emission, I will develop a novel approach allowing to identify a GRB-associated neutrino signal with unknown time shift with respect to the electromagnetic signal. In Section 9, its power to detect a presumable test signal will be discussed and quantified. In addition to a six-year data-set from the Antares detector, this technique will moreover be applied to scan public IceCube data from its IC40 period.

2. GAMMA-RAY BURSTS

Gamma-ray bursts (GRBs) are short and very intense flashes of high-energy gamma rays, which occur unpredictably and isotropically in the sky (Meegan et al., 1992). Over time scales of a few seconds, they release as much energy as the Sun in its entire lifetime, which makes them the most violent explosions known in the universe (see Piran, 2004; Mészáros, 2006; Woosley & Bloom, 2006; Gehrels & Mészáros, 2012, for recent reviews). The high-energy prompt emission that may outshine the whole gamma-ray sky is usually followed by rapidly fading afterglow radiation in lower energy bands, which can sometimes be observed up to several weeks later. GRBs were first discovered accidentally in 1967 by the *Vela* satellites, dedicated instruments to monitor the Nuclear Test Ban Treaty that has been put into force by the United States, Great Britain and the Soviet Union. In total, sixteen flashes of $\sim$ MeV photons were detected by the satellites in a period of three years, yet none of them matched any known nuclear weapon test signature. However, rough determination of the sky positions from triangulation could definitively rule out terrestrial or solar origin (Klebesadel et al., 1973).

In 1991, the *Compton Gamma Ray Observatory* with its Burst and Transient Source Explorer (BATSE) was launched to further investigate the bursts' nature. Within nine years of operation, it could identify 2704 GRBs as shown in Figure 2.1. Their isotropic distribution indicated an origin either in the closest vicinity or outside the Milky Way (Meegan et al., 1992). Together with the first afterglow measurements in 1997 (van Paradijs et al., 1997; Metzger et al., 1997), the cosmic origin of gamma-ray bursts could be confirmed beyond any doubt. The duration of a gamma-ray burst is usually given as the time T_{90} in which 90% of the photon flux is detected[1]. The respective distribution measured by BATSE shows a doubly peaked structure, which led Kouveliotou et al. (1993) to the classification of GRBs into two distinct types (see also Paciesas et al., 1999). In addition, the different spectral feature strengthened the discrimination into two separate populations – short bursts with $T_{90} \lesssim 2\,\mathrm{s}$ usually show harder photon spectra than long ones ($T_{90} \gtrsim 2\,\mathrm{s}$).

To allow for a better understanding of the GRB origins, longer observation times and the detection of counterparts to the gamma radiation in different wavelengths were mandatory. This required fast and accurate positioning of a burst and the immediate notification of its occurrence, so that ground-based telescopes could rapidly point towards the determined sky position and capture the fast-fading afterglow. BATSE began to send alerts of a detected GRB back to Earth and around the world, and since then, many spacecraft and telescopes have joined in doing so. Nowadays, a global network known as the Gamma-ray burst Coordinates Network (GCN) allows to quickly distribute the positions of bursts via the GCN Notices, and the refinement or follow-up analyses via GCN Circulars and Reports.

The Italian-Dutch satellite *BeppoSAX* launched in 1996 was able to localize GRBs with a precision of arcminutes. The immediate distribution of the accurate sky positions allowed

[1] See Zhang et al. (2014) for a recently proposed alternative approach introducing T_{burst}.

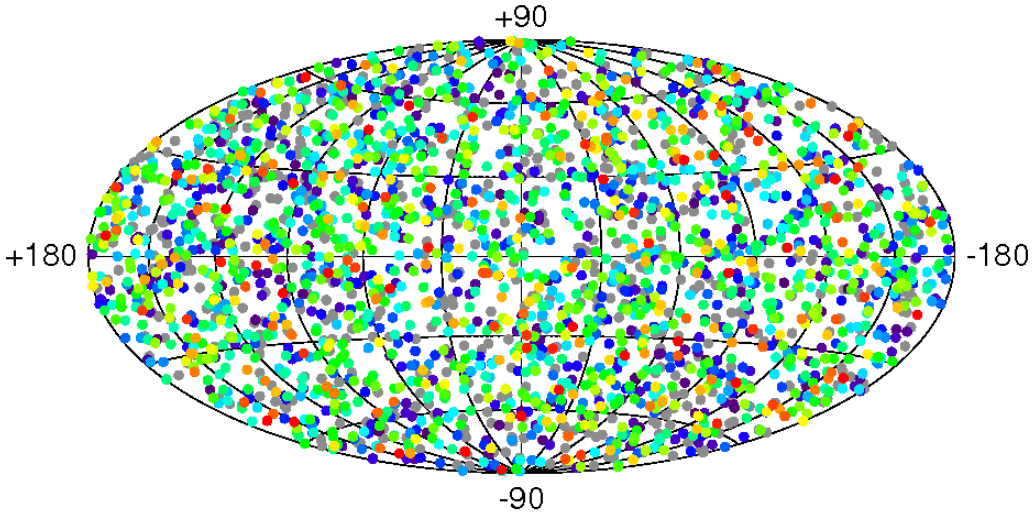

FIGURE 2.1.: The distribution of 2704 bursts detected by BATSE between 1991 and 2000 in galactic coordinates. The uniformity of the distribution strongly points toward an extragalactic origin of the bursts (Meegan et al., 1992) (Figure from `http://www.batse.msfc.nasa.gov/batse/grb/skymap`)

for fast follow-up observations with telescopes on Earth, and the first X-ray and optical afterglow could be measured (Costa et al., 1997; van Paradijs et al., 1997). The spectral features of the optical counterpart are highly valuable for determining the distance of the source. When absorption or emission lines of particular elements can be unambiguously identified in the optical spectrum, their shift with respect to the original line energy directly reflects the cosmological redshift z of the burst. In this way, the cosmic origin of gamma-ray bursts could be confirmed 25 years after their detection with the first measured redshift of $z = 0.695$ for GRB970228 (van Paradijs et al., 1997). Meanwhile, GRBs with cosmological redshifts up to a record-holding 9.4 could be found (Cucchiara et al., 2011). The large distances immediately implied enormous total energy releases exceeding 10^{50} erg, if isotropic emission is assumed.

The detection of the burst GRB980425 in 1998 that was directly followed by the Supernova SN 1998 bw (Galama et al., 1998) implied the connection between long GRBs and the death of very massive stars (see Woosley & Bloom, 2006, for more details), which was later on supported by more precise localization of long bursts within star forming regions and the association of most of the nearby long GRBs with supernovae of type Ib or Ic (e.g. Hjorth et al., 2003). These facts encouraged the growing evidence that long bursts originate from so-called collapsars, in which the core of a massive rotating star, presumably a Wolf-Rayet star (Mészáros & Gehrels, 2012), collapses either into a black hole (MacFadyen & Woosley, 1999) or a strongly magnetized neutron star (Usov, 1992; Soderberg et al., 2006).

The light-curve variability on time scales of milliseconds required very compact sources of $\sim 10^7$ cm, which would in turn imply enormous photon densities with huge optical depths. On the other hand, the observation of clearly non-thermal spectra with photons up to and exceeding GeV energies appeared to contradict this fact and suggested optically thin sources to e^+-e^--pair production. This so-called compactness problem can be overcome by assuming an emission region that is moving relativistically towards the observer. Due to the

relativistic beaming, photons would be observed at higher energies than in the laboratory frame (Schmidt, 1978; Goodman, 1986). To explain the hardness of the observed spectra, Lorentz factors of a few hundred are required. This would on the one hand side reduce the photon energy at the source, while at the same time allowing the emission region to be larger.

With growing observational evidence, a global picture could be established in which GRBs are explained by a cataclysmic explosion and the formation of a central compact object. This inner engine powers highly relativistic outflows of material collimated in jets along the rotational axis. The observed electromagnetic radiation is explained by an over-pressured fireball of electrons and photons that is moving relativistically along the line of sight (Mészáros & Rees, 1993; Piran, 1998). Instabilities in the ejecta give rise to shock fronts, in which kinetic energy is dissipated into internal energy. Electrons are accelerated via the Fermi mechanism (Fermi, 1949; Longair, 1994) up to ultra-relativistic energies. The synchrotron emission of the relativistic electrons in the local magnetic field and subsequent inverse Compton-scattering of the emitted photons result in the observed gamma radiation (Daigne & Mochkovitch, 1998). When the ejecta crash into the surrounding medium, an external shock and an accompanying reverse shock are produced (Mészáros & Rees, 1993, 1997). As the outflow is decelerated further when sweeping up the external matter, the bulk Lorentz factor of the shock decreases constantly, giving rise to the long-lasting decaying afterglow emission in the X-ray, optical and radio wavelengths. However, key questions remained that included the origin of short GRBs, the GRBs' redshift distribution particularly in the early universe, the underlying physics of the ejected material and the most energetic GRB emission.

The launch of the multi-wavelength mission *Swift* (Gehrels et al., 2004) in 2004 has helped enormously to strengthen the previously established collapsar scenario and to address these persisting open issues. With three instruments covering the hard X-ray down to the ultraviolet energy bands, it allowed for the first time to observe the afterglow within minutes after the prompt gamma radiation. It enabled a record-breaking number of GRBs to be detected and well localized, including many short GRBs. Naturally, the measurement of the fast-fading afterglow at lower energies is considerably more challenging for those short bursts, so their origin remained unknown for a long time. However, the fast localization with *Swift* and the *High Energy Transient Explorer* (*HETE-2*) and subsequent follow-up observations revealed that in contrast to the long GRBs, short bursts are not constrained to star-birth regions (Bloom et al., 2006). Nowadays, they are widely accepted to be associated with the merging of two compact objects, neutron stars or black holes, to a final black hole (Eichler et al., 1989; Nakar, 2007). The early afterglow observations by *Swift* have furthermore helped to establish a canonical description of the afterglow, and distinct features could be identified that were associated to late activity of the central engine and to the interaction of the ejecta with the interstellar medium (Nousek et al., 2006; Zhang et al., 2006).

With the *Swift* mission being dedicated to study the prompt and low-energy components of the GRB emission, the *Fermi* satellite was launched in 2008 with two instruments sensitive up to high-energy gamma rays. Covering basically the entire sky (except the part occulted by the Earth), the Gamma-ray Burst Monitor GBM (Meegan et al., 2009) detects around 300 GRBs per year and provides spectroscopic information of the gamma-ray

emission in unprecedented detail. Together with the Large Area Telescope LAT (Atwood et al., 2009), energies over seven orders of magnitude are covered from $\sim$ keV up to and exceeding 300 GeV. The LAT instrument observed the late onset of a distinct GeV power-law component with a smooth and slow decay associated with several bright GBM bursts (Ackermann et al., 2013), which supports models of high-energy photon emission from synchrotron processes in the external shock (Kumar & Barniol Duran, 2009; Ghisellini et al., 2010). However, the observations of a very exceptional burst in 2013, GRB130427A, seemed to challenge these interpretations: The main GeV emission began only after the strongest MeV emission had faded, with the record-holding highest energy photon of 95 GeV being observed as late as 244 s after the prompt emission. Together with another photon of 32 GeV after more than 9 hours, this observation contradicts the standard interpretation of the synchrotron afterglow from Fermi-accelerated electrons in the external shock, since both exceed the maximum photon energy as a function of time as expected within this scenario (Ackermann et al., 2014).

However, the delayed and long-lasting high-energy emission could also be explained by hadronic models including synchrotron radiation or photohadronic cascades (Asano et al., 2009; Razzaque et al., 2010; Wang et al., 2006). It is assumed and also a natural requirement in these scenarios, that the ejecta not exclusively contain electrons, but also baryonic material. The charged particles would be accelerated in the shock fronts similarly to the electrons. Waxman (1995b) showed that protons could be accelerated up to $\sim 10^{20}$ eV, which might serve to explain part of the observed cosmic rays at ultra-high energies. The interaction of the accelerated protons with the present photon field would inevitably result in the emission of high-energy neutrinos accompanying the electromagnetic signal of the burst (Waxman, 1995a; Waxman & Bahcall, 1997; Waxman, 2000). The detection of neutrinos from GRBs would consequently bring unambiguous proof for the hadronic acceleration in these sources, and could help to understand the nature of the most energetic cosmic rays. High-energy neutrino detectors could therefore hold valuable information to put such models to the proof.

Several limits over a wide range of energies have been placed on the coincident neutrino emission from gamma-ray bursts, for instance from experiments such as Super-Kamiokande (Fukuda et al., 2002), AMANDA (Achterberg et al., 2008), Baikal (Avrorin et al., 2011), RICE (Besson et al., 2007), and ANITA (Vieregg et al., 2011). Data from the Antares detector in its construction phase in 2007 with the first five detection lines deployed (Adrián-Martínez et al., 2013c) and from IceCube in its IC22, IC40, and IC59 detector phases (Abbasi et al., 2010, 2011, 2012) have previously been analyzed in the search for this emission, with corresponding limits set in the TeV to PeV energy range.

Beyond the standard searches for neutrino emission in the regularly collected data from the Antares telescope, other search strategies have been implemented that can notably enhance the detection capabilities. A dedicated triggering algorithm is operating that stores all raw data to disk as soon as a burst alert from the GCN network is received (Bouwhuis, 2005; Bouwhuis, 2007, 2008). Requiring spatial and timing coincidence with an announced GRBs allows for relaxed constraints in the photon pulse selection with respect to the standard data filters. Bouwhuis (2005) could show that this approach increases the sensitivity in particular for neutrinos of $\sim$ TeV energies. Analyses of these data are in progress. Moreover, a multi-messenger detection technique has been implemented as proposed by

Kowalski & Mohr (2007). It is based on the optical and X-ray follow up of peculiar events in the data such as several coincident neutrinos in space and time, or signatures of exceptionally high energies (Dornic et al., 2011; Ageron et al., 2012). Within the so-called TAToO project, a network of robotic optical telescopes and the XRT instrument on-board *Swift* are triggered by specifically selected ANTARES data events to enhance the sensitivity to transient sources such as GRBs, flaring active galactic nuclei or supernovae. Alternative approaches have been developed that include the search for downgoing muon tracks induced by $\sim$ TeV photons from gamma-ray bursts (Astraatmadja, 2011) or the search for coincident gravitational wave and neutrino signals from short GRBs without any electromagnetic counterpart (Baret et al., 2011, 2012; Adrián-Martínez et al., 2013a). However, none of the aforementioned analyses has brought any compelling evidence for neutrino signals from GRBs yet.

2.1. PROMPT PHOTON EMISSION

Internal shocks emerge in the relativistic outflows from the central engine due to collisions and instabilities within the ejecta (see, e.g., Gehrels & Mészáros, 2012, and references therein). Charged particles can be accelerated up to ultra-relativistic speeds by passing these shock fronts multiple times, experiencing a slight energy gain with each passage of the shock front. Inhomogeneities in the local magnetic field can reflect the particles so that they pass the front repeatedly, each time experiencing a slight energy gain (Fermi, 1949; Longair, 1994). By this Fermi shock acceleration mechanism, the particles will eventually be power-law distributed in energy, i.e. $\mathrm{d}N/\mathrm{d}E \propto E^{-p}$, with spectral index $p = 2$. Due to the local magnetic field, the accelerated electrons will emit synchrotron radiation, and the emitted photons themselves can subsequently be up-scattered off the electrons via the inverse Compton process. The photon energy spectrum is determined by the electron distribution, and is consequently expected to follow a power-law. A steepening of the energy distribution as observed in most of the GRBs' photon spectra is introduced by the effective radiative cooling of the most energetic electrons.

Different functional forms are used to describe the observed photon spectra, depending not only on the quality of the measurement by a satellite and its energy range, but also on apparent intrinsic differences in the individual GRBs' energy spectra, which have prevented establishing a global model for the electromagnetic emission so far (see, e.g., the spectral diversity in the *Fermi*:GBM catalog as described in Gruber et al., 2014). These functions include single or broken power-laws, power-laws with exponential cut-off (comptonized models) or smoothly broken power-laws. A very successful empirical model to describe the photon spectra observed from many GRBs was introduced by Band et al. (1993). It smoothly combines two power-laws at a transition energy ϵ_{peak}, where the curvature at this transition introduces another free parameter. The emission observed by the LAT instrument in the GeV range can be described in most cases by an additional high-energy power-law component (Ackermann et al., 2013).

2.2. MODELS FOR NEUTRINO EMISSION

Waxman & Bahcall (1997) were the first to calculate the expected neutrino flux in coin-

cidence with the electromagnetic GRB in the framework of the standard fireball internal shock model, using averaged burst parameters as measured by the BATSE instrument onboard the *CGRO* satellite (Band et al., 1993). Their calculation was based on the assumption of Fermi-accelerated protons in the relativistic ejecta of the burst interacting with the associated photon field to produce pions via the Δ^+-resonance. The protons are assumed to follow a power-law-like distribution from the Fermi acceleration, while the photon field corresponds to the measured electromagnetic spectra at Earth; for simplicity reasons, the authors based their first calculations on a broken power-law spectrum with typical photon indices $\alpha \sim 1$ and $\beta \sim 2$, with a transition at the break energy $\epsilon_{\mathrm{break}} \sim 1\,\mathrm{MeV}$.

The photohadronic interactions via the Δ-resonance produce charged and neutral pions, where the subsequent decay of the charged pions and muons gives rise to a high-energy neutrino signal accompanying the electromagnetic emission:

$$
\begin{aligned}
p + \gamma \xrightarrow{\Delta^+} & \begin{cases} p + \pi^0 \\ n + \pi^+ \end{cases} \\
& \pi^0 \longrightarrow \gamma + \gamma \\
& \pi^+ \longrightarrow \mu^+ + \nu_\mu \\
& \mu^+ \longrightarrow e^+ + \nu_e + \overline{\nu}_\mu \\
& n \longrightarrow p^+ + e^- + \overline{\nu}_e \,.
\end{aligned}
\tag{2.1}
$$

Within this picture, the shape of the neutrino flux is basically determined by the proton and photon-field distributions, with a steepening of the neutrino spectrum introduced by the photon spectral break. The authors emphasize that the secondary charged pions would be subject to synchrotron losses in the ambient magnetic field similarly to the electrons, such that high-energy pions efficiently loose energy before they can decay. This introduces a second steepening of the neutrino energy distribution. Waxman & Bahcall (1997) normalized the neutrino spectrum assuming that gamma-ray bursts are the unique source of the cosmic ray flux between $10^{10}\,\mathrm{GeV}$ and $10^{12}\,\mathrm{GeV}$, and that it is composed entirely of protons. Their prediction is referred to as the standard Waxman-Bahcall GRB neutrino flux, and was for instance used to set limits on the coincident neutrino flux from GRBs with the BAIKAL (Avrorin et al., 2011) and AMANDA (Achterberg et al., 2008) experiments.

Guetta et al. (2004) modified the formulae of Waxman and Bahcall to derive individual neutrino fluxes for the bursts. In addition to accounting for the particular parameters of each GRB, the authors introduced a per-burst normalization of the neutrino prediction based on the respectively measured photon fluence. Moreover, the calculations incorporated the transformations between the observer's and laboratory reference frames. The prompt neutrino spectrum (see Abbasi et al., 2010, Appendix A) is thus given by a double broken power-law

$$
F_\nu(E_\nu) = \frac{\mathrm{d}N(E_\nu)}{\mathrm{d}E_\nu} = f_\nu \cdot \begin{cases} \left(\frac{\epsilon_1}{\mathrm{GeV}}\right)^{\alpha_\nu} \left(\frac{E_\nu}{\mathrm{GeV}}\right)^{-\alpha_\nu} & \text{for } E_\nu < \epsilon_1 \\ \left(\frac{\epsilon_1}{\mathrm{GeV}}\right)^{\beta_\nu} \left(\frac{E_\nu}{\mathrm{GeV}}\right)^{-\beta_\nu} & \text{for } \epsilon_1 < E_\nu < \epsilon_2 \\ \left(\frac{\epsilon_1}{\mathrm{GeV}}\right)^{\beta_\nu} \left(\frac{\epsilon_2}{\mathrm{GeV}}\right)^{\gamma_\nu - \beta_\nu} \left(\frac{E_\nu}{\mathrm{GeV}}\right)^{-\gamma_\nu} & \text{for } \epsilon_2 \leq E_\nu \,, \end{cases}
\tag{2.2}
$$

with photon indices

$$\alpha_\nu = 3 - \beta_\gamma \, , \, \beta_\nu = 3 - \alpha_\gamma \, , \, \gamma_\nu = \beta_\nu + 2 \tag{2.3}$$

and break energies

$$\epsilon_1 = 5 \cdot 10^5 \, \mathrm{GeV} \frac{1}{(1+z)^2} \left(\frac{\Gamma}{10^{2.5}} \right)^2 \left(\frac{\mathrm{MeV}}{\epsilon_\gamma} \right) \tag{2.4}$$

$$\epsilon_2 = 10^7 \, \mathrm{GeV} \frac{1}{1+z} \sqrt{\frac{\epsilon_e}{\epsilon_B}} \left(\frac{\Gamma}{10^{2.5}} \right)^4 \left(\frac{t_{\mathrm{var}}}{0.01 \, \mathrm{s}} \right) \sqrt{\frac{10^{52} \, \mathrm{erg/\,s}}{L_\gamma^{\mathrm{iso}}}} \, . \tag{2.5}$$

The first break is introduced by the steepening of the photon spectrum at ϵ_γ and is thus due to effective synchrotron cooling of the electrons in the magnetic field. The same mechanism leads to energy losses of the secondary muons resulting in another steepening of the neutrino flux at ϵ_2, which then depends on the fraction of the total jet energy in electrons ϵ_e and the magnetic field ϵ_B. The jet Lorentz boost factor Γ and the assumed isotropic luminosity L_γ^{iso} (in case of no collimation of the outflow) as well as the variability time scale t_{var} also influence the energy breaks. The term $(1+z)$ accounts for the cosmological redshift z of the GRB.

The normalization depends on the strength of the photon flux as well as on the total fraction of the energy transferred from protons to pions. On average, $\langle x_{p\to\pi} \rangle$ = 20% of the proton energy is transferred to the pion in each interaction (Guetta et al., 2004; Waxman & Bahcall, 1997). In total, $1 - (1 - \langle x_{p\to\pi} \rangle)^{\Delta R / \lambda_{p\gamma}}$ of the energy is converted, where ΔR is the size of the shock region and $\lambda_{p\gamma}$ is the mean free path of a proton for photo–meson interactions. Their ratio is given by

$$\frac{\Delta R}{\lambda_{p\gamma}} = \left(\frac{L_\gamma^{\mathrm{iso}}}{10^{52} \, \mathrm{erg/\,s}} \right) \left(\frac{0.01 \, \mathrm{s}}{t_{\mathrm{var}}} \right) \left(\frac{10^{2.5}}{\Gamma} \right)^4 \left(\frac{\mathrm{MeV}}{\epsilon_\gamma} \right) . \tag{2.6}$$

This yields the neutrino spectrum normalization of

$$\int_0^\infty \mathrm{d}E_\nu F_\nu(E_\nu) = \frac{1}{8} \frac{1}{f_e} \left(1 - (1 - \langle x_{p\to\pi} \rangle)^{\Delta R / \lambda_{p\gamma}} \right) \cdot \mathcal{F}_\gamma \, , \tag{2.7}$$

with the gamma fluence $\mathcal{F}_\gamma$ measured by the satellite, and the fraction of jet energy in electrons f_e.

The intrinsic parameters of the emission regions like the boost factor, the energy partitions in the jet and the variability time scales cannot reliably be determined and are usually set to default values. To ensure consistency with other published analyses, standard parameters as given in Table 6.2 (Section 6.1) will be used throughout this work.

In principle, different break energies are predicted for muon neutrinos and antineutrinos, since the first are produced in pion decays, while the latter are produced in the muon decay (see Guetta et al., 2004, Equation A10 and A11, and Equation 2.1). This yields three breaks in the combined $\nu_\mu + \bar{\nu}_\mu$ spectrum as shown in Figure 2.2 (a), blue dashed. In the previous ANTARES analysis of data from the detector's construction phase in 2007 (Adrián-Martínez et al., 2013c), this effect has been accounted for. Other searches with the ICECUBE (Abbasi et al., 2010, 2011, 2012), RICE (Besson et al., 2007), and ANITA (Vieregg et al., 2011)

experiments made use of the simplified predictions (see Figure 2.2 (a), blue solid). Note in particular that the most recent IceCube limit was a factor of 2.1 below the predicted neutrino flux. This could either indicate the need for rejection of the model, a modification of the parameters upon which it is based, or for more detailed modeling of the neutrino emission within the fireball paradigm.

However, more recent calculations for instance by Hümmer et al. (2012) demonstrated that the neutrino flux predictions from Guetta et al. (2004) are reduced by one order of magnitude when taking into account the full photon distribution, the full width of the Δ^+ resonance, the energy losses of secondary particles and the energy dependence of the proton mean free path in the source (see also He et al., 2012).

Furthermore, the group developed numerical calculations of GRB neutrino spectra based on the Monte Carlo algorithm SOPHIA (Mücke et al., 2000) to simulate the underlying particle physics. Their 'Neutrinos from Cosmic Accelerators' code (NeuCosmA) is described and discussed in detail in Hümmer et al. (2010); Hümmer (2013); Baerwald (2013). It accounts for the full proton-photon cross section and includes not only the interaction via the Δ^+ resonance (Equation 2.1), but also the production of kaons leading to a high-energy component in the ν_μ flux via

$$\begin{aligned} p + \gamma \longrightarrow & K^+ + \Lambda/\Sigma \\ & K^+ \longrightarrow \mu^+ + \nu_\mu \\ & \pi^- \longrightarrow \mu^- + \overline{\nu}_\mu \end{aligned} \tag{2.8}$$

In addition, the authors emphasize that simultaneously produced multiple pions dominate the photohadronic cross section above $\sim 1\,\mathrm{GeV}$ (Hümmer et al., 2010). The decay of the negatively charged pions also contributes to the expected neutrino flux via

$$\begin{aligned} \pi^- \longrightarrow & \mu^- + \overline{\nu}_\mu \\ & \mu^- \longrightarrow e^- + \overline{\nu}_e + \nu_\mu \,. \end{aligned} \tag{2.9}$$

The interaction products and their energy losses are treated individually, and the mixing of neutrino flavors on their way to Earth is included. No new assumptions on the sources are introduced, but known particle physics governing the photohadronic interactions are applied in greater detail within the fireball model.

In Figure 2.2 (a), the predicted neutrino spectrum from Guetta et al. (2004) is compared to the NeuCosmA model for GRB110918. Figure 2.2 (b) shows all individual numerical neutrino spectra for the 296 gamma-ray bursts selected for the search that will be presented in Section 6, and their cumulative spectrum.

Predictions made by the NeuCosmA model were used to optimize the analyses presented in Sections 6 & 7. None of the previously published searches had employed any of the second-generation numerical calculations.

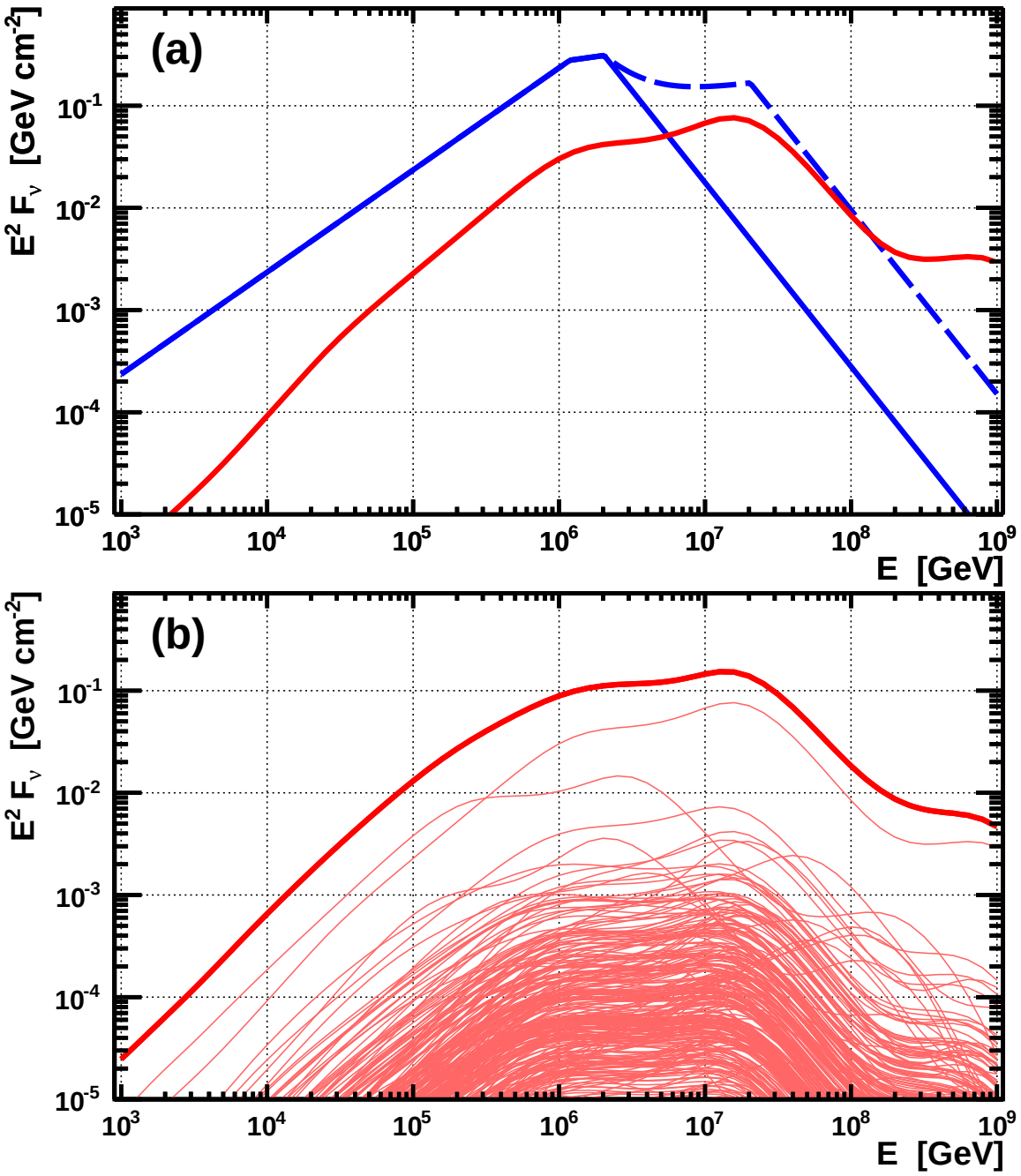

FIGURE 2.2.: (a): Predicted neutrino spectra E^2F_ν versus neutrino energy from $\nu_\mu + \bar{\nu}_\mu$ for GRB110918. The analytic model by Guetta et al. (2004) (blue) is shown with the usual simple treatment (blue solid) and accounting for different break energies of ν_μ and $\bar{\nu}_\mu$ (blue dashed). The numerical NeuCosmA prediction is presented in red. (b): Individual $\nu_\mu + \bar{\nu}_\mu$ NeuCosmA spectra of 296 GRBs from late-2007 to 2011 selected in Section 6.1 (thin lines) and their sum (thick line). (Figure from Adrián-Martínez et al., 2013d)

3. The Antares neutrino telescope

The underwater neutrino telescope Antares (see Ageron et al., 2011) is primarily designed for detecting highly relativistic muons from charged current interactions of cosmic muon neutrinos[1] with matter in or close-by to the detector. The passage of these muons through the seawater induces the emission of Cherenkov light that is then detected by a three-dimensional array of photo-multiplier tubes (PMTs). Using the time and position information of the detected photons, the muon trajectory is reconstructed, from which the original neutrino direction can be inferred (for further details on the detection principle, see Katz & Spiering, 2012).

The detector is located in the Mediterranean Sea at a water depth of 2.4 km. It comprises twelve vertical 'strings' anchored to the seabed, each of which is held upright by a buoy at the top. They are separated from each other by a typical distance of 70 m. The twelve strings, each with a length of 480 m, are equipped with 25 triplets of PMTs – so-called storeys –, building an array of 885 PMTs in total[2]. The storeys have a vertical spacing of 14.5 m between them, whereas the first is placed at a height of 100 m above the seabed. The construction of the telescope started in 2007 with the first five detection lines. Between December 2007 and May 2008, it was then completed to its final twelve-line configuration with an instrumented volume of $\sim 11 \cdot 10^6\,\mathrm{m}^3$. An artist's view of the detector in the deep sea is shown in Figure 3.1.

Radioactive ^{40}K in the deep-sea water produces a constant rate of light of $\sim$ 37 kHz in the photodetectors due to the Cherenkov radiation of the protons produced by its β decay. Together with a dark noise of $\sim$ 3 kHz, it constitutes one of the main random optical background contributions in the data (Amram et al., 2000). Bioluminescent organisms in the deep sea introduce additional sources of background light. Large-scale creatures such as shrimps passing through the instrumentation volume can produce flashes of light in the PMTs close-by, which vary on time scales of seconds and are confined to the direct vicinity of an optical module. Large clouds of luminous bacteria, on the other hand, also emit photons and increase the optical background in the whole detector. The organic activity shows slow variations of hours up to months with a maximum in the spring seasons, during which the background rate can increase up to several hundred kHz per PMT. This basically prevents regular data taking in these periods. The dependency of the bioluminescent rate on the seawater salinity, the oxygen content, the temperature and the speed of the sea current has been investigated in detail in Tamburini et al. (2013). The authors emphasize in particular the influence of the convection of water layers in the Mediterranean Sea that can transport large amounts of organic material from the surface layers to the deep.

Within the Antares data acquisition concept, all recorded signals are first sent to shore, where a multi-level online triggering procedure operates on the data stream to select pos-

[1] Throughout this work, 'neutrino' will denote both ν and $\bar{\nu}$, and 'muon' will denote both μ^- and μ^+.

[2] One string is equipped with 60 instead of 75 PMTs.

sible particle signatures. The number of active filtering algorithms can be adjusted to the background conditions. In addition to the cosmic neutrino signal that the ANTARES experiment is searching for, there are other processes as shown schematically in Figure 3.1 that can produce muon tracks in the detector and are considered as particle background. High-energy cosmic rays hitting the Earth's atmosphere give rise to cascades of particles, the so-called air showers. The seawater above the detector absorbs most of these particles, but muons and neutrinos are still capable of reaching the instrumented volume from above. However, since only neutrinos are capable of traversing the Earth, it can effectively be used as a shield against all other particles. By selecting only upgoing signatures therefore, the atmospheric muon background of $\sim 4/\mathrm{s}$ can be rejected. Nevertheless, muons from above still produce signals in the detector that can be mis-reconstructed as upgoing events ($\sim 0.4/\mathrm{s}$). Requiring certain quality of the reconstructed tracks, these falsely reconstructed atmospheric muon can efficiently be suppressed to a rate of 0.4 events per day (Adrián-Martínez et al., 2012b). Atmospheric neutrinos produced by cosmic rays below the horizon can also traverse the Earth, and represent the main background component of $\sim 3/\mathrm{d}$ to the cosmic neutrinos. This flux is homogeneously distributed in angle and time and comprises on average less energetic neutrinos than the astrophysical signal. Hence, it can be distinguished from the cosmic flux statistically, yet not on a per-event basis. In total, around 4 signatures per day meet the rather stringent criteria on the reconstruction quality in the ANTARES data (Adrián-Martínez et al., 2012b).

In the searches for coincident neutrino emission from gamma-ray bursts that will be presented in the following, the requirement of temporal and spatial coincidence with a recorded GRB reduces the number of expected background events to $\sim \mathcal{O}(10^{-4})$ per GRB (see Table C.1), and advanced methods like the extended likelihood method can furthermore distinguish statistically between signal and background signatures.

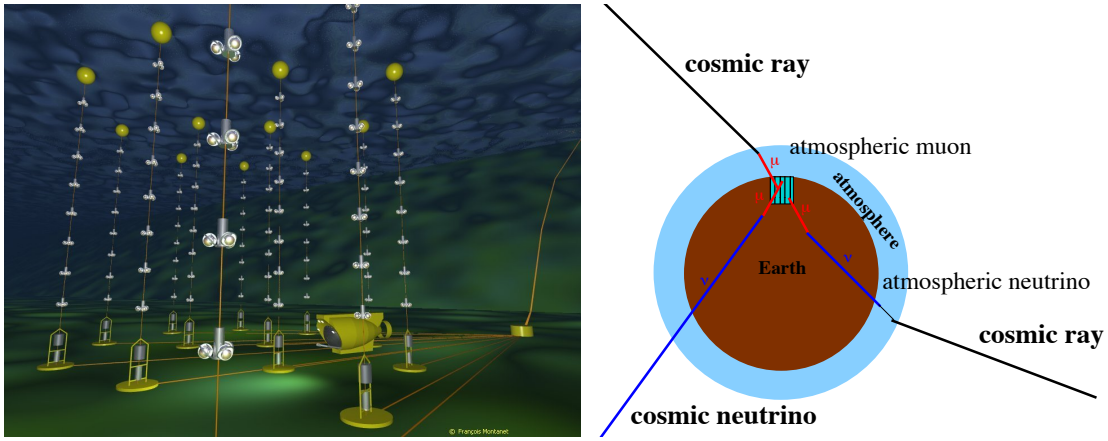

FIGURE 3.1.: *Left:* Artist's view of the ANTARES detector. (Figure by François Montanet). *Right:* Schematic drawing of the signal and background components in the data of neutrino telescopes.

The local coordinate system of the ANTARES detector is defined by means of the two angles zenith and azimuth. The zenith Θ describes the angle between a particle trajectory and a vertical line through the instrumented volume, while rotations around this axis are expressed by the azimuth Φ. The instantaneous field of view of the ANTARES detector when selecting only upgoing signatures is 2π and within a period of 24 hours, the sky up to a

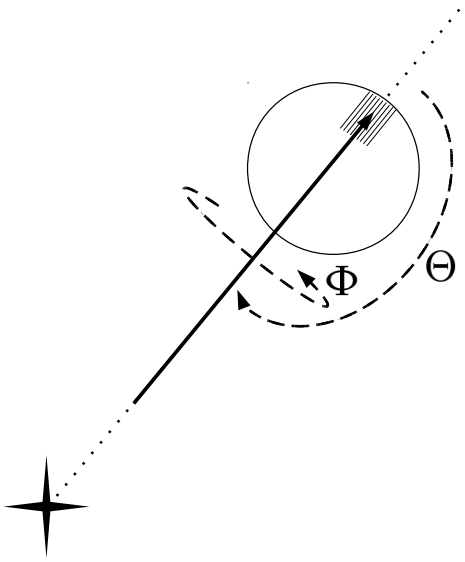

FIGURE 3.2.: Local coordinate system of the ANTARES detector with zenith angle Θ giving the angle with respect to the vertical axis of the detector and azimuth angle Φ for rotations around this axis. The Earth is usually used as a shield against all particles but the neutrino flux, so that only upgoing particle signatures with $\Theta > 90^\circ$ are selected.

declination of 47° is covered.

3.1. DATA TRIGGERING

To manage the enormous amount of data that is recorded by the optical modules, it is crucial to filter those that were taken simultaneously with the presumable passage of a relativistic muon. The algorithms consequently search for Cherenkov light patterns that fit to a particle track hypothesis, and subsequently trigger data acquisition.

Following the 'all-data-to-shore' concept, all PMT signals that exceed a threshold of 0.3 photoelectrons are sent to the data processing farms on shore. In a first step, a sample of photon pulses is selected by requiring either coincident signals in two neighboring PMTs in the same storey within 20 nanoseconds or high-charge pulses above a certain threshold, mostly 3 photoelectrons. This set builds the basis for most of the more sophisticated algorithms, including those sensitive to high-energy muons from the whole sky or from specific directions like the galactic center, triggers for slowly moving particles like magnetic monopoles and algorithms dedicated to multi-messenger searches. Filters for relativistic muons, for instance, select those photon detections that conform with certain space-time causality relations so that they could originate from the same particle track. If the requirements of one of the operational algorithms is met, all PMT signals above 0.3 photoelectrons within a time window of ± 2200 ns around the triggering light pattern are recorded.

The data acquisition can handle more than 50 activations of a single trigger per second.

However, since only at most a few tens of neutrinos per day are expected, and the atmospheric muons arrive at a rate of $\sim$ 4 Hz, trigger rates significantly exceeding 50 Hz are basically dominated by accidental coincident photon pulses from the optical background. If the rate of an individual filtering algorithm exceeds that value, it is therefore disabled. Hence, depending in particular on the background rate, more or less stringent trigger algorithms can be enabled. To continuously monitor the environmental conditions and for trigger efficiency and data quality studies, every ten seconds all raw data within 105 ms is stored directly to disc.

3.2. DATA CALIBRATION

To ensure accurate reconstruction of particle trajectories, it is crucial to determine the exact locations of the optical modules that recorded the Cherenkov signal. Since the detection lines are flexible strings that move slowly with the sea current, an acoustic positioning system monitors the line movements every two minutes (Adrián-Martínez et al., 2012a). It consists of acoustic emitters at the bottom and five hydrophones along each string. The positions of the hydrophones is inferred from geometric lateration of acoustic signals. The shape of each line in the sea current is then fitted using this position information and the data from compasses and tiltmeters that are installed on each storey. In this way, the locations of the optical modules can be determined to a precision of 20 cm.

The exact timing of the recorded data is ensured by a master-clock system located on shore that synchronizes the whole detector down to a nanosecond relative precision (Escoffier & Lambard, 2008; Ageron et al., 2011). Individual time offsets of each optical module with respect to this reference time are determined by means of flashing light sources that can be activated externally. Each detection string is equipped with four LED light sources distributed among the storeys. These beacons are used to calibrate the optical modules above them. For the lowest storeys and the timing difference between the detection lines, laser beacons are installed at the bottom of two strings. In this way, the relative timing of individual OMs as well as the PMT transit times and delays introduced by the electronics can be determined. Two time-to-voltage converters measure precisely the time of a photon hit of each PMT in flip-flop mode. A saw-tooth-like voltage profile allows to interpolate between the received clock pulses to a precision of 0.2 nanoseconds (Escoffier & Lambard, 2008). The overall relative timing resolution is then dominated by the spread in the transit times within the PMTs of $\sim$ 3 ns, with the absolute timing of the data being accurate down to $\mathcal{O}(100\,\text{ns})$.

The amplitude of a recorded signal in the amplitude-to-voltage converter (AVC) has to be converted to the according number of photoelectrons that had triggered the signal (Ageron et al., 2011). This is of particular importance in order to identify the signal representing individual photoelectrons and consequently single photons from the electronic noise. The pedestal AVC signal can be obtained by recording the photo-multiplier signal at random times in dedicated data-taking runs. However, the signal amplitude corresponding to one photoelectron varies in time, so that its distribution has to be compared to the electronic noise regularly. For instance, when resuming data acquisition after the high voltage in the optical modules had been off, one photoelectron gives rise to a higher AVC amplitude than after an extended period of stable data taking. Every two weeks, the single photoelectron

distribution is therefore extracted from measuring the random optical background photon counts in the optical modules. Since the optical background is largely dominated by individual photons, this allows to determine the single photoelectron peak. By comparing this peak to the pedestal AVC signal, the threshold amplitude can be found that distinguishes a photon signal from pure noise from the electronics. This threshold should correspond to 0.3 photoelectrons.

Data from the ANTARES detector are grouped in data-taking runs of several hours. For each of them, the operating trigger algorithms as well as the detector and calibration setup can be adapted to the prevailing environmental conditions. In spring periods, for instance, the increased bioluminescent activity requires the use of very stringent data filtering algorithms, the reduction of voltage at the PMTs, sampling of the data or even stopping of data acquisition.

3.3. EVENT RECONSTRUCTION

For efficient reconstruction of the trajectory of a passing muon through the detector, it is mandatory to first single out those photon counts in a recorded data event that were produced by its Cherenkov light. Relativistic muon trajectories are reconstructed using the timing and position information of detected photon pulses. The algorithm tries to identify the most probable particle track, defined by a starting point and its velocity vector, that could have caused the light pattern of Cherenkov hits recorded by the optical modules (a detailed introduction of the reconstruction algorithm used in this work can be found in Heijboer, 2004). A multi-step algorithm searches for the track hypothesis that maximizes the likelihood to match the measured event signatures. The main ingredient for this likelihood is the probability density function of arrival times of photons for a given particle trajectory and energy.

The reconstruction returns two quality parameters, namely the track-fit quality parameter Λ and the estimated angular uncertainty on the muon track direction β. The quality of a fit is given by

$$\Lambda = \frac{\log(\mathcal{L})}{N_{\mathrm{dof}}} + 0.1(N_{\mathrm{comp}} - 1) \,, \tag{3.1}$$

where $\mathcal{L}$ is the likelihood of a fitted track hypothesis to cause the detected light pulses and N_{dof} is the number of degrees of freedom of the fit. If the algorithm returned several tracks with compatible directions N_{comp}, the fit is assumed to be more robust and the Λ parameter is improved. The estimated angular error of each particle track fit β is calculated from the estimated zenith and azimuth errors σ_Φ and σ_Φ,

$$\beta = \sqrt{\sin^2(\Theta)\sigma_\Phi^2 + \sigma_\Theta^2} \,. \tag{3.2}$$

Event selection criteria based on these two parameters can be used to improve the signal-to-noise ratio. To ensure solid directional reconstruction of the selected neutrino candidates, usual analyses require $\beta < 1^\circ$. Additionally selecting simulated tracks with high reconstruction quality ($\Lambda > -5.2$), most of the atmospheric muons that were falsely reconstructed as upgoing are suppressed without significantly affecting the neutrino signal:

atmospheric muons from above are reduced by a factor of $1.2 \cdot 10^{-5}$, while atmospheric neutrinos are reduced by 0.19. The total background due to cosmic-ray-induced events is decreased by 10^{-6} (Adrián-Martínez et al., 2012b). In searches for associated neutrinos from GRBs as presented in the following (e.g. Section 6), this cut combination would leave $\sim 60 \ldots 70\%$ of a typical gamma-ray-burst neutrino signal unaffected. However, the narrow time windows of a few tens of seconds yield intrinsically low background in coincidence with each burst, allowing for less stringent cuts on the Λ parameter than required in searches for steady sources.

The accuracy to which the primary neutrino direction can be reconstructed is naturally subject to different stochastic processes inherent in the detection technique. Statistical fluctuations are introduced for example by the kinematic scattering of the secondary muon direction with respect to that of the neutrino. With a mean square root of $\sim 1.5^\circ / \sqrt{E_\nu \,/\, \mathrm{TeV}}$ (Gaisser, 1991), however, this becomes a sub-dominant effect at energies exceeding 10^5 GeV. The emitted photon statistics, scattering and absorption of the Cherenkov light in the ambient seawater are additional intrinsic stochastic processes of the detection method that cannot be avoided and that determine and constrain the angular resolution of the experiment. It is furthermore limited by the efficiency and precision to which the arrival times and positions of the detected photons can be determined. Given the relative timing resolution of the photodetectors of 3 ns and their position uncertainty of 20 cm, the limited size of the detector leaves a certain lever arm for the determination of the muon's direction in the order of 0.3°. Prior to the construction of the apparatus, Heijboer (2004) determined an intrinsic limitation of the angular resolution after reconstruction in the order of $\sim 0.2^\circ$, while recent analyses estimate a median pointing resolution of $\sim 0.38^\circ$ for a signal of the shape $\propto E^{-2}$ (Adrián-Martínez et al., 2014).

In Section 4, I will discuss the possibility that the exact location of a muon trajectory and in particular its orientation with respect to the photon detectors might give rise to systematic effects in the reconstructed particle trajectories in addition to the statistical fluctuations that were discussed here.

3.4. MONTE CARLO SIMULATION

In order to determine and understand the response of the ANTARES detector to high-energy neutrinos and to develop and optimize the reconstruction and analysis algorithms, Monte Carlo simulations are employed for both the neutrino signals and the particle background induced by cosmic-ray air showers. All processes from the incident cosmic neutrino at the opposite side of the Earth to the pattern of Cherenkov light pulses detected by the photo-multiplier tubes have to be taken into account. To avoid the unnecessary simulation of neutrinos that might eventually not produce any observable signal in the detector, only neutrino-nucleon interactions in the vicinity of the instrumented volume are simulated. The probabilities for the neutrinos to reach this volume through Earth and interact with a nucleon there are comprised in weights for each individual recorded signal in the detector. In doing so, the number of simulated events can be adjusted to provide sufficient statistics in the high-energy range of $10^6 - 10^8$ GeV, where the detector is most efficient. In addition, a further weighting factor can mimic different incoming neutrino fluxes.

The probability that a cosmic neutrino traverses the Earth and reaches the vicinity of the

instrumented volume is given by its energy-dependent cross-section $\sigma(E_\nu)$ and the incident zenith angle Θ that determines the column density ρ of matter that has been traversed (see, e.g., Katz & Spiering, 2012):

$$P_{\text{Earth}}(E_\nu, \Theta_\nu) = \exp\left(-N_A \sigma(E_\nu) \int \mathrm{d}l\, \rho_\Theta(l)\right) , \tag{3.3}$$

with the Earth density profile $\rho_\Theta(l)$ given by the preliminary reference Earth model introduced by Dziewonski & Anderson (1981). If the high-energy neutrino interacts with a nucleon sufficiently close or within the detector, the hadronic shower from the break-up of the target nucleon and the propagation of secondary leptons are simulated. For the energies under consideration ($\sim 10^3 - 10^9$ GeV), the secondary muon from a charged current interaction of a muon neutrino with a nucleon carries between 60% ... 80% of the neutrino energy, while the remaining goes into the hadronic cascade (see, e.g., Katz & Spiering, 2012). For sufficiently high energies, when the velocity exceeds the speed of light in the seawater, the relativistic leptons induce the emission of Cherenkov light along their trajectory. Around 250 photons per centimeter are emitted with a typical angle of $\Theta_C = \arccos(1/\beta n) \sim 43^\circ$ in seawater.

The response of the PMTs to the emitted Cherenkov light is then simulated, including the conversion of photon hits to detected charge pulses and electronic smearing effects. The software also allows the detector and environmental conditions at a given time to be simulated, for example by adding random optical background noise mimicking the radioactive decay of ^{40}K and the activity of bioluminescent organisms in the seawater. The simulation of Cherenkov light emission itself is confined to a cylindrical volume surrounding the detector, the so-called can. It extends the instrumented volume by approximately 100 m in horizontal and vertical direction, which is well above the absorption length of photons in the seawater ($\sim$ 60 m). High-energy neutrino interactions are simulated within the so-called generation volume V_{gen}. It exceeds the size of the can by the energy-dependent muon range in the medium, so that all interactions are taken into account with secondary particles that could produce any detectable signals in the PMTs. Similarly, muons from cosmic-ray-induced air showers coming from above the detector's local horizon are simulated.

The detection rate R relates to the incoming neutrino flux Φ at Earth as

$$R(E_\nu, \Theta_\nu) = \Phi(E_\nu) \times V_{\text{eff}}(E_\nu, \Theta_\nu) \times \sigma(E_\nu) \times \rho \cdot N_A \times P_{\text{Earth}}(E_\nu, \Theta_\nu) , \tag{3.4}$$

where the detector's efficiency to detect the charged lepton is quantified by the effective volume V_{eff} given by the ratio of the number of well-reconstructed signatures N_{sel} to the number of simulated neutrino interactions N_{gen} times the generation volume V_{gen}.

To account for the probability that a neutrino interacts in the generated volume, each simulated event is weighted by the Earth transmission factor P_{Earth} (Equation 3.3) and the probability for the interaction $\sigma(E_\nu) \times \rho \cdot N_A$. This so–called generation weight $w2$ also comprises the angular and energy phase space factors I_Θ and I_E, in which interactions have been simulated, and the generation volume V_{gen}:

$$w2 = V_{\text{gen}} \times I_\Theta \times I_E \times E^\gamma \times \sigma(E) \times \rho \cdot N_A \times P_{\text{Earth}} . \tag{3.5}$$

The term E^{γ} compensates for the simulated spectrum $\propto E^{-\gamma}$. The energy phase space factor takes into account the number of simulated events in the energy interval:

$$I_E = \int_{E_{\min}}^{E_{\max}} E^{-\gamma} \mathrm{d}E = \begin{cases} \left(E_{\max}^{1-\gamma} - E_{\min}^{1-\gamma}\right) / (1-\gamma) & \text{if } \gamma \neq 1 \\ \ln\left(\frac{E_{\max}}{E_{\min}}\right) & \text{if } \gamma = 1 \,. \end{cases} \tag{3.6}$$

The angular phase space factor I_{Θ} is given by the solid angle in which neutrinos have been simulated:

$$I_{\Theta} = 2\pi \cdot (\cos(\Theta_{\max}) - \cos(\Theta_{\min})) = 2\pi \quad \text{for } \Theta = [90^{\circ}, 180^{\circ}] \,. \tag{3.7}$$

Hence, the weight $w2$ encompasses the ability of the experiment to detect neutrinos of a certain energy and direction.

To estimate the actual number of astrophysical neutrinos that would be measured in an analysis, the simulated events are furthermore weighted by the expected neutrino flux $\Phi(E)$ as predicted by the neutrino-emission model under consideration. In the same way, the background contribution from atmospheric neutrinos can be estimated by weighting the simulated events to the predicted flux from cosmic-ray interactions with the atmosphere (Agrawal et al., 1996).

To account for the changing environmental conditions in time, Monte Carlo simulations are performed for each data run separately, mimicking the detector and triggering setup and the environmental conditions of the respective period.

3.5. EFFECTIVE AREA

The instrument's efficiency to detect neutrinos of given energy and direction can be expressed in terms of the effective area A_{eff}. It can be considered the equivalent area of a 100% efficient detector, and is defined as the ratio between the detected neutrino event rate and the incident cosmic neutrino flux (Katz & Spiering, 2012). For a given neutrino energy E_{ν} with incident zenith angle Θ, it is thus defined as:

$$A_{\text{eff}}(E_{\nu}, \Theta_{\nu}) = R(E_{\nu}) / \Phi(E_{\nu}) = V_{\text{eff}}(E_{\nu}, \Theta_{\nu}) \times \sigma(E_{\nu}) \times \rho \cdot N_A \times P_{\text{Earth}}(E_{\nu}, \Theta_{\nu}) \,. \tag{3.8}$$

Accordingly, it can be calculated from the generation weight using Equation 3.5:

$$A_{\text{eff}} = \frac{N_{\text{sel}}}{N_{\text{gen}}} \times w2 \times \frac{1}{I_{\Theta}} \times \frac{1}{E^{\gamma} \cdot I_E} \,. \tag{3.9}$$

It is interesting to evaluate the effective area in certain declination bands, as it demonstrates the actual detection capability of the instrument for sources in the sky. Equivalently, the angular phase space factor I_{Θ} in Equation 3.7 transforms to account for the number of simulated interactions in different declination bands. For an isotropic sky distribution, the angular phase space factor is given by the solid angle of the declination band $\Delta\delta$. I made use of the per-run Monte Carlo simulations corresponding to the data taken between December 2007 and 2011 (Rivière, 2012) to derive the effective area. Since for each run, an equal number of neutrino interactions N_{gen} had been generated, the different durations of the runs need to be accounted for by weighting each of them by its relative contribution

to the total livetime of the data. Figure 3.3 shows the derived effective areas for different declination bands, selecting upgoing particle signatures that fulfilled the reconstruction quality criteria $\Lambda > -5.4, \beta < 1^\circ$. The rise with energy, a common feature of neutrino telescopes, is due not only to the increase of the neutrino cross-section, but also to that of the muon range, which can reach several kilometers at the highest energies. The ANTARES detector has best visibility for sources in the declination range of -90° to -45°, while the other declination bands are less favorable.

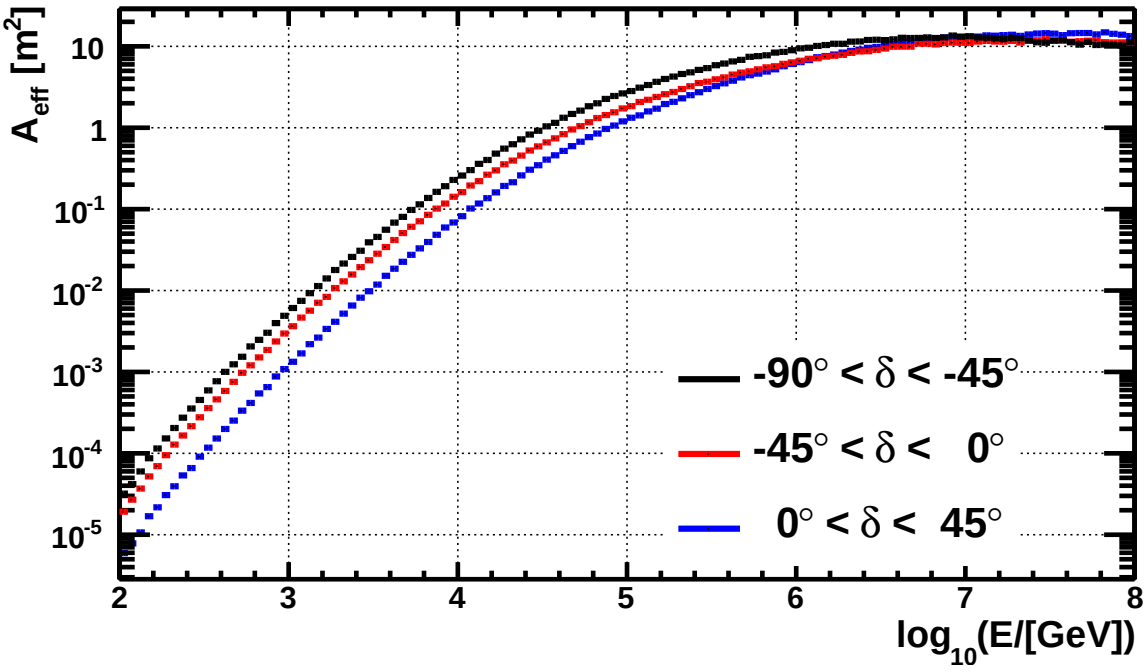

FIGURE 3.3.: Time-averaged muon-neutrino effective area of the ANTARES neutrino telescope as a function of energy for different declination bands δ for the period from December 2007 to 2011. Typical quality cuts ($\Lambda > -5.4$, $\beta < 1^\circ$, $\Theta > \pi/2$) are applied. (Figure from Adrián-Martínez et al., 2013d)

4. Investigation of Track Reconstruction Systematics

As has been described in Section 6.3, the reconstruction of muon-neutrino signatures in the Antares data makes use of the arrival times and positions of detected Cherenkov photons that have been emitted by the secondary muon from a charged current interaction of a cosmic neutrino with the detection medium. Numerous stochastic processes inherent in the detection method limit the precision to which this particle trajectory can be determined. Since the algorithm is based on the detected light pattern, its performance is assumed to be strongly sensitive to the position of the track within the instrumented volume and in particular its orientation with respect to the photon detectors. In the following, I will investigate how the exact location of a particle trajectory within the detector might affect the directional reconstruction and conceivably lead to systematic deviations of the reconstructed trajectory from the simulated muon. In contrast to the intrinsic statistical fluctuations, such an effect could, in principle, be corrected for on an event-by-event basis. This would first require the detection and quantification of any systematic shifts and an exact determination of the parameters of the particle track that introduce them.

Monte Carlo simulations as described in Section 3.4 allow the differences in the primary and reconstructed particle to be compared, which might reveal the existence of such systematic effects. For a large number of simulated muon tracks with fixed position in the detector, direction and particle energy, the reconstructed angles would be expected to show a Gaussian-like distribution around the initial Monte Carlo direction, its width representing the detector's resolution. A systematic error in the reconstruction would show up as a shift of this Gaussian with respect to the true track direction, in particular if the displacement is larger than the detector's resolution. To test for the occurrence of such effects, the detector was systematically scanned with simulated muon tracks, varying both the directions of the particles and their precise position inside the detector. Each of the trajectories had to be simulated repeatedly in order to investigate the distributions of the reconstructed angles.

For each track configuration determined by the direction in local coordinates zenith and azimuth, the position in the detector and the particle's simulated energy, I searched for deviations of the reconstructed coordinates from their initial Monte Carlo value. This is quantified by the median $m(x)$, for which

$$\int_{-\infty}^{m(x)} P(x)\mathrm{d}x = 0.5 \cdot \int_{-\infty}^{+\infty} P(x)\mathrm{d}x \,, \tag{4.1}$$

and standard deviation of the distributions

$$\sigma(x) = \sqrt{\frac{1}{N-1}\sum_{i}^{N}(x - \langle x \rangle)^2} \tag{4.2}$$

$$x = \chi_{\mathrm{reco}} - \chi_{\mathrm{MC}} \qquad \text{for } \chi = (\Theta, \Phi)\,.$$

4.1. TRACK GENERATION

The local coordinates zenith Θ and azimuth Φ were simulated in the ranges

$$\Theta = [0^\circ \dots 180^\circ) \text{ with } \Delta\Theta = 10^\circ \,, N_\Theta = 19 \tag{4.3}$$

$$\Phi = [0^\circ \dots 120^\circ) \text{ with } \Delta\Phi(\Theta) = \lfloor 20^\circ / \sin(\Theta) \rfloor \,, \tag{4.4}$$

where the number of azimuth steps was adjusted to the solid angle of a respective band in zenith. Since the detector's footprint is symmetrical in rotations in azimuth, only one third of the 360° range was scanned. In this way, $N_{(\Theta,\Phi)} = 87$ different directions were generated in total.

For each set of local coordinates, one muon trajectory is defined pointing directly to the detector's center of gravity (CoG). We refer to its origin point as $\mathbf{p_0}$. The (unit) velocity vector of the trajectory pointing to the CoG in spherical coordinates (r, Θ, Φ) is simply given by

$$\mathbf{e_v} = -\mathbf{e_r} = -\begin{pmatrix} \sin\Theta \cdot \cos\Phi \\ \sin\Theta \cdot \sin\Phi \\ \cos\Theta \end{pmatrix} \,,$$

so it will mimic a muon from the direction (Θ, Φ). To illuminate the whole detector, 50 tracks were generated parallel to $\mathbf{p_0}$ with the same velocity vector $\mathbf{e_v}$ but displaced starting points $\mathbf{p}$

$$\mathbf{p_{a,b}} = \mathbf{p_o} + a \cdot \mathbf{e_a} + b \cdot \mathbf{e_b}$$

$$\text{with } \mathbf{e_a} = \mathbf{e_\Theta} = \begin{pmatrix} \cos\Theta \cdot \cos\Phi \\ \cos\Theta \cdot \sin\Phi \\ -\sin\Theta \end{pmatrix} \text{ and } \mathbf{e_b} = \mathbf{e_\Phi} = \begin{pmatrix} -\sin\Phi \\ \cos\Phi \\ 0 \end{pmatrix}$$

as shown schematically in Figure 4.1. All points were thus generated on a plane spanned by the unit vectors of the coordinate system $\mathbf{e_\Theta}$ and $\mathbf{e_\Phi}$ perpendicular to $\mathbf{e_r}$. The dimensions were chosen so as to simulate trajectories through the entire instrumented volume and beyond:

$$a = [-200\,\text{m} \dots 200\,\text{m}) \text{ with } \Delta a = 40\,\text{m}, N_a = 10$$

$$b = [-100\,\text{m} \dots 100\,\text{m}) \text{ with } \Delta b = 40\,\text{m}, N_b = 5 \,.$$

In total, $N_a \cdot N_b = 50$ parallel tracks were generated for each muon direction defined by Θ and Φ. For each $\mathbf{p_{a,b}}$, the intersection point with the can in the direction of $\mathbf{e_v}$ is calculated. This is the cylindrical volume around the instrumented detector, within which the Cherenkov light emission is simulated (see Section 3.4). For each of these defined tracks, muons with eight logarithmically spaced energies in the range $E \in [10^{1.5}\,\text{GeV}, 10^5\,\text{GeV})$ were simulated. This corresponds to primary neutrinos that carry $\sim 25\% \dots 70\%$ more energy (see Section 6.3). Consequently, $N_{(\Theta,\Phi)} \cdot N_a \cdot N_b \cdot N_E = 34800$ different track configurations were defined; each of them was simulated 500 times in order to yield sufficient statistics to study the distributions of the reconstructed attributes. In total, $17.4 \cdot 10^6$ muons were simulated. To mimic realistic environmental conditions, random optical background noise of 60 kHz was added for each optical module, and the simulations were subsequently triggered with standard data filters (see Section 3.1).

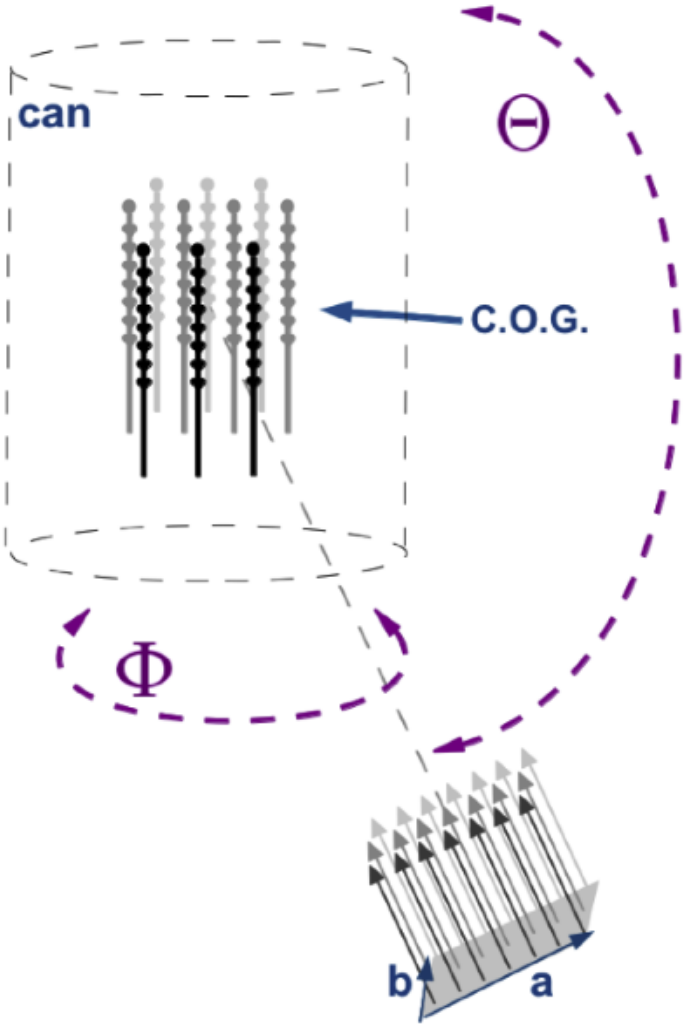

FIGURE 4.1: Schematic view of the simulation setup of muon tracks: 50 equidistant tracks were produced on a plane with its normal pointing to the center of the detector inclined by azimuth Φ and zenith Θ. Their trajectory is then projected onto the can, where the simulation of Cherenkov light emission starts. Each individual track is simulated 500 times. Track generation is repeated for various muon energies and local coordinates.

4.2. RESULTS

Figure 4.2 shows how the number of reconstructed signatures evolves with the simulated local coordinates and the track reconstruction qualities Λ and β. Slices in zenith were normalized to one since the number of different simulated azimuth values was chosen dependent on the zenith angle (see Equation 4.4). One obvious trend is the rising number of well reconstructed particle tracks (defined by larger Λ) with increasing incident zenith angles. Especially downgoing trajectories with $\Theta < 90^\circ$ could be less efficiently reconstructed than those from below. This is a natural consequence of the orientation of the optical modules being optimized for upgoing particle signatures. However, the poor efficiency to reconstruct particles coming from above is quite disadvantageous considering the identification of cosmic-ray-induced atmospheric muons. Hence, data analyses have to cope with a non-negligible background contribution from falsely reconstructed downgoing muons. Having learned from this experience, the next-generation KM3NeT detector will feature optical modules with multiple PMTs, pointed both up and down. In this way, the background of downgoing particles will be quantified more precisely, allowing for efficient suppression of this contribution. The estimated angular error β on the other hand does not

significantly improve for upgoing events, but is rather spread out for large zenith angles. The two parameters Λ and β evolve differently with zenith angle, demonstrating their sensitivity to different qualities of the particle track. It is consequently justified to use both in the selection of neutrino-like signatures in the data.

In Figure 4.3, the number of well reconstructed events as a function of the distance from the detector's center a and b in vertical and horizontal direction and the incident muon energy and zenith angle are shown. Particle trajectories lying farther away from the center of the detector with large absolute values of a and b were less successfully reconstructed, an effect which is particularly apparent for low-energy muons crossing the outer part of the detector. Only for particle tracks crossing the detector horizontally with $\Theta \sim 90^\circ$, the vertical displacements up to 150 m do not affect the reconstruction crucially, which can be understood from the height of the detector being more than 300 m. However, a slight asymmetry is apparent regarding the horizontal distance a from the center of the instrumented volume. The region with most well reconstructed trajectories does not lie at the center ($a = 0$ m), but rather shifted towards the top of the detector by 50 m. This might be explained by the asymmetry in the surrounding medium, with the seabed below the detector and water around and above the detector.

Figure 4.4 shows the evolution of the differences in the reconstructed coordinates $\Delta\Theta$ and $\Delta\Phi$ with the estimated angular error β of each signature. In the upper histograms, the slices with respect to the x-axis are normalized to 1, giving an estimation of the most probable actual error on the reconstructed angles when the reconstruction had returned a specific value of the estimated angular error β. Only events with $\Lambda > -5.4$ are shown. In standard analyses of the ANTARES data (see for example Section 6 or Adrián-Martínez et al., 2014), neutrino-like signatures are usually selected requiring $\beta < 1^\circ$. This criterion seems to be justified from the shown distributions, since above that value, both errors on the zenith and azimuth angles are diverging considerably.

Figure 4.5 depicts how the differences $\Delta\Theta$ and $\Delta\Phi$ of the reconstructed coordinates evolve with simulated incident zenith angle Θ, while the respective median is shown by the black line. As expected, no overall systematic shift of reconstructed angles in any direction can be identified, and the median $m(\Delta\Theta)$ is always close to zero. Naturally, the median is slightly shifted at the extreme values of $\Theta = 0^\circ$ and 180°, since only positive or negative values of $\Delta\Theta$ contribute. The azimuth, on the other hand, degenerates at these points and the difference between reconstructed and incident azimuth becomes meaningless. The approximated combined error on the reconstructed angle is

$$\sqrt{m(\Delta\Theta) + \sin^2(\Theta) m(\Delta\Phi)^2} \sim 0.3^\circ \,, \tag{4.5}$$

which is similar but somewhat better than the quoted median angular resolution using a spectrum of E^{-2} and standard Monte Carlo simulations of the whole-sky neutrino flux (Adrián-Martínez et al., 2014, and Section 3.3).

Figure 4.6 shows the median reported shift in the azimuth versus the displacement a and b from the center of the detector, and also the number of well reconstructed events that were used to derive this median. The most extreme negative values of both a and b lead to systematically shifted reconstructed azimuth values, while in most cases, no global deviation from $\Delta\Phi = 0^\circ$ was found.

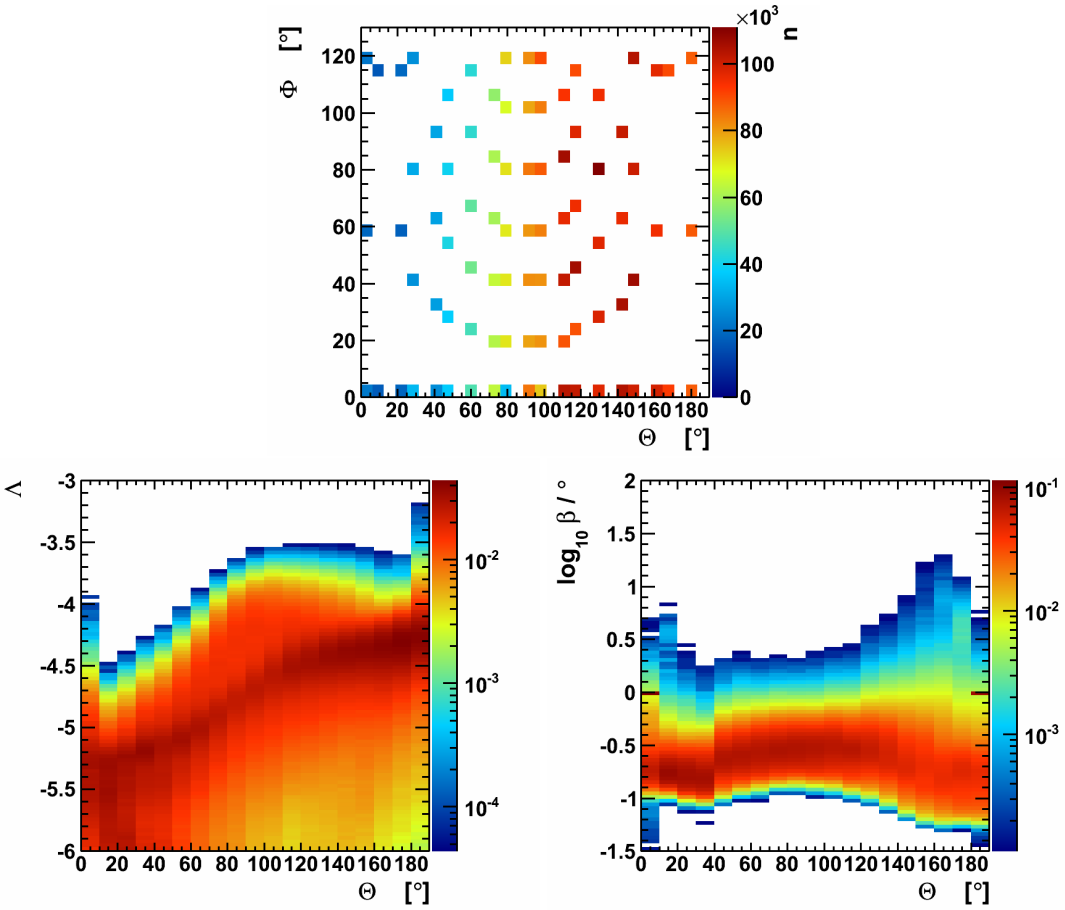

FIGURE 4.2.: Number of successfully reconstructed simulated muons n (color-coded) that fulfill $\Lambda > -5.4, \beta < 1°$ for each set of simulated local coordinates Θ and Φ (*top panel*), and the evolution of the quality parameter Λ (*bottom left*) and the estimated angular error β (selecting events with $\Lambda > -5.4$) with simulated zenith Θ (*bottom right*). The changing number of generated azimuth values (see Equation 4.4) is accounted for by normalizing the slices in Θ for the bottom panels, so that the color codes the probability of the simulated events to be reconstructed with a certain quality parameter.

MIRROR SOLUTIONS Figure 4.7 shows examples of double solutions – so-called mirror solutions – in the reconstructed zenith angles for two tracks with coordinates $\Theta = 130°, \Phi = 52°, a = -200\,\text{m}, b = -20\,\text{m}$ and $\Theta = 120°, \Phi = 69°, a = -200\,\text{m}, b - 60\,\text{m}$. Both events pass the lower edge of the instrumented volume. The reconstructed zenith angles cluster around $\Delta\Theta \sim 0°$ as expected, with an additional cluster around $\Delta\Theta \sim 84°$ in both cases. This corresponds to about double the Cherenkov angle of 42°, in which the photons are emitted by the relativistic muon in the water. Selecting only well reconstructed signatures reduces effectively the number of events with falsely reconstructed zenith angles, and only few pass the final selection criteria. Mirror solutions in azimuth were also found for events coming directly from below with $\Theta = 180°$ as shown in Figure A.1 (Appendix). However, at these coordinates the azimuth angle has no meaning due to the coordinate degeneracy at the poles. Yet still, the clustering of reconstructed azimuth values at two different angles is striking.

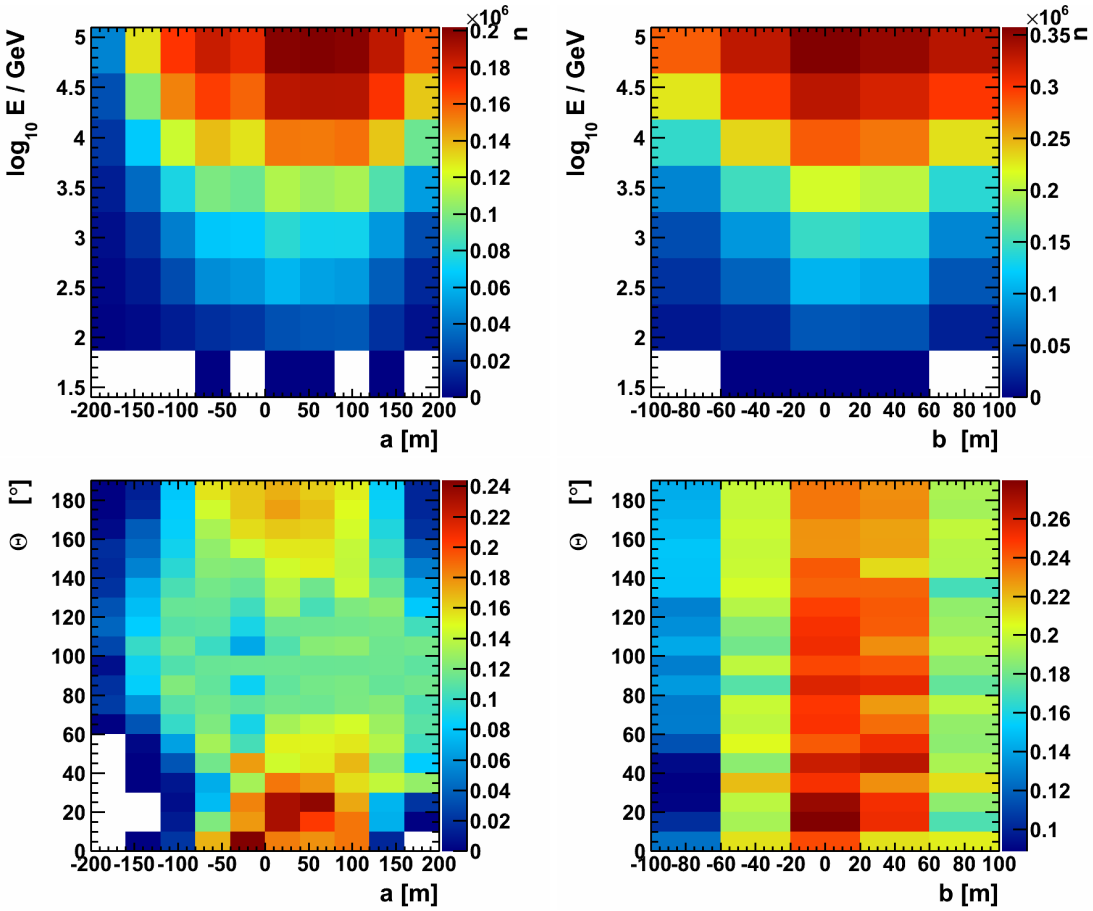

FIGURE 4.3.: Number of successfully reconstructed events as a function of the vertical and horizontal distances a (*left*) and b (*right*) from the detector's center and the simulated muon energy (*upper*) or incident zenith angle (*lower panels*). Only events fulfilling $\Lambda > -5.4, \beta < 1^\circ$ are shown. The distributions are normalized in slices in Θ to account for variable number of simulated azimuth values.

SCAN FOR SYSTEMATIC EFFECTS A methodological study was implemented searching for systematically shifted reconstructed local coordinates Θ and Φ. The differences in the reconstructed to the simulated Monte Carlo coordinates were scanned for deviations from zero, focusing on effects that shift the median of the $\Delta\Theta$ and $\Delta\Phi$ distributions by more than the detector's resolution of 0.5° (Adrián-Martínez et al., 2012b).

Since this study aims at identifying significant systematic shifts that are not dominated by a few outliers at low statistics, I defined certain criteria to ensure the validity of the result. An overall trend should be reported in at least three of the eight simulated energies, in particular for the highest energy tracks with 10^5 GeV. Furthermore, at least 25% of the simulated muons should have been reconstructed well enough to fulfill $\Lambda > -5.4$ and $\beta < 1^\circ$. The algorithm primarily searched for deviations in the individual $\Delta\Theta$ and $\Delta\Phi$ distributions, but then reports only those for which the space angle α of an event shifted

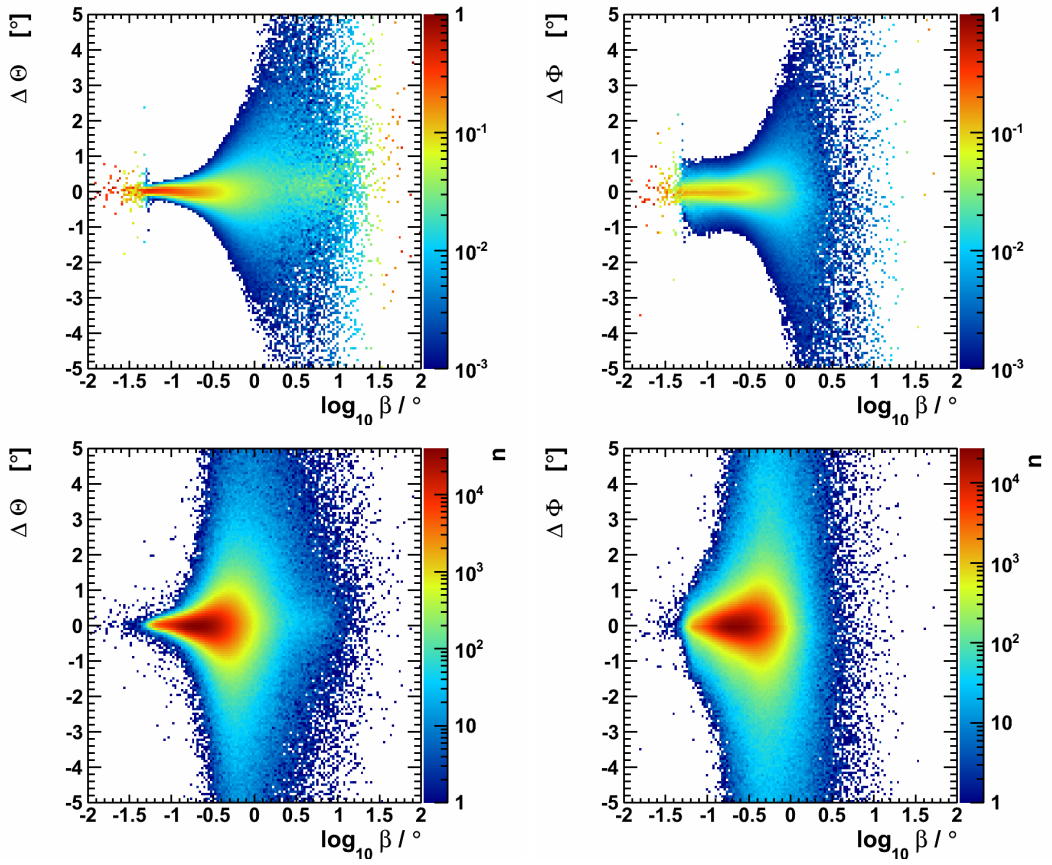

FIGURE 4.4.: Distribution of the error in the reconstructed coordinates $\Delta\Theta$ and $\Delta\Phi$ versus the estimated angular error of the reconstruction, β. Each slice on the respective x-axis has been normalized to 1 to compensate for the changing number of events. Only events with $\Lambda > -5.4$ are shown. The lower two panels are not normalized.

by both $m(\Delta\Theta)$ and $m(\Delta\Phi)$ is more than 0.5°, that is

$$m(\Delta\Theta) > 0.5^\circ \text{ or } m(\Delta\Phi) > 0.5^\circ \tag{4.6}$$

$$\text{and } m(\Delta\alpha) > 0.5^\circ \text{ with space angle } \alpha = \alpha(\Theta, \Phi, \Theta + m(\Delta\Theta), \Phi + m(\Phi)) \; . \tag{4.7}$$

The whole simulated Monte Carlo data set as described before was scanned for such an extraordinary systematic effect. Table A.1 (Appendix) lists the results of the scan for events selected with usual quality cuts $\Lambda > -5.4, \beta < 1^\circ$. Some examples of the systematics as reported in Table A.1 are shown in Figure 4.8 and Figure A.2 (Appendix). Most of the reported effects show up for simulated tracks lying far from the detector's center (with large distances of a and/or b). Systematics appear only in the reconstructed azimuth angles Φ and lead to tracks shifted by angles in the order of 1°. In total, 36 cases could be reported, which is $\sim 0.8\%$ of the 4350 different tracks that were simulated in total. However, considering only the track configurations for which more than 1000 (i.e., 25%) of the simulated muons could be reconstructed sufficiently well (2799 configurations), systematics occurred in 1.3% of all cases.

I want to emphasize here that the generated Monte Carlo sample is only marginally comparable with the standard simulation of ANTARES data as described in Section 6.3. First, the

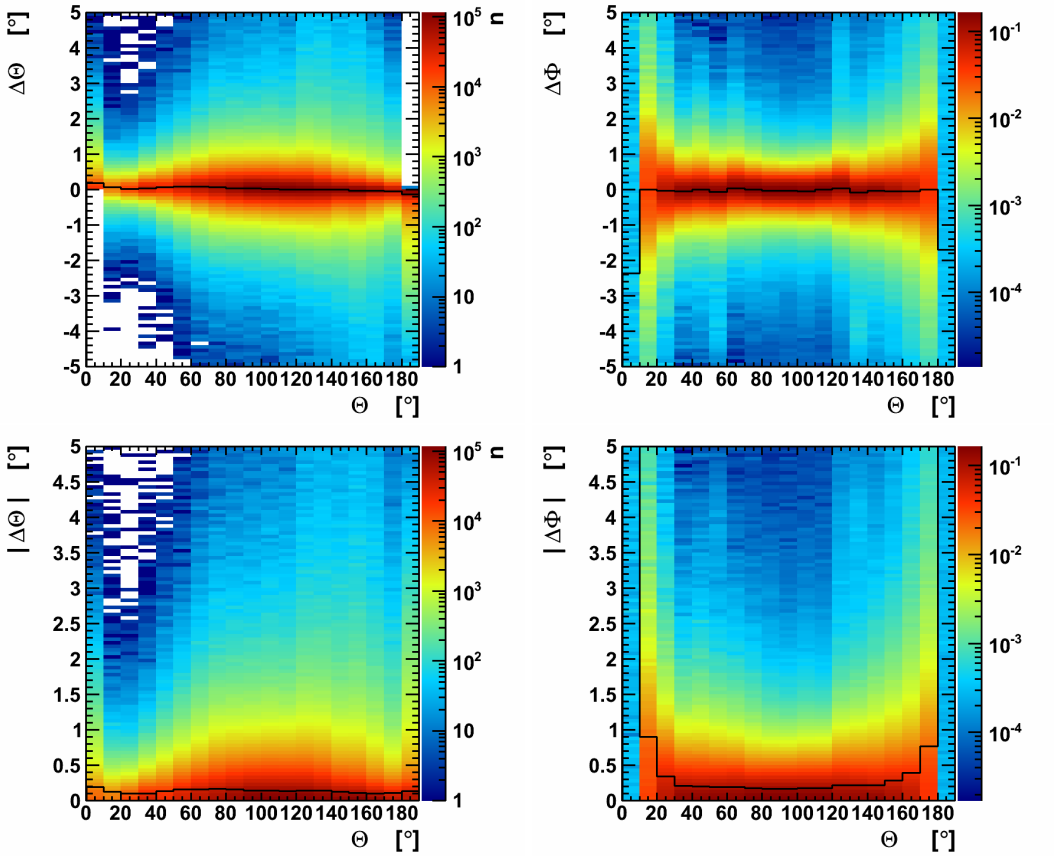

FIGURE 4.5.: Reconstruction errors on zenith and azimuth $\Delta\Theta$ *(left)* and $\Delta\Phi$ *(right)* versus the true Monte Carlo zenith Θ, selecting only well-reconstructed events ($\Lambda < -5.4, \beta > 1°$). The median of the (total) distribution is shown by the black lines. The lower panels show the distribution of the respective absolute values $|\Delta\Theta|$ and $|\Delta\Phi|$. The distributions of $\Delta\Phi$ *(right)* have been normalized to one in each slice in Θ.

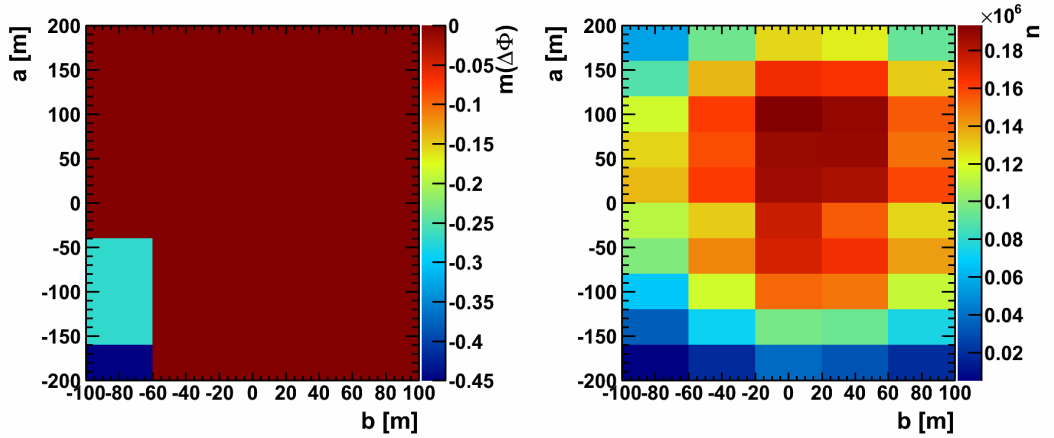

FIGURE 4.6.: Median systematic shift $m(\Delta\Phi)$ with the displacements a, b from the detector's center. The degeneration points at $\Theta = 0°$ and $\Theta = 180°$ have been excluded *(left)*. The number of tracks that could be well reconstructed in dependence of the displacements a and b is shown on the *right-hand panel*. Events are selected requiring $\Lambda > -5.4, \beta < 1°$.

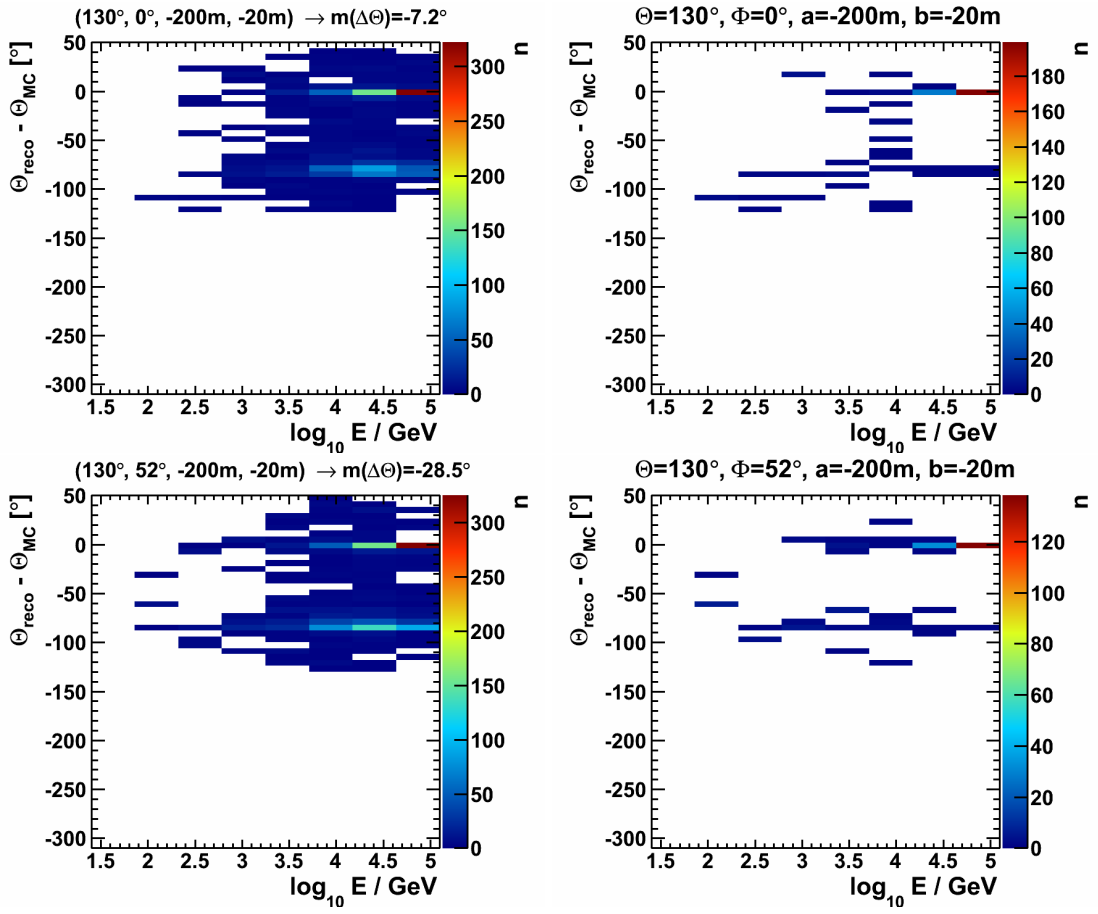

FIGURE 4.7.: Two cases of mirror solutions in reconstructed Θ for local coordinates $\Theta = 130°, \Phi = 0°$ and distance from the center $a = -200\,\mathrm{m}, b = -20\,\mathrm{m}$ (*upper panels*) and $\Theta = 130°, \Phi = 52°, a = -200\,\mathrm{m}, b = -20\,\mathrm{m}$ (*lower panels*). *Right:* Quality cuts of $\Lambda > -5.4$ and $\beta < 1°$ efficiently reject the falsely reconstructed events.

events were simulated with equal statistics for all energies, with no further re-weighting. This attributes more priority to the higher energies than when regarding a standard simulated spectrum with slope $E^{-1.4}$ or, after weighting with the generic flux, E^{-2}. Furthermore, the distances from the detector's center a and b were scanned linearly, whereas in a standard Monte Carlo production the track starting points are spread randomly in the generation volume. Consequently, due to geometrical considerations, more starting points would have been simulated outside the instrumented volume, and the reconstruction is expected to be less efficient for those trajectories that do not cross the detector itself. The better angular resolution found in this study (Equation 4.5) compared for instance to Adrián-Martínez et al. (2012b) is consequently understood from the differences in the data simulations.

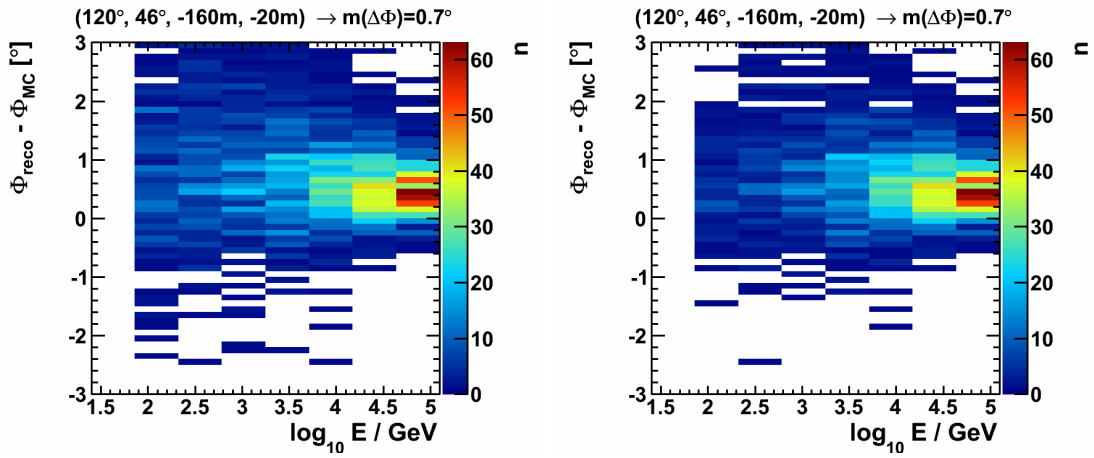

FIGURE 4.8.: An example of a reported systematic shift in the reconstructed azimuth distributions (see Table A.1) for local coordinates $\Theta = 120°, \Phi = 46°$ and distance from the center $a = -160\,\mathrm{m}, b = -20\,\mathrm{m}$. *Right:* Quality cuts of $\Lambda > -5.4$ and $\beta < 1°$ are applied. More examples are shown in Figure A.2 in the Appendix.

4.3. IMPLICATIONS

By scanning the detector with simulations of muons from charge-current interactions in a coarse grid, I have shown that in roughly 1% of all cases, the reconstructed muons' directions deviate systematically from the true Monte Carlo trajectory by more than the detector's resolution. It is clear that an exact quantification of the effects would require a finer scanning of the parameter space. However, from the point of view of a neutrino telescope like ANTARES, the inverse approach might be very promising: Since the amount of presumable signal-like neutrino candidates being selected in searches for astrophysical sources is – unfortunately – still easily manageable, I would propose to study each of them individually by re-simulating the best-fit trajectory and varying the parameter space around it. If such a systematic deviation in the reconstructed angles can be revealed, it can be corrected for, narrowing down the event's coordinates and consequently its most probable source of emission. For such a procedure, it is necessary to not only access the reconstructed particle's directions, but also the position of its track inside the detector. Indeed, recent evidence for an excess in the diffuse neutrino flux has been found in the ANTARES data from 2007 to 2012 (Folger, 2014), and studies are now ongoing that scrutinize each of the selected presumable cosmic signatures for possible systematic effects in a similar way as proposed here. Results of these investigations will demonstrate whether or not the reconstructed arrival directions and energies can be refined.

In the searches for gamma-ray-burst emissions that will be presented in the following sections, any signal candidate passing the event selections will likewise be examined for such an effect, enhancing the accuracy of the angular reconstruction and consequently the reliability of a possible connection between GRBs and high-energy neutrinos.

Let me emphasize here that the effects discussed in this section were entirely derived based on Monte Carlo simulations of highly relativistic muons through the detector and their reconstruction. In this way, a median angular resolution of approximately 0.3° was found. However, note that the overall pointing accuracy of the apparatus to astrophysical

sources in the sky is beyond the accessibility of the usual Monte Carlo simulations. It is subject to various effects, including not only the reconstruction of particles, but also for instance the uncertainties on the absolute orientation of the detector. The problem of quantifying this overall uncertainty has been tackled in two different ways. First, the absolute pointing has been tested by a surface array of muon detectors deployed on a ship cruising above the ANTARES site (Ernenwein et al., 2009). After singling out muon tracks that passed both detectors on the sea surface and the instrumented volume of ANTARES, the overall pointing of the telescope could be constrained to a precision of 0.5° in zenith and 2.5° in azimuth direction. In another approach, the shielding effect of the moon against cosmic rays has been used to determine the telescope's pointing precision to cosmic sources (Rivière, 2011). The imprint of the moon as a shadowing effect in the atmospheric muon flux has been used to derive an absolute accuracy of the telescope of 0.3° (Sanguineti & Distefano, 2014), which is similar to the uncertainty in the reconstruction of muon tracks.

5. Simple Counting Approach

In a first approach to study the capabilities of the Antares neutrino telescope to detect a high-energy neutrino signal associated with gamma-ray bursts, I examined a simple method based on the selection of presumable signal signatures in the data while simultaneously rejecting background. In the scope of this preparatory investigations, a readily available simulation of muon neutrinos from cosmic-ray interactions in the atmosphere was modified to represent a neutrino signal from a showcase gamma-ray burst as predicted by Guetta et al. (2004). Multiple selection parameters were studied for their potential to discriminate the presumable signal from background, and I will discuss several possibilities to optimize these selection criteria. Within this simple so-called binned or counting technique, all data events passing the chosen cuts carry equal weighting, while all others are discarded. I will discuss its performances to identify a neutrino signal over background; later on I will show how the use of an un-binned method can increase the detection possibilities for neutrinos from GRBs. The scrutinized selection parameters were the maximum space angle between a reconstructed data event and the gamma-ray-burst direction, minimum required quality of reconstruction and minimal presumable energy of the detected signatures.

Results will be shown exemplary for the burst GRB091026. Its parameters were read from a table as condensed from the Gamma-ray burst Coordinates Network (GCN). Note that the parsing of these messages is to some extend problematic and might lead to wrong parameter assignments. In the case of GRB091026, this lead to particularly strong instead of average neutrino flux predictions. Nevertheless, the method will be demonstrated based on this strong spectrum as an example to show the capabilities and limitations of the binned analysis for an exceptionally bright showcase GRB, and I will later on introduce required improvements and discuss how these problems can be overcome (see Section 6.1).

The Monte Carlo sample mimics the cosmic-ray-induced atmospheric neutrino flux distributed isotropically in the sky. Charged current interactions of muon neutrinos ν_μ and $\bar{\nu}_\mu$ had been generated with spectral slope $E^{-1.4}$, with increased statistics at energies above 10^6 GeV. In addition to the directional reconstruction of the simulations as described in Section 3.3, a neural network was employed that estimates the energy of each signature (see Schnabel, 2012, for more information about the energy reconstruction). I selected neutrinos that were simulated within 5° around the gamma-ray-burst position to derive the background contribution. The signal was simply mimicked by re-weighted these signatures according to the neutrino spectrum predicted by Guetta et al. (2004). Note that no background from atmospheric muons was included in this preparatory study, so the background considered in the following comprises only atmospheric neutrinos. The additional component from falsely reconstructed muons from above the local horizon will be taken into account in a more elaborate analysis presented in Section 6.

In the following, I will introduce the necessary statistical terms and tools that will be used throughout this work.

5.1. GENERAL STATISTICS

Data events in the ANTARES detector are assumed to occur independently of each other, so that the number of observed signatures n at a given mean rate μ follows a Poissonian distribution

$$\mathcal{P}(n|\mu) = e^{-\mu}\frac{\mu^n}{n!} \,. \tag{5.1}$$

In hypothesis testing, usually a single measure is calculated from the attributes describing an observation. Such a so-called test statistic quantifies the compatibility of the data with the background-only or background plus signal hypotheses. In the simplest case, this could be for instance the mere number of data events n that passed the selection criteria of a basic counting experiment, or any other value summarizing the measured data. A powerful test statistic is characterized by its capability to discriminate signal from pure background. The significance of a measurement is determined by its probability to originate from background only and is specified by the so-called p-value. It is derived from the probability to yield values of the test statistic Q at least as extreme as that observed if the background-only hypothesis (with rate μ_b) was true,

$$p = P(Q \geq Q_\mathrm{meas}|\,\mu_\mathrm{b}) \,. \tag{5.2}$$

The significance is then determined by the deviation of an observed Gaussian–like distributed variable from its mean value that corresponds to this p-value.:

$$p = \left[\frac{1}{2}\right]\frac{2}{\sqrt{\pi}}\int_{\sigma/\sqrt{2}}^{\infty} e^{-x^2}\mathrm{d}x \qquad = \left[\frac{1}{2}\right]\cdot\left(1-\mathrm{erf}(\sigma/\sqrt{2})\right) \,, \tag{5.3}$$

where the factor $[1/2]$ is used in the one-sided convention, in which only one of the sides of the Gaussian distribution is being considered. This yields

two–sided	one–sided	
$3\sigma : p_{3\sigma} = 1-\mathrm{erf}(3/\sqrt{2}) = 2.7\cdot 10^{-3}$	$\frac{1}{2}\cdot(1-\mathrm{erf}(3/\sqrt{2})) = 1.3\cdot 10^{-3}$	(5.4)
$5\sigma : p_{5\sigma} = 1-\mathrm{erf}(5/\sqrt{2}) = 5.7\cdot 10^{-7}$	$\frac{1}{2}\cdot(1-\mathrm{erf}(5/\sqrt{2})) = 2.8\cdot 10^{-7}$.	(5.5)

Following the ANTARES analysis policy, the two-sided convention will be employed throughout this work if not mentioned otherwise. For any significance level therefore, the threshold of a test statistic Q_thres can be derived that would correspond to an excess of the measurement at this level.

Upper limits can be set on the signal flux in cases where no significant excess can be identified: A 90% confidence-level upper limit can be placed, for instance, as that signal flux that would yield values of the test statistic as extreme as the measurement in 90% of all cases. In the case of a non-observation where no data event passes the selection criteria, an upper limit with 90% confidence can be set at a signal rate of 2.3. This value derives from Equation 5.1, since the probability to detect at least one data event at a mean rate of 2.3 is exactly 90%.

To derive the distributions of the test statistic in the background-only or signal hypothesis, usually a large number of pseudo experiments are implemented that mimic a measurement. These can be realized for instance by randomizing or scrambling input variables. To infer threshold values at an aimed at p-value, it is consequently necessary to generate more than $1/p$ pseudo experiments to yield sufficient statistics, particularly above the threshold that should be determined.

Note that in the case of a simple counting experiment, the p-value is given my the probability to observe at least n_{obs} events from a Poissonian distribution with the mean background rate μ_{b}:

$$\mathcal{P}(n \geq n_{\mathrm{obs}}|\mu_{\mathrm{b}}) \; . \tag{5.6}$$

In case of a single observed event $n_{\mathrm{obs}} = 1$, the formulae reduce to

$$p = \mathcal{P}(\geq 1|\mu_{\mathrm{b}}) = 1 - \mathcal{P}(0|\mu_{\mathrm{b}}) = 1 - e^{-\mu_{\mathrm{b}}} \; . \tag{5.7}$$

Due to the Taylor expansion of the exponential function for $\mu \ll 1$,

$$\mathcal{P}(\geq 1|\mu) = 1 - \mathcal{P}(0|\mu) = 1 - e^{-\mu} \sim 1 - 1 + \mu - \mu^2/2 - \cdots \sim \mu \; , \tag{5.8}$$

a suppression of the background rate μ_{b} to the level of a particular p-value ensures that a single event can be identified with the associated significance, i.e., $n_{\mathrm{thres}} = 1$.

There are different ways to optimize an analysis, for example to guarantee best discovery performances or to place a preferably low upper limit on the true signal flux in case of non-observation. In the following, I will introduce several parameters upon which such an optimization of the analysis' selection criteria can be based.

The probability to detect a signal with rate μ_{s} is called the statistical power or discovery potential

$$\mathcal{MDP} = P(Q \geq Q_{\mathrm{thres}}|\mu_{\mathrm{b}} + \mu_{\mathrm{s}}) \; , \text{ or} \tag{5.9}$$

$$= \mathcal{P}(n \geq n_{\mathrm{thres}}|\mu_{\mathrm{b}} + \mu_{\mathrm{s}}) \tag{5.10}$$

in the case of a counting search. It gives the probability to detect an excess at a predetermined significance level, i.e., to measure a test statistic above the critical threshold value Q_{thres}. The event selection should consequently maximize this discovery probability.

The least detectable signal μ_{lds} is the minimum signal strength that is needed to detect at least n_{thres} events with a specified probability. For predefined significance level and detection probability, the least detectable signal μ_{lds} only depends on the expected background rate μ_{b}. For instance, for background rates below the 5σ threshold and detection probability of 90%, Equation 5.1 yields $\mu_{\mathrm{lds}} = 2.3$. The ratio of the required signal to claim a detection to the predicted signal rate from a model is

$$r_{\mathrm{lds}} = \frac{\mu_{\mathrm{lds}}}{\mu_{\mathrm{s}}} \; . \tag{5.11}$$

This parameter is sometimes referred to as model discovery potential (e.g. by Hill et al., 2006), yet I will use the definition of Equation 5.10 throughout this work. A selection of events in the analysis that minimizes the r_{lds} would be preferred, and values below unity imply that the expected signal is stronger than the least detectable signal.

Braun et al. (2008) introduced another variable with respect to which analyses can be optimized, which is calculated from the ratio of the p-value to the statistical power,

$$\lambda = -2\log\left(\frac{p}{\mathcal{MDP}}\right) \ . \tag{5.12}$$

It basically encompasses the ratio of falsely making a discovery from the background-only hypothesis over the detection power for an assumed signal. Hence, maximum values of λ would be preferable in order to yield high signal discovery probabilities.

5.2. SELECTION CRITERIA

To suppress background and single out the neutrino signal from the burst GRB091026 as predicted by Guetta et al. (2004), I investigated how the different selection criteria affect the signal and background rates μ_s and μ_b. I focused on the size of the angular search window around Δ_{max}, the number of photon counts in the photo-multiplier tubes that activated the respective trigger algorithm n_{hits} as possible energy estimator, the reconstructed energy E_{reco}, and the two quality parameters of the track reconstruction Λ and β. Since the gamma-ray-burst signal should be mimicked coming from the direction of the burst in contrast to the uniformly distributed simulations, I assumed that the signatures representing the signal flux originate from the center of the 5° cone, so that a narrowing in of the search window basically acts on the space angle between the reconstructed and primary directions of the simulated muon. This approach is justified within the scope of this preparatory study in so far as the detector's response only varies on angular scales considerably larger than 5° (see Section 6.2).

RECONSTRUCTION QUALITY Figure 5.1 shows how the two quality parameters of the reconstruction algorithm Λ and β are distributed for the selected sub-sample of the simulation. A trend of well reconstructed events with high Λ values towards lower estimated errors β is apparent, while their correlation is less obvious for worse reconstructed events. The two quality parameters are shown in Figure 5.2 versus the space angle α between the simulated direction and the reconstructed trajectory. I also show the effect of cutting on the respective other parameter ($\Lambda > -5.3$ and $\beta < 1°$). The distribution of the space angle α is peaked at $\sim 0.3°$, but extends up to 180° with an additional small excess at $\sim 84°$, corresponding to twice the value of the Cherenkov angle in seawater. Such trajectories, being mirrored at the Cherenkov cone of the actual track, are called mirror solutions. Selecting signatures with $\beta < 1°$, however, reduces the number of events with large angular errors, yet a standard cut at $\Lambda > -5.3$ is even more efficient in rejecting these events, in particular the mirror solutions.

ENERGY ESTIMATORS In Figure 5.3, the number of triggered photon hits of each simulated signature versus its respective energy is shown. At energies below $\sim 10^3$ GeV, the filtering algorithms are activated by up to ~ 20 photon counts, whereas the more energetic events of $\sim 10^7$ GeV are capable of producing photon pulses in basically every PMT in the detector. Yet still, even the highest energy events ($\sim 10^8$ GeV) may trigger only as few as 10 light pulses. Consequently, cutting on a minimum number of triggered hits n_{hits} does effectively

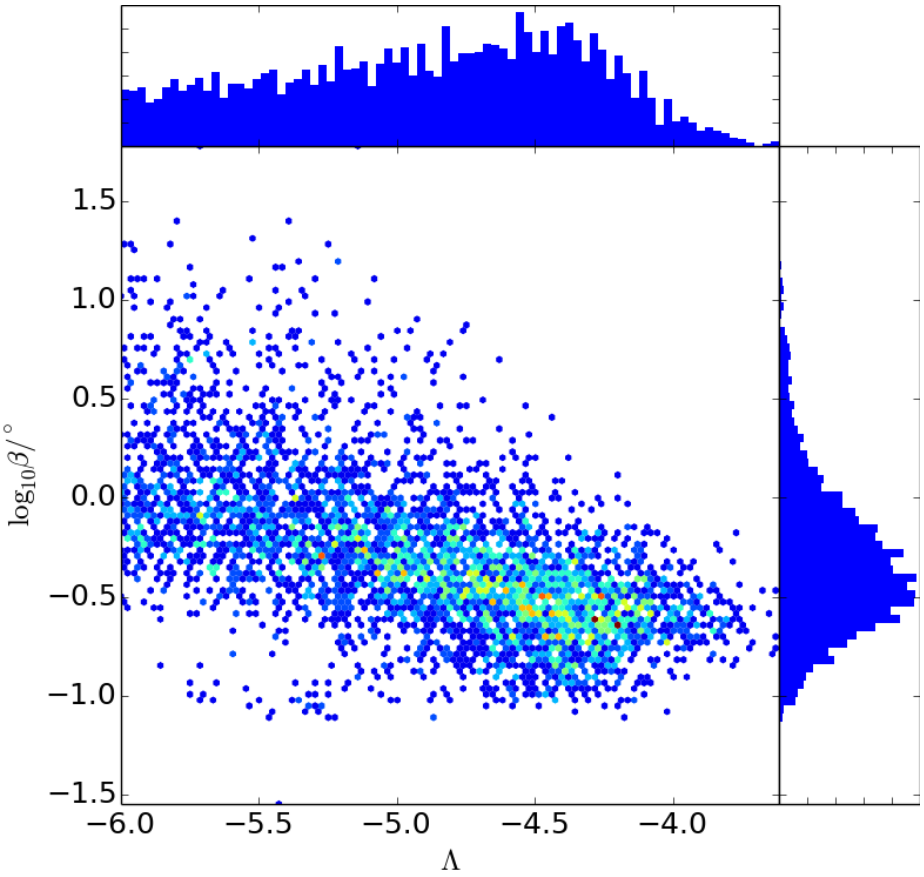

FIGURE 5.1.: Distribution of the estimated angular error β versus the track fit quality parameter Λ for each simulated event within a 5° search cone around GRB091026. The projected distribution of each individual parameter is shown in the upper and right panels.

reduce the low energy events $\lesssim 10^3\,\mathrm{GeV}$, but will also suppress higher energy signatures that are more likely associated with astrophysical signals. This effect is also apparent when regarding the expected background and signal fluxes, which are given by the sums of the respective signal and background weighting factors (see, e.g., Table 5.1).

Furthermore, an energy reconstruction algorithm based on a neural network (Schnabel, 2012) was implemented in the analysis to study the reconstructed energy as possible selection parameter and especially a putative improvement with respect to the selection based on the number of photon hits. In Figure 5.3, the reconstructed energies E_{reco} and number of triggered hits n_{hits} are plotted versus the respective Monte Carlo neutrino and muon energies E_ν and E_μ. Figure 5.4 demonstrates how the two estimators of the energy of an event signature relate to each other. Simulated trajectories that produced more light in the detector were naturally more likely reconstructed with higher energies. The muon energy could be robustly reconstructed within one order of magnitude for well-reconstructed events with $\Lambda \geq -5.3$. Yet since the energy transfer from the parent neutrino to the produced muon is a stochastic process, accurate energy determination of the neutrino from the muon's signature is excluded a priori. In fact, the ratio of the neutrino's energy to the

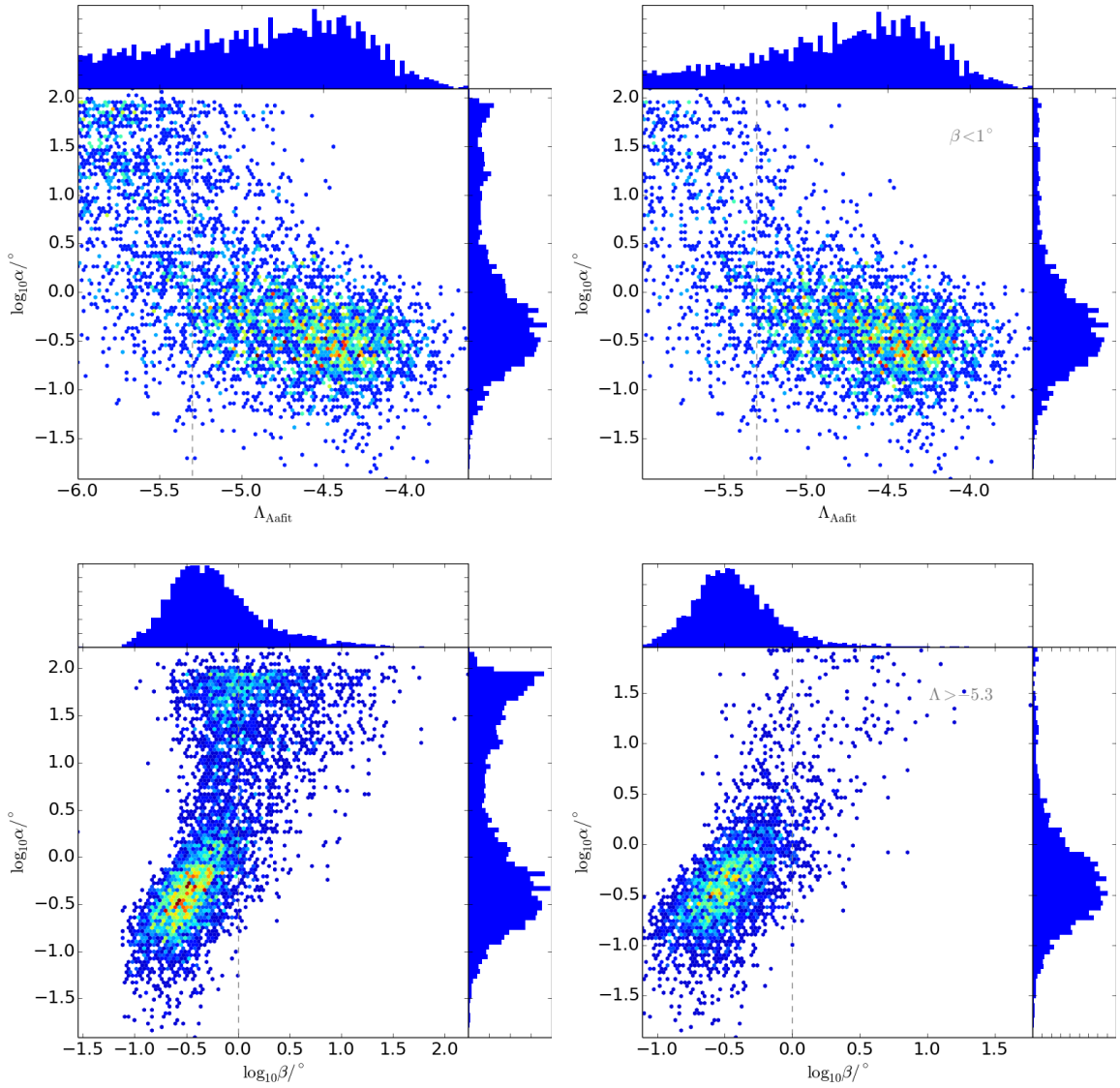

FIGURE 5.2.: *Left:* True angular error α of each fitted event versus the track fit quality parameters Λ and β of the reconstruction. *Right:* Cuts on the respective other parameter are applied. Distributions of the individual parameters are projected on the top and right of each panel.

reconstructed energy demonstrates that the primary's energy was most probably underestimated by a factor of four. In addition, the distribution is quite broad, so the actual energy might have exceeded that reconstructed by a factor of 10^3 or in rare cases even 10^4. Except for very few exceptions, in which the simulated energy is overestimated ($E/E_{\mathrm{reco}} < 1$), the reconstructed energy practically never exceeds the parent neutrino's energy, so that a cut on E_{reco} will always provide a rather robust lower limit on the neutrino's energy. Note that below $\lesssim 1$ TeV, the neural network might more probably overestimate the particle's energy. However, these energies are of little interest in searches for high-energy GRB signals.

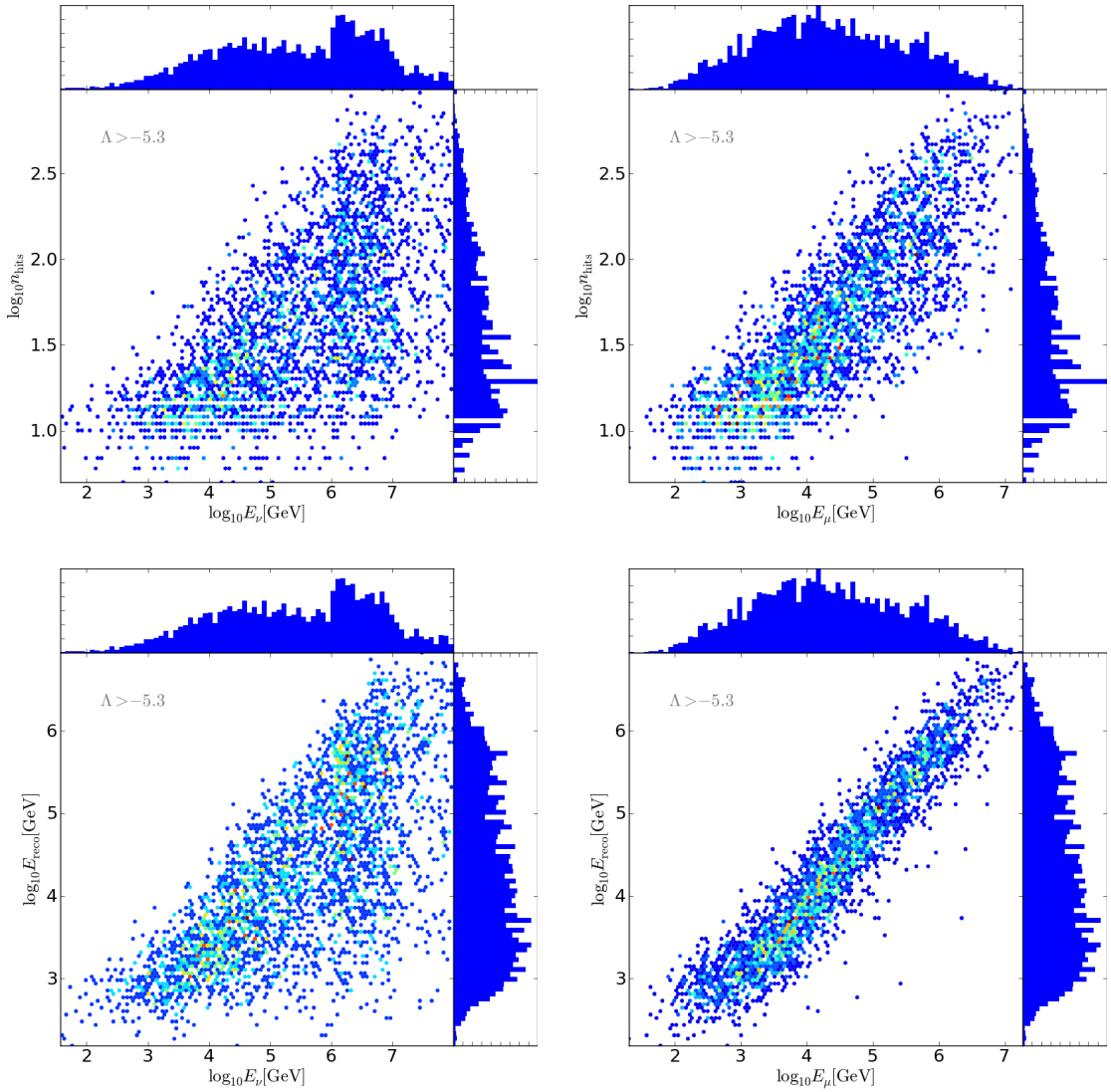

FIGURE 5.3.: Distribution of photon counts that activated one of the trigger algorithms n_{hits}*(upper panels)* and the energy E_{reco} as reconstructed by a neural network *(lower panels)* versus the primary neutrino energy E_ν *(left)* and the muon energy E_μ *(right)* for the simulated neutrino events chosen within a 5° cone around GRB091026. Note the increased statistics above 10^6 GeV that are due to more Monte Carlo simulations for higher energies. Only well-reconstructed events with track fit quality $\Lambda > -5.3$ are shown.

5.3. RESULTS

Figure 5.5 demonstrates how the signal and background fluxes μ_{s} and μ_{b} and the respective efficiencies $\eta = \mu_{\text{sel}}/\mu_{\text{all}}$ of the cuts evolve with the selection criteria $E_{\text{reco,min}}$, Δ_{max} and β_{max}. The angular search cone Δ_{max} is naturally most suited to select the signal flux and suppress the background, which is accumulated linearly with the solid angle of the search window. The accordingly calculated three parameters λ, r_{lds} and $\mathcal{MDP}$ (as introduced in Section 5.1) and their dependencies on the selection parameters are depicted

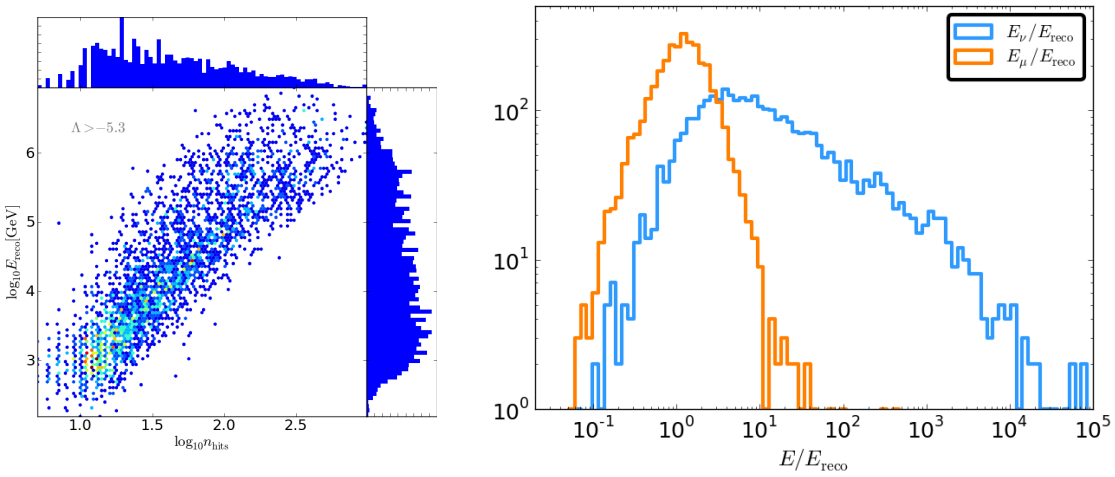

FIGURE 5.4.: *Left:* Number of triggered hits n_{hits} versus the reconstructed energy E_{reco} of each event. Only signatures with $\Lambda > -5.3$ are shown. *Right:* Ratio of the simulated energy of the primary neutrino E_ν to the secondary muon energy E_μ and the reconstructed energy E_{reco} for events fulfilling $\Lambda > -5.3$.

in Figure 5.6. For both Figures, well-reconstructed particle signatures are selected requiring $\Lambda > -5.3$, a cut that effectively constrains the contribution from falsely reconstructed downgoing muons in the data. The values of r_{lds} and $\mathcal{MDP}$ are derived requiring a significance of 5σ in the one-sided convention, which fixes the minimum number of events needed for a discovery – in most configurations, $n_{\text{thres}} = 1$ due to the low background. In additions, for the parameter r_{lds}, a detection power of 90% is demanded.

Remarkably, optimizing the selection criteria in terms of the r_{lds} and $\mathcal{MDP}$ are rather equivalent, with the maximum of the $\mathcal{MDP}$ corresponding to a minimum of the r_{lds} and vice verse. Regarding these two parameters, an angular cone of $\Delta_{\text{max}} = 2^\circ$ and basically no constraints on neither energy estimator n_{hits} nor E_{reco} or the estimated angular error β are preferred. This is due to the fact that by $\Delta_{\text{max}} = 2^\circ$ alone, the background rate is sufficiently suppressed below the 5σ level (see Figure 5.5), so that higher signal rates enhance the chance of a discovery. As soon as the significance level is ensured by efficient background suppression, non-restrictive selection parameters that maximize the signal rate are preferred. The similar behavior of the two parameters can be understood since at the same number of critical events required for a discovery n_{thres}, the two are roughly inversely proportional to each other. For example at $n_{\text{thres}} = 1$, the model discovery potential is $\mathcal{MDP} = \mathcal{P}(\geq 1|\mu_{\text{b}} + \mu_{\text{s}}) \sim \mu_{\text{s}}$ (see Equation 5.8), while $r_{\text{lds}} = \mu_{\text{lds}}/\mu_{\text{s}} = 2.3/\mu_{\text{s}}$.

An analysis optimized for the third investigated parameter, the test statistic λ as proposed by Braun et al. (2008), on the other hand, leads to the tightest cuts on the two energy estimators and the angular error estimate, where signal detection becomes more probable with respect to a discovery from background only. It is maximal for an angular search cone size of $\Delta_{\text{max}} = 0.1^\circ$. Note, however, the inhomogeneity at this maximum, which results from a transition between only few $\lesssim 10$ selected background events with $\alpha < 0.1^\circ$ and roughly four times more for larger search cones. This results in a sudden rise in the background rate μ_{b} and consequently in λ.

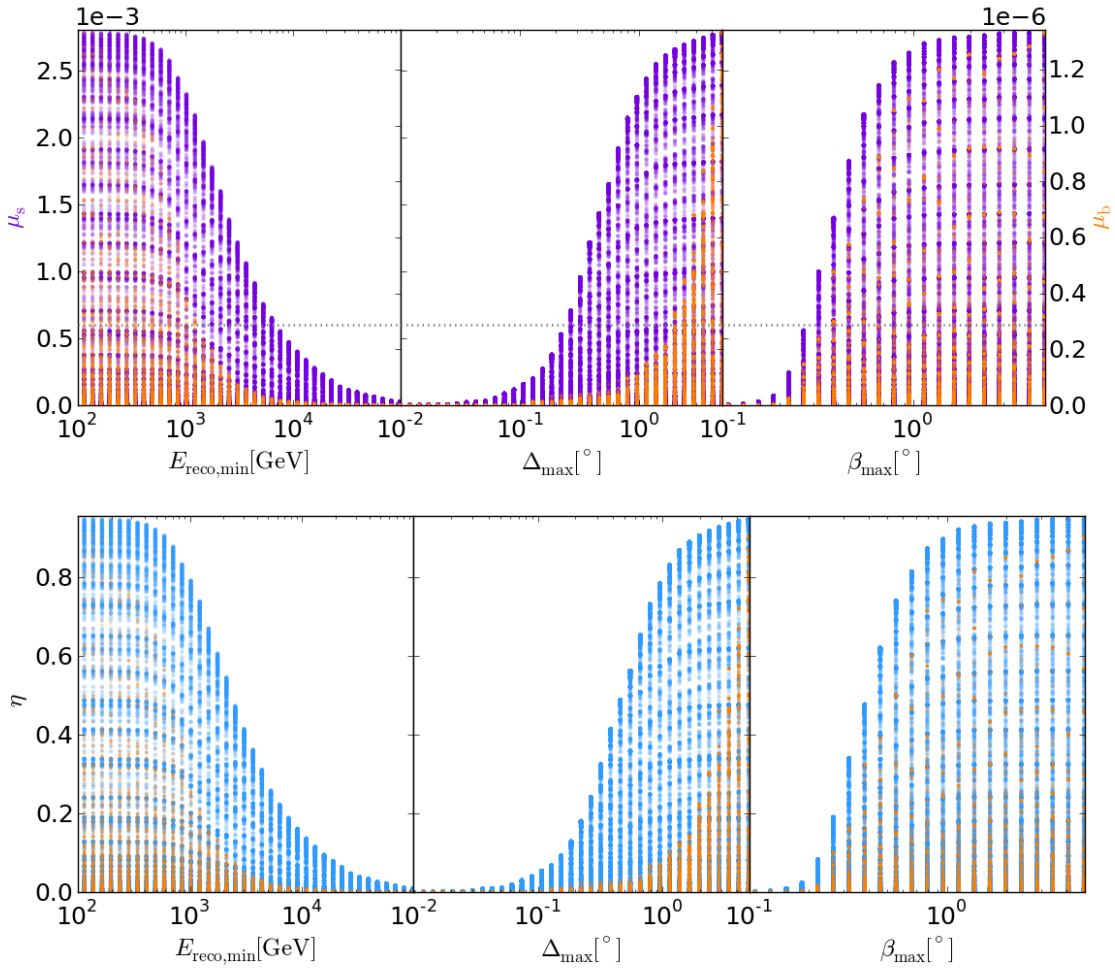

FIGURE 5.5.: The dependencies of the expected fluxes and efficiencies on the three selection criteria $E_{reco,min}$, Δ_{max} and β_{max}. For each of the panels, the other two parameters are free, while the cut on Λ is fixed at -5.3.

In contrast to that, both r_{lds} and $\mathcal{MDP}$ are robust against sudden changes in the background rate. Their values are already defined if not a single background event matches the search window and thus $\mu_b = 0$, which simply yields $n_{thres} = 1$ and $\mu_{lds} = 2.3$ up to the 5σ level of background. Both parameters evolve smoothly even for inhomogeneities in the background rate.

Interestingly, the two energy estimators of a recorded data event n_{hits} and E_{reco} are very similar in their capabilities to distinguish GRB signal events from background. Both of them are therefore equally suited as selection parameters in the search. Requiring events with minimal reconstructed energy or number of photon counts does not improve neither the model discovery potential as defined by Hill et al. (2006), r_{lds}, nor the probability to identify a signal, $\mathcal{MDP}$. Only when optimizing the analysis upon the third investigated parameter λ, tight selections on both energy estimators are preferred.

All three parameters are stable when selecting events with a cut on the estimated angular error at 1° or above, and get worse for more stringent cuts. However, selecting signatures with $\beta < 1^\circ$ has been shown to constrain efficiently the error on the reconstructed angles,

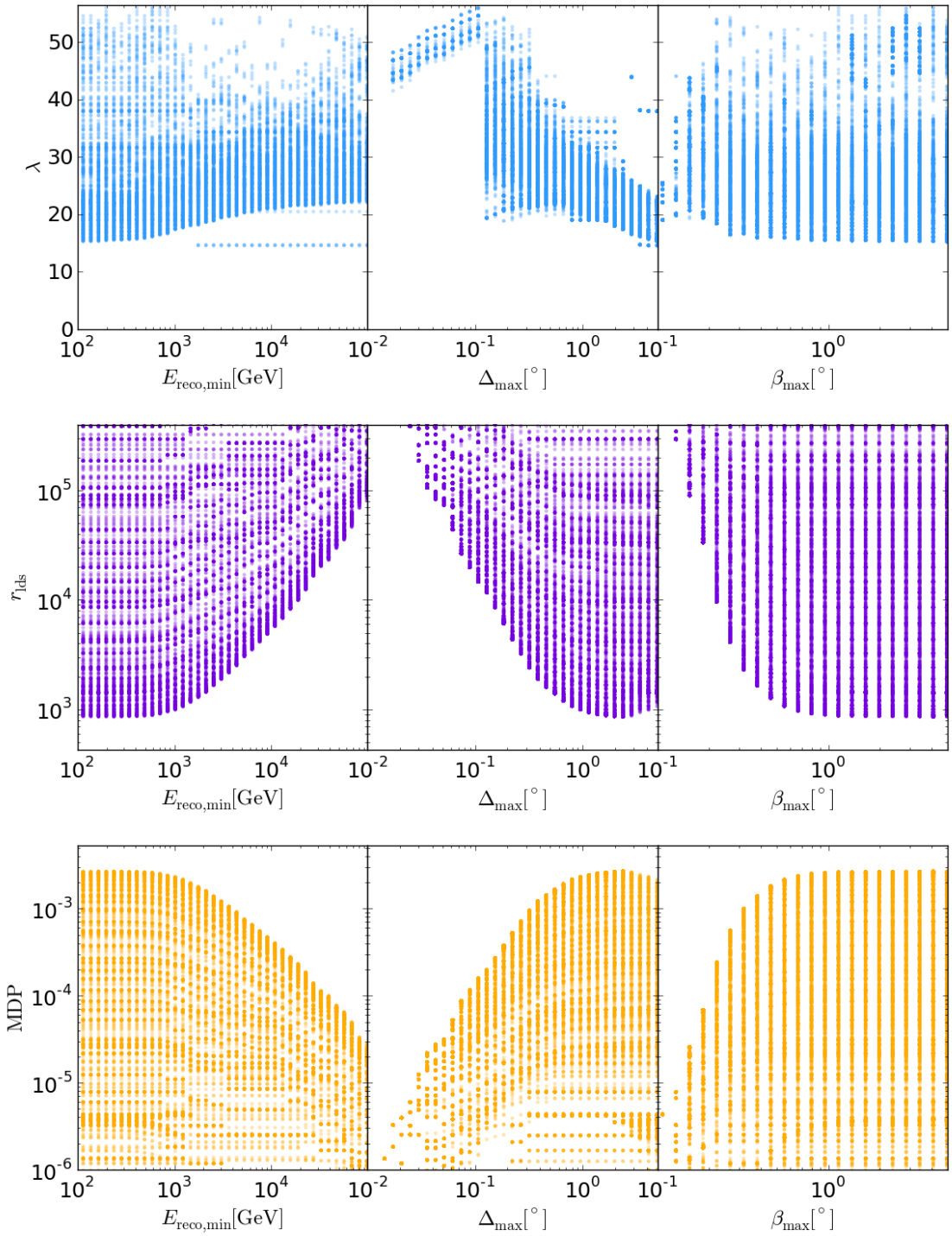

FIGURE 5.6.: The three investigated parameters λ, r_{lds} and $\mathcal{MDP}$ versus the selection parameters $n_{\mathrm{hits,min}}$, Δ_{max} and β_{max}. For each of the panels, the other two parameters are free, while the cut on Λ is fixed at -5.3.

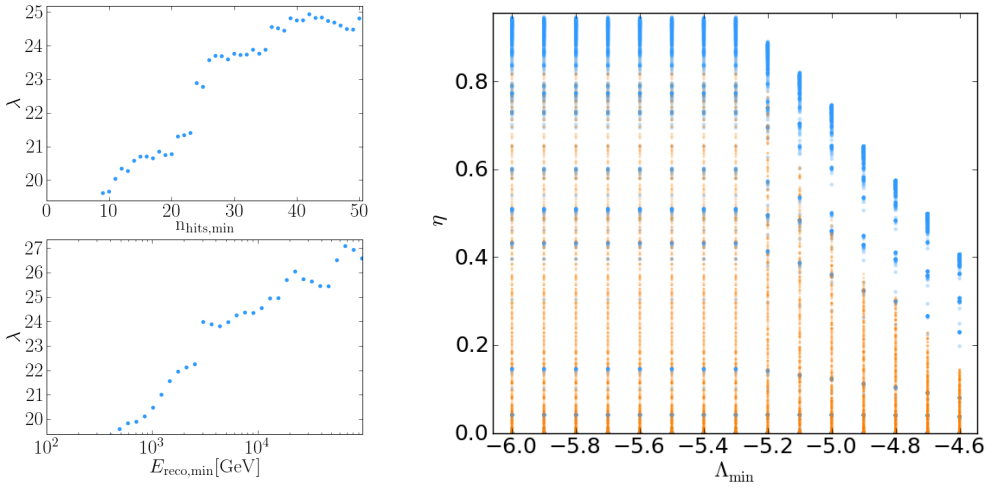

FIGURE 5.7.: *Left:* Comparison between the dependency of the parameter λ (Braun et al., 2008) on the two cut parameters $E_{\text{reco,min}}$ and $n_{\text{hits,min}}$. The other parameters were fixed at $\Lambda_{\text{min}} = -5.3$, $\Delta_{\text{max}} = 2^\circ$ and $\beta_{\text{max}} = 1^\circ$. *Right:* The efficiencies to cut on background and signal events, η_b and η_s in orange and blue, respectively, versus the minimal required reconstruction quality Λ_{min}.

which diverge considerably for larger angular error estimates (see Section 4). Requiring $\beta < 1^\circ$ consequently ensures both optimal search parameters r_{lds}, $\mathcal{MDP}$ and λ, and reasonable angular resolution.

Figure 5.7 demonstrates the dependency of λ on the energy estimators, if the other selection criteria are fixed to $\Lambda_{\text{min}} = -5.3$, $\Delta_{\text{max}} = 2^\circ$ and $\beta_{\text{max}} = 1^\circ$. It implies that selecting events with minimal estimated energy of $n_{\text{hits,min}} \sim 40$ or $E_{\text{reco,min}} \sim 10^4\,\text{GeV}$ increases the parameter λ and consequently the ratio of signal detection probability to that for a background-only discovery. Note, however, that this comes at the expense of reducing the signal rate considerably by more than a factor of six (see Figure 5.8 and Table 5.1), which decreases the detection probability $\mathcal{MDP}$ by approximately the same amount.

The efficiency of the cut on the reconstruction quality Λ is shown in Figure 5.7. Its effects on signal an background are rather similar so that it cannot efficiently be used to discriminate the two fluxes in the presented analysis. Note, however, that both signal and background were derived from the same Monte Carlo sample within is simple study, where only the relative weights were adjusted to represent the signal flux. The simulations were initially designed to represent atmospheric muon neutrinos, and the background from cosmic-ray-induced atmospheric muons is not included here. All signatures in the presented Monte Carlo sample are thus produced by upgoing neutrino tracks, while in most analyses, the quality parameter Λ is needed to effectively reduce the background of falsely reconstructed downgoing muons.

The effects of the selection criteria on the simulated sample is summarized in Table 5.1. For $\Lambda \geq -5.3$, $\Delta_{\text{max}} = 2^\circ$, $\beta \leq 1^\circ$ and not cuts on n_{hits} or E_{reco}, for instance, 2891 signal and 463 background events out of 3364 simulated events in total were selected from the given Monte Carlo sample, which yields rates of $\mu_{\text{s}} = 2.57 \cdot 10^{-3}$ and $\mu_{\text{b}} = 2.33 \cdot 10^{-7}$. The signal and background fluxes and selection efficiencies in dependence on the selection based on the energy estimators are shown in Figure 5.8.

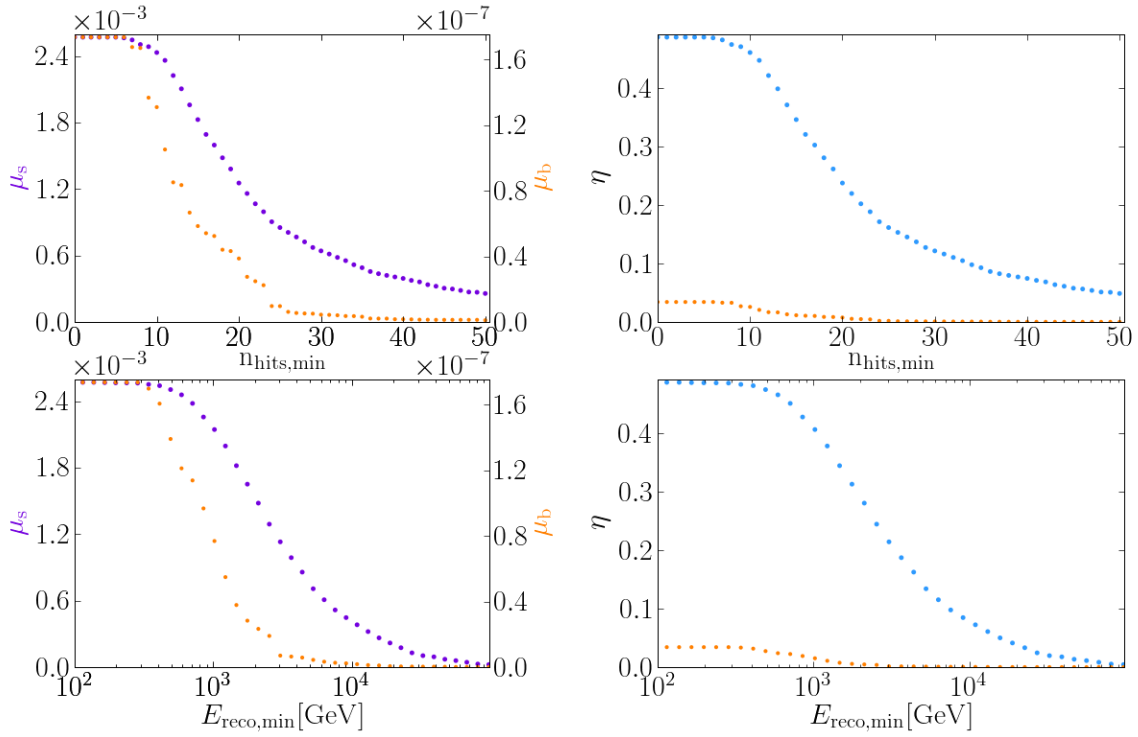

FIGURE 5.8.: Selecting reconstructed signatures with $\Lambda_{min} = -5.3$, $\Delta_{max} = 2°$ and $\beta_{max} = 1°$, signal and background fluxes μ_s and μ_b*(left)* are shown in violet and orange versus the minimal required number of triggering photon hits n_{hits}*(upper panels)* and reconstructed energy E_{reco}*(lower panels)*. *Right:* Dependencies of the signal and background efficiencies η in blue and orange of the selection criteria.

$\Lambda_{min} = -5.3$	$\Delta_{max} = 2°$	$\beta_{max} = 1°$	
$n_b = 463$	$n_s = 2891$	$\eta_b = 16\%$	$\eta_s = 88\%$
$\mu_b = 2.33 \cdot 10^{-7}$	$\mu_s = 2.56 \cdot 10^{-3}$	$\langle\delta_b\rangle = 1.4°$	$\langle\delta_s\rangle = 0.52°$
$\lambda = 18.6$	$\mu_{lds} = 2.3$	$r_{lds} = 896$	$\mathcal{MDP} = 2.56 \cdot 10^{-3}$
$\Lambda_{min} = -5.3$	$\Delta_{max} = 2°$	$\beta_{max} = 1°$	$n_{hits,min} = 40$
$n_b = 217$	$n_s = 1453$	$\eta_b = 0.12\%$	$\eta_s = 13.4\%$
$\mu_b = 1.8 \cdot 10^{-9}$	$\mu_s = 3.9 \cdot 10^{-4}$	$\langle\delta_b\rangle = 0.51°$	$\langle\delta_s\rangle = 0.39°$
$\lambda = 24.5$	$\mu_{lds} = 2.3$	$r_{lds} = 5857$	$\mathcal{MDP} = 3.9 \cdot 10^{-4}$
$\Lambda_{min} = -5.3$	$\Delta_{max} = 2°$	$\beta_{max} = 1°$	$E_{reco,min} = 10^4$ GeV
$n_b = 249$	$n_s = 1637$	$\eta_b = 0.16\%$	$\eta_s = 14\%$
$\mu_b = 2.3 \cdot 10^{-9}$	$\mu_s = 4.08 \cdot 10^{-4}$	$\langle\delta_b\rangle = 0.61°$	$\langle\delta_s\rangle = 0.46°$
$\lambda = 24.2$	$\mu_{lds} = 2.3$	$r_{lds} = 5637$	$\mathcal{MDP} = 4.08 \cdot 10^{-4}$

TABLE 5.1.: Summary of the results of some example selection criteria on the Monte-Carlo-simulated data sample as modified to represent the showcase GRB091026. See text for the definition of the variables. The numbers n of signal and background events passing the selection criteria, the respective efficiencies η and fluxes μ_s and μ_b are given. The mean angular errors $\langle\delta\rangle$ are also shown as well as the three parameters with respect to which the analysis could be optimized.

5.4. DISCUSSION

I have shown that finding the most suitable event selection criteria is not ambiguous, but depends on the parameter upon which the analysis should be optimized. Different configurations might be ideal, depending on whether more priority is given to the effective reduction of background or the most probable detection of a presumable signal. One main difference results from the requirements that are put on the analysis, as for example predefining a specific significance level (as in the case of r_{lds} and $\mathcal{MDP}$) yield different optimal configurations than when making use of the parameter λ, which is simply taking into account the ratio of the probabilities for discovery in the signal versus the background–only case. Optimizing with respect to λ, for example, would always yield very strict cuts on all parameters to increase the signal to noise ratio, but comes at cost of reducing the signal rate considerably. Aiming for high detection probability at a fixed significance level, on the other hand, allows for a reasonable trade-off between background rejection and the loss of signal events. In the discussed sample, the two parameters r_{lds} or $\mathcal{MDP}$ are optimal for a search cone size of 2° and relaxed requirements on the other selection criteria. The selection parameters based on the estimated energy of a reconstructed neutrino event have been shown to bring no significant improvement in these cases, so these will be omitted in the following analyses.

As mentioned before, the un-scrutinized parsing of the gamma-ray-burst attributes from the GCN messages might introduce defective parameter assignments. Parsing the circular 10089 (Ukwatta et al., 2009), for instance, the value of the burst duration $T_{90} = 41.6\,\mathrm{s}$ as measured by *Swift*:BAT was erroneously ascribed to the redshift. In a similar way, the photon spectral parameters were wrongly parsed so that the photon fluence, for example, was over-estimated by almost an order of magnitude. These effects added up and led to neutrino flux predictions significantly larger than estimated when using the correct GRB attributes. This experience calls for more scrutiny when collecting the GRB information and to carefully condensate a catalog of the source parameters with continuous checks of the assigned values. In fact, for GRB091026, no redshift could be determined, and the neutrino spectrum calculated from the correct photon spectral parameters is actually less than average in strength (for the final attributes, see Table C.1 in the Appendix). For the selection criteria as given on the top of Table 5.1, the actual signal flux using the analytical neutrino spectrum would be $\mu_{\mathrm{s}} = 3.6 \cdot 10^{-5}$, which is almost two orders of magnitude below the flux derived when using the deficient input parameters. Figure 5.9 demonstrates how the expected neutrino spectra for muon neutrinos ($\nu_\mu + \bar{\nu}_\mu$) change with the correctly parsed input parameters, and when the numerical model NeuCosmA (see Section 2.2) is used. With the selection criteria optimized for a discovery with the un-binned analysis that will be presented in Section 6, this burst contributes $4.2 \cdot 10^{-5}$ signal events predicted from Guetta et al. (2004) to the total expected neutrino flux and $5.5 \cdot 10^{-6}$ from the second-generation numerical model.

I demonstrated that the presented counting search depends extremely on the number of simulated events that coincide with the defined angular search window around the gamma-ray burst, and only a few events that may or may not be singled out by fixed selection cuts can introduce strong inhomogeneities in the derived fluxes or parameters such as λ. A sudden rise in the number of background events within the search cone, for instance, leads

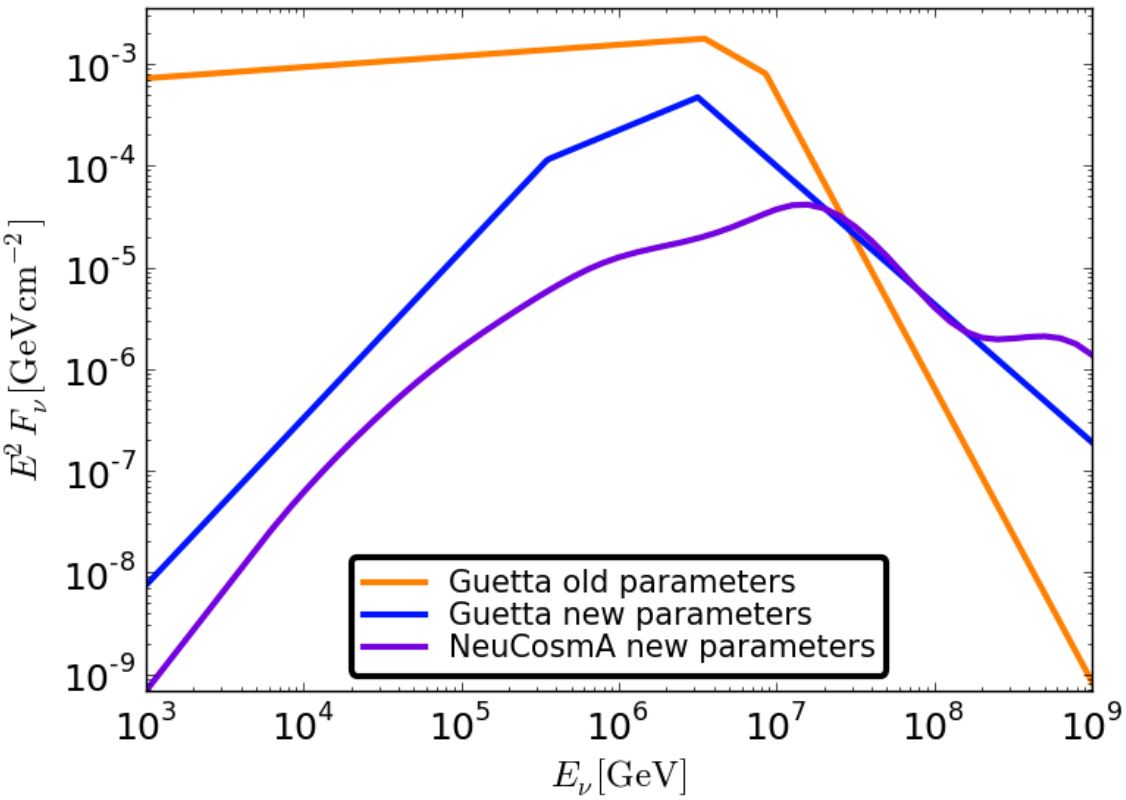

Figure 5.9.: Comparison between the neutrino spectra calculated for the analytic model from Guetta et al. (2004) with the old wrongly parsed parameters and the ones gathered as described in Section 6.1. The newly developed NeuCosmA spectrum (see Section 2.2) is also shown for comparison.

to inhomogeneities in λ which would result in an optimum choice at exactly this transition. The global optimum of the search may therefore be extremely sensitive to the Monte Carlo simulations that have been employed during the optimization procedure. Moreover, the use of an all-sky Monte Carlo neutrino simulation for the purpose of studying the atmospheric neutrino flux is only marginally justified when optimizing a method to search for neutrinos from astrophysical sources such as gamma-ray bursts. Instead, to allow for a reasonable handle on the detector's response to the high-energy neutrino flux from a particular gamma-ray burst, a dedicated simulation of the expected signal is required that accounts for the transient and point-like nature of the signal. In doing so, the variations of the detector's point spread function with changing configurations can also be incorporated.

An improved analysis method can take advantage of the fact that changing deep-sea environmental conditions and the status of the detector are immanent in the data that has been taken. Hence the evolution of the background rate with time can readily be derived from the data themselves, which will not only be sensitive to the variation of the environmental conditions but also to that of the detector configuration. In this way, the background introduced by falsely reconstructed atmospheric muons is naturally accounted for, and the quality parameter of the reconstruction Λ can effectively discriminate the upgoing neutrino

signatures from this background.

I will show in the following sections how the use of an un-binned likelihood method can increase the potential for identifying a neutrino signal associated with gamma-ray bursts by as much as 200% with respect to a simple counting search as shown here (see Section 6.5). Instead of a simple selection of events that pass certain criteria, particularly a predefined search window around the GRBs coordinates, a smooth function will be derived to describe the events' spread around the simulated position. In this way, information comprised in the spatial distributions of the expected background and signal, and in particular the differences between these two, can effectively be used to single out the most probable signal signatures. This improved search makes use of the capability to detect an associated neutrino signal from gamma-ray bursts by means of the probability to claim a discovery with certain significance $\mathcal{MDP}$, which has been introduced in this section.

6. Search for Neutrinos from Gamma-Ray Burst from late-2007 to 2011

In the following, I will present the search for prompt GRB neutrino emission in the data from the Antares neutrino telescope from more than four years of data. Within this period, 296 bursts were analyzed, out of which 90% have not been included in previous searches for neutrino signals from any instrument before. In contrast to others, this analysis has for the first time been optimized for the fully numerical neutrino-emission model NeuCosmA (see Section 2.2). Data collected between December 6, 2007 and the end of 2011 were analyzed. The first six months of this period comprised the last phase of construction of the apparatus, after the deployment of detection lines 6 to 10, with the last two lines installed in May 2008. In that period, the instrumented volume of the detector increased from $8 \cdot 10^6$ to $11 \cdot 10^6$ km^3 at full size. The corresponding average effective area to muon neutrinos as a function of the energy is shown in Figure 3.3 for different declination bands. The total integrated livetime of the data in coincidence with the selected 296 GRB search-time windows was 6.6 hours.

The analysis was developed and optimized together with Colas Rivière at the CPPM in Marseille. It was internally presented in an Antares internal note (Rivière & Schmid, 2012) and finally published in the journal A&A (Adrián-Martínez et al., 2013d) with a full catalog of the selected gamma-ray bursts available online (Adrián-Martínez et al., 2013b). My main contributions were first the condensation of a suitable gamma-ray-burst catalog (see Section 6.1) and the choice of default parameters. I established contact with the authors of the numerical model NeuCosmA in Würzburg, especially Walter Winter, Philipp Baerwald and Mauricio Bustamante, with whom I worked closely together to simulate the neutrino predictions of the selected sample from their model (see Section 2.2 and 6.3), and to finally make the necessary algorithms available for further use in the Antares collaboration. In addition, I developed and performed cross-checks for the rest of the analysis, for example by calculating the effective area, evaluating the background contributions, refining the background calculations and quantifying the improvement of the detection capabilities using an un-binned method with respect to the binned technique as studied before. I also placed the final limits after non-observation and wrote the according publication (Adrián-Martínez et al., 2013d). In the next sections, I will describe the analysis following mostly this document and the internal note (Rivière & Schmid, 2012).

6.1. GRB selection

A reliable collection of gamma-ray-burst alert timings and positions in the sky was needed to define windows to search for coinciding neutrino signatures in the Antares data. Furthermore, based on the measured electromagnetic spectra, the models presented in Sec-

tion 2.2 predict neutrino fluxes upon which the analysis was optimized. Simple parsing of the Gamma-ray burst Coordinates Network (GCN) messages had turned out to be prone to errors, so more scrutiny was required when condensing a catalog of GRB parameters.

In the following, I present how I consolidated a GRB catalog for the search and the simulation of expected neutrino fluxes from different tables provided by the *Swift* and *Fermi* collaborations. This information was then cautiously supplemented using a table prepared by the IceCube Collaboration (Aguilar, 2011), which was created by parsing the GCN messages. I will shortly describe the different catalogs, specify how these were merged, how often burst parameters were taken from each of them, and how the search-time windows were defined. Finally, I will explain how the Bursts for the final analysis were selected from the derived catalog.

CATALOGS The table of the *Swift* satellite (Gehrels et al., 2004)[1] contains data from the three on-board instruments BAT (gamma rays), XRT (X-rays), and UVOT (ultraviolet), ordered with increasing position-measurement accuracy Δ_{err} from arcminutes to sub-arcseconds. BAT spectral measurements are provided in the energy range from 15 to 150 keV. Within the late-2007 to 2011 period, the *Swift* table comprises 509 bursts, for 132 of them, the redshift z could be determined ($\sim$ 26%). Information on the redshift from different ground-based observations are also provided. If the individual measurements differed by less than 0.1, their average value was considered. However, in three cases with larger discrepancies, the value was searched manually in the literature[2].

The *Swift* BAT2 Catalog (Sakamoto et al., 2011)[3] provides re-analyzed *Swift* data, so that the spectral information should be more accurate. In the considered time period, the BAT2 Catalog contains 278 bursts with 82 estimated redshifts ($\sim$ 29.5%). 269 of these overlapped with the above-mentioned table.

The FERMIGBRST catalog (Goldstein et al., 2012; Gruber et al., 2014; Paciesas et al., 2012)[4] comprises information on bursts measured by the GBM instrument on-board *Fermi* (Meegan et al., 2009). It supplies the best spectral information for bursts between July 2008 and July 2010 in the instrument's energy range from 10 keV to 1 MeV. The spectrum is fitted with four different functions: A single power-law (the best-fit model in $\sim$ 23% of the cases), a comptonized power-law ($\sim$ 48%), a Band function (Band et al., 1993) ($\sim$ 15%) and a smoothly broken power-law ($\sim$ 14%). The large field of view of the instrument which enables to detect around 1.5 bursts per day comes at the expense of a rather poor angular resolution in the order of degrees. The catalog comprises 812 bursts in total, out of which 118 (49) appear also in the *Swift* (BAT2) catalog. The overlap of all three catalogs is 47 GRBs.

The IceCube Collaboration also provides a table with GRB parameters[5] (Aguilar, 2011), which is created by parsing the GCN messages[6]. This table is used to supplement missing information for GRBs that have been found in at least one of the other catalogs. Since the parsing of the GCN messages without further scrutiny of the data had turned out to be

[1] *Swift*: `http://swift.gsfc.nasa.gov/docs/swift/archive/grb_table.html`
[2] *Swift* GRBs 110205A: Groot et al. (2010), 100219A: Vreeswijk et al. (2011), 080913: Greiner et al. (2009).
[3] BAT2: `http://vizier.u-strasbg.fr/viz-bin/VizieR?-source=J/ApJS/195/2`
[4] *Fermi*: `http://heasarc.gsfc.nasa.gov/W3Browse/fermi/fermigbrst.html`
[5] IceCube: `http://grbweb.icecube.wisc.edu`
[6] GCN: `http://gcn.gsfc.nasa.gov/gcn3_archive.html`

Source	Position	Time	Fluence	Spectrum	Duration	Redshift	Start & Stop
Swift:BAT	3.7% [3]	11.2% [3]	10.5% [3]	14.2% [3]	8.8% [3]	4.4% [2]	—
Swift:XRT	17.2% [2]						
Swift:UVOT	11.2% [1]						
Swift BAT2		11.2% [2]	10.1% [2]	9.8 % [2]	11.2% [2]	4.4 % [1]	10.1% [2]
Fermi	67.9% [4]	77.7% [1]	77.7% [1]	36.2% [1]	77.4% [1]	—	77.7% [1]
IceCube			1.7% [4]	4.4% [4]	2.4% [4]	0.3% [3]	11.2% [3]

TABLE 6.1.: Usage of the GRB parameter catalogs. The numbers in square brackets give the assigned priority of each catalog with respect to the parameter(s), reflecting the considered accuracy of that measurement.

erroneous to some extend, numerous consistency checks such as for incompatible values have been implemented to ensure reliability of the collected information.

CONDENSING THE GRB CATALOG When consolidating the gamma-ray-burst information, priorities were assigned to the measured values according to their considered accuracy. The usage of each catalog as well as the priorities (in square brackets) are shown in Table 6.1. When a parameter could not be measured, standard values as given in Table 6.2 were used to calculate the spectra. The form of the photon spectrum is determined by the spectral indices α and β with the break energy ϵ_{peak} giving their transition. The isotropic luminosity L_{iso} is related to the redshift z and the total measured fluence in gamma rays $\mathcal{F}_\gamma$ via

$$L_{\text{iso}} = 4\pi d_{\text{L}}^2 \frac{\mathcal{F}}{T_{90}} \,, \tag{6.1}$$

with the luminosity distance d_{L}. In case of unknown redshift, the luminosity could be either calculated from Equation 6.1 or the standard value for L_{iso} can be used. While the first option seems to make better use of the available data, a nearby GRB would generally appear to be brighter than average. Hence, we took the default value of L_{iso} in cases of no redshift measurement to not overestimate the overall neutrino yield.

The duration T_{90} is given by the time in which 90% of the fluence is emitted. The time window of the search T_{search} for prompt emission from each burst was designated by the start and stop times as measured by the satellites or, when these are not provided in the catalogs, as the time T_{90} with a 30% safety margin around. Additionally, we accounted for the detector's data acquisition uncertainty[7] (0.4 s), the satellite time given in integer seconds (1 s), and the light propagation from a satellite through Earth to the detector (0.5 s) by adding another ± 2 s to the search-time window.

The other parameters such as the jet Lorentz boost factor Γ, the fraction of jet energy in electrons ϵ_e and in the magnetic field ϵ_B, the ratio of energy in electrons and protons f_e, the average fraction of proton energy transferred to a pion $\langle x_{p\to\pi} \rangle$ and the variability of the gamma-ray light curve t_{var} do not appear in the catalogs and hence were set to default. The standard values were chosen consistently with the most recent IceCube analysis (see

[7] At the beginning of data taking, the photodetectors resume recording the signals with the following reset signal received from the master clock system. It is sent with a frequency of 2.4 Hz, so that the absolute timing of the data within one run can be offset by up to 0.42 s. This effect can in principle be corrected for, but was not yet for the data production used in this analysis.

default, if not measured	$\alpha = 1$	$\beta = \alpha + 1$	$\epsilon_{\text{peak}} = 200$ keV
	$z = 2.15$	$L_{\text{iso}} = 10^{52}$ erg s^{-1}	
always default	$\Gamma = 316$	$\epsilon_e = 0.1$	$\epsilon_B = 0.1$
	$f_e = 0.1$	$\langle x_{p\to\pi} \rangle = 0.2$	$t_{\text{var}} = 0.01$ s

TABLE 6.2.: Standard gamma-ray-burst parameters as described in the text.

Aguilar, 2011), with some differences to the IC22 (Abbasi et al., 2010) default values[8]. Baerwald et al. (2012) give a very elaborate overview about the neutrino flux predicted by NeuCosmA changing with the input parameters, demonstrating that the input parameters might introduce uncertainties on the neutrino fluxes up to an order of magnitude.

Figures 6.3 show how some of the gamma-ray-burst attributes are distributed in the different catalogs and in the final selection (labeled 'full'). Typical redshifts were around $z \sim 2$, with exceptionally far bursts up to record-holding redshifts exceeding 8. The individual photon fluences were in the order of $\lesssim 3 \cdot 10^{-6}\,\text{erg}/\,\text{cm}^2$, demonstrating that default values of $10^{-5}\,\text{erg}/\,\text{cm}^2$ as used in other analyses (Abbasi et al., 2010; Aguilar, 2011) overestimate the true distribution by some extend – in particular when considering that GRBs without determined photon fluence are most probably fainter than average. Interestingly, the distributions of the durations shows almost no second peak for short GRBs except from the *Fermi*:GBM table. The long GRBs last $\mathcal{O}(10)$ s, with exceptional ones up to 1000 s. The location accuracies given by the error radii Δ_{err} show the clear distinction between the different instruments with a large range from sub-arcseconds (e.g. with ground-based observations or *Swift*:UVOT) up to several degrees (*Fermi*:GBM). Distributions of the photon index α in case of power-law photon spectra are depicted in Figure 6.4, as well as the break energies ϵ_{peak} where the electromagnetic spectrum could be described best with a comptonized power-law. The chosen standard values (see Table 6.2) are compatible with the distributions of the measured attributes.

SELECTION OF GRBS For the final sample, gamma-ray bursts were required to meet certain criteria as specified in Table 6.4 – short bursts, for instance, were excluded as this class is much less understood. A total of 296 bursts passed these selection cuts, of which 10% had also been included in the most recent gamma-ray-burst search from ICECUBE (Abbasi et al., 2012). The distribution of the selected bursts in equatorial coordinates is shown in Figure 6.1. Their neutrino spectra as predicted by NeuCosmA (see Section 2.2) are shown in Figure 6.2.

Out of this selection, GRB110918 outshines all others by at least half an order of magnitude in the expected neutrino flux. It is at the same time one of the most intense bursts ever observed by the *Konus-Wind* instrument (Aptekar et al., 1995; Golenetskii et al., 2011). Unfortunately, both *Swift* and *Fermi* satellites were Earth-occulted at the time of the burst (Krimm et al., 2011), but *Swift* could still observe the afterglow emission after $\sim$ 30 h. The measured parameters for this exceptional event are given in Table 6.3, the predicted neutrino spectra for the individual neutrino flavors are shown in Figure 6.2 on the right.

[8] IC22 standard values: $z = 2.0$, $\Gamma = 300$, $L_{\text{iso}} = 10^{51}$ erg s^{-1} (Abbasi et al., 2010)

$\alpha = 1.2$	$\beta = 2.0$	$\epsilon_{\text{peak}} = 150$ keV
$\mathcal{F} = 7.5 \cdot 10^{-4}$ erg cm^{-2}	$E_{\text{min}} = 0.02$ MeV	$E_{\text{max}} = 10$ MeV
UT $= 21:26:57$	$dec = 32.5°$	$RA = -27.1°$
$\Delta_{\text{err}} = 0.5$ arcsec	$T_{100} = 69.4$ s	$z = 0.982$

TABLE 6.3.: Gamma-ray-burst parameters of GRB110918 as described in the text. All values are read from the ICECUBE table, most of them are based on *Konus-Wind* measurements (Golenetskii et al., 2011). The GRB was located most precisely by the *Isaac Newton Telescope* (Tanvir et al., 2011), the redshift was determined by *Gemini-N* (Levan et al., 2011) and the *GTC* telescope (de Ugarte Postigo et al., 2011). The duration T_{100} is given by the integration time of *Konus-Wind* (Golenetskii et al., 2011).

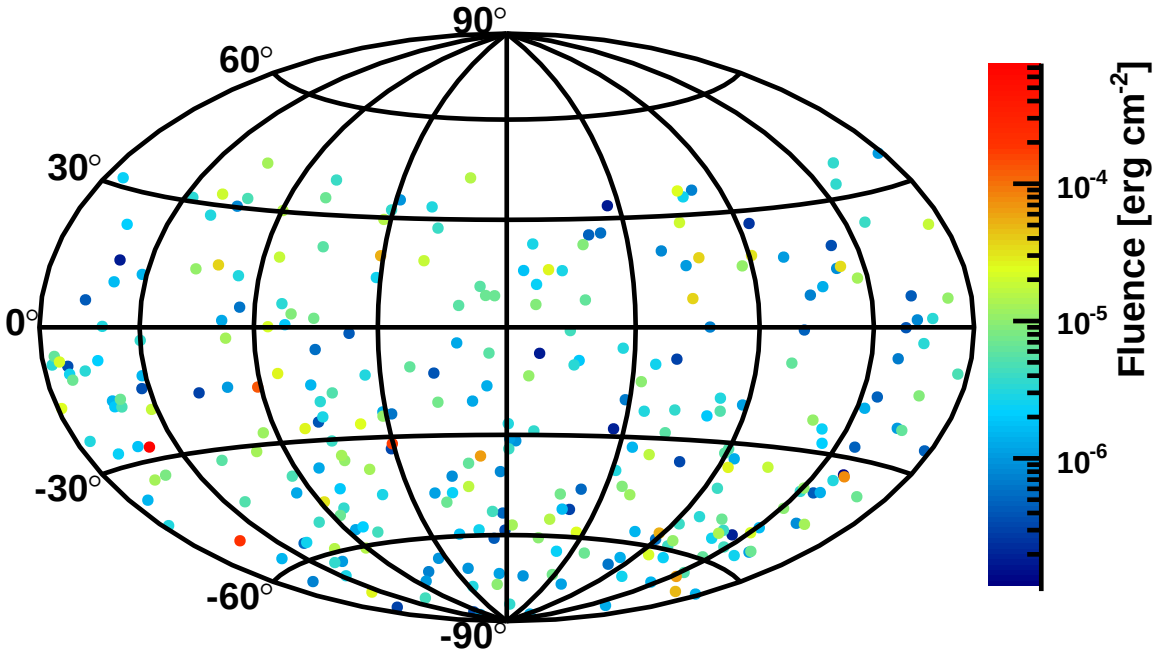

FIGURE 6.1.: Sky distribution of the selected 296 GRBs in equatorial coordinates RA and δ. The gamma-ray fluence of each burst is colour-coded. (Figure from Adrián-Martínez et al., 2013d)

6.2. BACKGROUND ESTIMATION

Atmospheric neutrinos from below the local horizon constitute the main background component in the search for cosmic neutrinos, with a smaller contribution coming from falsely reconstructed downgoing atmospheric muons (see Section 3). To estimate the expected number of background events μ_{b} in coincidence with each burst as realistically as possible, data were used. However, as the number of upgoing events is very low ($\sim 4/\text{d}$), long time periods are needed to yield sufficient statistics, which in turn requires averaging over different data-taking conditions (in particular because of seasonal variations of the optical background). To compensate for this effect, we first estimated the average rate of reconstructed events in the GRB's direction $\langle n(\Theta, \Phi)_{\text{GRB}} \rangle_{\text{all runs}}$ in local coordinates zenith Θ and azimuth Φ using data recorded during the entire period from December 6, 2007 to the end of 2011, then adjusted it for varying data-taking conditions. The total number of events in

TABLE 6.4.: Selection of gamma-ray bursts

Criterion	Selected
all GRBs (end of 2007 – 2011)	1110
long GRBs	942
measured fluence	930
below ANTARES horizon	508
detector running and stable data-taking conditions	296

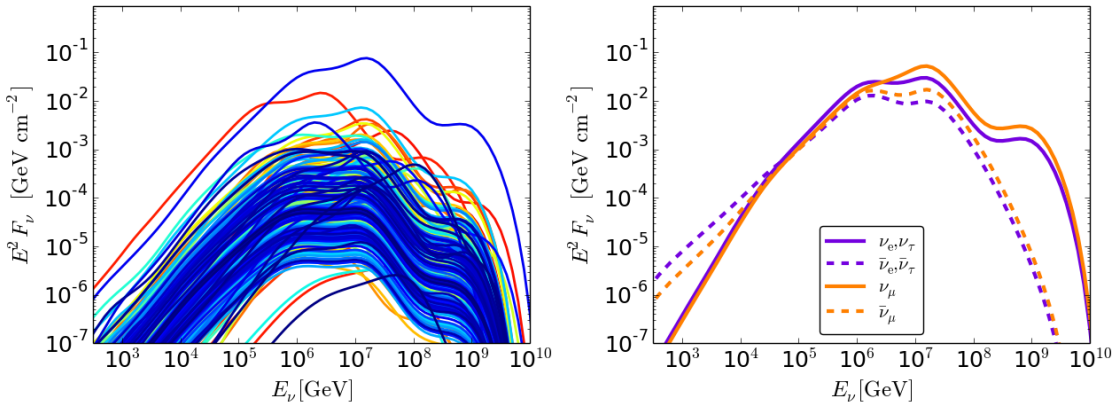

FIGURE 6.2.: *Left:* Neutrino spectra $E^2 F_\nu$ from $\nu_\mu + \bar{\nu}_\mu + 10\%(\nu_\tau + \bar{\nu}_\tau)$ versus energy as predicted by the NeuCosmA calculations (see Section 2.2) for the 296 gamma-ray bursts selected within the period from late-2007 to 2011. *Right:* Spectrum of the brightest burst GRB110918 from the different neutrino flavors.

local coordinates is shown in Figure 6.5 and Figure B.1 (Appendix) for different selections regarding the reconstruction quality Λ. Either the corresponding rate at the GRB's position $(\Theta, \Phi)_{\mathrm{GRB}}$ was used, or – if resulting in a higher rate – the mean of the corresponding time-averaged rates within a 10° cone around this position. This established a conservative estimate, accounting for non-uniformity of the background in the vicinity of the GRB's position.

To take into account the varying efficiency of the detector due to changing environmental conditions with time, this average rate was then scaled by a correction c_i for each data-taking run i of $\sim$ 2.5 hours. This factor was calculated from the ratio of the total number of events (in all directions) in the corresponding run n_i to the average total number of events for the respective run duration t_i (see Equation 6.2). As n_i may be very small for short runs, the 90% C.L. upper limit assuming a Poissonian distribution (Section 5.1) was used instead. Additionally, factors for specific run periods c_{period} were applied taking into account differences between longer phases of similar run conditions. These values were obtained by fitting the background rate in certain periods separately.

This approach assumes that the total number of events – dominated mostly by downgoing atmospheric muons – is proportional to the number of upgoing events. To test this assumption, we determined the measured and estimated rates of upgoing events in longer time periods of a few days, excluding data-taking runs in which GRBs have been reported. The measured rate was always found to be $\mu_{\mathrm{meas}} < 1.5 \cdot \mu_{\mathrm{est}}$, thus we conservatively in-

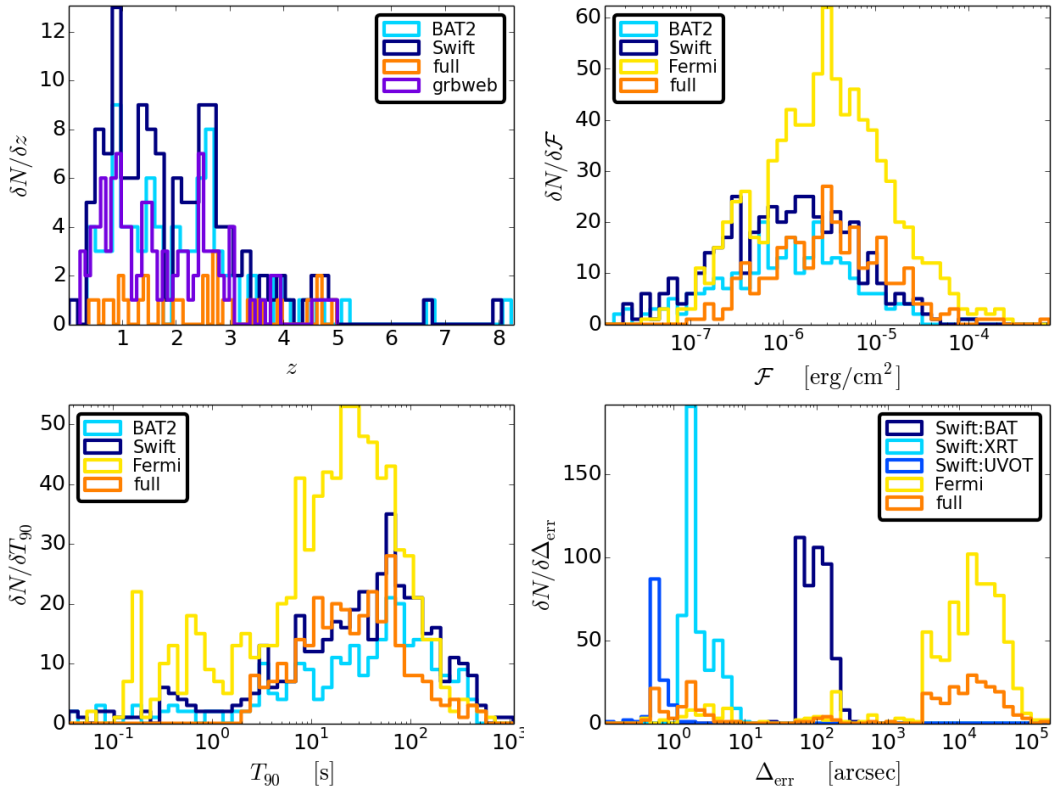

FIGURE 6.3.: The distributions of redshift, z, photon fluence $\mathcal{F}_\gamma$, T_{90} and the error box $r_{\rm err}$ in the different catalogs. In orange, the distributions of the final selection is shown. Parameters which were not measured and consequently assigned a default value are not depicted here.

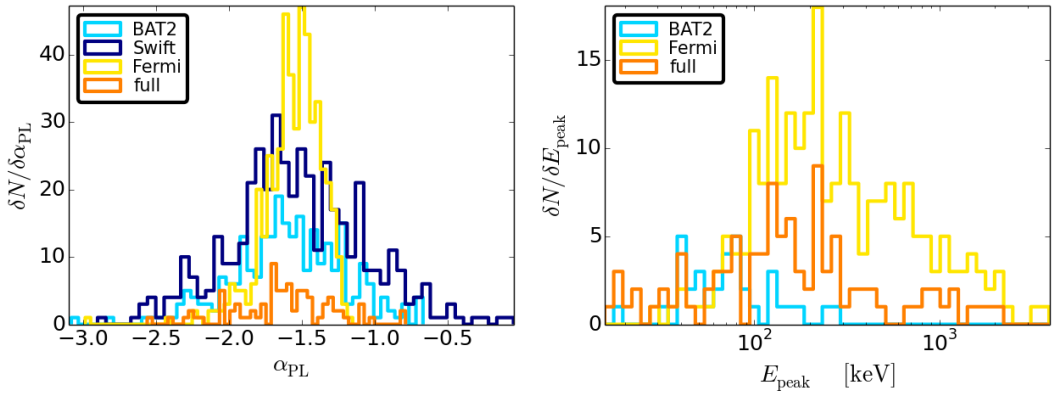

FIGURE 6.4.: The distributions of the photon index α for GRBs for which the photon spectrum is best fitted by a power-law and the break energy $\epsilon_{\rm peak}$ for exponentially cut-off power-laws.

creased the estimate by 50%. Consequently, the expected number of background events in coincidence with each GRB's search-time window T_{search} was calculated via

$$\begin{aligned} \mu_{\text{b}}(\Theta,\Phi)_{\text{GRB}} &= T_{\text{search}} \times \langle n(\Theta,\Phi)_{\text{GRB}} \rangle_{\text{all runs}} \cdot c_i \cdot c_{\text{period}} \cdot 1.5 \\ \text{with } c_i &= \frac{[n_i]^{90\%}}{t_i \sum n_j / \sum t_j} = \frac{[n_i]^{90\%}}{t_i} \frac{\sum t_j}{\sum n_j}\,, \end{aligned} \tag{6.2}$$

where j includes all data-taking runs. The evolution of the average background rate $\sum n_j / \sum t_j$ with different reconstruction quality cuts Λ is given in Table B.1 in the Appendix.

For the final search, the number of background events in coincidence with each burst and within 10° around its position was evaluated to be in the order of 10^{-4} (see Table 6.5 and C.1 in the Appendix for per-GRB values). The background PDF, $\mathcal{B}(\alpha)$, is assumed to be flat in solid angle within this cone as shown exemplary in Figure 6.6 for GRB110918.

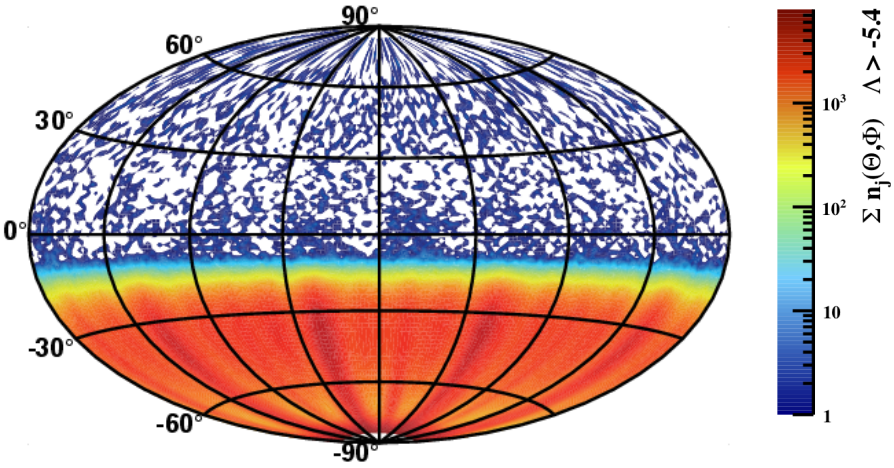

FIGURE 6.5.: All events $\sum n_j(\Theta,\Phi)$ in the late-2007 to 20011 period as used to evaluate the mean rate in the GRB's direction (see Equation 6.2) for data reconstructed with quality parameters $\Lambda > -5.4, \beta < 1°$. For other selection criteria, see Figure B.1 in the Appendix.

6.3. SIGNAL PROBABILITY DENSITY FUNCTION

For each gamma-ray burst in the selection, neutrino events were generated with high statistics to simulate the predicted NeuCosmA spectrum from the collected input parameters. They were then reconstructed to compute the acceptance of the detector. To ensure well reconstructed directions of the selected neutrino candidates, we required $\beta < 1°$ (see Section 4). Since the narrow time windows (typically a few tens of seconds, see Tables 6.5 & C.1 for per-GRB values) yield intrinsically low background in coincidence with each gamma-ray burst, event selection regarding the quality parameter Λ can be relaxed with respect to searches for steady astrophysical point sources (as for instance Adrián-Martínez et al., 2014). Depending on the expected background and signal fluxes, this criterion was then optimized for each burst individually.

To account for the satellite's uncertainty Δ_{err} on the direction of the GRB, the reconstructed position was additionally smeared with a Gaussian of the appropriate width. The

spread of the reconstructed tracks around the primary direction gave the signal probability density function (PDF) labeled $\mathcal{S}(\alpha) = \mathrm{d}N(\alpha)/\mathrm{d}\Omega$, with the space angle α between the reconstructed track direction and the gamma-ray burst's coordinates.

For each GRB, more than $4 \cdot 10^9$ neutrinos were simulated, and the resulting distribution of events relative to the GRB direction for each cut on Λ was then fitted with a smooth function of the form

$$\log \mathcal{S}(\alpha) = \log \frac{\mathrm{d}N(\alpha)}{\mathrm{d}\Omega} = \begin{cases} A, & \text{if } \alpha \leq \alpha_0 \\ A - B \cdot \left(1 - \exp\left(\frac{-(\log\alpha - \log\alpha_0)^2}{2\sigma^2}\right)\right) & \text{if } \alpha > \alpha_0\,, \end{cases} \tag{6.3}$$

with the free parameters A, B, α_0, and σ as shown in Figure 6.6. Events with an angular distance of up to 10° from the burst positions were taken into account.

Mainly those signatures associated with long straight particle tracks in the detector contributed to the detectable neutrino flux within the 10° search windows. These are produced by relativistic muons from charge-current interactions of muon neutrinos, with a smaller contribution from tau-neutrinos: In some cases, the secondary τ can decay into a muon, mimicking the signal from a muon neutrino (Bogazzi et al., 2010). Most of the ν_τ and ν_e, as well as neutral current interactions of ν_μ, produce spherical signatures in the detector, for which the angular reconstruction is quite challenging. An investigation of these cascade-like events revealed that these contribute only negligibly to the signal PDF up to 10°, as the original neutrino direction cannot be adequately reconstructed.

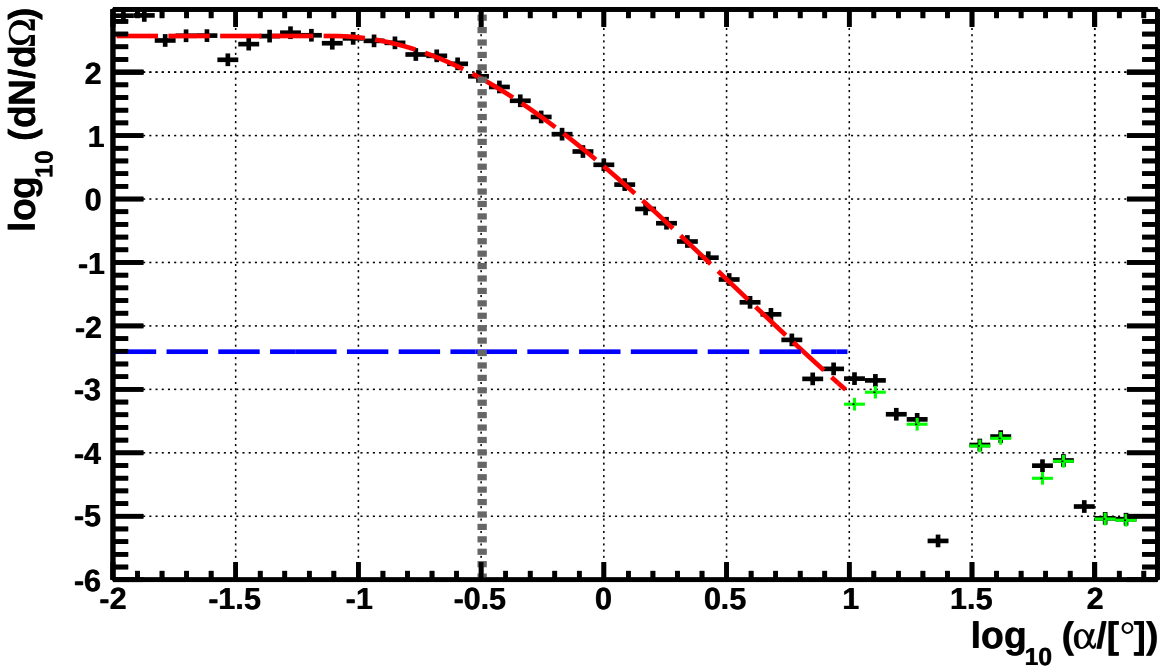

FIGURE 6.6.: Simulated and reconstructed signal events per solid angle Ω versus the logarithm of the space angle α in degrees for the burst GRB110918: muon tracks are plotted in black, shower-like events are drawn in green. The corresponding fit is shown in red (see Equation 6.3). The gray dotted line indicates the median angular spread of events $m(\alpha) = 0.32°$. The blue dashed line shows the flat background distribution $\mathcal{B}(\alpha)$ (Section 6.2). Cut values $\Lambda > -5.5$ and $\beta < 1°$ are applied here. (Figure from Adrián-Martínez et al., 2013d)

6.4. PSEUDO EXPERIMENTS AND EXTENDED MAXIMUM-LIKELIHOOD RATIO

In the following, I show how pseudo experiments were generated to compute the significance of a measurement, then how the cut on the reconstruction quality parameter Λ was optimized for each GRB to yield the highest discovery probability for a signal according to the NeuCosmA model. For the pseudo experiments, signal and background events i with space angle α_i were drawn randomly from the normalized signal $\mathcal{S}(\alpha)$ and background $\mathcal{B}(\alpha)$ PDFs corresponding to each chosen cut on Λ (see Figure 6.6). For each pseudo experiment with a total number of events n_{tot}, the test statistic Q was calculated as follows:

$$Q = \max_{\mu'_{\mathrm{s}} \in [0, n_{\mathrm{tot}}]} \left(\sum_{i=1}^{n_{\mathrm{tot}}} \log \frac{\mu'_{\mathrm{s}} \cdot \mathcal{S}(\alpha_i) + \mu_{\mathrm{b}} \cdot \mathcal{B}(\alpha_i)}{\mu_{\mathrm{b}} \cdot \mathcal{B}(\alpha_i)} - (\mu'_{\mathrm{s}} + \mu_{\mathrm{b}}) \right). \tag{6.4}$$

This is the so-called extended maximum-likelihood ratio (Barlow, 1990) with an a priori knowledge of the expected number of background events μ_{b}. Higher values of Q indicate that the measurement is more compatible with the signal hypothesis (see Section 5.1). The signal contribution μ'_{s} is scanned between 0 and n_{tot}, its value corresponding to the maximum of the sum in Equation 6.4 returns the estimated signal $\mu_{\mathrm{s}}^{\mathrm{est}}$. In contrast to the simple counting of events as in the analysis shown in Section 5, the test statistic proposed here makes use of the information incorporated in the spatial distributions of the expected signal and background flux. While the background is uniformly distributed, the signal is expected to be centered at the gamma-ray burst's position.

In the following, $h_{n_{\mathrm{s}}}(Q) = (\delta N / \delta Q)_{n_{\mathrm{s}}}$ denotes the distribution of Q-values for n_{s} injected signal events with a Poisson-distributed number of background events with expectation value μ_{b} as derived from the data. The significance of a measurement is determined by its p-value, which is given by the probability to yield Q-values at least as high as that observed if the background-only hypothesis were true. Hence, using the background-only distribution $h_0(Q)$, the lowest Q-value Q_p^{thres} that is necessary to claim a discovery with a certain p-value can be calculated via

$$P(Q \geq Q_p^{\mathrm{thres}} | \, \mu_{\mathrm{b}}) = \int_{Q_p^{\mathrm{thres}}}^{\infty} h_0(Q) \, \mathrm{d}Q = p \, . \tag{6.5}$$

The probability distributions $h_{n_{\mathrm{s}}}(Q)$ for different n_{s} are shown in Figure 6.7, with the threshold Q-values indicated by the gray dashed lines. The probability distribution of Q values for any number of expected signal events μ_{s} is calculated via

$$P(Q | \, \mu_{\mathrm{s}}) = \sum_{n_{\mathrm{s}}=0}^{\infty} \mathcal{P}(n_{\mathrm{s}} | \, \mu_{\mathrm{s}}) \cdot h_{n_{\mathrm{s}}}(Q) \, , \tag{6.6}$$

with the Poissonian distribution $\mathcal{P}(n_{\mathrm{s}} | \, \mu_{\mathrm{s}})$ giving the probability of observing n_{s} events from a mean number of expected events μ_{s}. The integral of $P(Q | \, \mu_{\mathrm{s}})$ gives the model discovery potential $\mathcal{MDP}$ (see also Section 5.1); it is the probability to make a discovery

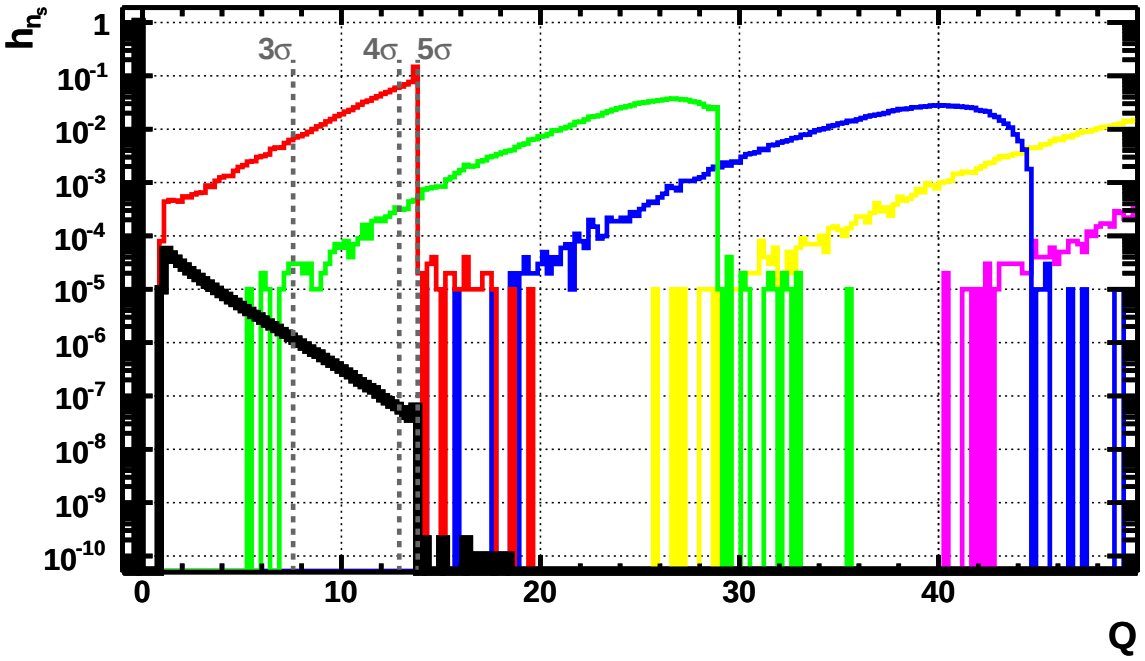

FIGURE 6.7.: Probability distributions of Q-values, $h_{n_s}(Q)$, for different numbers of injected signal events n_s. Black: background only, $h_0(Q)$; red, green, blue...: $n_s = 1, 2, 3\ldots$ injected signal events. Gray vertical lines indicate the threshold values Q_p^{thres} for different significances after accounting for a trial factor of 296 (see Sect. 6.5) as calculated from $h_0(Q)$. This example shows GRB110918 with $\Lambda > -5.5$ and $\mu_b = 3.7 \cdot 10^{-4}$ background events. (Figure from Adrián-Martínez et al., 2013d)

assuming that the model was correct:

$$\begin{aligned} \mathcal{MDP} &= P(Q \geq Q_p^{\text{thres}} | \, \mu_s) = \int_{Q_p^{\text{thres}}}^{\infty} P(Q | \, \mu_s) \, dQ \\ &= \sum_{n_s=0}^{\infty} \mathcal{P}(n_s | \, \mu_s) \cdot \int_{Q_p^{\text{thres}}}^{\infty} h_{n_s}(Q) \, dQ. \end{aligned} \tag{6.7}$$

The value of the Λ cut for each GRB was then chosen as that which maximizes the $\mathcal{MDP}$ for the value of μ_s predicted by the NeuCosmA model (see Section 2.2). This optimum is naturally dependent on the significance level for which the $\mathcal{MDP}$ should be maximal. Note that the p-value had to be adjusted by a statistical penalty factor of 296 to account for the size of the analyzed sample. Figure 6.8 shows the discovery probability of GRB110918 for 3σ, 4σ, and 5σ versus an arbitrary number of signal events. The distribution $P(Q | \, \mu_s)$ from Equation 6.6 is also used to set upper limits on the number of signal events when no discovery is made. When the search for correlated neutrino signatures in the ANTARES data returns a value Q_{meas} of the test statistic, a 90% confidence level (C.L.) upper limit $\mu_s^{90\%}$ on the signal strength can be set by rejecting all event expectations μ_s that lead to values $Q > Q_{\text{meas}}$ in 90% of all pseudo experiments:

$$P(Q \geq Q_{\text{meas}} | \, \mu_s^{90\%}) = \int_{Q_{\text{meas}}}^{\infty} P(Q | \, \mu_s^{90\%}) \, dQ = 0.9 \, . \tag{6.8}$$

When no event is found ($Q_{\text{meas}} = 0$), a 90% C.L. upper limit can be set at 2.3, the lowest possible value (see Section 5.1).

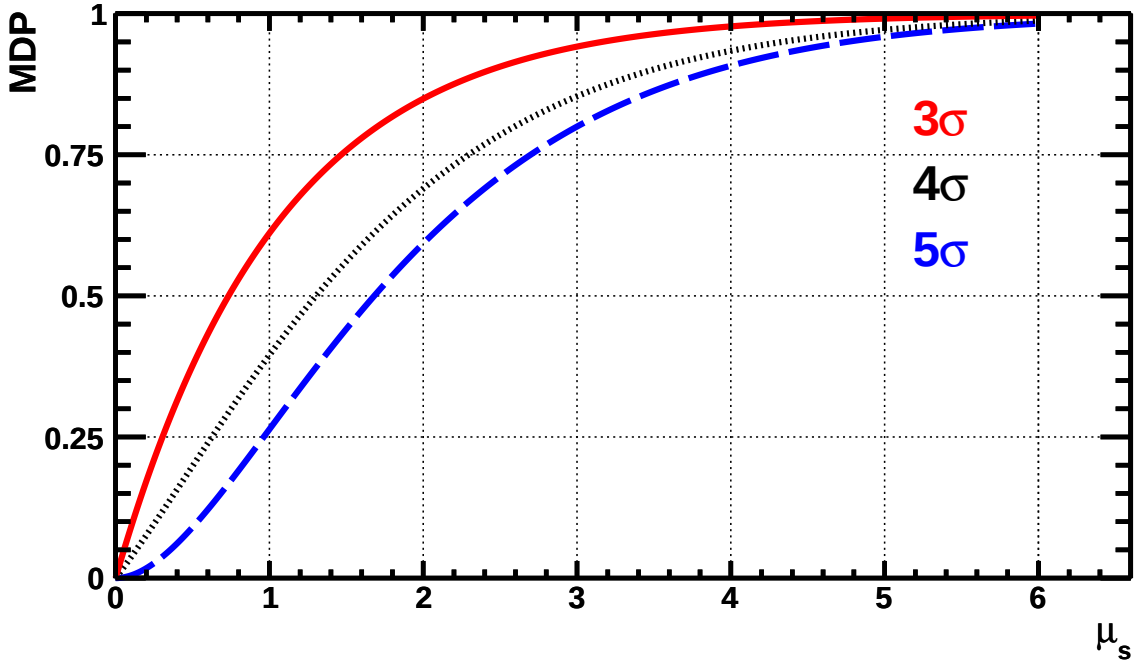

FIGURE 6.8.: Model discovery potential $\mathcal{MDP}$ versus signal flux μ_s for 3σ (red solid line), 4σ (black dotted), and 5σ (blue dashed) for GRB110918. (Figure from Adrián-Martínez et al., 2013d)

For each number of injected signal events n_s, 10^5 pseudo experiments were generated to derive the signal distributions $h_{n_s}(Q)$, while more than 10^{10} background-only pseudo experiments were run to allow determining Q_p^{thres} at p-values as low as $p_{5\sigma}/296 \sim 2 \cdot 10^{-9}$. Using this procedure, the model discovery potential was calculated for the predicted signal flux μ_s, and the final cut on Λ for each GRB was found.

6.5. SEARCH OPTIMIZATION

In the following, the optimal trade-off between an increased sample size and the associated statistical penalty is investigated. In general, a weighting factor w_i could be assigned to each GRB according to the predicted flux from the model. However, this would result in the search being very sensitive to the combined uncertainty from the NeuCosmA model and especially to the parameters upon which it is based. An alternative approach is to include only the N_{GRB} most promising candidates, where to maintain the same overall probability of making a false discovery, the p-value for each burst must be divided by the total trial factor N_{GRB}. By ordering the bursts from highest to lowest $\mathcal{MDP}_i$, the most promising N_{GRB} can be chosen to maximise the combined probability of making a significant discovery from any of them. The total model discovery potential is then calculated via

$$\mathcal{MDP}(N_{\text{GRB}}) = 1 - \prod_{i=1}^{N_{\text{GRB}}} (1 - \mathcal{MDP}_i). \tag{6.9}$$

The resulting distributions of $\mathcal{MDP}(N_{\text{GRB}})$ as a function of the size of the considered sub-sample of GRBs are shown in Figure 6.9 for significance levels of 3σ, 4σ and 5σ (thick

lines). The 3σ $\mathcal{MDP}$ distribution rises to a maximum of 5.9% at a sample size of 106 GRBs, but is relatively flat around its highest value. For a search optimized for 3σ evidence it is therefore reasonable to chose the whole set of GRBs, as it does not decrease the $\mathcal{MDP}$ significantly (around 3.4%) and the search remains less model-dependent. The 5σ $\mathcal{MDP}$ distribution, on the other hand, is prominently peaked at $N_{\mathrm{GRB}} = 1$, with $N_{\mathrm{GRB}} = 2$ being almost equivalent ($\mathcal{MDP}(1) = \mathcal{MDP}(2) = 2.5\%$) – the model discovery potential then decreases for larger samples. Even for $N_{\mathrm{GRB}} = 2$, the second strongest GRB contributes only a small fraction to the discovery potential. This demonstrates again how the brightest GRB110918 dominates the neutrino flux of the whole selection.

For comparison, the distributions for a simple counting search (see also Section 5) are also shown in Figure 6.9 (thin lines). To mimic this search, a search radius was calculated for each GRB from the known background μ_{b} at fixed reasonable quality cuts ($\Lambda > -5.5, \beta < 1^{\circ}$) and the given significance level p/N_{GRB}, so that each detected event would be a discovery at this level. Applying this search radius cut on the signal PDF $\mathcal{S}(\alpha)$, the expected number of signal events μ_{s} can be estimated and consequently the $\mathcal{MDP}_i$ evaluated as the probability of detecting more than zero events from a Poissonian distribution with the respective mean rate μ_{s}. Again, this calculation is repeated on each sub-sample of size N_{GRB} of all bursts with the highest individual $\mathcal{MDP}_i$ to evaluate the total discovery probability of the optimized sample.

As expected, the discovery probability for a counting analysis are well below those for the likelihood method, showing the advantage of the more sophisticated search method used in this analysis. In some cases, for instance considering a sub-sample of the ten strongest bursts optimized for 5σ, the likelihood search can identify a neutrino signal twice as efficient as the mimicked counting search. The shapes of the curves, on the other hand, are quite similar, and the same conclusions can be drawn from them, namely that using the whole sample gives the best discovery probability at a 3σ level and using only the individual GRB110918 at 5σ. Based on these results, the ANTARES collaboration decided to search the data of the entire sample of 296 GRBs with the quality cut Λ optimized to find 3σ evidence of a signal. To maximize the chances for a significant detection, a cut on Λ as optimized for a 5σ discovery was predefined, which was then used for a separate search for the neutrino emission from GRB110918 only.

Optimised cuts Λ_{cut} for the final analysis as well as the accordingly expected number of background and signal events, the median angular resolution, and the search-time window are shown in Table 6.5 for the ten most promising gamma-ray bursts. A full list for the 296 selected bursts can be found in Table C.1 in the Appendix, and is also available online[9].

[9]The table is available in electronic form at the CDS via anonymous ftp to cdsarc.u-strasbg.fr (130.79.128.5) or via `http://cdsarc.u-strasbg.fr/viz-bin/qcat?J/A+A/559/A9`

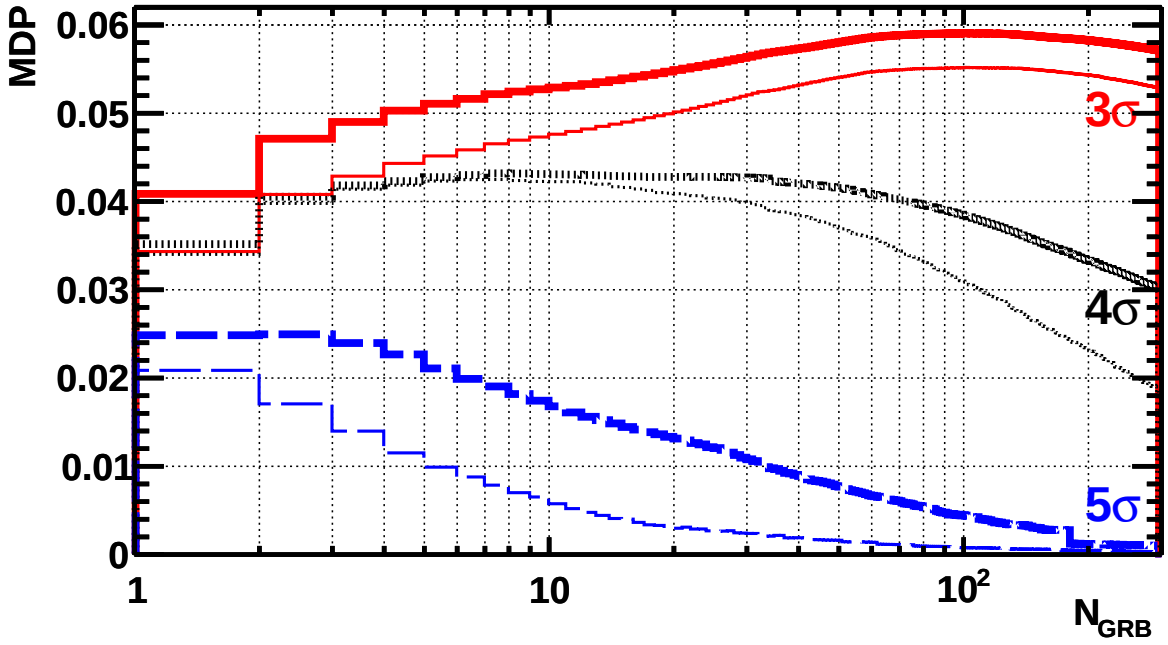

FIGURE 6.9.: Model discovery potential $\mathcal{MDP}$ versus the number of GRBs in an optimized sub-sample, N_{GRB}, for 3σ, 4σ, and 5σ significance levels in red solid, black dotted, and blue dashed lines. For each sub-sample, only the N_{GRB} bursts with the best $\mathcal{MDP}_i$ at the given trial factor N_{GRB} are chosen. The thick lines show the $\mathcal{MDP}$ distributions of the likelihood method used in this analysis, the thin lines show the distributions for a simple counting search with fixed quality cuts $\Lambda > -5.5$, $\beta < 1^\circ$. (Figure from Adrián-Martínez et al., 2013d)

6.6. RESULTS AND DISCUSSION

Using the strategy outlined above and the chosen optimization, in total 0.06 neutrino events from GRBs were expected from the NeuCosmA model, where only a small contribution of $4.6 \cdot 10^{-5}$ events is not due to particle tracks produced by muon neutrinos – the Guetta model predicts 0.5 signals from muon neutrinos. The overall background in the 10° cones is 0.05 events. Note that even though the number of expected detected signal events is comparable to that from background, the implemented test statistic is a powerful tool to discriminate between the two. The discovery probability for a signal as predicted from the NeuCosmA model is 5.7%.

We consequently analyzed ANTARES data from the end of 2007 to 2011 searching for neutrino signatures in coincidence with the defined search-time windows and within 10° around each gamma-ray burst. No data events passed this selection within the accumulated search duration of 6.6 hours. Hence, the measured Q-value is zero. The 90% C.L. upper limits on the expected number of signal events μ_s from each model are thus set to 2.3 events, and the corresponding limits on the muon neutrino flux, F_ν, from GRB110918 as well as on the cumulative flux from the whole sample are shown in Figure 6.10. For the NeuCosmA model, the limit on the total flux lies a factor of 38 above the expected spectrum (4.4 for the predictions by Guetta et al., 2004). The right-hand axis of Figure 6.10 (b) represents the

GRB	Λ_{cut}	μ_{b}	$\mu_{\text{s}}^{\text{NeuCosmA}}$	$\mu_{\text{s}}^{\text{Guetta}}$	$\langle\alpha\rangle$ (°)	T_{search} (s)	σ_{tot}
11091889	-5.3	$1.1{\cdot}10^{-4}$	$3.0{\cdot}10^{-2}$	$1.5{\cdot}10^{-1}$	0.30	73.4	5σ
11091889	-5.5	$3.7{\cdot}10^{-4}$	$3.5{\cdot}10^{-2}$	$1.7{\cdot}10^{-1}$	0.32	73.4	
08060725	-5.4	$5.5{\cdot}10^{-4}$	$6.5{\cdot}10^{-3}$	$1.4{\cdot}10^{-2}$	0.33	164.3	
11100892	-5.5	$3.6{\cdot}10^{-4}$	$2.2{\cdot}10^{-3}$	$2.6{\cdot}10^{-3}$	0.35	75.4	
10101417	-5.1	$4.1{\cdot}10^{-4}$	$1.2{\cdot}10^{-3}$	$1.7{\cdot}10^{-2}$	0.89	723.1	
10072809	-5.6	$1.6{\cdot}10^{-4}$	$9.6{\cdot}10^{-4}$	$1.4{\cdot}10^{-2}$	0.49	268.6	
09020174	-5.4	$5.3{\cdot}10^{-4}$	$7.0{\cdot}10^{-4}$	$2.4{\cdot}10^{-2}$	0.39	126.6	
11122048	-5.2	$1.4{\cdot}10^{-4}$	$6.2{\cdot}10^{-4}$	$1.2{\cdot}10^{-2}$	1.13	66.5	
09082967	-5.4	$1.7{\cdot}10^{-4}$	$3.9{\cdot}10^{-4}$	$5.7{\cdot}10^{-3}$	1.02	112.1	
11062215	-5.4	$1.7{\cdot}10^{-4}$	$4.3{\cdot}10^{-4}$	$9.5{\cdot}10^{-3}$	1.42	116.6	
08100914	-5.5	$1.2{\cdot}10^{-4}$	$3.5{\cdot}10^{-4}$	$1.9{\cdot}10^{-3}$	0.94	70.2	
all GRBs:							3σ
mean	-5.4	$1.7{\cdot}10^{-4}$	$2.0{\cdot}10^{-4}$	$1.6{\cdot}10^{-3}$	2.85	80.4	
sum		$5.0{\cdot}10^{-2}$	$6.1{\cdot}10^{-2}$	$4.8{\cdot}10^{-1}$		$2.4{\cdot}10^{4}$	

TABLE 6.5.: Optimization results for the ten most promising GRBs. Optimised Λ_{cut} values for the ten gamma-ray bursts with the highest discovery probabilities and the resulting expected number of background and signal events μ_{b} and μ_{s} at the significance level σ_{tot}. The corresponding median angular spread of events $m(\alpha)$ is also provided. In the last rows, the sum and mean of the values for all 296 GRBs at the 3σ level are given. A full table is provided in Appendix C. The naming convention for the GRBs is similar to that used by *Fermi*, the last two digits of the GRB name correspond to the fraction of the day at which the burst occurred.

limits translated into limits on the inferred quasi-diffuse neutrino flux:

$$E^2\Phi_\nu = \sum E^2 F_\nu \times \frac{1}{4\pi} \cdot \frac{1}{N_{\text{GRB}}} \cdot 667\ \text{y}^{-1}, \tag{6.10}$$

assuming that the analyzed sample represents an average burst distribution and that the annual rate of long bursts is 667 per year.

The first ANTARES limit (Adrián-Martínez et al., 2013c) derived for 40 GRBs during the construction phase of the detector in the year 2007 is also shown in Figure 6.10 (b). That analysis was based on the model by Guetta et al. (2004) (accounting for different break energies of ν_μ and $\bar{\nu}_\mu$) and employed a counting method searching for neutrino events in a two-degree cone around each burst. Using the data from the IC40 and IC59 detector phases in 2008 to 2010, ICECUBE recently published a more stringent limit on the neutrino emission as predicted by the same model (Abbasi et al., 2012), which is also shown in Figure 6.10 (b).

Because of the larger effective area of the IceCube detector, the new ANTARES limit derived in this work does not set additional constraints on the quasi-diffuse neutrino emission. Note, however, that both detectors have complementary sky coverage and therefore the analyzed sample of GRBs differs significantly. 90% of the analyzed bursts have not previously had their neutrino emission constrained. When comparing limits obtained in different analyses, however, one should keep in mind that the precise shapes of the spectra – and thus, of the limits – depend on the actual selected sample, the measured parameters

of the individual bursts and their uncertainty, the set of default parameters and on the chosen model.

6.7. CONCLUSION

Using data from the ANTARES detector, a search for muon neutrinos in coincidence with 296 gamma-ray bursts occurring between the end of 2007 and 2011 has been performed. No data events passed the selection criteria and limits on the neutrino flux were derived. For the NeuCosmA model, an upper limit at E^2F_ν of $0.35 - 5.6$ GeV cm^{-2} was placed in the energy range from $7.5 \cdot 10^4$ GeV to $1.0 \cdot 10^7$ GeV and compared with limits obtained in previous analyses.

The presented work is the first analysis based on an advanced numerical calculation of GRB neutrinos: the NeuCosmA code includes full photohadronic interaction cross-sections, energy losses of secondary particles, and flavor mixing (see Section 2.2). The neutrino flux has been shown to be an order of magnitude below that predicted by previous analytic approaches. This helps to resolve the tension between the non-observation of a neutrino signal and the most stringent experimental constraint currently available (Abbasi et al., 2012), which was a factor of 2.1 below the predictions made following Guetta et al. (2004).

Hence, existing limits do not yet constrain realistic neutrino emission models based on an internal shock scenario. Nevertheless, the collection of more data with active experiments such as ANTARES and ICECUBE, as well as with the planned neutrino telescope KM3NET (see Section 8) and potential extensions of ICECUBE, will certainly allow the widely established fireball paradigm for gamma-ray bursts to be probed in the near future. The presented work was published in the article Adrián-Martínez et al. (2013d).

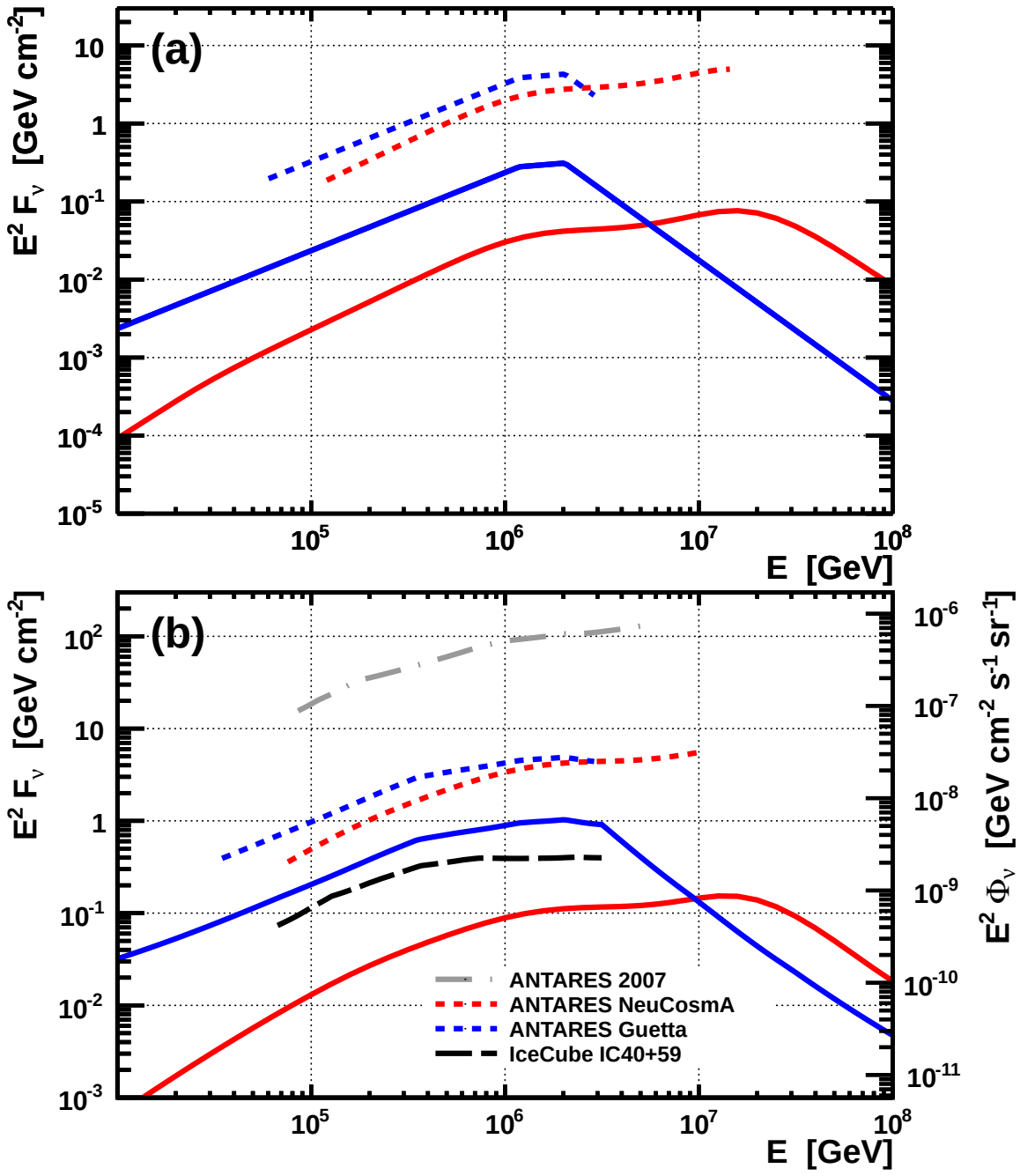

FIGURE 6.10.: (a): Expected muon neutrino spectra of the most promising burst GRB110918 (solid lines) from NeuCosmA (Hümmer et al., 2010) (red) and Guetta et al. (2004) (blue). Limits on these predictions are shown in the energy ranges where we expect 90% of the flux (dashed lines). (b): Sum of the 296 individual gamma-ray-burst muon-neutrino spectra (red and blue solid lines) and limits set by this analysis on the total flux expected from the sample (red and blue dashed lines). The IceCube IC40+IC59 limit (Abbasi et al., 2012) on the neutrino emission from 300 GRBs and the first ANTARES limit from 2007 using 40 GRBs (Adrián-Martínez et al., 2013c) are also shown in black (dashed) and gray (dash-dotted), respectively. The right-hand axis represents the inferred quasi-diffuse flux limit $E^2\Phi_\nu$ (Equation 6.10). (Figure from Adrián-Martínez et al., 2013d)

7. Search for high-energy neutrinos from GRB130427A

On April 27th, 2013 at 7:74 UT, one of the brightest gamma-ray bursts ever detected lit up the high-energy sky. It could be observed by a record-setting number of satellites and ground-based telescopes[1], and with a measured photon fluence in the order of $10^{-3}\,\mathrm{erg/cm^2}$, GRB130427A turned out to be the strongest burst since 1983 (GRB830801B). Numerous coincident and follow-up optical observations soon measured a redshift of only 0.34 (e.g. Levan et al., 2013), which is exceptionally close for a gamma-ray burst. Figure 7.1 shows the sky above 100 MeV as observed by the LAT instrument on-board the *Fermi* satellite. GRB130427A significantly outshined the high-energy sky with emission being visible for LAT almost the entire day. Two high-energy photons of a record-holding 95 GeV after 244 s and 32 GeV more than 9 hours after the onset of the prompt emission (Zhu et al., 2013; Ackermann et al., 2014) began to severely challenge prevailing models for the late GeV emission, yet might support scenarios of hadronic material within the ejecta. Such assumptions can only be tested beyond any doubt by the detection of simultaneously emitted neutrinos. Data of both operating neutrino telescopes IceCube and Antares could therefore hold valuable proof for the aforementioned models. However, the IceCube collaboration had already announced the non-observation of any coincident neutrino signal in their data within ± 1 day around the burst via the GCN network on May 1st, 2013 (Blaufuss, 2013).

A dedicated follow-up analysis of the data taken simultaneously by the Antares telescope during the prompt emission phase was established, based on the methods presented in Section 6. The data selection was optimized for the discovery of a neutrino signal as predicted by the state-of-the-art numerical model NeuCosmA (Section 2.2). The fast response to this extraordinary GRB required dedicated detector calibration and data processing of the respective data run, taking into account the particular conditions at that time.

Data-Taking Conditions At the end of April 2013, the Antares detector was just resuming regular data taking after a six-week period of unusual bioluminescent activity in the deep sea, in which the high voltage in the optical modules had been switched off. This security measure had been previously introduced to prevent the photo multipliers from suffering high optical rates in the spring periods, when the background due to bioluminescence can exceed 500 kHz per PMT. The detector had been running in this state from March, 5, to April, 23, with only a few optical modules taking data with usual high voltage to monitor the deep-sea conditions continuously. In the first week after after the optical modules had been turned on, the photo multipliers were stabilizing slowly back to usual data taking. During this time, the threshold value for filtering highly charged photon pulses had

[1] see `http://gcn.gsfc.nasa.gov/other/130427A.gcn3` for all GCN messages on GRB130427A

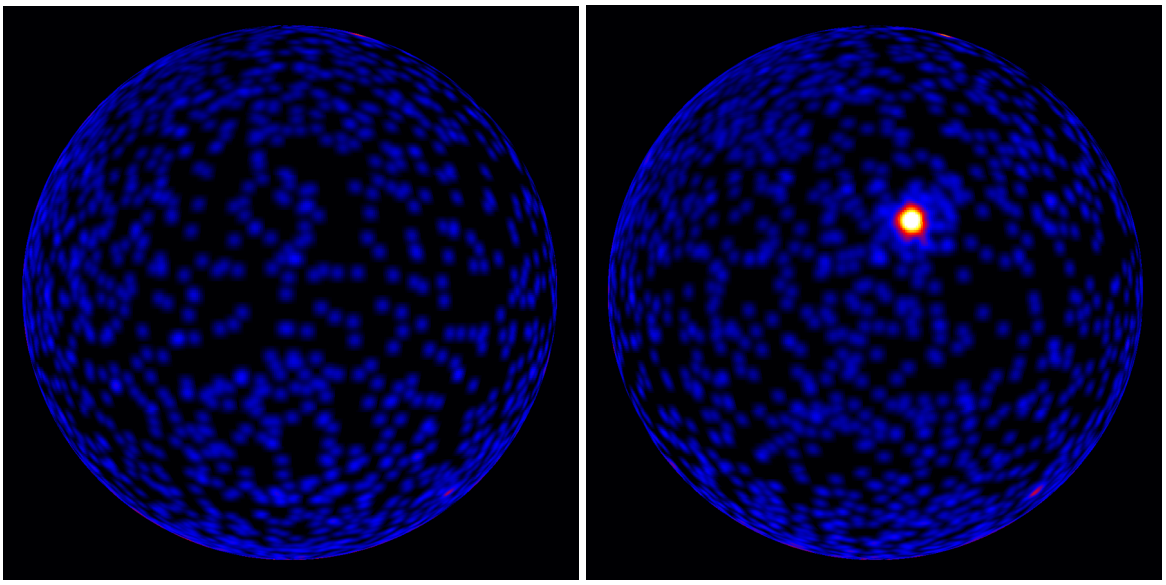

FIGURE 7.1.: The sky as seen by *Fermi*:LAT in the 3 hours before the burst GRB130427A and when it occurred, to give an impression of the burst's brightness with respect to the rest of the gamma-ray sky. Credit: NASA/DOE/Fermi Collaboration

been increased from 3 to 10 photoelectrons to limit the rate of accidental data triggering from background. Under these conditions, the telescope was recording data with a stable frequency of 3.6 Hz with a mean optical background rate of 127.8 kHz (see Table 7.1).

BURST PROPERTIES The properties of GRB130427A needed for the definition of the coincident data search windows and the simulation of its neutrino emission predicted by the NeuCosmA model were collected from the GCN announcements and the catalog provided by the *Fermi* collaboration. The burst's coordinates were measured by the ISON-NM observatory to a precision of 1 arcsecond (Elenin et al., 2013), the photon spectrum for the calculation of the neutrino flux is provided in the *Fermi*:GBM catalog[2]. I defined a search time window T_{search} as the time T_{90} measured by the *Swift*:BAT instrument (Barthelmy et al., 2013) with a $\pm 30\%$ margin around it. All parameters are summarized in Table 7.1.

BACKGROUND Besides the twelve-hour data-taking run 70515 recorded simultaneously with GRB130427A, no processed data was yet available for the spring-2013 period. However, to derive the expected background rate similarly to Equation 6.2 (Section 6.2), we made use of the average rate in the direction of the GRB $\langle n(\Theta, \Phi)_{\text{GRB}} \rangle$ from the four-year period late-2007 to 2011, and the data-taking efficiency c could be derived as before from the ratio of the measured data rate to this average. However, it was essential to robustly estimate the uncertainty of this value, in particular considering the challenging conditions in spring 2013 after data taking had just been resumed. Previously, the fluctuations of the instantaneous correction factor had been quantified from the data of the surrounding four-year period that had not been taken simultaneously with any reported GRB (see Section 6.2). To evaluate the variations in the background estimation for GRB130427A, the

[2] `http://heasarc.gsfc.nasa.gov/W3Browse/fermi/fermigbrst.html`

RA $= 173.14^\circ$	$\delta = 27.70^\circ$	$\Delta_{\mathrm{err}} = 1\,\mathrm{arcsec}$
$\Theta = 108.31^\circ$	$\Phi = 101.66^\circ$	MJD $= 56409.325$
$T_{90} = 138.242\,\mathrm{s}$	$T_{\mathrm{search}} = 264.5\,\mathrm{s}$	$z = 0.3399$
$\mathcal{F} = 2.462 \cdot 10^{-3}\,\mathrm{ergcm}^{-2}$	$E_{\mathrm{min}} = 0.01\,\mathrm{MeV}$	$E_{\mathrm{max}} = 1\,\mathrm{MeV}$
$\alpha = -0.789$	$\beta = 3.06$	$E_{\mathrm{peak}} = 830\,\mathrm{keV}$
run : 70515	$T_{\mathrm{run}} = 12.02\,\mathrm{h}$	high-charge threshold $= 10$ photoelectrons
$\langle\mu\rangle = 127.8\,\mathrm{kHz}$	$m(\mu) = 66.6\,\mathrm{kHz}$	$\mu_{\mathrm{baseline}} = 62.7\,\mathrm{kHz}$
setup: *Line 1-12 Physics Trigger 3N+2T3+K40+TS0 SNbuffer Apr2013 hT=10 post-OFF*		

TABLE 7.1.: Parameters of GRB130427A (see also Section 6.1) and the respective ANTARES data-taking conditions, including the average and median of the optical background rate μ and its baseline and the data-taking run setup.

total number of upgoing data signatures $n^{\mathrm{up}}_{\mathrm{meas}}$ was compared to that expected $n^{\mathrm{up}}_{\mathrm{exp}}$ from the average of the four-year period and the correction c, when varying the cuts on the data reconstruction quality Λ. The search time window around the burst with an additional margin of 1/4 h was excluded for this estimation, resulting in a data livetime in the off-source region of 11.7 hours. The instantaneous efficiency for run 70515 (see Table B.2 in the Appendix) was always found to be $c < 55\%$, which reflects the poor data-taking conditions after a six-week period of high background rates and data acquisition turned off. The efficiency for well-reconstructed events was even worse with less than 30% of the four-year average. The measured number of data events was found to be $n^{\mathrm{up}}_{\mathrm{meas}} \leq 2.9 \cdot n^{\mathrm{up}}_{\mathrm{exp}}$ for all quality cuts, so the collaboration decided to conservatively increase the background estimate of GRB130427A by a factor of 3 in Equation 6.2[3]. The spatial distribution of background events $\mathcal{B}(\alpha)$ was assumed to be flat within the 10° search cone around GRB130427A.

SIMULATION I modeled the expected neutrino fluence according to the burst parameters both using the predictions by Guetta et al. (2004) and the numerical NeuCosmA model (see Section 2.2), with the latter being used for optimization of the data selection. GRB130427A was found to be approximately a factor of 2.5 fainter in the light of neutrinos than the brightest burst of the late-2007 to 2011 analysis, GRB110918, but still at least a factor of 2 stronger than any other of the previous sample. The burst was simulated as a neutrino point source using the dedicated calibration for this data-taking run. The simulated data were then reconstructed to derive the signal probability density function $\mathcal{S}(\alpha)$ for different cuts on the reconstruction quality Λ (see Section 6.3 for more details). The angular error estimate was required to be $\beta < 1^\circ$ to ensure good angular resolution.

[3] In the spring periods of the years 2009 and 2010, the rate-tuning factor had been found to be $c_{\mathrm{period}} = 1.5$, yielding a total uncertainty factor of $1.5 \cdot 1.5 = 2.25$ in the background estimation for GRBs in these periods.

σ	Λ_{cut}	μ_{b}	$\mu_{\text{s}}^{\text{NeuCosmA}}$	$\mu_{\text{s}}^{\text{Guetta}}$	$m(\alpha)$ (°)	$\mathcal{MDP}$
5σ	-5.3	$2.2{\cdot}10^{-4}$	$4.4{\cdot}10^{-3}$	$6.0{\cdot}10^{-2}$	0.26	$3.6{\cdot}10^{-3}$
3σ	-5.9	$1.0{\cdot}10^{-2}$	$6.2{\cdot}10^{-3}$	$8.4{\cdot}10^{-2}$	0.37	$8.6{\cdot}10^{-3}$

TABLE 7.2.: Optimized Λ_{cut} at the 3σ and 5σ level and the corresponding background and signal rates μ_{b} and μ_{s}, the median angular resolution $m(\alpha)$ and the probability $\mathcal{MDP}$ to discover an excess as predicted from the NeuCosmA model (Hümmer et al., 2010) at the given significance.

SEARCH OPTIMIZATION More than 10^8 pseudo experiments were generated for each cut on the reconstruction quality Λ with events drawn from the background and signal probability density functions $\mathcal{S}(\alpha)$ and $\mathcal{B}(\alpha)$. For each of the realizations, the maximum likelihood ratio Q was calculated according to Equation 6.4, so that the discovery probability $\mathcal{MDP}$ for each of the quality cuts could be derived.

The probability to find evidence for an excess in the data at the 3σ level based on the NeuCosmA predictions was found to be maximal when selecting signatures with $\Lambda > -5.9$, while a discovery of 5σ was most probable for $\Lambda > -5.3$. Table 7.2 summarizes the consequently expected number of background and signal events from both models. With the selection criteria optimized for 3σ significance, the expected background in the predefined search window of 264.5 s and within 10° around the GRB's position is reduced to 10^{-2} events. The two models respectively predict $6.2 \cdot 10^{-3}$ (NeuCosmA) and $8.4 \cdot 10^{-2}$ (Guetta et al., 2004) detected signal neutrinos in the ANTARES data. Note that even if the background contribution exceeds the expected signal, the maximum likelihood ratio Q (Equation 6.4) can reliably distinguish between the flat background distribution and the signal that is peaked at the burst's location. The number of signals expected in the ANTARES detector from the NeuCosmA model is a factor of ~ 5 lower than that expected from GRB110918, the brightest burst in the period between December 2007 and 2011. This is partly due to the lower model predictions, but also a result of the less favorable data-taking conditions, which are reflected by the small data efficiency of the run ($c = 44\%$ at $\Lambda > -5.9$ and $\beta < 1°$, see Table B.2). With a chance of almost 1%, 3σ evidence of a neutrino signal associated with GRB130427A as predicted from the NeuCosmA model can be found in the ANTARES data.

After the capability of the analysis was demonstrated using Monte Carlo simulations and pseudo experiments, it was decided to search the data of GRB130427A with the selection criteria being optimized to find 3σ evidence for a neutrino excess. Even if this configuration lowers the detection probability at the 5σ level by a factor of 60, it allows at the same time to place more stringent limits in case of a non-detection, while still leaving open the possibility to observe more than one simultaneous neutrino signature. As demonstrated by the pseudo experiments, this would in most cases yield a definitive discovery at the 5σ level and provide sound confidence in a presumable first claim of the detection of a neutrino signal associated with gamma-ray bursts.

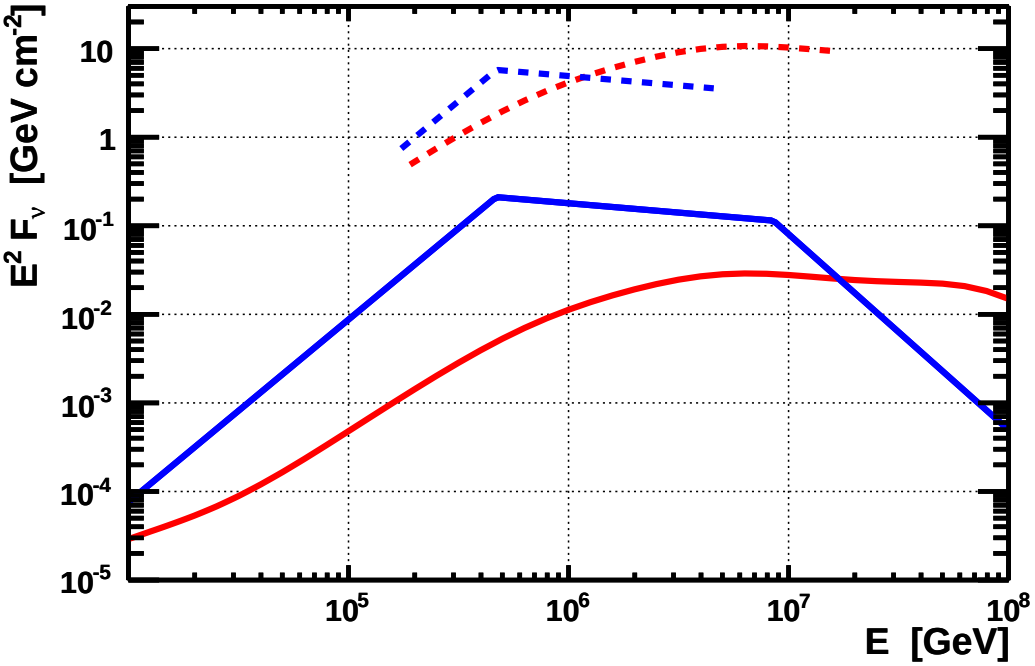

FIGURE 7.2.: Expected neutrino fluences (solid lines) from the analytical model from Guetta et al. (2004) and the numerical NeuCosmA-model (Hümmer et al., 2010) and derived limits on the coincident neutrino emission with GRB130427A (dashed) in the energy range where 90% of the signal is expected to be detected.

RESULTS After approval of the analysis within the collaboration, the ANTARES data were searched for neutrino signatures within the defined burst's search window, selecting events that fulfilled the reconstruction quality parameters optimized for detections at the 3σ level (see Table 7.2). No excess over background could be found in the data recorded simultaneously with the prompt GRB emission. Consequently, only 90% confidence-level upper limits on the coincident neutrino emission with GRB130427A can be placed at $E^2F_\nu \sim 1 - 10\,\mathrm{GeV/\,cm^2}$ in the energy range $2 \cdot 10^5 - 1 \cdot 10^7\,\mathrm{GeV}$ as shown in Figure 7.2. Note that this is the first time that the neutrino emission from the extraordinarily bright GRB130427A has been constrained.

Over and above that, no prominent high-energy signature or event multiplet was reported by the TAToO filters during ANTARES data acquisition (Dornic et al., 2011) within two days before and after the burst. Data of the ANTARES detector can therefore only confirm the non-observation of any neutrino signal as announced by ICECUBE (Blaufuss, 2013). In the following section, I will discuss the detection potential of the planned KM3NET telescope for neutrino signals from GRBs, demonstrating that the future telescope will be capable of discovering GRB neutrinos from single bright bursts similar to GRB130427A or put severe constrains on the parameter space that the model predictions are based on.

8. Expectations for High-Energy Neutrinos from GRBs with KM3NeT

So far, having studied the performances of the operational Antares detector, the potential of the planned next-generation neutrino telescope KM3NeT (KM3NeT Consortium, 2008, 2011) to detect high-energy neutrinos associated with gamma-ray bursts will be studied in the following. The future detector will make use of the same detection techniques as the preceding in-water experiments Antares and Baikal, while considerably exceeding the size of the largest currently running neutrino telescope IceCube at the South Pole. In its final configuration, it will comprise six building blocks of 115 detection strings each, which will be deployed in the Mediterranean Sea. With an instrumented volume of several cubic kilometers and a latitude on Earth ensuring optimal visibility of the Milky Way and in particular the galactic center, the final telescope will be able to confirm the diffuse neutrino flux as reported by IceCube (Aartsen et al., 2014) and allow the universe to be studied in the light of high-energy neutrinos with unprecedented detail. The optical modules of KM3NeT will be equipped with 31 PMTs, pointing in all directions. This should substantially facilitate the rejection of the downgoing particle background induced by cosmic-ray air showers and the random optical noise in the deep sea. In this way, the expected background in the data will be rejected more efficiently than for example with the Antares detector.

The efficiency of the planned KM3NeT detector to detect high-energy neutrinos is comprised in its effective area as shown in Figure 8.1 (from Coniglione, 2013). It was derived from Monte Carlo simulations, where the data selection criteria were optimized for the detection of point-like sources with a generic E^{-2} flux. Note that depending on the final detector configuration, potential improvements in the reconstruction algorithms and the data selection of a specific analysis, the effective area might change considerably. Convolving with the neutrino fluxes as predicted by Guetta et al. (2004) or the NeuCosmA model (see Section 2.2) yields the number of signal events in the data which could be produced by different gamma-ray bursts. Naturally, the neutrino flux expected from GRBs depends crucially on the attributes of each of them, which are varying considerably from one burst to another. Consequently, estimations of the number of signal neutrinos in this future detector can only be based on a previous sample, assuming it represents to some extend an average distribution of gamma-ray-burst parameters. Table 8.1 summarizes the number of neutrinos that would have been expected from a neutrino flux from the two strong bursts GRB110918 (Section 6.1) and GRB130427A (Section 7) as well as from the 296 bursts from late-2007 to 2011 (see Section 6), if the detector had already been operating.

For the four-year sample, Guetta et al. (2004) would predict around 36 neutrinos in the KM3NeT data, with 6 of them from the brightest burst (GRB110918) of the period alone. A similar number of signal signatures would be expected from a burst like the exceptional one in 2013, GRB130427A. Considering the more realistic NeuCosmA model, naturally less associated signal events would be anticipated. Nonetheless, the GRBs from

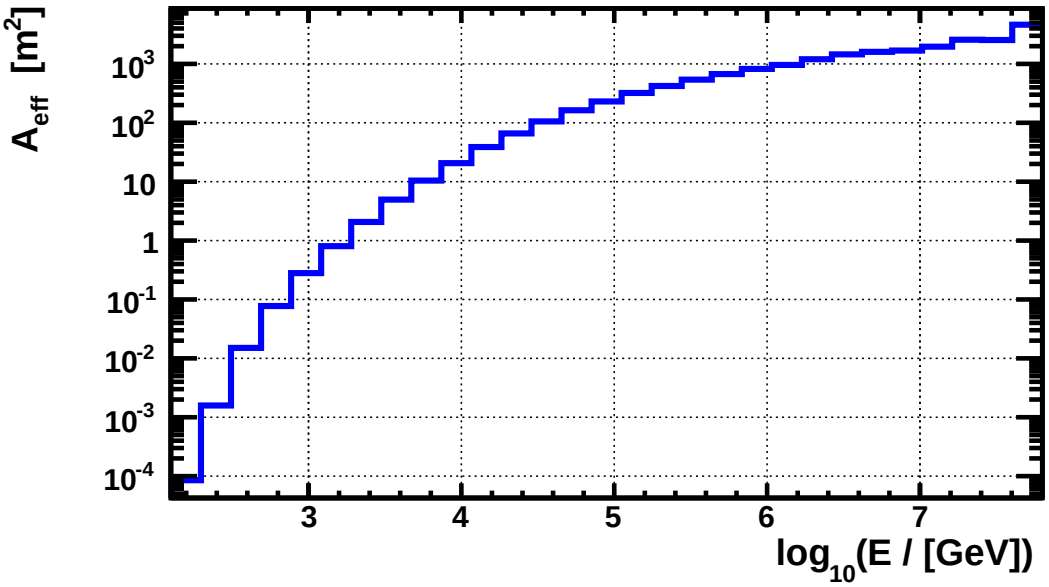

FIGURE 8.1.: Preliminary effective area of the planned KM3NeT detector versus neutrino energy (from Coniglione, 2013). Selection criteria are optimized for searches of point-like astrophysical sources emitting a generic E^{-2} spectrum.

between December 2007 and 2011 would still have produced a few detectable events in the telescope. Even individual bright bursts could have given rise to one detectable neutrino in the detector. This could – according to experiences of the ANTARES analyses – yield an excess over background at a significance level of at least 3σ. Due to presumably more efficient background rejection with the KM3NeT detector, even the detection of a single neutrino signature might bring compelling evidence for the correlation with a gamma-ray burst.

Around $50 - 75$ more detectable neutrino events are predicted in the KM3NeT data than for the ANTARES telescope. This is consistent with previous investigations that had estimated an increase in sensitivity of ~ 50 for point-like sources with a generic E^{-2} spectrum with respect to its predecessor (KM3NeT Consortium, 2011). The differences in the factors for individual bursts are mainly due to fluctuations in the neutrino spectra, which are subject to strong variations of the burst attributes. Note that the accumulated neutrino flux from the four-year period is significantly dominated by the strongest burst GRB110918 (see for instance Table 6.5), which puts the assumption of a representative sample into question.

Regardless of the individual fluctuations in the gamma-ray-burst sample, the next-generation neutrino telescope KM3NeT in its final configuration will certainly allow the detection of the neutrino flux from GRBs as predicted by state-of-the-art numerical calculations. In the case of a non-observation of such a signal, the parameter space upon which these predictions are based would be severely constrained, putting increasing tension on the hadronic acceleration model within the fireball paradigm.

GRB	RA ($^\circ$)	δ ($^\circ$)	$\mathcal{F}_\gamma$ ($10^{-6}\,\mathrm{erg/cm^2}$)	T_{search} (s)	$n_{\mathrm{exp}}^{\mathrm{NeuCosmA}}$	$n_{\mathrm{exp}}^{\mathrm{Guetta}}$
all 296 GRBs	-	-	3254	23785	3	36
110918	32.5	-27.1	750	73	1	6
130427A	173.1	27.7	2462	264	0.4	6

TABLE 8.1.: Equatorial Coordinates, photon fluence $\mathcal{F}_\gamma$ and search time windows T_{search} for the entire gamma-ray-burst selection from late-2007 to 2011 and the two strong bursts GRB110918 and GRB130427A. Convolution of the predicted neutrino fluxes from Guetta et al. (2004) and the NeuCosmA model with the effective area of the planned KM3NET detector yields the numbers of expected signal events, n_{exp}.

9. Search for GRB Neutrino Emission with variable Time Delays

This work as well as many others (see for instance the references given in Section 2) have so far focused mostly on the search for coincident emission of neutrinos with the prompt electromagnetic signal of gamma-ray bursts. However, up to now no neutrino signal could be identified above the background in the data from any neutrino detector during the prompt emission phases, and the first optimistic analytical models from Guetta et al. (2004) based on Waxman & Bahcall (1997) have already been excluded by IceCube (Abbasi et al., 2012). There has also been some effort to successively relax the constraints on the search time windows in the IceCube data from -1h to +3h and up to $\pm$1 day (Abbasi et al., 2010, 2012), and recently up to $\pm$15 days (Casey, 2013), to account for neutrino emission possibly extended in time. Nevertheless, none of these could find any significant excess protruding the expected background. Three neutrino candidates had been found with arrival directions roughly correlated with GRB alerts but in the order of $\mathcal{O}(10^3\,\mathrm{s})$ before the respective gamma-ray burst in the IceCube data (Abbasi et al., 2012; Whitehorn, 2012). In Casey (2013), the most significant neutrino coincidence was found to be 4.9 days before a GRB alert announced by *Fermi*:GBM[1]. However, due to the large time windows, none of these excesses could bring compelling evidence for a GRB signal. Even though the search for a signal of neutrinos coincident with the emission of high-energy photons is the most generic ansatz, there are many models that predict time-shifted neutrino signals, such as neutrino precursors (Razzaque et al., 2003) or afterglows (e.g. Waxman & Bahcall, 2000), or different Lorentz Invariance Violation (LIV) effects for photons and neutrinos on their way to Earth (Amelino-Camelia & Smolin, 2009; Jacob & Piran, 2007). Amelino-Camelia et al. (2013) discuss, for instance, the possibility that the three neutrino-like events found in the IceCube data (Abbasi et al., 2012) could have been produced by gamma-ray bursts but arrived before the photon signal due to LIV effects.

Probing such scenarios requires a completely different approach to the search for simultaneous emission, since the most simple generalization of the method, an extended symmetric time window, accumulates background linearly to the size of the window and thus prevents a small signal to protrude significantly. Moreover, in all aforementioned scenarios the neutrino signal is simply shifted in time with respect to the electromagnetic signal, with none of these anticipating any considerably prolonged neutrino emission. It is clear that a presumable signal must be weak (between zero and one neutrino per GRB), as otherwise it would have been discovered in previous searches for neutrino point sources or data multiplets. Hence the approach presented in the following aims at identifying a

[1]Results of this analysis were presented at the *Gamma-Ray Bursts in the Multi-messenger Era* workshop, `www.grbparis2014.fr`

presumably faint neutrino signal that is delayed[2] with respect to the electromagnetic GRB emission by an unknown time shift, while still imposing as few assumptions as possible on the origin of such a delay.

PRINCIPLE OF THE SEARCH For each gamma-ray burst with given time and position in the sky, neutrino telescope data are searched for signal signatures within a maximum time range that have been reconstructed within a certain angular cone around this position. For any such spatial coincidence, the time difference with respect to the gamma-ray-burst alert is recorded. This procedure is iterated for each of the bursts, and the collected time differences are stacked in a common timing profile. In the case of no signal, purely accidental spatial coincidences of the neutrino candidates with the defined search cones around the GRB positions would be expected. The observed time shifts should then be completely randomized yielding a flat cumulative distribution with each shift being equally likely. Even faint signals can give rise to a cumulative effect, such as a peak, in these stacked profiles, which can be identified by their discrepancy from the background hypothesis. An optimal choice of the search cone size δ_{max} naturally depends on the gamma-ray burst's position accuracy and the neutrino pointing uncertainty of the detector, while the size of the probed time window τ_{max} should be defined as the largest assumable shift in any of the models. Such a procedure had already been proposed for example by van Eijndhoven (2008), who considered windows of $\pm 1\,\mathrm{h}$ around the GRB satellite triggers under study. The approach presented in the following is extended to first allow significantly larger time windows, but also to account for different origins of the time shift.

Note that the presented technique is intrinsically different from the methods previously developed by IceCube (Casey, 2013; Abbasi et al., 2012). These focused on successively widening symmetric search time windows around the GRB alerts, while the approach pursued here aims at identifying a systematically time shifted neutrino signal with respect to the electromagnetic emission. The IceCube studies searched for extended signals spread equally over each of the considered time windows, with the signal PDF described by a flat temporal component (Casey, 2013). Consequently, they suffered from reduced significance due to the accumulated background in the increasingly large time windows. Contrary to that, the presented technique distinguishes a time-shifted signal as a peak in addition to flat background.

9.1. GAMMA RAY BURST AND NEUTRINO EVENT SAMPLES

Remaining as signal independent as possible, the usual methods of selecting high-energy neutrino candidates by optimizing event selection criteria for the best limit or detection probability given a particular signal model were not applicable. However, neutrino candidates which had previously been singled out in searches for neutrino point sources in the sky naturally provided suitable data for this kind of approach. Stringent quality criteria were optimized to identify sources that emit a generic neutrino spectrum of shape E^{-2}. This ensures efficient suppression of the background contamination from falsely reconstructed

[2]Here and in the following, the term 'delay' will denote both negative and positive shifts in time of the neutrino emission with respect to the electromagnetic signal.

atmospheric muons, and yields excellent angular resolution of the data adapted for the search for directional coincidences.

Neutrino samples of the two neutrino experiments ANTARES, with data from March 2007 to 2012, and ICECUBE, with data from April 2008 to May 2009, were considered.

The ANTARES neutrino candidates have been selected from data that spanned the entire period from the connection of the first detection lines in March 2007 to the end of 2012 (Adrián-Martínez et al., 2014). After selecting well-reconstructed events ($\Lambda > -5.2, \beta < 1^\circ$) that were required to cross the detector from below ($\cos\Theta < 0.1$), 5516 possible neutrinos were identified. Monte Carlo Simulations derived a median angular resolution of 0.38°. The contamination from falsely reconstructed cosmic-ray-induced atmospheric muons was estimated to 10%. The ICECUBE collaboration grants public access to data of 12877 neutrino candidates that have been selected for the point-source analysis using data from the experiment from April 2008 to May 2009 (Abbasi et al., 2011), when the detector was in its 40-string configuration[3]. Monte Carlo simulations with the same reconstruction quality criteria yielded a median angular resolution of 0.7° (Karle, 2009). The respective time and right-ascension distributions for both neutrino telescope data sets are shown in Figure 9.2. In contrast to a rather flat distribution of the IC40 neutrino rate in time, the number of recorded candidates in the ANTARES data is much less constant. This can be understood from the different duty cycles of both detectors. The data acquisition of ANTARES is subject to large fluctuations of the deep-sea conditions such as the rate of bioluminescent light. These variations can result in periods in which regular data-taking has to be stopped for weeks or even months to prevent the photo-detectors from being subjected to too high a rate. In contrast, the glacial environment of the ICECUBE detector, the absence of such environmental effects ensures stable conditions. Both data samples are distributed uniformly in right ascension with no obvious signal excess above $\sim 1.8\sigma$.

A suitable gamma-ray-burst sample was consolidated similarly to the description in Section 6.1. It was merged using catalogs from the *Swift* (Gehrels et al., 2004) and *Fermi* satellites (Atwood et al., 2009; Meegan et al., 2009) and was supplemented by a table from the ICECUBE Collaboration[4] (Aguilar, 2011), with information parsed from the Gamma-ray burst Coordinates Network (GCN) messages. Since only the time and position information (and the measured redshift, if available) of each announced GRB was used, no selection based, for instance, on the quality of the spectral measurements as in Table 6.4 was required. Naturally, only GRB alerts were taken into account that occurred both within the maximal visible declination range of the neutrino telescope, and during the covered neutrino data collection time. However, to avoid any boundary effects, a safety margin of the size of the search time window was excluded at the beginning and the end of the livetime of the neutrino data,

$$t_{\mathrm{GRB}} \in \left[\min(t_{\mathrm{event}}) + \tau_{\mathrm{max}}, \max(t_{\mathrm{event}}) - \tau_{\mathrm{max}}\right] .$$

Figure 9.1 shows the distribution of both neutrino telescope samples and the accordingly selected gamma-ray bursts in equatorial coordinates. The two neutrino data sets are complementary in sky coverage, since the ICECUBE detector covers the Northern Hemisphere sky, while the ANTARES telescope at a latitude of 43° is most sensitive to sources in the

[3] ICECUBE IC40 neutrino candidates are available at `http://icecube.wisc.edu/science/data/ic40`

[4] available online at `http://grbweb.icecube.wisc.edu/`

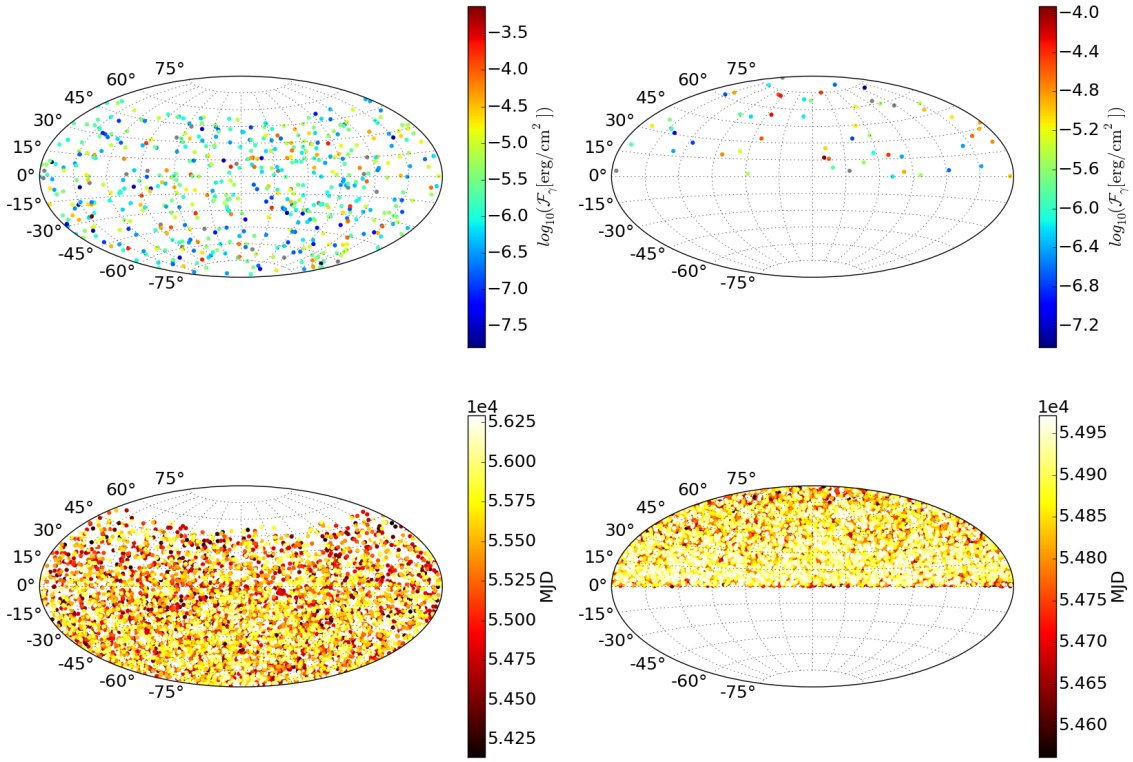

FIGURE 9.1.: Distribution of selected GRBs *(upper panel)* and recorded neutrino candidates *(lower panel)* in equatorial coordinates, for the ANTARES event sample *(left)* and the ICECUBE IC40 sample *(right)*. Each GRB's location is color-coded with the photon fluence $\mathcal{F}_\gamma$, those with no measurement are drawn in gray. The color of neutrino events represents their detection time. For the final selection of the GRBs, see also Section 9.4.

Southern Hemisphere. Moreover, ANTARES data covered almost six years, while the ICECUBE sample from the IC40 period comprised only approximately one year of data. Note also that, due to the larger instrumented volume of the detector, the ICECUBE data set contains more neutrino candidates than the ANTARES data, while at the same time covering a smaller time period in which less GRB alerts were recorded. Both samples will therefore explore completely different statistical regimes.

9.2. POTENTIAL PHYSICAL DELAYS CONSIDERED

The common timing profile comprises a discrete representation of the stacked deviations of detection times ($\tau = t_\nu - t_{\mathrm{GRB}}$) between the (first) detected photon signal t_{GRB}, as announced by a satellite via the GCN network, and the time of a possibly associated neutrino candidate t_ν. However, different processes could lead to time shifts between the electromagnetic and the neutrino signal. Consequently, the signatures of these processes might manifest most evidently in other stacked profiles than that for the generic shift of detection times τ. Different emission times of the neutrino and photon signal at the source, for instance, would translate into observed time delays at Earth that depend on the cosmological

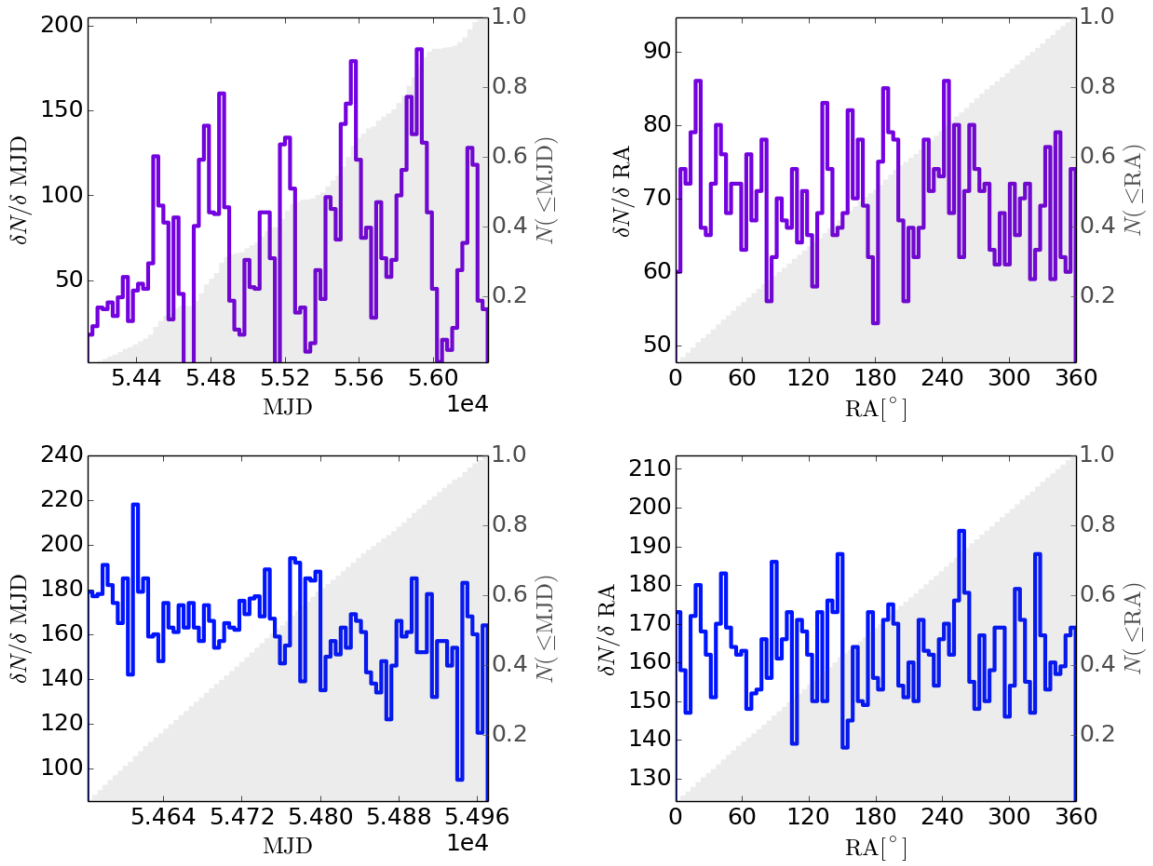

FIGURE 9.2.: Distributions of time in Modified Julian Date (MJD) and right ascension RA of the ANTARES neutrino event sample (March 2007 – 2012) in the *top panels*, and for the ICECUBE sample (April 2008 – May 2009) in the *bottom panels*. The respective cumulative distributions are shown in gray.

redshift z of the GRB,

$$\mathrm{d}t_{\mathrm{obs}}/\mathrm{d}t_{\mathrm{em}} = R(t_{\mathrm{obs}})/R(t_{\mathrm{em}}) = 1+z \tag{9.1}$$

$$\tau_{\mathrm{obs}} = \tau_{\mathrm{em}} \cdot (1+z)\,, \tag{9.2}$$

with the scale factor R. To test for these intrinsic time shifts, the distribution of the measure $\tau_z = \tau/(1+z)$ is investigated, with τ being the observed difference in the detection times. Note that the redshift is only measured for approximately 10% of all gamma-ray bursts, so the statistics of the cumulative profile is significantly reduced when omitting all GRBs without determined redshift. Pure randomly distributed data would result in a time profile with a broad maximum around zero and the extreme values of τ_z being less probable. This is a result of evenly distributed time differences in the maximum allowed range $\tau \in [-\tau_{\mathrm{max}}, +\tau_{\mathrm{max}}]$, where the range of τ_z is limited by the factor $1/(1+z)$. Such a distribution generated by randomizing the times and right ascensions of neutrino candidates in the ANTARES data is shown on Figure 9.3 (left), with the envelope following $\pm\tau_{\mathrm{max}}/(\tau_z - 1)$.

Moreover, effects due to different broken Lorentz Invariance (LIV) (see e.g. Amelino-Camelia et al., 2013; Amelino-Camelia & Smolin, 2009; Jacob & Piran, 2007) for photons

and neutrinos of high energy would yield time shifted arrival times that depend on the energy of the neutrino, the luminosity distance of the source as well as the energy scale M_{LIV} at which the symmetry is broken:

$$\Delta t_{\mathrm{LIV}} = -(\pm 1) \cdot E / M_{\mathrm{LIV}} \cdot D(z)/c \,. \tag{9.3}$$

These effects are expected to appear most significantly in a stacked profile that accounts for both the presumable neutrino energy and the luminosity distance of the source. Consequently, a variable to be probed is defined as

$$\tau_{\mathrm{LIV}} = \frac{\tau}{E_{\mathrm{est}} \cdot D(z)} \propto \pm \frac{E}{E_{\mathrm{est}}} \cdot \frac{1}{M_{\mathrm{LIV}} \cdot c} \,, \tag{9.4}$$

which should be proportional to the inverse of the LIV breaking scale M_{LIV} and the unavoidable uncertainty on the estimated energy E_{est}. The number of photon hits in the optical modules that have been used to reconstruct the particle track direction n_{hits} can serve as a first-guess energy estimator of a neutrino event (see Section 5.2). We expect the τ_z distribution of purely accidental coincidences without any signal signature to be peaked around zero, since the range $\tau \in [-\tau_{\mathrm{max}}, +\tau_{\mathrm{max}}]$ is confined by the factor $1/E_{\mathrm{est}} \cdot D(z)$ (see Figure 9.3, right).

Consequently, in the search for an associated neutrino signal from gamma-ray bursts, three stacked time profiles for the measures τ, τ_z and τ_{LIV} were generated for all neutrino candidates which matched the coordinates of a reported GRB alert. I will show in the following section how a signal can be identified as deviation from the pure background profiles.

Note that the effect introduced by the non-vanishing rest mass of neutrinos can be neglected in this scope: for a neutrino rest mass of $m \lesssim 0.2\,\mathrm{eV}/c^2$ and an energy of 1 TeV, the Lorentz factor is $\beta_\nu = \sqrt{1 - 4 \cdot 10^{-26}}$. For an assumed age of the universe of around $13 \cdot 10^9$ years, this would yield a travel time delay of

$$\Delta t = t_\gamma - t_\nu = t_\gamma \cdot (1/\beta_\nu - 1) = 2.6 \cdot 10^{-16}\,\mathrm{y} = 8 \cdot 10^{-9}\,\mathrm{s} \,, \tag{9.5}$$

which is well below the standard GRB duration.

9.3. ASSOCIATED STATISTICAL TESTS

From the cumulative timing profiles, test statistics are calculated that distinguish a systematically time shifted neutrino signal from gamma-ray bursts from the background-only hypothesis of merely accidental coincidences. A large number of background realizations are generated from the existing data sets by randomizing the time and right ascension of detected neutrino candidate events in order to simulate purely accidental data distributions, while still preserving the telescope's acceptance. This is justified by the flatness of the corresponding data distributions as shown in Figure 9.2. The p-value, and thus the significance σ (see Equation 5.3), of an excess in the data is then given by the probability to measure the test statistic in question (or more extreme values) from the background-only distribution.

The ratio of spacial coincident data events before and after the respective GRB alert $r = n(\tau > 0)/n(\tau < 0) = n_+/n_-$ is a very simple measure to probe the distributions while

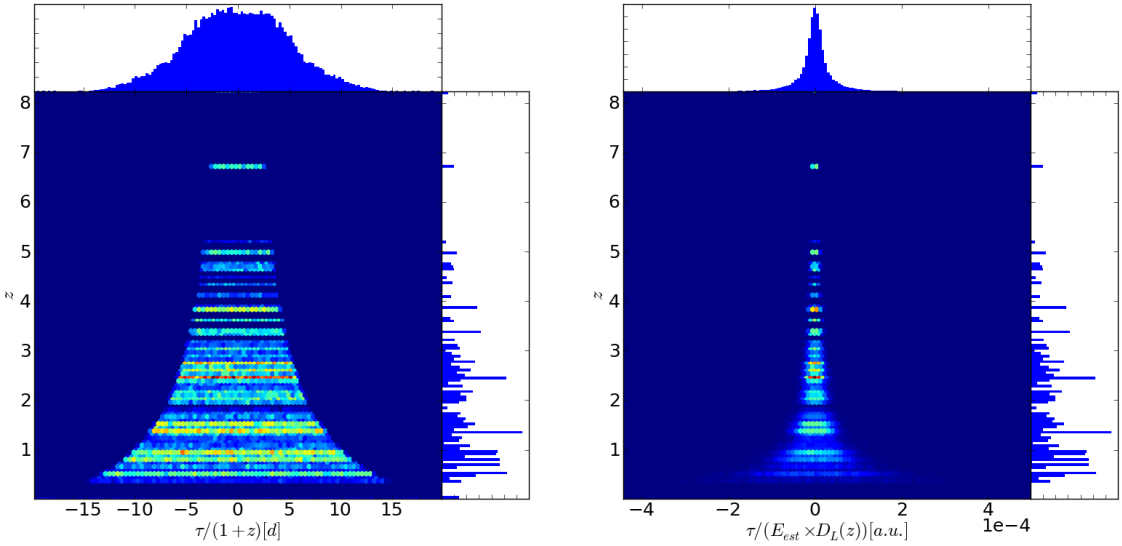

FIGURE 9.3.: Time shift measures τ_z *(left)* and τ_{LIV} *(right)* for purely accidental coincidences of neutrino candidates in the ANTARES data with GRB alerts (background-only) plotted against the gamma-ray bursts' redshift. The projections of the distributions along the x and y axis are also shown on the top and right of each panel.

making the fewest assumptions on any model. Any effect leading to different arrival times of ν and γ from GRBs is expected to yield either positive or negative time shifts.[5] This ratio was calculated if both n_+ and n_- are non-zero; for purely random coincidences, we expect to measure a ratio of $r = 1$.

A more elaborated test statistic was proposed by van Eijndhoven (2008): The author introduced the Bayesian observable ψ to estimate the compatibility of a given stacked (and binned) time profile with the expectations from background (see also Bose et al., 2013). This test statistic depends on the probability to observe data D under the hypothesis H with a given set of information I, and has been shown to constrain the belief in the hypothesis H:

$$\begin{aligned}\psi &= -10 \log_{10} p(D|HI) \\ &= -10 \left[\log_{10} n! + \sum_{k=1}^{m} n_k \log_{10} p_k - \log_{10} n_k! \right] , \end{aligned} \tag{9.6}$$

with n events in the histogram in total, distributed in the $k \in [1 \dots m]$ bins. The probability to fall within bin k is p_k; for a uniform background distribution (i.e. in the case of the τ profile), $p_k = 1/m$ is simply given by the total number of bins m. For the non-uniform profiles τ_z and τ_{LIV}, these probabilities have to be determined by a large number of background realizations[6]. The value of ψ is calculated for each of the τ, τ_z and τ_{LIV} profiles, with corresponding values ψ, ψ_z and ψ_{LIV}.

[5] Note that the ratio can simply be translated into the asymmetry $a = (n_+ - n_-)/(n_+ + n_-) = r - 1/r + 1$. This would yield different bin sizes of $\delta a = 2/(r+1)^2 \delta r$.

[6] The number of realizations to produce the distributions of p_k should be larger than the number of pseudo experiments required to derive conclusions at a given confidence level. Consequently, if thresholds for 5σ significance should be derived, significantly more than $1.7 \cdot 10^6 = 1/p_{5\sigma}$ realizations are necessary.

The binning of the histograms can, in principle, have a non-negligible influence on the distribution of the test statistic ψ and thus the distinguishing power of a signal over background. However, the number of coincident events in the stacked profiles is expected to be rather low in the order of $\mathcal{O}(10)$ (see, e.g., Figure 9.6). In this range, ψ is discretely distributed since the histograms are filled with isolated events, and the choice of the bins' size has no considerable effect on the discovery power of the analysis. We consequently chose a binning that isolates signals from different GRBs, while the emission associated with single bursts was basically comprised in one time bin.

Note that even if the presented technique is aimed at identifying the mere deviation of an observation from the hypothesis of randomized correlations, instead of quantifying the observed time shift, the information of the most significant excess in the timing profile is still conserved and can be accessed in terms of the largest single contribution of a bin in Equation 9.6.

9.4. OPTIMAL PARAMETERS OF THE ANALYSIS

Background from uncorrelated data events is accumulated linearly with the solid angle of the search cones $\Omega(\delta_{\max})$ around each GRB's position and the maximum time delay $\tau_{\max}$ that is considered,

$$\mu_b \propto \Omega(\delta_{\max}) \cdot \tau_{\max} \, . \tag{9.7}$$

Hence, the choice of the search cone size and the probed time window should be optimized reasonably under physical considerations in order to stay as independent of any model assumption as possible and still allow even a faint signal to protrude the background.

SIZE OF THE COINCIDENCE CONE The determination of an optimally-sized search cone for spatially coincident neutrino candidates with a GRB alert will be based on the minimum of the ratio $\sqrt{\text{background}}/\text{signal}$ as shown for example in Alexandreas et al. (1993). With the signal coming from the GRB's location, the reconstructed neutrinos are assumed to follow a Gaussian profile around this position, with its width representing the instrumental pointing accuracy of the detector. This approach yields an optimum search cone size of $1.58 \cdot \sigma$ to find a signal with standard deviation σ above random background.

The angular resolution of the neutrino samples is given in terms of the median angular error on the reconstructed arrival directions of neutrino candidates. Empirically, it is straightforward to show that this median can simply be translated into the respective Gaussian standard deviation σ by $m(\sin(\delta) \cdot \text{Gauss}(\delta, \sigma)) = 1.17 \cdot \sigma$ (see Figure 9.4), which holds true in the range of σ around 0.3° and up to 5°.

However, the effect of large uncertainties on the GRBs' positions as given by the angular error boxes of the satellites Δ_{err} should not be ignored, since these can vary from sub-arcseconds (from observations with the *Swift*:UVOT instrument or ground-based telescopes) up to several tens of degrees for *Fermi*:LAT alerts without any other follow-up observation (in the worst case, for GRB110911, the *Fermi*:LAT error box is as large as 50°). So the size of the search window around each GRB is widened accordingly, if its respective

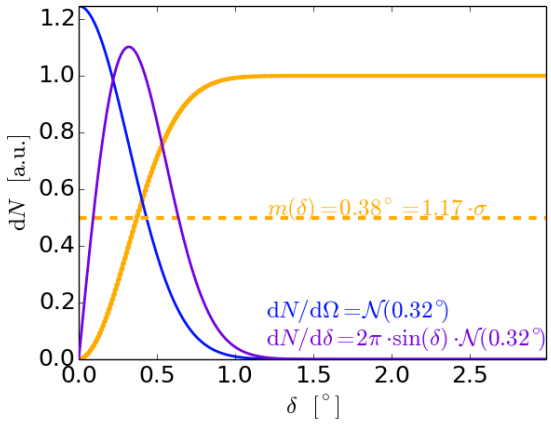

Figure 9.4.: Empirical determination of the relation between the median of events to the width of the respective Gaussian $\mathcal{N}$. In blue, the Gaussian distribution of events per solid angle $\mathrm{d}N/\mathrm{d}\Omega = \mathcal{N}$ with standard deviation $\sigma = 0.32^\circ$ as a function of the space angle δ is shown. In terms of events per space angle, the distribution translates to $\mathrm{d}N/\mathrm{d}\delta = 2\pi \cdot \mathcal{N}$ as shown in violet. The cumulated distribution $N(\leq \delta)$ is shown in orange. The median $m(\delta) = 1.17 \cdot \sigma$ is indicated by the dashed orange line.

localization accuracy Δ_{err} exceeds the neutrino candidates' angular resolution σ:

$$\delta_{\mathrm{cut}} = 1.58 \cdot \max(\sigma_\nu, \Delta_{\mathrm{err,GRB}}) \; . \tag{9.8}$$

In doing so, the contribution of random coincidences scales with the localization accuracy of each gamma-ray burst, thus the background in the cumulative profile might be dominated considerably by a few bursts with very large error boxes. Consequently, a reasonable trade-off should be found: On the one-hand side, we wanted to avoid reducing the statistics too much by excluding a large amount of badly-localized bursts (see Figure 9.5, left, for the distribution of the error box sizes). For example, a cut at 3° (10°) would reduce the number of bursts by 40% (8%). Figure 9.5 also shows the photon fluence of each burst versus its error box size. The cumulative distribution of the fluence-weighted number of GRBs gives an estimation of the total power output up to a given error box size Δ_{err}. Selecting GRBs with localization accuracies better than 3° or 10° reduces the total power by 11% and 0.9%, respectively.

On the other hand, the stacked timing profiles should not be dominated by one burst with a large error box and thus angular search cone, which naturally leads to many accidental spatial coincidences. Given, for instance, a search cone increased in size by a factor of 3 for a poorly localized burst, the associated coincident background would already dominate that of the bursts with small error boxes by one order of magnitude. To limit this effect, the maximal search-cone size was chosen such that no GRB contributed more than an order of magnitude more of uncorrelated background than one with the smallest associated search radii $1.58 \cdot \sigma_\nu$ from Equation 9.8. This yields a maximum search cone of 1.59° when using the Antares pointing resolution of 0.32°. All bursts which were localized with an accuracy less than 1.01° were consequently discarded from the search, which reduced the sample by $\sim 54\%$:

$$\delta_{\mathrm{cut}} = 1.58 \cdot \max(\sigma_\nu, \Delta_{\mathrm{err,GRB}}, 1.01^\circ) \in [0.51^\circ, 1.59^\circ] \; . \tag{9.9}$$

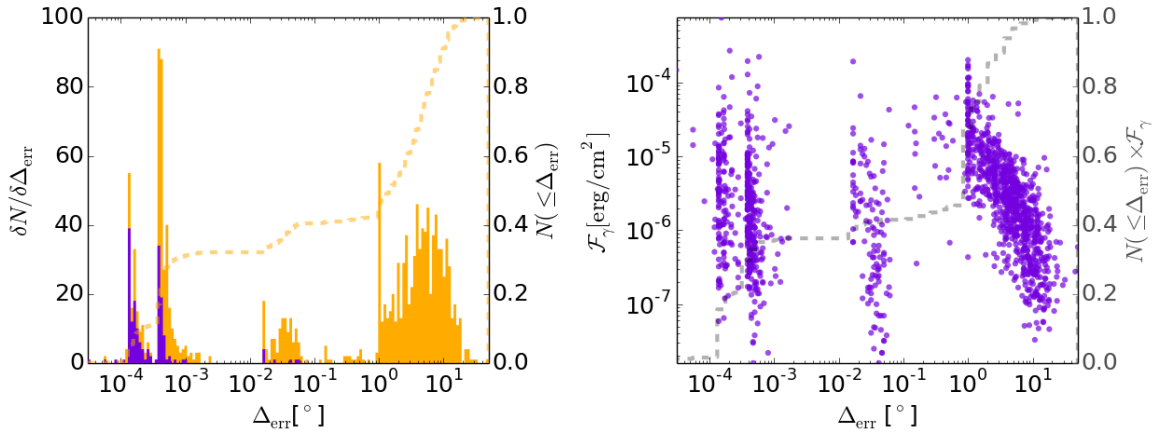

FIGURE 9.5.: *Left:* Number of GRBs with a given error box $\Delta_{\rm err}$ (orange). The cumulative distribution is shown by the dashed orange line. For GRBs with measured redshift, the distribution is shown in violet. *Right:* Scatter plot of photon fluence $\mathcal{F}_\gamma$ of each GRB versus its error box $\Delta_{\rm err}$. The gray dashed line shows the cumulative distribution of the fluence-weighted number of GRBs with an error box $\leq \Delta_{\rm err}$.

Accordingly, the worse point-spread resolution of the IC40 data sample led to a maximum search-cone size of 2.99°.

MAXIMUM TIME DELAY The maximum considered time window should be limited to constrain the number of accidental coincidences from uncorrelated neutrino candidates in the GRB search cones. Even if this approach aims at being as model independent as possible, the maximum time shift as anticipated from any physical process should be taken into account here. Intrinsic shifts in the emission times of neutrinos were predicted, for instance, by Razzaque et al. (2003) with neutrinos $\sim 100\,$s before the electromagnetic GRB signal. Granot & Guetta (2003) derived a precursor neutrino signal that might be emitted even tens of years before the actual GRB. Since these time scales significantly exceed the operational times of the current neutrino telescopes, we will omit such scenarios here. Waxman & Bahcall (2000) and Murase (2007) predicted early afterglow emission of neutrinos $\sim 10\,$s after the burst, but some models derive extended neutrino fluxes up to 1 day after the prompt emission (Razzaque, 2013b). These intrinsic time shifts between neutrino and photon signals are still well within the time scopes that have already been probed, for example, in the ICECUBE searches (Abbasi et al., 2012; Casey, 2013).

The time delays between the arrival times of neutrinos and photons that might be introduced by the violation of Lorentz Invariance (Amelino-Camelia & Smolin, 2009; Jacob & Piran, 2007) is poorly known, and depend not only on the energy scale at which the symmetry is broken but also on the energy of the particles and the distance of the source. However, a maximum expected time shift between high-energy neutrinos and the photon signal from a gamma-ray burst as introduced by these effects can be inferred using the existing limit on the energy scale, which has been set by the *Fermi*:LAT collaboration at $M_{\rm LIV} = 7.6 \cdot M_{\rm Planck}$ (Vasileiou et al., 2013), and a maximal neutrino energy and gamma-ray burst distance in Equation 9.3. Neutrino telescopes cover an energy range up to $\sim E_{\rm max} = 10^9\,$GeV, which can serve as an upper estimation of the expected neutrino energy. Furthermore, this en-

ν telescope data	τ_{tot} (d)	N_{events}	$m(\delta)$ (°)	δ_{max} (°)	τ_{max} (d)	N_{GRB}	$N_{\text{GRB},z}$	n_{coinc} (uncorrelated)	$n_{\text{coinc},z}$ (uncorrelated)
ANTARES (07-12)	2154	5516	0.38	0.51 – 1.59	40	563	150	4.4	0.7
IC40 (08-09)	408	12876	0.70	0.95 – 2.99	40	60	12	35.0	4.0

TABLE 9.1.: Total livetime of the considered neutrino telescope data sets τ_{tot} and the respective number of neutrino candidate events N_{events} with their median angular resolution $m(\delta)$. The range of search cone sizes δ_{max} around each gamma-ray burst is determined by Equation 9.9, while the maximal search time window τ_{max} is fixed at 40 days. With these parameters, samples of N_{GRB} gamma-ray bursts are identified (out of which $N_{\text{GRB},z}$ have measured redshifts) for the search of correlations. Assuming totally uncorrelated neutrino data, the mean number of coincident events that would be expected within the GRB's search windows n_{coinc} are also given (see Section 9.5).

ergy lies well above a potential cut-off at 2 PeV of the first neutrino signal observed by ICECUBE (Aartsen et al., 2013a, 2014). Using the luminosity distance at a redshift of $z = 3.5$, which corresponds to the 90% quantile of the gamma-ray bursts and the 95% quantile of the fluence-weighted redshift distribution, a maximum time shift between photon and neutrino signals of $\tau_{\text{max}} = 40$ days was derived.

A discretization of the cumulative timing profiles into 150 bins was chosen, which allowed to probe time scales down to 13 hours. This choice ensured that the signal associated with individual GRBs is basically comprised in single time bins, while the emissions from different GRBs were isolated from each other.

FINAL SAMPLES Having chosen the maximal search time window and the largest angular search cone that should be taken into account, the final gamma-ray burst selections associated with each neutrino telescope data set were determined. The initially selected GRB catalog (see Section 6.1) comprised 1488 bursts that had occurred between 2007 to 2012, which gives a detection rate of 0.68 bursts per day. Out of these, 563 have been selected for the search of associated neutrinos in the ANTARES data, with 150 of them having measured redshift z. For the ICECUBE IC40 data-set, 60 GRBs have been singled out with only 12 redshift measurements (see Figure 9.1). It shows significantly lower statistics, which can be understood from the facts that the considered data-taking time is only around one year compared to almost six years in the ANTARES sample. Secondly, due to the location of the detectors on Earth, 87% of the sky is visible for the ANTARES detector over one day, whilst the ICECUBE experiment covers only 50% of the sky. Table 9.1 gives the statistics for the selected gamma-ray burst and neutrino telescope data samples, including the number of coincident events n_{coinc} that would be expected if the neutrino data was completely uncorrelated with the chosen gamma-ray bursts (the background-only hypothesis).

9.5. PSEUDO EXPERIMENTS

We made use of pseudo experiments to generate the large number of background realizations that is required to derive the significance of a given measurement. Sky-maps of uncorrelated neutrino candidate events were generated by randomizing the events' times and right ascensions (as shown in Figure 9.2). For each of these randomized sets, spatial coincidences with the given GRBs were searched and the τ, τ_z and τ_{LIV} histograms were

filled. From these, the respective test statistics ratio, ψ, ψ_z and ψ_{LIV} were calculated accordingly. Their distributions yield the values above which a measurement can be claimed a detection with a given significance.

Around $1.4 \cdot 10^7$ pseudo experiments were generated to simulate the case of purely accidental coincidences (background-only) between the ANTARES neutrino data and the GRB catalog. On average, 4.4 of the neutrino candidates matched the bursts' search windows in time and space, with 0.7 of them coinciding accidentally with the bursts with measured redshift. Using the ICECUBE data sets, 35 of the IC40 neutrino candidates coincided accidentally with the 60 gamma-ray bursts (4.0 with the GRBs with measured redshift.

To verify these figures, I approximated the number of expected coincidences from N_{events} randomly distributed neutrino events in the sky with the search cones of N_{GRB} GRBs in search time windows τ_{max}. Assuming a fixed search-cone size δ_{max}, a fraction of the visible sky $\Omega_{\mathrm{visible}}$ is covered with coincidence cones of GRBs[7], and a fraction of the total data-taking time τ_{tot} falls within these search time windows. Hence, the average number of expected coincidences from uncorrelated data can be estimated by

$$\langle n_{\mathrm{coinc}} \rangle = \frac{\Omega(\delta_{\mathrm{max}})}{\Omega_{\mathrm{visible}}} \cdot \frac{\tau_{\mathrm{max}}}{\tau_{\mathrm{tot}}} \cdot N_{\mathrm{events}} \cdot N_{\mathrm{GRB}} \,. \tag{9.10}$$

Figure 9.6 shows this mean expected number of accidental coincidences, assuming a number of 5516 neutrino candidates that are uncorrelated with a sample of 563 gamma-ray bursts being distributed in the sky up to a declination of 47°. Note that these numbers correspond to the ANTARES selection. Within the range of search cones δ_{max} (given by Equation 9.9) and a fixed time window of 40 d, around $\mathcal{O}(10)$ coincidences were expected by chance. This simple calculation confirms the numbers that were derived in the pseudo experiments (see Section 9.5), where an average of 4.4 events matched the GRBs' search windows by chance.

To investigate the performance of the proposed technique to identify hypothetical neutrinos from GRBs, a test signal was mimicked by associating neutrino candidates artificially with part of the GRBs. The size of this GRB sub-selection with a spatially coincident test-signal neutrino thus represented the signal strength. In each realization, the probability f determined whether or not each GRB should have an assigned signal neutrino. In that case, one of the neutrino candidates was shifted in time and space to the GRB's location. Consequently, the test signal was simulated by one associated neutrino signature with a randomly chosen sub-selection of the GRBs of average size $\langle N_{\mathrm{GRB}}^{\mathrm{signal}} \rangle = f \cdot N_{\mathrm{GRB}}$. In the following, results will be shown for a hypothetical neutrino emitted 5 days after the respective GRB. The simulated signal neutrino was therefore put at time $t_\nu = t_{\mathrm{GRB}} + 5\,\mathrm{d} \cdot (1+z)$, since the cosmological redshift z affects the observed time shift between photons and neutrinos at Earth (see Equation 9.1). Hence the signal was only simulated for those bursts for which the redshift could be determined, that is, for a fraction

$$f_z = \langle N_{\mathrm{GRB}}^{\mathrm{signal}} \rangle / N_{\mathrm{GRB},z} \,, \tag{9.11}$$

corresponding to a fraction

$$f_{\mathrm{all}} = f_z \cdot N_{\mathrm{GRB},z} / N_{\mathrm{GRB}} = \langle N_{\mathrm{GRB}}^{\mathrm{signal}} \rangle / N_{\mathrm{GRB}} \tag{9.12}$$

of all GRBs.

[7] Effects due to overlapping search cones are discarded here.

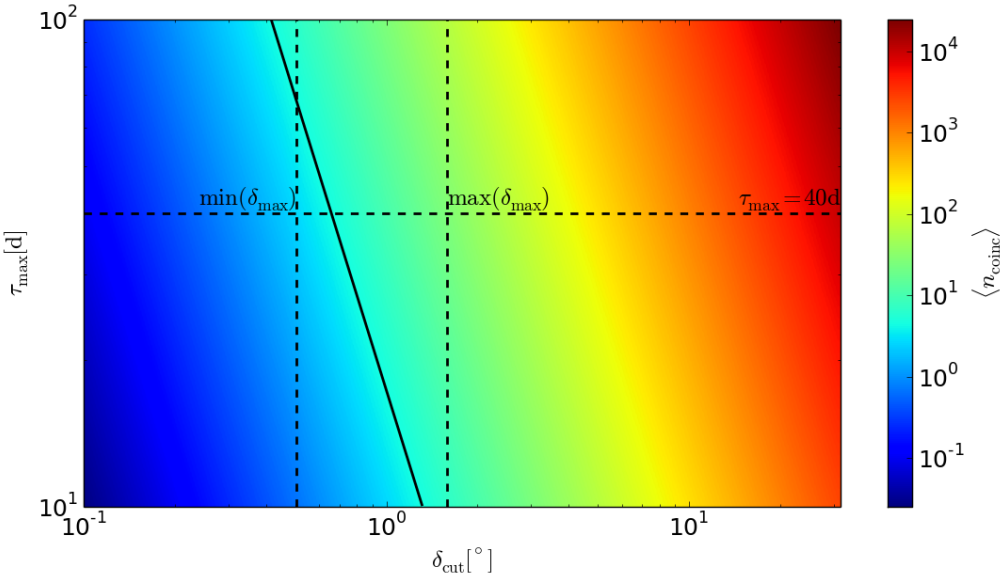

FIGURE 9.6.: Average number of expected coincidences from random background (color) as a function of the (fixed) search radius δ_{max} around each gamma-ray burst and the search time window τ_{max} under the assumption that the 5516 neutrino candidates from the 2007–2012 data from the ANTARES telescope are not associated to the accordingly selected 563 gamma-ray bursts. The chosen value of $\tau_{\mathrm{max}} = 40\,\mathrm{d}$ and the minimum and maximum ranges of the search cone sizes δ_{max} around each GRB are indicated by black dashed lines. The black solid line marks the parameters that would yield an average coincidence rate of $\langle n_{\mathrm{coinc}} \rangle = 4.4$.

9.6. SIGNAL DETECTION POWER

Figures 9.7 shows the distribution of the stacked timing profiles τ, τ_z and τ_{LIV} from more than $1.4 \cdot 10^7$ pseudo experiments using the ANTARES neutrino candidates and accordingly selected gamma-ray bursts, and the respective test statistics calculated corresponding to Equation 9.6. The test-signal peak at $\tau_z = 5$ days corresponding to an intrinsic delay of neutrino and photon emission at the source appears clearly in the τ_z timing profile (top middle panel), and leads to a broader distribution in the τ profile (top left panel). The threshold values of the test statistics above which a measurement represents an excess of 3σ or 5σ are indicated by gray lines. The discovery probability $\mathcal{MDP}$ is given by the fraction of pseudo experiments that led to values of the test statistics above the threshold

$$\mathcal{MDP} = P(Q > Q_{\mathrm{thres}}) \,, \tag{9.13}$$

and represents the efficiency of the analysis and the specific test statistic to identify a signal being associated with a fraction of GRBs. The evolution of these efficiencies as a function of the signal strength is shown in Figure 9.8, left. The signal leading to discoveries at the 5σ level (dashed lines) must naturally be stronger than for 3σ (solid lines).

The measure ψ as evaluated from the timing profile of the generic time delay τ identifies a signal very efficiently, both at 3σ and 5σ significance levels. For instance, if only 1.3% of the GRBs would give rise an associated signal neutrino[8], it would produce an excess

[8]That is 3.75% of all gamma-ray bursts with measured redshift z.

of 3σ significance with 50% probability, whereas a stronger signal in 2.4% of the bursts would be identified at the 5σ level (see gray dashed line marking the 50% probability in Figure 9.8, left). Being evaluated on the sample of GRBs with given redshift z only, the measure ψ_z is naturally more suited to identify the test signal that was simulated for these gamma-ray bursts. In 50% of the cases, it can distinguish the signal from background if it occurs in 2.2% of the GRBs with z measured at 3σ, and with 5σ in 4% of the GRBs. The introduced time-stacking technique is consequently capable of robustly finding an intrinsically delayed neutrino emission from GRBs as long as it is associated with at least 3 of the 563 bursts. The test statistic chosen to identify Lorentz invariance violation ψ_{LIV} is, as anticipated, less powerful at identifying the simulated test signal, which was chosen to mimic an intrinsic delay of neutrino and photon emission at the source. Figure 9.7, upper right panel, demonstrates clearly that the timing profiles do not change significantly with this type of test signal.

The probability of measuring values of the test statistics exceeding the median background value for different signal strengths are shown in Figure 9.8 (right), with the respective numbers given in Table 9.3. The sensitivity is defined as the 90% confidence-level upper limit that can be placed on the signal strength when observing the median background (see gray dashed line marking 90%). The sensitivity of the proposed analysis for the given test signal simulating neutrino emission delayed by 5 days at the source in a mean fraction of all bursts is $m(f_{\mathrm{all}}^{90\%\mathrm{CL}}) = 0.6\%$. Considering only the sub-sample of bursts with determined redshift and the test statistics ψ_z and ψ_{LIV}, the method is even sensitive to a signal in only 1.1% of the bursts, which corresponds to 0.3% of the entire sample (see Table 9.3).

Also tested was how the change of the parameters around the chosen values $\tau_{\mathrm{max}} = 40\,\mathrm{d}$ and $\delta_{\mathrm{max}} = 1.59^\circ$ affects the efficiency of the test statistics for a test signal of the form $5\,\mathrm{d} \cdot (1+z)$. In general, the best performances were observed for the tightest chosen cut configurations – both for the angular search cones and the time window around the gamma-ray bursts. This is a natural consequence of the test signal being associated only with the well-localized bursts without any angular offset, so only background ($\propto \tau_{\mathrm{max}} \cdot \Omega(\delta_{\mathrm{max}})$) would be affected by widening the coincidence windows. Another effect is the reduction of the gamma-ray-burst sample by those with large error boxes and no simulated signal. In the most extreme case, the efficiency to find a test signal associated with 1% of all GRBs with measured redshift using the test statistic ψ can improve by $\sim 60\%$ if the angular search-cone size would be chosen as the smallest possible value. However, in most of the cases and, in particular, regarding the other test statistics, the improvement is much less prominent and mostly below 1%.

Considering more extended test signal shapes in time, a general trend towards reduced detection powers for smeared or plateau-like signals is apparent, in contrast to a signal peaked in one bin. However, changes are not crucial, so the whole procedure proves to be robust against changing signal shapes. For instance, in the case of a signal being emitted within a time window of five days at the sources, the detection power for most of the signal strengths is reduced by 10% with respect to the signal being comprised in one single bin. Apart from that, having injected the signal in one bin in the τ_z profile mimics already a spread-out signal in the profile of the generic time shift τ (see Figure 9.7, top left), which still allows for robust identification of the signal.

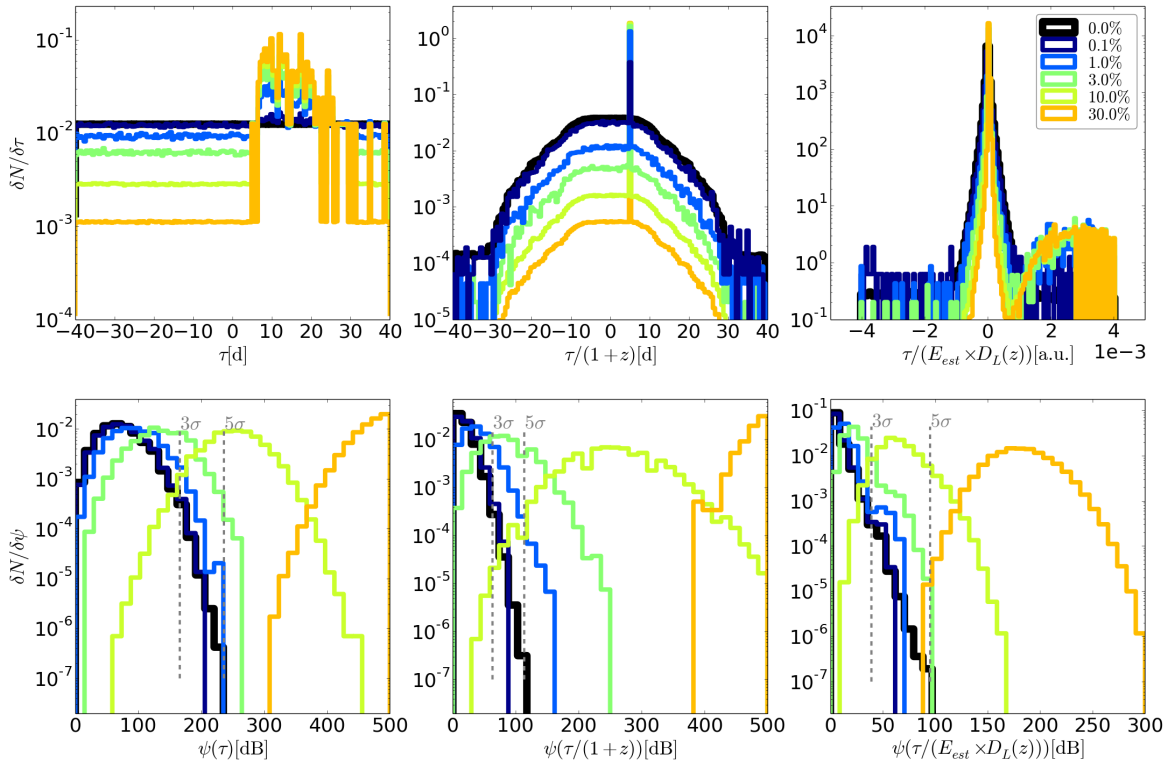

FIGURE 9.7.: *Top panels:* Normalized distributions of the three timing measures τ, τ_z and τ_{LIV} *(from left to right)* for more than $1.4 \cdot 10^7$ pseudo experiment realizations using the ANTARES 07-12 data set. Timing profiles from purely accidental coincidences of the neutrino candidates with the GRBs from randomizing time and right ascension of the ANTARES data are shown in black. For a mean fraction $f_z \in [0.1\%, 30\%]$ of GRBs with measured redshift z, one signal event was added at $\tau_s = 5\,\mathrm{d} \cdot (1+z)$ (colored profiles). *Bottom panels:* Distributions of the accordingly calculated test statistics ψ, ψ_z and ψ_{LIV}. Gray lines indicate the 3σ and 5σ threshold values derived from background-only.

IC40 DATA SAMPLE The capabilities of the analysis to identify signal neutrinos within the public IC40 data set from a sub-sample of the selected GRBs are considerably worse, which is a natural consequence of the different statistical regimes that are accessed by the two samples. Only 12 suitable bursts with measured redshift z were selected corresponding to the respective data-taking livetime, and due to the large number of 12876 presumable neutrino candidates, 35 alone are expected to coincide accidentally with the gamma-ray-burst search windows. Artificially adding one signal neutrino to a small average percentage of these 12 GRBs will have only marginal effect. Given this high background rate, a significantly stronger signal would be needed to yield a clear excess.

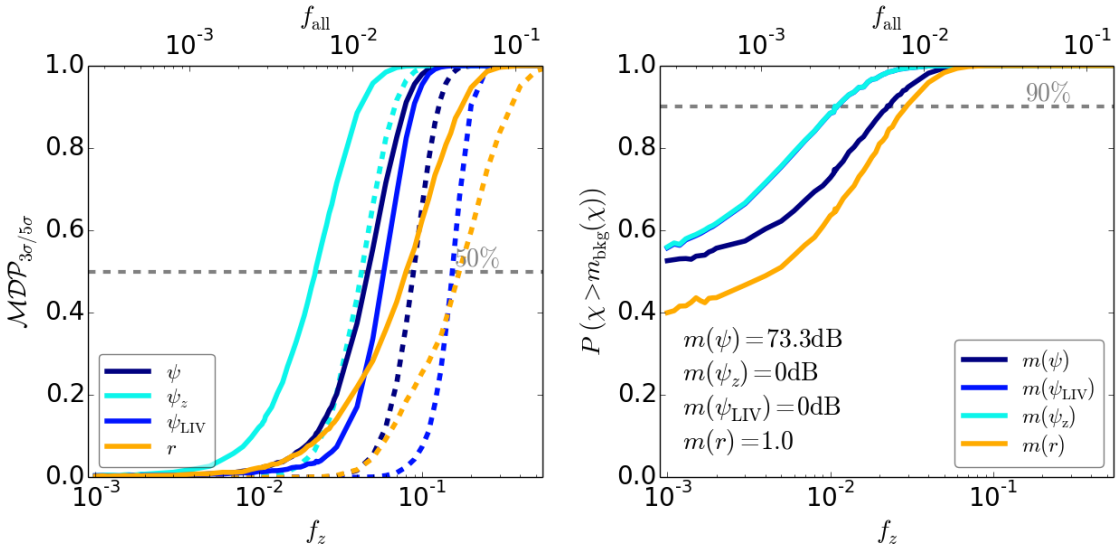

FIGURE 9.8.: *Left:* Efficiencies or detection probability P at 3σ (solid) and 5σ (dashed lines) for the test statistics ψ, ψ_z, ψ_{LIV} and the ratio as a function of the mean fraction f of GRBs with one associated signal neutrino at $t_\nu = t_{\mathrm{GRB}} + 5\,\mathrm{d} \cdot (1+z)$. The fraction f_z denotes the fraction of GRBs in the sample with determined redshift z, whereas f_{all} gives the fraction of the whole sample. *Right:* Probabilities P to measure values of the test statistics above the median value from the background-only realizations. The sensitivity is given by the signal fraction f where the curves reach 90% probability (gray dashed line). Note that the curves for ψ_z and ψ_{LIV} lie on top of each other. Probabilities were derived using the ANTARES data from 2007-2012.

9.7. RESULTS

Having shown and discussed the capability of the proposed analysis to identify an intrinsically shifted neutrino test signal at the source by its cumulative effect on stacked timing profiles with the use of pseudo experiments, the search method was accepted by the ANTARES collaboration. Subsequently, the data of the telescope from the years 2007 to 2012 were searched for neutrinos within the predefined angular and timing search windows associated with the gamma-ray-burst catalog. None of the neutrino candidates in the data matched these search windows, where 4.4 would have been expected to coincide with the entire sample by mere chance (0.7 coincidences were expected for the GRBs with measured redshift z). The measured values of the test statistics are thus zero, and the ratio $r = n_+/n_-$ is undefined. The probability to observe not a single event coinciding with all GRBs is relatively small with $\mathcal{P}(0|4.4) = 1.2\%$ (and 51.4% for GRBs with measured z). The result was checked by opening the time window further, confirming that the anticipated average rate of coincident events of 4.4/80 days was observed in the additional time window.

Under normal circumstances, a 90% confidence-level limit would have been set on the maximum fraction of GRBs that had induced one associated neutrino with a fixed intrinsic time delay of $\tau_{\mathrm{s}} = \tau_{\mathrm{s,int}} \cdot (1+z)$: It would have been defined as that fraction of GRBs with a signal strength f that yielded values of the test statistic in question (e.g. ψ) exceeding the measurement in 90% of all pseudo-experiment realizations. However, since an extraordinary under-fluctuation with 1.2% probability of zero events was observed with 4.4 expected

from pure background, no exclusion of a signal strength at 90% confidence level could be derived. There are several approaches to handle such cases of unusual under-fluctuations of the measurement. One option is to set the upper limit to the sensitivity, as it is done for example in the IceCube search for neutrino point sources (Aartsen et al., 2013b). This is naturally a very conservative approach, since it prevents placing limits lower than the upper limit from the median expectation from pure background realizations. On the other hand, in 50% of all measurements, when values below the median were observed, this method would ignore the information comprised in the measurement by setting the resulting limit to a predefined value. In order to still make use of the information contained in the actual non-observation, a 99% confidence-level upper limit could be set on the signal strength, which would hence be the value f giving rise to higher measured values of a test statistic with 99% probability.

In Table 9.3, the probabilities P to measure test statistics above the measurements and the expected values from the median background realizations are given. Following the ideas as outlined above, we can state a sensitivity of $m(f_{\mathrm{all}}^{90\%\mathrm{CL}}) = 0.6\%$ of all gamma-ray bursts (2.2% for those with measured z), which is the median upper limit on the fraction of bursts that contain a signal of the form $\tau_{\mathrm{s}} = 5\,\mathrm{d} \cdot (1+z)$. Furthermore, we see that 99% of all realizations with a signal fraction $f_{\mathrm{all}} = 0.04\%$ would yield higher ψ as that observed, so we could exclude such a signal with 99% confidence. Regarding the sample of bursts with measured redshift z, the observation of zero events matched the median expectation from background, so we could exclude that 1.1% of them produced a signal neutrino with a delay shape $\tau_{\mathrm{s}} = 5\,\mathrm{d} \cdot (1+z)$ with 90% confidence, in accordance with the sensitivity that had previously been derived.

In conclusion, the test statistics ψ_{z} and ψ_{LIV}, being calculated from the sample of GRBs with measured redshift z, lead to better sensitivity than considering the full sample. This in turn allows, after non-observation of any excess, to exclude the associated signal neutrinos with 1% of these bursts. Yet since a considerable under-fluctuation is observed, the limit that can be derived from the sample of all GRBs is even more stringent ($f_{\mathrm{all}} < 0.04\%$ with 99% confidence) than the sensitivity that was expected, $m(f_{\mathrm{all}}^{90\%\mathrm{CL}}) = 0.6\%$.

IC40 Data Sample Considering the IceCube IC40 data from April 2008 to May 2009, 35 of the neutrino candidates were expected to coincide with all GRBs' search windows (and 4.0 with the GRBs that have redshift determinations). In the actual data, 42 of the candidates matched the search windows, with 8 of them coinciding with the bursts with measured z. The timing profiles of these candidates are shown in Figure 9.9 for the three investigated time measures τ, τ_{z} and τ_{LIV}. This is a slight fluctuation above the expectations from background with p-values of 13.5% (whole sample) and 5.1% (GRBs with measured redshift), yielding excesses of moderate 1.5σ and 1.9σ significances, respectively. However, the observation is still perfectly compatible with totally uncorrelated coincidences of the IceCube data with the gamma-ray bursts that were investigated. Moreover, the timing profiles show no indication for any preferred time delay.

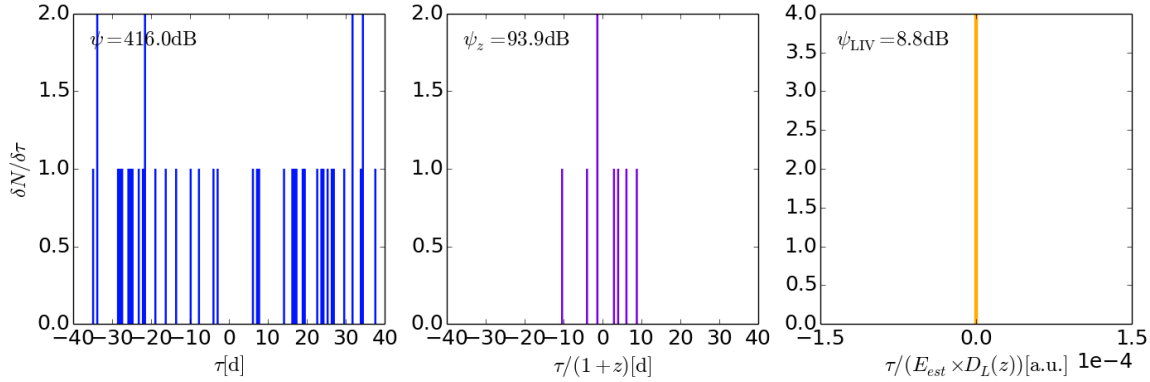

FIGURE 9.9.: Number of neutrino candidates from the ICECUBE IC40 data-taking period that coincided spatially with one of the gamma-ray-burst alerts as reported by the *Swift* and *Fermi* satellites and the GCN network with the relative time delays τ, τ_z and τ_{LIV} *(from left to right)*.

	ANTARES 07-12					ICECUBE IC40 08-09				
	all GRBs		GRBs /w z			all GRBs		GRBs /w z		
	n_{coinc}	ψ (dB)	n_{coinc}	ψ_z (dB)	ψ_{LIV} (dB)	n_{coinc} (dB)	ψ	n_{coinc}	ψ_z (dB)	ψ_{LIV} (dB)
$\langle Q \rangle_{\mathrm{bkg}}$	4.4	77.4	0.7	11.9	4.5	35.0	371.3	4.0	56.6	10.4
$m(Q)_{\mathrm{bkg}}$	4	73.3	0	0	0	35	371.8	4	56.3	7.9
Q_{meas}	0	0	0	0	0	42	416.0	8	93.9	8.8
$P(> Q_{\mathrm{meas}})$	98.8%	98.8%	48%	48.6%	48.6%	10.4%	14.0%	2.1%	6.1%	45.1%
$P(\geq Q_{\mathrm{meas}})$	100%	100%	100%	100%	100%	13.5%	14.0%	5.1%	6.1%	45.1%

TABLE 9.2.: Mean and median values of the different test statistics $Q \in [\psi, \psi_z, \psi_{\mathrm{LIV}}]$ as derived in the pseudo experiments and in the measurement using the neutrino candidates as selected in the ANTARES data from 2007 to 2012 and ICECUBE data from the IC40-period from April 2008 to May 2009. The number of data events coinciding spatially with the respective gamma-ray-burst samples (and only those with measured redshift z) n_{coinc} are also given. The probabilities $P(Q > Q_{\mathrm{meas}})$ and the p-value, $P(Q \geq Q_{\mathrm{meas}})$ give the fraction of background-only pseudo experiments that yield test statistics (at and) above the measurement.

f_{all}	$P(> \psi_{\mathrm{meas}})$ $\psi_{\mathrm{meas}} = 0$	$P(> m(\psi))$ $m(\psi) = 73.3$	f_z (all z)	$P(> \psi_{\mathrm{z,meas}})$ $\psi_{\mathrm{z,meas}} = 0$	$P(> m(\psi_z))$ $m(\psi_z) = 0$	$P(> \psi_{\mathrm{LIV,meas}})$ $\psi_{\mathrm{LIV,meas}} = 0$	$P(> m(\psi_{\mathrm{LIV}}))$ $m(\psi_{\mathrm{LIV}}) = 0$
0.0%	98.8%	50.0%	0.0%	48.5%	48.5%	48.2%	48.2%
0.04%	99%	54%	0.15%	59%	59%	59%	59%
0.29%	99%	75%	1.10%	90%	90%	90%	90%
0.60%	100%	90%	2.25%	98%	98%	98%	98.4%
2.1%	100%	100%	8.0%	100%	100%	100%	100%

TABLE 9.3.: Probabilities P to yield values of the test statistic $Q \in [\psi, \psi_z, \psi_{\mathrm{LIV}}]$ above the measurement Q_{meas} and above the median value $m(Q)$ as expected from pure background realizations for fraction f_{all} (f_z) of all GRBs (with measured redshift z) with one associated signal neutrino.

9.8. CONCLUSION

I have presented a powerful method to identify a neutrino signal associated with gamma-ray bursts if it is shifted in time with respect to the photon signal. The signal is distinguished from random coincidences as a cumulative effect in stacked timing profiles of spatially coincident neutrinos in the data from the ANTARES and ICECUBE neutrino telescopes. The discrepancy between the signal and background-only measurements is quantified in terms of a test statistic ψ, which is calculated on the cumulative profiles.

Simulating the behavior of the search for a large number of possible measurements using randomized sky maps of the neutrino events, and comparing these with the actual neutrino telescope data, significances of the observations were derived. Using data from the ANTARES experiment between the years 2007 and 2012, an unusual deficit of spatial coincident neutrinos with the selected gamma-ray-burst catalog was observed, given that 98.8% of the randomized data sets led to more coincidences between the neutrino data and the GRBs. The presented work could have identified an intrinsically time-shifted signal even if only in the order of one in a hundred GRBs would have given rise to a single associated neutrino in the ANTARES data.

No assumption on any model for neutrino emission had been assumed in this study, yet for comparison, the average signal strength of 0.01 (corresponding to one signal neutrino per 100 GRBs) can still be compared to the models that had been considered in the search for simultaneous emission presented in the previous sections. The detectable neutrino signal predicted by the NeuCosmA model is on average only in the order of $\sim 2 \cdot 10^{-4}$ in the ANTARES detector, and only the strongest individual burst yields a neutrino detection rate exceeding 0.01 (see Section 6 and in particular Table 6.5). However, as demonstrated in Section 8, the future KM3NET telescope will probably detect an average rate of 0.01 neutrinos from gamma-ray bursts (see Table 8.1), so that the method presented here will be capable of distinguishing time-shifted neutrino emission from GRBs, if the neutrino flux would be of the same order of magnitude than that of the NeuCosmA model.

Regarding the ICECUBE data from the IC40 detector configuration between April 2008 and May 2009, the observed neutrino events that coincide with the gamma-ray-burst search windows exceed the number that would have been expected from randomized data. However, even in the most significant case where eight candidates, instead of four, were observed in the search windows of the gamma-ray bursts with measured redshift z, the surplus is still compatible with the background expectation.

In conclusion, the absence of a neutrino signal being associated with gamma-ray bursts that has so far been measured in the simultaneous time windows can only be confirmed when extending the search to allow for time displacements between the neutrino and electromagnetic signal of a gamma-ray burst of up to 40 days.

10. Conclusions

In this work, I have presented searches for neutrino signals from gamma-ray bursts (GRBs) using data from the Antares neutrino telescope. GRBs are short and intense flashes of high-energy gamma rays in the sky most likely associated with the cataclysmic collapse of extremely massive stars or the coalescence of two compact objects into a black hole. Within relativistic outflows of material expelled from a central engine, electrons are thought to be accelerated in internal shocks, which serves to explain the gamma radiation that is observed at Earth. If protons are simultaneously accelerated in these outflows, their interactions with the local photon field would give rise to a flux of neutrinos at energies of $\sim 10^6$ GeV that would accompany the electromagnetic signal. The first detection of such a signal would unambiguously substantiate that GRBs are hadronic accelerators, a fact that cannot be proven beyond doubt by purely electromagnetic observations. The conclusive identification of the astrophysical sources that are capable of accelerating hadrons to the energies exceeding 10^{18} eV would be essential to explain the hitherto mysterious flux of cosmic rays at ultra-high energies.

The Antares neutrino telescope aims at detecting cosmic muon neutrinos above $\sim$ TeV by identifying the secondary muons from charged current interactions in the surrounding medium, which induce Cherenkov light emission. In Section 4, I first examined whether or not the reconstruction of muon trajectories in the Antares data is subject to systematic effects in addition to the unavoidable stochastic fluctuations that determine the detector's pointing accuracy. Since the reconstruction depends crucially on the detected photon pattern of the emitted Cherenkov light, it is supposed to be sensitive to the precise location of the particle track within the detector and its orientation with respect to the photodetectors. My investigations have demonstrated that there is a non-negligible chance for systematic trends in the reconstruction of individual particles that should not be disregarded when claiming the detection, and in particular the coordinates, of only a handful of presumed cosmic neutrino signatures. Having sampled the instrumented volume with tens of millions of simulated muons, I analyzed the reconstructed directions for systematic discrepancies from the input values. Indeed, I could reveal overall deviations from the primary muon's direction by more than the detector's resolution in around 1% of the analyzed sample. This shows promising possibilities to improve searches, such as for transient sources for which the expected number of detected neutrino signatures is naturally small. With considerable possibility, re-simulating the best-fit particle track and scanning the parameter space around it can refine the directional reconstruction. Any quantified systematic trend in this scan can subsequently be corrected for, thereby narrowing down the most probable source of emission of the detected signal-like event. In the search for associated neutrinos from GRBs, which comprised the main body of this work, any particle signature in the data matching the selection criteria would have been scrutinized to reveal, and eventually correct for, such an effect.

In approaching the subject of identifying simultaneous neutrino emission from gamma-

ray bursts, I initially investigated the discovery capabilities of a simple counting method (Section 5). Having discussed multiple selection criteria and how these can be optimized, I derived an optimal set of criteria that can distinguish a neutrino signal from background for the showcase burst GRB091026. The neutrino flux was estimated from predictions by Guetta et al. (2004), based on photon-spectrum parameters announced in the GCN messages. Within this preparatory approach, isotropically simulated atmospheric neutrinos were modified in order to represent both signal and background of the example GRB. Surprisingly, the parameters estimating the event energy, e.g. the number of photon counts or the reconstructed energy, were found to only marginally increase the statistical power for distinguishing signal events from background.

I pointed out various limitations of this simple technique and the improvements that are required to allow for more accurate description of the detector's response to the expected neutrino signal. The strong dependence of this study on the simulated data set was discussed, emphasizing the need for a devoted Monte Carlo simulation of the signal.

In the simple counting technique, any information incorporated in the event distributions is basically discarded since all signatures matching the selection criteria are treated equally, while all events outside the defined search window are rejected. Any approach making use of the different behavior of signal and background, in particular their different spatial distributions, is naturally more powerful in discriminating between those two.

Furthermore, the un-scrutinized use of gamma-ray-burst information parsed from the GCN messages turned out to be defective, demonstrating the need for more elaborate compilation of the necessary parameters. For the analysis of late-2007 to 2011 data from ANTARES, a substantially refined catalog of gamma-ray burst parameters was condensed (Section 6) using information from the *Fermi* and *Swift* satellites, supplemented by data from the GCN announcements. Numerous consistency checks were performed to ensure the reliability of the collected data. Meanwhile, elaborate simulations of particle interactions within astrophysical sources using numerical algorithms have been developed. These treat the particle physics governing the radiation processes in greater detail, and hence are expected to predict the neutrino yield from gamma-ray bursts more accurately than precedent analytical models. The response of the ANTARES detector to the individual GRBs' signals was derived from dedicated simulations of these predictions, calculated from the aforementioned consolidated GRB information. Realistic background was estimated from the rate of recorded data over time, which is sensitive to both changing environmental conditions in the deep sea and the detector's configuration, and consequently accounts for the varying data-taking efficiency of the detector. The spatial distributions of both signal and background are described by smooth functions, and an un-binned log-likelihood method has been implemented that efficiently distinguishes signal from the expected background. It could be proven to enhance the detecting potential for GRB-neutrino emission by up to 200% with respect to an equivalent counting experiment.

Data from the ANTARES experiment from December 2007 to the end of 2011 were scanned in the search for a neutrino excess in coincidence with 296 gamma-ray bursts, with the event selection being optimized for a most probable discovery. None of the data events passed the selection criteria, with a total of 0.06 neutrinos being expected. Hence only upper limits on the neutrino flux could be derived, lying with a factor of 38 above the model predictions. I subsequently published the work as one of the two corresponding authors with the title

'Search for muon neutrinos from gamma-ray bursts with the ANTARES neutrino telescope using 2008 to 2011 data' in the journal A&A (see Adrián-Martínez et al., 2013d). Despite there having previously been searches for coincident neutrino emission from gamma-ray bursts in comparable energy ranges, 90% of the selected sample had not been included in any of the former analyses. This work has been the first of this kind that was optimized based on second-generation numerical calculations of neutrino fluxes. I have shown that the current upper limits on the neutrino flux are still compatible with the non-observation of any neutrino signal associated with GRBs and do not yet constrain the parameter space of the hadronic acceleration models within the fireball paradigm.

An exceptionally bright gamma-ray burst lit up the sky on April 27, 2013. Due to its proximity to Earth, it was detected as the most luminous burst in the few last decades with record-holding high-energy photon emission up to almost 100 GeV. I adapted the technique as developed before to enable a fast follow-up search for any coincident neutrino signal in the ANTARES data (Section 7). Unfortunately, the GRB alert was reported during unfavorable conditions, as the detector was in the process of resuming regular data-taking after a seven-week period with data acquisition turned off due to high bioluminescent activity in the deep sea. In these circumstances, data acquisition was only half as efficient as the average of the four-year period considered before. With the data selection being optimized for a discovery, $6.2 \cdot 10^{-3}$ signal events were expected from the simulations. However, no neutrino excess was identified in the ANTARES data within the 264 s search-time window of GRB130427A, hence neutrino emission exceeding $1 - 10\,\mathrm{GeV/cm^2}$ between $2 \cdot 10^5 - 2 \cdot 10^7$ GeV could be excluded with 90% confidence. This has been the first time that the neutrino flux from this particular GRB was constrained.

I furthermore discussed the detection capabilities of the future KM3NeT telescope to a similar neutrino signal to that from the 296 gamma-ray bursts in 2007 to 2011 in Section 8. Using a preliminary estimation of the effective area of the final detector with six building blocks of 115 detection strings each, an order-of-magnitude estimate for the expected number of neutrino events could be derived. The 296 GRBs would give rise to a total of 3.4 detected neutrino signatures from the second-generation numerical predictions, and more than 36 if the analytical model from Guetta et al. (2004) was considered. Even with the realistic predictions, the strongest burst of the sample alone would have produced one associated neutrino in the KM3NeT detector, while GRB130427A would have accounted for 0.4. Based on the experience in the analysis of the ANTARES data, the detection of a single neutrino coinciding in space and time with a reported gamma-ray burst can bring evidence at the 3σ level. Since KM3NeT will be able to discriminate neutrino signatures from cosmic-ray-induced muons and random optical background noise in the deep-sea water more efficiently than its predecessor, the observation of a single event might give definitive proof for the connection of high-energy neutrinos with gamma-ray bursts.

In addition to the searches for coincident neutrino emission, a powerful method has been established in Section 9 to identify a neutrino signal from gamma-ray bursts that is systematically shifted up to 40 days in time with respect to the detected electromagnetic emission. Such a signal can give rise to a cumulative effect in a large sample of GRBs, so that even faint signals can efficiently be distinguished from background. Data sets from the neutrino detectors ICECUBE and ANTARES that comprised neutrino signatures of presumable cosmic origin were searched for spatial coincidences with the GRB alerts as announced by

the satellites. The time difference between neutrino-like events and the associated GRB trigger were collected and stacked in common timing profiles. A test statistic calculated from their discrete representations has been scrutinized for its capability to discriminate a time-shifted neutrino signal as a collective effect from the background hypothesis of mere accidental coincidences. I could demonstrate that a signal can efficiently be detected in the six years of ANTARES data if it gave rise to as little as only one associated neutrino with 1% of the considered GRBs.

No significant excess over the expected accidental coincidence rate could be found in neither of the two data sets, with marginally significant evidence in the one-year ICECUBE data sample at the 1.9σ level. As a matter of fact, the ANTARES neutrino candidates revealed an unexpected deficit of spatial coincidences: No events from six years of data matched the search cones of the gamma-ray bursts, where 4.4 would have been anticipated assuming purely randomized data. This novel technique allowed for the first time a search for essentially model-independent, time-shifted neutrino emission in association with gamma-ray bursts in six years of data from a neutrino telescope.

In conclusion, I could not find any significant neutrino excess over background in the presented searches for neutrinos associated with gamma-ray bursts, neither simultaneously with the electromagnetic observation, nor in extended time windows up to 40 days around the photon detections. Mainly data from the ANTARES neutrino telescope was analyzed, where not a single neutrino-like signature could be observed. Consequently, the technique to enhance the detector's angular resolution could not be applied to any data event. Hence, only limits on the maximum neutrino flux could be derived from the ANTARES data, which are compatible with other experiments but complementary in sky coverage, data livetime and energy ranges.

However, novel techniques have been developed that employed for the first time state-of-the-art numerical neutrino emission models and allowed neutrino signals from gamma-ray bursts in time windows in the order of months to be probed. None of the existing limits yet constrain the model of hadronic acceleration within the fireball paradigm or the parameters that are commonly used. However, I could demonstrate that the future telescope KM3NET will be capable of putting these models to the test with unprecedented sensitivity, allowing for the first time the neutrino flux as predicted by second-generation models to be detected, or the parameter space upon which they are based to be severely constrained.

REFERENCES

Aartsen M.G., Abbasi R., Abdou Y., et al., 2013a, Science 342

Aartsen M.G., Abbasi R., Abdou Y., et al., 2013b, ApJ 779, 132

Aartsen M.G., Ackermann M., Adams J., et al., 2014, Phys. Rev. Lett. accepted for publication

Abbasi R., Abdou Y., Abu-Zayyad T., et al., 2012, Nature 484, 351

Abbasi R., Abdou Y., Abu-Zayyad T., et al., 2011, Phys. Rev. D 84, 082001

Abbasi R., Abdou Y., Abu-Zayyad T., et al., 2010, ApJ 710, 346

Abbasi R., Abdou Y., Abu-Zayyad T., et al., 2011, Phys. Rev. Lett. 106, 141101

Achterberg A., Ackermann M., Adams J., et al., 2008, ApJ 674, 357

Ackermann M., Ajello M., Asano K., et al., 2014, Science 343, 42

Ackermann M., Ajello M., Asano K., et al., 2013, ApJS 209, 11

Ackermann M., Ajello M., Atwood W.B., et al., 2012, ApJ 750, 3

Adrián-Martínez S., Ageron M., Aguilar J.A., et al., 2012a, JINST 7, 8002

Adrián-Martínez S., Al Samarai I., Albert A., et al., 2013a, JCAP 6, 8

Adrián-Martínez S., Albert A., Al Samarai I., et al., 2013b, VizieR Online Data Catalog 355, 99009

Adrián-Martínez S., Albert A., Al Samarai I., et al., 2013c, JCAP 2013, 006

Adrián-Martínez S., Albert A., Al Samarai I., et al., 2013d, A&A 559, A9

Adrián-Martínez S., Albert A., Al Samarai I., et al., 2012b, ApJ 760, 53

Adrián-Martínez S., Albert A., André M., et al., 2014, Astrophys. J., Lett. 786, L5

Ageron M., Aguilar J.A., Al Samarai I., et al., 2012, Astroparticle Physics 35, 530

Ageron M., Aguilar J.A., Albert A., et al., 2011, Nucl. Instr. Meth. A 656, 11

Aglietta M., Badino G., Bologna G., et al., 1987, Europhysics Letters 3, 1315

Agrawal V., Gaisser T.K., Lipari P., Stanev T., 1996, Phys. Rev. D 53, 1314

Aguilar J.A., 2011, In: IUPAP (ed.) ICRC, Vol. 8. Proceedings of the 32nd International Cosmic Ray Conference, Institute of High Energy Physics, Beijing, p. 235

Ahlers M., Anchordoqui L.A., Gonzalez-

Garcia M.C., et al., 2010, Astroparticle Physics 34, 106

Alekseev E.N., Alekseeva L.N., Volchenko V.I., Krivosheina I.V., 1987, ZhETF Pisma Redaktsiiu 45, 461

Alexandreas D.E., Berley D., Biller S., et al., 1993, Nucl. Instr. Meth. A 328, 570

Amelino-Camelia G., Guetta D., Piran T., 2013, ArXiv e-prints arXiv:1303.1826

Amelino-Camelia G., Smolin L., 2009, Phys. Rev. D 80, 084017

Amram P., Anvar S., Aslanides E., et al., 2000, Astropart. Phys. 13, 127

Aptekar R., Frederiks D., Golenetskii S., et al., 1995, Space Sci. Rev. 71, 265

Asano K., Inoue S., Mészáros P., 2009, ApJ 699, 953

Astraatmadja T.L., 2011, MNRAS 418, 1774

Atwood W.B., Abdo A.A., Ackermann M., et al., 2009, ApJ 697, 1071

Avrorin A., Aynutdinov V., Belolaptikov I., et al., 2011, Astron. Lett. 37, 692

Baerwald P., 2013, Ph.D. thesis, Julius-Maximilians-Universität Würzburg

Baerwald P., Hümmer S., Winter W., 2012, Astropart. Phys. 35, 508

Band D., Matteson J., Ford L., et al., 1993, ApJ 413, 281

Baret B., Bartos I., Bouhou B., et al., 2012, Phys. Rev. D 85, 103004

Baret B., Bartos I., Bouhou B., et al., 2011, Astroparticle Physics 35, 1

Barlow R., 1990, Nucl. Instr. Meth. A 297, 496

Barthelmy S.D., Baumgartner W.H., Cummings J.R., et al., 2013, GCN Circular 14470

Besson D., Razzaque S., Adams J., Harris P., 2007, Astropart. Phys. 26, 367

Bionta R.M., Blewitt G., Bratton C.B., et al., 1987, Phys. Rev. Lett. 58, 1494

Blaufuss E., 2013, GCN Circular 14520

Bloom J.S., Prochaska J.X., Pooley D., et al., 2006, ApJ 638, 354

Bogazzi C., Hartman J., Heijboer A., 2010, Point Source Search with 2007 and 2008 data, ANTARES-Physics/2010-008

Bose D., Brayeur L., Casier M., et al., 2013, Astroparticle Physics 50, 57

Bouwhuis M., 2005, Ph.D. thesis, Universiteit van Amsterdam

Bouwhuis M., 2007, Data blinding for GRB data analyses, ANTARES-Software/2007-006

Bouwhuis M., 2008, GRB position and time information, ANTARES-Software/2008-002

Braun J., Dumm J., De Palma F., et al., 2008, Astroparticle Physics 29, 299

Carretti E., Crocker R.M., Staveley-Smith L., et al., 2013, Nature 493, 66

Casey J., 2013, In: IUPAP (ed.) ICRC. Proceedings of the 33nd International Cosmic

Ray Conference, to be published

Coniglione R., 2013, Private Communication, on the estimated KM3NeT effective area.

Costa E., Frontera F., Heise J., et al., 1997, Nature 387, 783

Crocker R.M., Aharonian F., 2011, Phys. Rev. Lett. 106, 101102

Cucchiara A., Levan A.J., Fox D.B., et al., 2011, ApJ 736, 7

Daigne F., Mochkovitch R., 1998, MNRAS 296, 275

de Ugarte Postigo A., Gorosabel J., Castro-Tirado A.J., Thoene C.C., 2011, GCN Circular 12375

Dornic D., Brunner J., Basa S., et al., 2011, Nucl. Instr. Meth. A 626, 183

Dziewonski A.M., Anderson D.L., 1981, Physics of the Earth and Planetary Interiors 25, 297

Eichler D., Livio M., Piran T., Schramm D.N., 1989, Nature 340, 126

Elenin L., Volnova A., Savanevych V., et al., 2013, GCN Circular 14450

Ernenwein J.P., Tsirigotis A., Tzamarias S., 2009, Nucl. Instr. Meth. A 602, 88

Escoffier S., Lambard G., 2008, Comparison of Dark Room and on-line computation of the hit time, ANTARES-Calibration/2008-001

Fermi E., 1949, Physical Review 75, 1169

Folger F., 2014, Ph.D. thesis, Friedrich-Alexander-Universität Erlangen-Nürnberg

Fukuda S., Fukuda Y., Ishitsuka M., et al., 2002, ApJ 578, 317

Gaisser T., 1991, Cosmic Rays and Particle Physics, Cambridge University Press

Gaisser T.K., Halzen F., Stanev T., 1995, Phys. Rep. 258, 173

Galama T.J., Vreeswijk P.M., van Paradijs J., et al., 1998, Nature 395, 670

Gehrels N., Chincarini G., Giommi P., et al., 2004, ApJ 611, 1005

Gehrels N., Mészáros P., 2012, Science 337, 932

Ghisellini G., Ghirlanda G., Nava L., Celotti A., 2010, Monthly Notices of the Royal Astronomical Society 403, 926

Goldstein A., Burgess J.M., Preece R.D., et al., 2012, ApJS 199, 19

Golenetskii S., Aptekar R., Frederiks D., et al., 2011, GCN Circular 12362

Gonzalez-Garcia M.C., Halzen F., Niro V., 2014, Astroparticle Physics 57, 39

Goodman J., 1986, Astrophys. J., Lett. 308, L47

Gould A., 1988, ApJ 328, 919

Granot J., Guetta D., 2003, Phys. Rev. Lett. 90, 191102

Greiner J., Krühler T., Fynbo J.P.U., et al., 2009, ApJ 693, 1610

Greisen K., 1966, Phys. Rev. Lett. 16, 748

Groot P., Kaper L., Ellerbroek L., et al., 2010, GCN Circular 10441

Gruber D., Goldstein A., Weller von Ahlefeld V., et al., 2014, ApJS 211, 12

Guetta D., Hooper D., Alvarez-Muñiz J., et al., 2004, Astropart. Phys. 20, 429

He H.N., Liu R.Y., Wang X.Y., et al., 2012, ApJ 752, 29

Heijboer A.J., 2004, Ph.D. thesis, Universiteit van Amsterdam

Herschel W., 1801, Annalen der Physik 7, 137

Hertz H.R., 1887, Annalen der Physik 267, 421

Hess V.F., 1912, Physikalische Zeitschrift 13, 1048

Hill G.C., Hodges J., Hughey B., et al., 2006, In: L. Lyons & M. Karagöz Ünel (ed.) Statistical Problems in Particle Physics, Astrophysics and Cosmology., p.108

Hirata K.S., Kajita T., Koshiba M., et al., 1988, Phys. Rev. D 38, 448

Hjorth J., Sollerman J., Møller P., et al., 2003, Nature 423, 847

Hümmer S., 2013, Ph.D. thesis, Julius-Maximilians-Universität Würzburg

Hümmer S., Baerwald P., Winter W., 2012, Phys. Rev. Lett. 108, 231101

Hümmer S., Rüger M., Spanier F., Winter W., 2010, ApJ 721, 630

Jacob U., Piran T., 2007, Nature Physics 3, 87

Jansky K., 1933, Proc. IRE 21, 1387

Karle A., 2009, In: Giller M., Szabelski J. (eds.) ICRC. Proceedings of the 31nd International Cosmic Ray Conference, Department of High Energy Astrophysics, University of Łódź

Katz U.F., Spiering C., 2012, Progress in Particle and Nuclear Physics 67, 651

Klebesadel R.W., Strong I.B., Olson R.A., 1973, ApJ 182, 85

KM3NeT Consortium 2008, Conceptual Design for a Deep-Sea Research Infrastructure Incorporating a Very Large Volume Neutrino Telescope in the Mediterranean Sea, ISBN 978-90-6488-031-5

KM3NeT Consortium 2011, Technical Design Report for a Deep-Sea Research Infrastructure in the Mediterranean Sea Incorporating a Very Large Volume Neutrino Telescope, ISBN 978-90-6488-033-9

Kouveliotou C., Meegan C.A., Fishman G.J., et al., 1993, Astrophys. J., Lett. 413, L101

Kowalski M., Mohr A., 2007, Astroparticle Physics 27, 533 arXiv:astro-ph/0701618

Krimm H.A., Mangano V., Siegel M.H., 2011, GCN Report 350

Kumar P., Barniol Duran R., 2009, MNRAS 400, 75

Lacki B.C., 2014, MNRAS 444, 39

Learned J.G., Mannheim K., 2000, Annual Review of Nuclear and Particle Science 50, 679

Levan A.J., Cenko S.B., Perley D.A., Tanvir N.R., 2013, GCN Circular 14455

Levan A.J., Tanvir N.R., Wiersema K., et al., 2011, GCN Circular 12368

Levinson A., Waxman E., 2001, Phys. Rev. Lett. 87, 171101

Longair S., 1994, High Energy Astrophysics: Stars, the galaxy and the interstellar medium, High Energy Astrophysics Bd. 2, Cambridge University Press

MacFadyen A.I., Woosley S.E., 1999, ApJ 524, 262

Meegan C., Lichti G., Bhat P.N., et al., 2009, ApJ 702, 791

Meegan C.A., Fishman G.J., Wilson R.B., et al., 1992, Nature 355, 143

Mészáros P., 2006, Rep. Prog. Phys. 69, 2259

Mészáros P., Gehrels N., 2012, Research in Astronomy and Astrophysics 12, 1139

Mészáros P., Rees M.J., 1993, ApJ 405, 278

Mészáros P., Rees M.J., 1997, ApJ 476, 232

Metzger M.R., Djorgovski S.G., Kulkarni S.R., et al., 1997, Nature 387, 878

Mücke A., Engel R., Rachen J.P., et al., 2000, Comput. Phys. Comm. 124, 290

Murase K., 2007, Phys. Rev. D 76, 123001

Nakar E., 2007, Phys. Rep. 442, 166

Nousek J.A., Kouveliotou C., Grupe D., et al., 2006, ApJ 642, 389

Paciesas W.S., Meegan C.A., Pendleton G.N., et al., 1999, ApJS 122, 465

Paciesas W.S., Meegan C.A., von Kienlin A., et al., 2012, ApJS 199, 18

Piran T., 1998, In: H. Sato & N. Sugiyama (ed.) Black Holes and High Energy Astrophysics., p. 217

Piran T., 2004, Reviews of Modern Physics 76, 1143

Razzaque S., 2013a, Phys. Rev. D 88, 081302

Razzaque S., 2013b, Phys. Rev. D 88, 103003

Razzaque S., Dermer C.D., Finke J.D., 2010, The Open Astronomy Journal 3, 150

Razzaque S., Mészáros P., Waxman E., 2003, Phys. Rev. D 68, 083001

Ritter J., 1810, Fragmente aus dem Nachlasse eines jungen Physikers: ein Taschenbuch für Freunde der Natur, Fragmente aus dem Nachlasse eines jungen Physikers: ein Taschenbuch für Freunde der Natur Bd. 2, Mohr und Zimmer

Rivière C., 2011, In: IUPAP (ed.) ICRC, Vol. 4. Proceedings of the 32nd International Cosmic Ray Conference, Institute of High Energy Physics, Beijing, p. 115

Rivière C., 2012, Run-by-Run Monte Carlo simulation for ANTARES: v2, ANTARES-Physics/2012-001

Rivière C., Schmid J., 2012, Offline search of up-going neutrino from GRBs, 2008-2011, ANTARES-Physics/2012-012

Sakamoto T., Barthelmy S.D., Baumgartner W.H., et al., 2011, ApJS 195, 2

Sanguineti M., Distefano C., 2014, Cosmic ray Moon shadow analysis with the ANTARES detector, ANTARES-Calibration/2014-001

Schmidt W.K.H., 1978, Nature 271, 525

Schnabel J., 2012, The ANNergy estimator, ANTARES-Software/2012-010

Soderberg A.M., Kulkarni S.R., Nakar E., et al., 2006, Nature 442, 1014

Stecker F.W., 1979, ApJ 228, 919

Tamburini C., Canals M., de Madron X.D., et al., 2013, PloS one 8, e67523

Tanvir N.R., Wiersema K., Levan A.J., et al., 2011, GCN Circular 12365

Taylor A.M., Gabici S., Aharonian F., 2014, Phys. Rev. D 89, 103003

Thoudam S., 2013, Astrophys. J., Lett. 778, L20

Ukwatta T.N., Barthelmy S.D., Baumgartner W.H., et al., 2009, GCN Circular 10089

Usov V.V., 1992, Nature 357, 472

van Eijndhoven N., 2008, Astroparticle Physics 28, 540

van Paradijs J., Groot P.J., Galama T., et al., 1997, Nature 386, 686

Vasileiou V., Jacholkowska A., Piron F., et al., 2013, Phys. Rev. D 87, 122001

Vieregg A.G., Palladino K., Allison P., et al., 2011, ApJ 736, 50

Vreeswijk P., Groot P., Carter P., et al., 2011, GCN Circular 11640

Wang X.Y., Li Z., Mészáros P., 2006, Astrophys. J., Lett. 641, L89

Waxman E., 1995a, Phys. Rev. Lett. 75, 386

Waxman E., 1995b, Astrophys. J., Lett. 452, L1+

Waxman E., 1998, Astropart. Phys. arXiv:astro-ph/9804023

Waxman E., 2000, ApJS 127, 519

Waxman E., Bahcall J., 1997, Phys. Rev. Lett. 78, 2292

Waxman E., Bahcall J.N., 2000, ApJ 541, 707

Whitehorn N., 2012, Ph.D. thesis, University of Wisconsin-Madison

Woosley S.E., Bloom J.S., 2006, ARA&A 44, 507

Zatsepin G.T., Kuz'min V.A., 1966, Soviet Journal of Experimental and Theoretical Physics Letters 4, 78

Zhang B., Fan Y.Z., Dyks J., et al., 2006, ApJ 642, 354

Zhang B.B., Zhang B., Murase K., et al., 2014, ApJ 787, 66

Zhu S., Racusin J., Kocevski D., et al., 2013, GCN Circular 14471

APPENDIX

A. Track Reconstruction Systematics

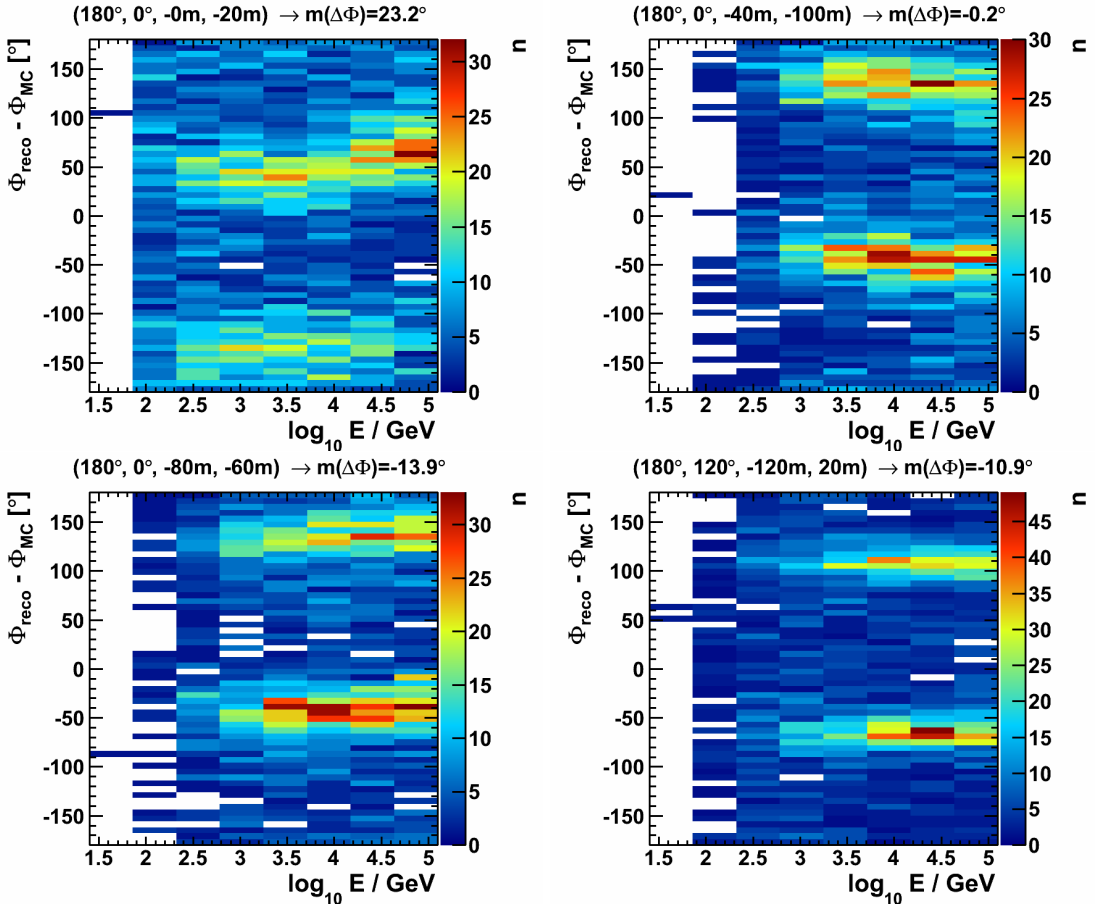

Figure A.1.: Four examples of double solutions in the reconstructed azimuth at the degeneration point $\Theta = 180°$. The simulated muons had distances from the detector's center of $(a, b) = (0\,\mathrm{m}, 20\,\mathrm{m})$, $(-40\,\mathrm{m}, 100\,\mathrm{m})$, $(-80\,\mathrm{m}, -60\,\mathrm{m})$ and $(-120\,\mathrm{m}, 20\,\mathrm{m})$. Only events passing the quality criterion $\Lambda > -5.4$ and $\beta < 1°$ are shown.

Θ (°)	Φ (°)	a (m)	b (m)	$m(\Delta\Theta)$ (°)	$\sigma(\Delta\Theta)$ (°)	$m(\Delta\Phi)$ (°)	$\sigma(\Delta\Phi)$ (°)	α (°)	N_{rec}	$N_{\text{rec}}/N_{\text{sim}}$
10	0	-80	-60	0.3	3.3	-4.3	34.9	0.8	1140	28.5 %
60	0	120	-100	0.4	9.2	0.4	11.4	0.6	1008	25.2 %
120	23	40	-100	-0.2	6.3	-0.8	21.0	0.7	1084	27.1 %
120	23	80	-100	-0.2	6.3	-0.8	18.8	0.7	1077	26.9 %
120	23	160	-100	-0.2	6.1	-0.8	20.7	0.7	1061	26.5 %
120	46	-160	-20	0.1	0.4	0.7	4.9	0.7	2291	57.3 %
130	0	-160	60	0.0	5.6	0.7	22.2	0.6	1068	26.7 %
130	0	40	-60	0.3	3.2	-0.8	16.8	0.7	1529	38.2 %
130	0	160	-60	0.3	5.3	-0.8	18.1	0.7	1526	38.1 %
130	26	-120	-100	0.0	4.3	-0.8	19.1	0.6	1167	29.2 %
130	26	-80	-100	0.0	1.8	-0.8	16.9	0.6	1436	35.9 %
130	26	160	-20	0.3	0.7	-0.8	8.4	0.7	2140	53.5 %
130	52	160	-60	0.0	2.5	-0.8	13.8	0.6	1583	39.6 %
130	78	160	60	0.3	6.7	-0.8	20.7	0.7	1475	36.9 %
140	0	160	-60	0.2	4.0	-0.8	26.2	0.5	1354	33.9 %
140	0	160	20	0.2	2.6	0.7	20.4	0.5	1445	36.1 %
140	31	-200	-60	-0.0	4.0	-1.1	25.4	0.7	1184	29.6 %
140	31	-160	-60	-0.0	5.5	-1.1	24.6	0.7	1208	30.2 %
140	31	120	-100	-0.3	1.2	-0.8	9.6	0.6	1421	35.5 %
140	31	160	-20	0.2	1.5	-0.8	18.0	0.5	1607	40.2 %
140	31	160	60	0.2	3.8	1.1	24.9	0.7	1282	32.0 %
140	62	-120	-100	0.2	3.4	-0.8	15.2	0.5	1280	32.0 %
140	93	-160	60	-0.0	4.6	1.1	22.8	0.7	1198	29.9 %
140	93	160	-60	0.2	4.5	-1.4	23.8	0.9	1307	32.7 %
140	93	160	20	0.2	2.8	1.1	17.0	0.7	1871	46.8 %
150	0	-160	-20	-0.2	4.8	-1.1	18.2	0.5	1282	32.0 %
150	0	-120	60	-0.2	1.0	1.1	28.5	0.5	2046	51.1 %
150	0	160	20	0.1	5.2	1.3	33.5	0.7	1274	31.9 %
150	40	120	-100	-0.5	2.9	-1.1	17.1	0.7	1029	25.7 %
150	40	160	20	-0.2	3.2	1.3	29.8	0.7	1224	30.6 %
150	80	160	-20	-0.2	3.0	-1.4	29.5	0.7	1338	33.5 %
150	120	-160	20	-0.2	1.1	1.3	24.6	0.7	1230	30.8 %
150	120	160	-20	0.1	3.8	-1.7	31.7	0.8	1500	37.5 %
160	0	-160	60	-0.3	0.8	1.3	27.6	0.5	2384	59.6 %
160	0	-120	60	-0.3	0.9	1.3	25.7	0.5	2360	59.0 %
160	116	120	60	0.0	1.9	1.6	34.9	0.6	2533	63.3 %

TABLE A.1.: Systematics found in the methodological scan of the ANTARES detector. All reported systematic effects with criteria as described in Section 4.2. The track parameters (Θ, Φ, a, b) of the reported cases are given as well as the median m and standard deviation σ of the zenith and azimuth differences $\Delta\Theta$ and $\Delta\Phi$ to the initial Monte Carlo track. Furthermore, the number and fraction of events that pass the reconstruction quality selection $\Lambda > -5.4, \beta < 1^\circ$, N_{rec} and $N_{\text{rec}}/N_{\text{sim}}$ are listed. A total of $N_{\text{sim}} = 8 \cdot 500$ tracks have been simulated for each set of track parameters.

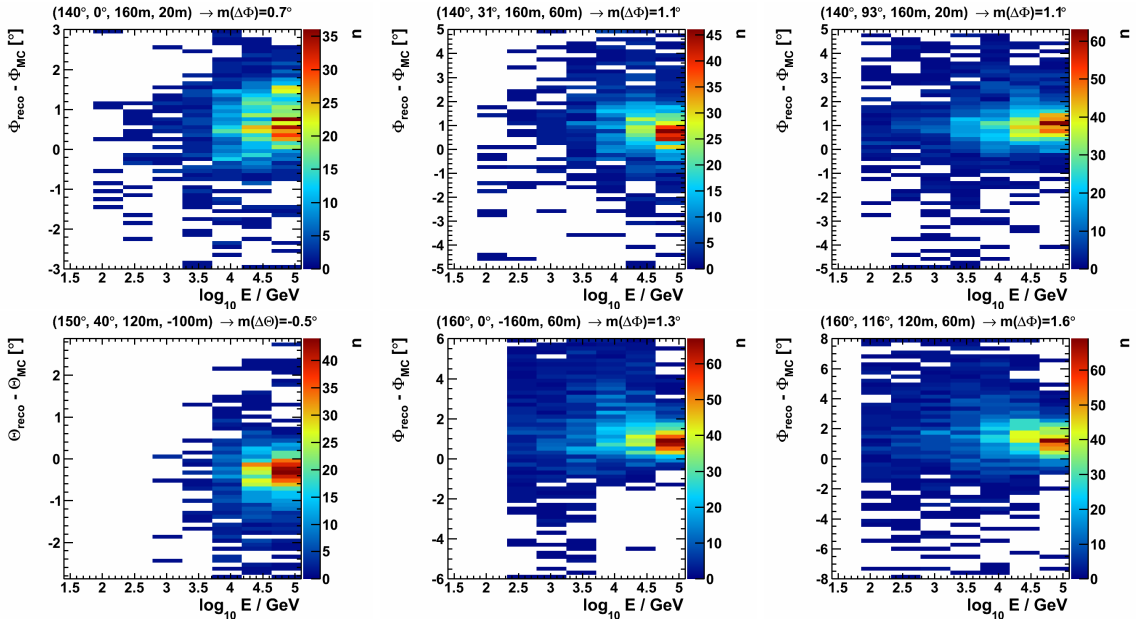

FIGURE A.2.: More examples of reported systematics as given in Table A.1. Events are shown that pass the selection $\Lambda > -5.4$ and $\beta < 1^\circ$.

B. Background

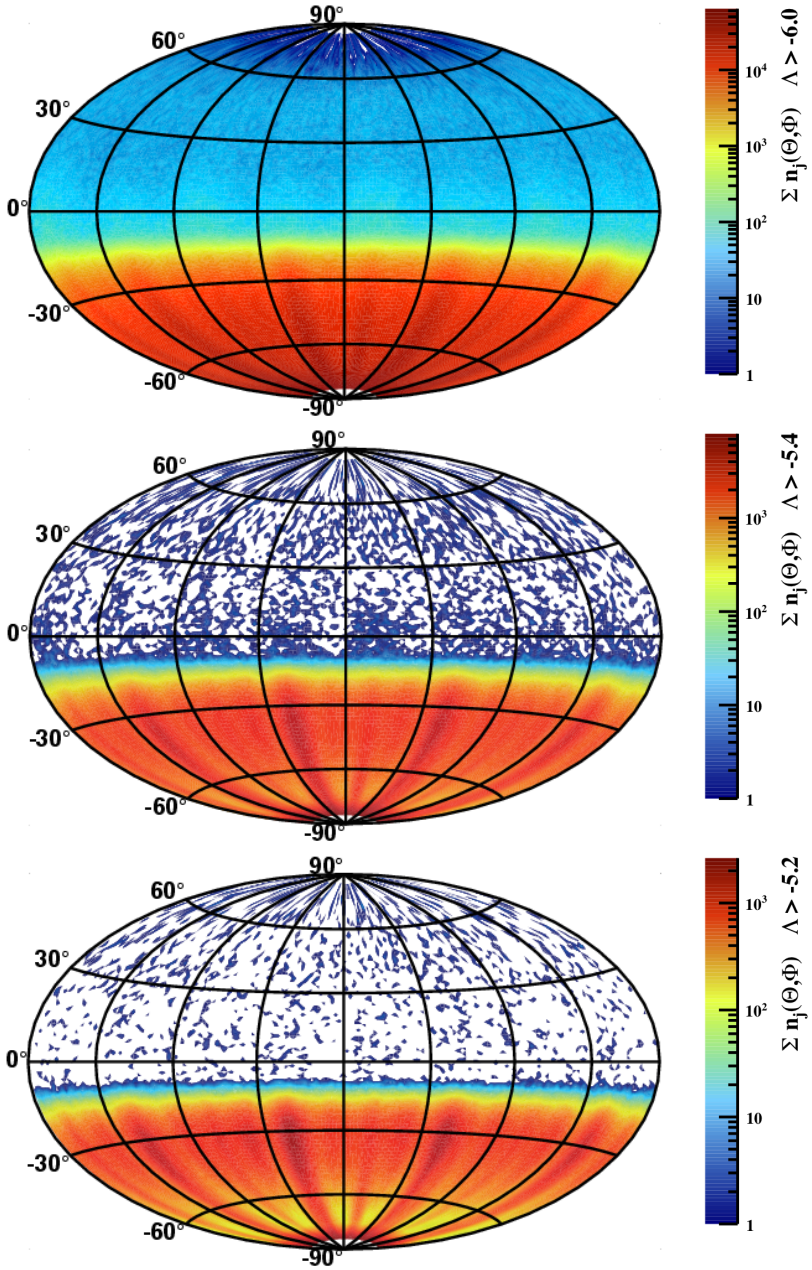

Figure B.1.: All data events $\sum n_j(\Theta, \Phi)$ in the Antares data-taking period from December 7, 2007 to December 31, 2011, used to evaluate the mean rate in the GRB's direction (see Equation 6.2). For $\beta < 1^\circ, \Lambda > -6.0, -5.4, -5.2$ *(upper to lower panel)*, respectively.

Λ_{cut}	—- 5 line —-		—- 12 line —-	
	$\sum n_j$	$\sum n_j / \sum t_j$ (1/s)	$\sum n_j$	$\sum n_j / \sum t_j$ (1/s)
-7.0	$1.12 \cdot 10^7$	0.563	$3.34 \cdot 10^8$	4.257
-6.9	$1.11 \cdot 10^7$	0.556	$3.12 \cdot 10^8$	3.983
-6.8	$1.09 \cdot 10^7$	0.547	$2.90 \cdot 10^8$	3.695
-6.7	$1.06 \cdot 10^7$	0.534	$2.67 \cdot 10^8$	3.407
-6.6	$1.03 \cdot 10^7$	0.516	$2.45 \cdot 10^8$	3.120
-6.5	$9.76 \cdot 10^6$	0.491	$2.21 \cdot 10^8$	2.823
-6.4	$9.12 \cdot 10^6$	0.459	$1.97 \cdot 10^8$	2.508
-6.3	$8.34 \cdot 10^6$	0.419	$1.71 \cdot 10^8$	2.180
-6.2	$7.42 \cdot 10^6$	0.373	$1.45 \cdot 10^8$	1.847
-6.1	$6.40 \cdot 10^6$	0.322	$1.19 \cdot 10^8$	1.519
-6.0	$5.32 \cdot 10^6$	0.268	$9.48 \cdot 10^7$	1.209
-5.9	$4.26 \cdot 10^6$	0.214	$7.26 \cdot 10^7$	0.926
-5.8	$3.26 \cdot 10^6$	0.164	$5.33 \cdot 10^7$	0.680
-5.7	$2.39 \cdot 10^6$	0.120	$3.74 \cdot 10^7$	0.477
-5.6	$1.67 \cdot 10^6$	0.084	$2.52 \cdot 10^7$	0.321
-5.5	$1.12 \cdot 10^6$	0.056	$1.63 \cdot 10^7$	0.208
-5.4	$7.24 \cdot 10^5$	0.036	$1.03 \cdot 10^7$	0.131
-5.3	$4.54 \cdot 10^5$	0.023	$6.32 \cdot 10^6$	0.081
-5.2	$2.76 \cdot 10^5$	0.014	$3.81 \cdot 10^6$	0.049
-5.1	$1.64 \cdot 10^5$	0.008	$2.24 \cdot 10^6$	0.029
-5.0	$9.37 \cdot 10^4$	0.005	$1.29 \cdot 10^6$	0.016

TABLE B.1.: Number of data events n in all directions and all data-taking runs j, applying varying reconstruction quality cuts Λ_{cut}, with fixed $\beta < 1^\circ$. Two detector configurations are distinguished: The period from January 27 to December 7, 2007, where the first five detection strings have been deployed is denoted *5–line*, and the period from December 7, 2007, where the detector has been completed to the full *12-line* configuration, to December 31, 2011. The mean rate of events in all directions $\sum n_j / \sum t_j$ (as used to calculate the correction factor c_i in Equation 6.2) in the two configurations is also given, evaluated on a total livetime of the according data $\sum t_j$ of 230.2 days (*5–line)* and 907.5 days (*12–line)*, respectively. Note that only the *12–line* period is considered in the analysis presented in Section 6.

Λ_{cut}	$n^{\text{all}}_{\text{meas}}$	$n^{\text{all}}_{\text{meas}}/t$ (1/s)	$n^{\text{up}}_{\text{meas}}$	c_i	$n^{\text{up}}_{\text{exp}}$	$n^{\text{up}}_{\text{exp}}$ / t (1/s)	$(n^{\text{up}}_{\text{meas}} - n^{\text{up}}_{\text{exp}})/n^{\text{up}}_{\text{exp}}$
-7	90848	2.16	$5.21 \cdot 10^3$	0.509	$5.8 \cdot 10^3$	0.138	-0.103
-6.9	$8.77 \cdot 10^4$	2.08	$4.43 \cdot 10^3$	0.525	$3.96 \cdot 10^3$	0.0942	0.117
-6.8	$8.35 \cdot 10^4$	1.98	$3.47 \cdot 10^3$	0.539	$2.56 \cdot 10^3$	0.0607	0.358
-6.7	$7.82 \cdot 10^4$	1.86	$2.43 \cdot 10^3$	0.547	$1.61 \cdot 10^3$	0.0383	0.505
-6.6	$7.18 \cdot 10^4$	1.71	$1.66 \cdot 10^3$	0.549	$1.02 \cdot 10^3$	0.0242	0.629
-6.5	$6.46 \cdot 10^4$	1.53	$1.13 \cdot 10^3$	0.546	645	0.0153	0.753
-6.4	$5.68 \cdot 10^4$	1.35	831	0.541	405	0.00963	1.05
-6.3	$4.85 \cdot 10^4$	1.15	636	0.531	249	0.00591	1.55
-6.2	$3.94 \cdot 10^4$	0.936	212	0.51	147	0.00348	0.447
-6.1	$3.12 \cdot 10^4$	0.74	135	0.491	84.6	0.00201	0.595
-6	$2.35 \cdot 10^4$	0.558	76	0.465	47.1	0.00112	0.612
-5.9	$1.69 \cdot 10^4$	0.4	40	0.437	25.1	0.000597	0.592
-5.8	$1.15 \cdot 10^4$	0.273	22	0.407	13	0.000308	0.697
-5.7	$7.39 \cdot 10^3$	0.176	11	0.373	6.44	0.000153	0.709
-5.6	$4.59 \cdot 10^3$	0.109	9	0.346	3.3	$7.83 \cdot 10^{-5}$	1.73
-5.5	$2.7 \cdot 10^3$	0.064	5	0.315	1.8	$4.26 \cdot 10^{-5}$	1.79
-5.4	$1.57 \cdot 10^3$	0.0372	2	0.293	1.12	$2.66 \cdot 10^{-5}$	0.788
-5.3	910	0.0216	1	0.279	0.778	$1.85 \cdot 10^{-5}$	0.285
-5.2	512	0.0122	1	0.265	0.569	$1.35 \cdot 10^{-5}$	0.759
-5.1	293	0.00696	1	0.262	0.449	$1.07 \cdot 10^{-5}$	1.23
-5	158	0.00375	1	0.251	0.342	$8.11 \cdot 10^{-6}$	1.93

TABLE B.2.: Estimations on the uncertainty on the background rate for the ANTARES data run 70515 coincident with GRB130427, selecting data reconstruction quality of $\Lambda_{\text{cut}} \in [-7.0, -5.0]$ and $\beta < 1^\circ$. The instantaneous efficiency c_i is derived according to Equation 6.2. The expected number of upgoing data events with this correction $n^{\text{up}}_{\text{exp}}$ is then compared to the observed number $n^{\text{up}}_{\text{meas}}$ in the run. Their ratio gives an estimation on the error introduced by using Equation 6.2 to estimate the background. To comply with the ANTARES blinding policy, a conservative window of ± 15 min around the GRB has been excluded. Using Equation 6.2, the number of events is overestimated by at most a factor of 2.9, so a conservative uncertainty of 3 is assumed in the background calculation.

C. Gamma-Ray-Bursts Catalogue late-2007–2011

Table C.1.: Optimization results for all gamma-ray bursts selected for the search from late-2007 to 2011 (see Section 6). For each of them, the equatorial coordinates RA and δ are given with the size of the error box Δ_{err}, the measured photon fluence $\mathcal{F}_\gamma$, the defined search time window T_{search} and the measured redshift. Optimised Λ_{cut} and the resulting expected number of background and signal events μ_{b} and μ_{s} at the 3σ significance level. The corresponding median angular spread of events $m(\alpha)$ is also provided. In the last rows, the sum and mean of the values (without default values) for all 296 GRBs at the 3σ level are given. The model discovery potential for the entire sample is 5.7% (see Equation 6.9). The naming convention for the GRBs is similar to that used by *Fermi*, the last two digits of the GRB name correspond to the fraction of the day at which the burst occurred. The table is also available in electronic form at the CDS via anonymous ftp to cdsarc.u-strasbg.fr (130.79.128.5) or via `http://cdsarc.u-strasbg.fr/viz-bin/qcat?J/A+A/559/A9`.

GRB	RA (°)	δ (°)	Δ_{err} (°)	$\mathcal{F}$ (erg cm^{-2})	T_{search} (s)	z	Λ_{cut}	μ_{b}	$\mu_{\text{s}}^{\text{NeuCosmA}}$	$\mu_{\text{s}}^{\text{Guetta}}$	$m(\alpha)$ (°)	$\mathcal{MDP}_i^{296}$
07122784	58.13	-55.98	$1.67 \cdot 10^{-4}$	$5.05 \cdot 10^{-7}$	161	0.38	-5.7	$3.78 \cdot 10^{-3}$	$1.60 \cdot 10^{-9}$	$6.03 \cdot 10^{-10}$	0.40	$9.12 \cdot 10^{-6}$
08020789	207.51	7.50	$8.06 \cdot 10^{-4}$	$6.10 \cdot 10^{-6}$	468	2.09	-5.3	$2.16 \cdot 10^{-3}$	$3.93 \cdot 10^{-5}$	$3.32 \cdot 10^{-4}$	0.36	$3.99 \cdot 10^{-5}$
08021273	231.15	-22.74	$5.56 \cdot 10^{-4}$	$3.05 \cdot 10^{-6}$	152	2.15	-5.5	$4.08 \cdot 10^{-4}$	$6.08 \cdot 10^{-6}$	$7.55 \cdot 10^{-3}$	0.28	$1.46 \cdot 10^{-5}$
08021899	177.96	-53.10	$6.67 \cdot 10^{-4}$	$4.97 \cdot 10^{-7}$	11	2.15	-5.6	$1.54 \cdot 10^{-4}$	$1.21 \cdot 10^{-5}$	$2.95 \cdot 10^{-3}$	0.38	$2.06 \cdot 10^{-5}$
08022971	228.22	-14.70	$3.89 \cdot 10^{-4}$	$9.10 \cdot 10^{-6}$	100	2.15	-5.5	$3.67 \cdot 10^{-4}$	$2.83 \cdot 10^{-5}$	$1.68 \cdot 10^{-4}$	0.29	$3.48 \cdot 10^{-5}$
08030338	112.06	-70.23	$1.67 \cdot 10^{-4}$	$6.68 \cdot 10^{-7}$	78	2.15	-5.4	$2.33 \cdot 10^{-4}$	$2.09 \cdot 10^{-6}$	$2.21 \cdot 10^{-5}$	0.26	$1.11 \cdot 10^{-5}$
08030747	136.63	35.14	$5.00 \cdot 10^{-4}$	$9.27 \cdot 10^{-7}$	145	2.15	-5.4	$5.81 \cdot 10^{-4}$	$2.98 \cdot 10^{-5}$	$1.85 \cdot 10^{-4}$	0.44	$3.47 \cdot 10^{-5}$
08040538	162.60	-4.29	$1.97 \cdot 10^{-3}$	$1.20 \cdot 10^{-6}$	122	2.15	-5.5	$3.24 \cdot 10^{-4}$	$8.91 \cdot 10^{-6}$	$1.32 \cdot 10^{-4}$	0.36	$1.72 \cdot 10^{-5}$
08040905	84.33	5.08	$5.56 \cdot 10^{-4}$	$5.62 \cdot 10^{-7}$	28	2.15	-5.6	$1.22 \cdot 10^{-4}$	$4.55 \cdot 10^{-6}$	$3.35 \cdot 10^{-4}$	0.40	$1.34 \cdot 10^{-5}$
08041188	37.98	-71.30	$1.39 \cdot 10^{-4}$	$2.65 \cdot 10^{-5}$	82	1.03	-5.5	$1.94 \cdot 10^{-4}$	$4.13 \cdot 10^{-5}$	$1.62 \cdot 10^{-4}$	0.34	$4.75 \cdot 10^{-5}$
08052389	20.80	-64.03	$4.17 \cdot 10^{-4}$	$7.25 \cdot 10^{-7}$	52	2.15	-5.5	$8.55 \cdot 10^{-5}$	$1.27 \cdot 10^{-6}$	$6.66 \cdot 10^{-4}$	0.31	$1.03 \cdot 10^{-5}$
08060206	19.18	-9.23	$4.72 \cdot 10^{-4}$	$3.26 \cdot 10^{-6}$	85	2.15	-5.4	$3.06 \cdot 10^{-4}$	$1.08 \cdot 10^{-4}$	$1.34 \cdot 10^{-3}$	0.32	$1.12 \cdot 10^{-4}$
08060431	236.97	20.56	$1.39 \cdot 10^{-4}$	$7.89 \cdot 10^{-7}$	91	1.42	-5.4	$2.93 \cdot 10^{-4}$	$7.00 \cdot 10^{-7}$	$1.19 \cdot 10^{-6}$	0.31	$9.78 \cdot 10^{-6}$
08060725	194.95	15.92	$1.39 \cdot 10^{-4}$	$2.47 \cdot 10^{-5}$	164	3.04	-5.4	$5.53 \cdot 10^{-4}$	$6.51 \cdot 10^{-3}$	$1.44 \cdot 10^{-2}$	0.33	$5.94 \cdot 10^{-3}$
08061346	173.80	-7.11	$6.39 \cdot 10^{-4}$	$5.71 \cdot 10^{-6}$	139	2.15	-5.4	$5.43 \cdot 10^{-4}$	$2.03 \cdot 10^{-4}$	$2.24 \cdot 10^{-3}$	0.32	$1.95 \cdot 10^{-4}$
08091236	25.80	-7.20	7.10	$2.13 \cdot 10^{-6}$	30	2.15	-5.1	$2.97 \cdot 10^{-5}$	$1.99 \cdot 10^{-5}$	$1.41 \cdot 10^{-4}$	4.64	$2.18 \cdot 10^{-5}$
08091373	45.10	-3.00	5.90	$3.54 \cdot 10^{-6}$	70	2.15	-5.0	$9.98 \cdot 10^{-5}$	$1.27 \cdot 10^{-5}$	$1.91 \cdot 10^{-3}$	4.07	$1.45 \cdot 10^{-5}$
08091500	17.95	-76.02	$1.81 \cdot 10^{-3}$	$2.91 \cdot 10^{-7}$	33	2.15	-5.6	$1.09 \cdot 10^{-4}$	$4.49 \cdot 10^{-6}$	$3.82 \cdot 10^{-5}$	0.33	$1.35 \cdot 10^{-5}$
08092476	72.80	32.50	4.40	$4.73 \cdot 10^{-6}$	68	2.15	-5.2	$9.29 \cdot 10^{-5}$	$6.61 \cdot 10^{-5}$	$6.22 \cdot 10^{-4}$	3.05	$4.44 \cdot 10^{-5}$
08092577	96.10	18.20	1.20	$1.85 \cdot 10^{-5}$	55	2.15	-5.5	$1.22 \cdot 10^{-4}$	$1.35 \cdot 10^{-4}$	$2.51 \cdot 10^{-3}$	1.10	$1.35 \cdot 10^{-4}$
08092748	61.30	27.40	4.60	$2.96 \cdot 10^{-6}$	77	2.15	-5.1	$6.51 \cdot 10^{-5}$	$3.77 \cdot 10^{-5}$	$7.58 \cdot 10^{-4}$	3.30	$3.21 \cdot 10^{-5}$
08092862	95.07	-55.20	$1.39 \cdot 10^{-4}$	$1.17 \cdot 10^{-6}$	27	1.69	-5.8	$2.07 \cdot 10^{-4}$	$3.37 \cdot 10^{-7}$	$1.01 \cdot 10^{-6}$	0.33	$9.42 \cdot 10^{-6}$
08100687	172.20	-61.00	8.70	$3.87 \cdot 10^{-7}$	9	2.15	-5.3	$1.65 \cdot 10^{-5}$	$4.12 \cdot 10^{-7}$	$3.20 \cdot 10^{-6}$	6.69	$9.43 \cdot 10^{-6}$
08100883	279.96	-57.43	$1.67 \cdot 10^{-4}$	$1.03 \cdot 10^{-5}$	244	1.97	-5.5	$6.25 \cdot 10^{-4}$	$2.25 \cdot 10^{-5}$	$4.14 \cdot 10^{-4}$	0.32	$2.95 \cdot 10^{-5}$
08100914	250.50	18.40	1.00	$3.83 \cdot 10^{-5}$	70	2.15	-5.5	$1.20 \cdot 10^{-4}$	$3.47 \cdot 10^{-4}$	$1.89 \cdot 10^{-3}$	0.94	$3.40 \cdot 10^{-4}$
08100969	64.60	14.20	2.10	$1.08 \cdot 10^{-5}$	286	2.15	-5.4	$1.08 \cdot 10^{-4}$	$7.28 \cdot 10^{-5}$	$1.66 \cdot 10^{-3}$	1.68	$7.14 \cdot 10^{-5}$
08101102	220.34	33.54	$4.17 \cdot 10^{-4}$	$1.69 \cdot 10^{-7}$	15	2.15	-5.7	$2.10 \cdot 10^{-4}$	$5.30 \cdot 10^{-6}$	$5.00 \cdot 10^{-5}$	0.37	$1.41 \cdot 10^{-5}$
08101254	30.20	-17.64	$5.00 \cdot 10^{-4}$	$4.51 \cdot 10^{-6}$	53	2.15	-5.5	$2.21 \cdot 10^{-4}$	$1.11 \cdot 10^{-5}$	$2.45 \cdot 10^{-3}$	0.28	$1.94 \cdot 10^{-5}$
08101682	14.56	-43.53	$5.83 \cdot 10^{-4}$	$1.08 \cdot 10^{-7}$	7	2.15	-5.6	$1.41 \cdot 10^{-4}$	$8.42 \cdot 10^{-6}$	$2.18 \cdot 10^{-4}$	0.36	$1.72 \cdot 10^{-5}$
08101628	255.57	-23.34	$1.00 \cdot 10^{-3}$	$1.80 \cdot 10^{-6}$	38	2.15	-5.5	$2.61 \cdot 10^{-4}$	$2.93 \cdot 10^{-5}$	$7.03 \cdot 10^{-4}$	0.34	$3.66 \cdot 10^{-5}$
08101747	109.00	-15.20	8.00	$1.39 \cdot 10^{-6}$	49	2.15	-5.1	$8.85 \cdot 10^{-5}$	$1.16 \cdot 10^{-5}$	$2.76 \cdot 10^{-4}$	5.42	$1.35 \cdot 10^{-5}$
08101798	230.21	-32.79	0.04	$1.42 \cdot 10^{-6}$	324	2.15	-5.3	$1.18 \cdot 10^{-3}$	$3.03 \cdot 10^{-6}$	$2.39 \cdot 10^{-5}$	0.23	$1.17 \cdot 10^{-5}$
08102485	145.80	-10.80	4.50	$6.27 \cdot 10^{-6}$	94	2.15	-5.2	$1.02 \cdot 10^{-4}$	$1.41 \cdot 10^{-5}$	$3.00 \cdot 10^{-4}$	3.02	$1.66 \cdot 10^{-5}$
08102853	16.00	-27.20	6.90	$2.27 \cdot 10^{-6}$	25	2.15	-5.0	$2.24 \cdot 10^{-5}$	$4.18 \cdot 10^{-6}$	$1.69 \cdot 10^{-4}$	4.77	$1.22 \cdot 10^{-5}$
08110439	100.49	-54.72	$4.44 \cdot 10^{-4}$	$2.10 \cdot 10^{-6}$	85	2.15	-5.5	$2.16 \cdot 10^{-4}$	$2.39 \cdot 10^{-5}$	$1.22 \cdot 10^{-4}$	0.33	$3.18 \cdot 10^{-5}$
08110929	330.79	-54.71	$2.22 \cdot 10^{-4}$	$6.55 \cdot 10^{-6}$	97	2.15	-5.5	$3.88 \cdot 10^{-4}$	$7.79 \cdot 10^{-6}$	$4.82 \cdot 10^{-5}$	0.31	$1.59 \cdot 10^{-5}$
08111060	111.70	21.40	1.80	$5.41 \cdot 10^{-6}$	23	2.15	-5.4	$7.47 \cdot 10^{-5}$	$4.83 \cdot 10^{-5}$	$1.28 \cdot 10^{-3}$	1.52	$5.37 \cdot 10^{-5}$
08111887	54.60	-43.30	3.60	$4.94 \cdot 10^{-6}$	37	2.15	-5.3	$9.41 \cdot 10^{-5}$	$9.97 \cdot 10^{-5}$	$1.03 \cdot 10^{-3}$	2.63	$7.25 \cdot 10^{-5}$
08111862	82.59	-43.30	$5.56 \cdot 10^{-4}$	$1.15 \cdot 10^{-6}$	64	2.58	-5.4	$1.89 \cdot 10^{-4}$	$1.07 \cdot 10^{-6}$	$8.01 \cdot 10^{-7}$	0.24	$1.01 \cdot 10^{-5}$
08112061	205.40	-9.10	6.00	$1.94 \cdot 10^{-6}$	45	2.15	-5.2	$9.50 \cdot 10^{-5}$	$5.10 \cdot 10^{-5}$	$3.72 \cdot 10^{-4}$	4.05	$3.17 \cdot 10^{-5}$
08112185	89.28	-60.60	$1.67 \cdot 10^{-4}$	$1.53 \cdot 10^{-5}$	71	2.51	-5.5	$3.95 \cdot 10^{-4}$	$3.49 \cdot 10^{-4}$	$4.22 \cdot 10^{-3}$	0.33	$3.31 \cdot 10^{-4}$
08112406	340.10	-14.60	2.50	$8.59 \cdot 10^{-6}$	35	2.15	-5.2	$7.93 \cdot 10^{-5}$	$1.88 \cdot 10^{-4}$	$5.39 \cdot 10^{-4}$	1.92	$1.71 \cdot 10^{-4}$
08112549	42.70	-18.90	1.00	$1.85 \cdot 10^{-5}$	19	2.15	-5.5	$1.12 \cdot 10^{-4}$	$4.63 \cdot 10^{-5}$	$8.29 \cdot 10^{-4}$	0.99	$5.32 \cdot 10^{-5}$
08112729	332.06	6.85	$4.72 \cdot 10^{-4}$	$4.02 \cdot 10^{-7}$	23	2.15	-5.5	$1.31 \cdot 10^{-4}$	$5.84 \cdot 10^{-6}$	$2.59 \cdot 10^{-5}$	0.33	$1.47 \cdot 10^{-5}$
08120400	63.30	-62.60	4.80	$1.02 \cdot 10^{-6}$	16	2.15	-5.2	$3.20 \cdot 10^{-5}$	$1.02 \cdot 10^{-5}$	$3.78 \cdot 10^{-4}$	3.26	$1.66 \cdot 10^{-5}$
08121149	328.12	-33.84	$1.94 \cdot 10^{-4}$	$1.30 \cdot 10^{-7}$	8	2.15	-5.7	$1.84 \cdot 10^{-4}$	$1.07 \cdot 10^{-5}$	$3.24 \cdot 10^{-5}$	0.37	$1.92 \cdot 10^{-5}$

TABLE C.1.: Optimization results for all gamma-ray bursts selected from late-2007 to 2011 (cont.)

GRB	RA (°)	δ (°)	Δ_{err} (°)	$\mathcal{F}_\gamma$ (erg cm^{-2})	T_{search} (s)	z	Λ_{cut}	μ_{b}	$\mu_{\text{s}}^{\text{NeuCosmA}}$	$\mu_{\text{s}}^{\text{Guetta}}$	$m(\alpha)$ (°)	$\mathcal{MDP}_i^{296}$
08122220	22.74	-34.09	$1.39 \cdot 10^{-4}$	$1.19 \cdot 10^{-5}$	34	2.77	-5.6	$1.55 \cdot 10^{-4}$	$1.44 \cdot 10^{-4}$	$8.21 \cdot 10^{-4}$	0.28	$1.44 \cdot 10^{-4}$
08122525	234.10	-64.60	6.90	$6.75 \cdot 10^{-6}$	70	2.15	-5.0	$6.35 \cdot 10^{-5}$	$2.82 \cdot 10^{-5}$	$3.83 \cdot 10^{-4}$	4.65	$2.26 \cdot 10^{-5}$
09010175	77.80	-31.60	1.20	$1.23 \cdot 10^{-5}$	178	2.15	-5.3	$3.07 \cdot 10^{-4}$	$2.47 \cdot 10^{-4}$	$3.09 \cdot 10^{-3}$	0.97	$2.18 \cdot 10^{-4}$
09011199	251.68	0.08	$4.72 \cdot 10^{-4}$	$6.66 \cdot 10^{-7}$	33	2.15	-5.5	$1.95 \cdot 10^{-4}$	$1.41 \cdot 10^{-5}$	$4.58 \cdot 10^{-5}$	0.32	$2.25 \cdot 10^{-5}$
09011233	110.90	-30.40	1.00	$3.92 \cdot 10^{-6}$	97	2.15	-5.2	$2.66 \cdot 10^{-4}$	$1.20 \cdot 10^{-5}$	$1.43 \cdot 10^{-4}$	0.93	$1.98 \cdot 10^{-5}$
09011763	121.60	-38.80	1.90	$1.19 \cdot 10^{-5}$	125	2.15	-5.2	$3.80 \cdot 10^{-4}$	$3.07 \cdot 10^{-5}$	$3.65 \cdot 10^{-4}$	1.52	$2.76 \cdot 10^{-5}$
09011764	164.04	-58.23	$6.67 \cdot 10^{-4}$	$2.53 \cdot 10^{-6}$	29	2.15	-5.7	$1.55 \cdot 10^{-4}$	$3.24 \cdot 10^{-6}$	$7.67 \cdot 10^{-6}$	0.34	$1.20 \cdot 10^{-5}$
09012332	6.79	-23.50	$1.39 \cdot 10^{-4}$	$2.90 \cdot 10^{-6}$	177	2.15	-5.4	$3.27 \cdot 10^{-4}$	$2.82 \cdot 10^{-5}$	$2.43 \cdot 10^{-4}$	0.33	$3.55 \cdot 10^{-5}$
09012988	269.11	-32.79	0.02	$5.57 \cdot 10^{-6}$	31	2.15	-5.6	$4.16 \cdot 10^{-5}$	$3.48 \cdot 10^{-6}$	$3.75 \cdot 10^{-5}$	0.31	$1.24 \cdot 10^{-5}$
09013109	352.30	21.20	1.00	$1.75 \cdot 10^{-5}$	60	2.15	-5.5	$1.21 \cdot 10^{-4}$	$1.43 \cdot 10^{-4}$	$1.56 \cdot 10^{-3}$	1.00	$1.43 \cdot 10^{-4}$
09020174	92.05	-46.59	$3.89 \cdot 10^{-4}$	$3.14 \cdot 10^{-5}$	127	2.15	-5.4	$5.33 \cdot 10^{-4}$	$7.03 \cdot 10^{-4}$	$2.40 \cdot 10^{-2}$	0.39	$6.44 \cdot 10^{-4}$
09020596	220.91	-27.85	$5.00 \cdot 10^{-4}$	$1.73 \cdot 10^{-7}$	14	4.65	-5.6	$1.35 \cdot 10^{-4}$	$4.68 \cdot 10^{-6}$	$5.78 \cdot 10^{-4}$	0.44	$1.35 \cdot 10^{-5}$
09020777	252.70	34.90	3.80	$2.41 \cdot 10^{-6}$	44	2.15	-5.1	$8.47 \cdot 10^{-5}$	$1.86 \cdot 10^{-5}$	$2.48 \cdot 10^{-4}$	2.64	$2.11 \cdot 10^{-5}$
09021323	330.60	-55.00	3.10	$1.10 \cdot 10^{-6}$	36	2.15	-5.3	$4.74 \cdot 10^{-5}$	$5.11 \cdot 10^{-6}$	$1.20 \cdot 10^{-4}$	2.44	$1.33 \cdot 10^{-5}$
09022731	3.30	-43.00	1.20	$2.86 \cdot 10^{-6}$	30	2.15	-5.5	$1.10 \cdot 10^{-4}$	$2.98 \cdot 10^{-5}$	$2.95 \cdot 10^{-4}$	1.17	$3.66 \cdot 10^{-5}$
09022897	357.60	36.70	3.30	$9.64 \cdot 10^{-7}$	17	2.15	-5.3	$3.02 \cdot 10^{-5}$	$1.04 \cdot 10^{-5}$	$3.46 \cdot 10^{-4}$	2.47	$1.82 \cdot 10^{-5}$
09030421	195.90	-73.40	12.30	$8.99 \cdot 10^{-7}$	9	2.15	-5.0	$9.08 \cdot 10^{-6}$	$2.46 \cdot 10^{-6}$	$2.57 \cdot 10^{-5}$	8.26	$1.15 \cdot 10^{-5}$
09031962	283.30	-8.90	2.60	$6.03 \cdot 10^{-6}$	92	2.15	-5.6	$3.62 \cdot 10^{-5}$	$2.36 \cdot 10^{-5}$	$6.12 \cdot 10^{-4}$	2.14	$3.11 \cdot 10^{-5}$
09050921	241.42	-28.39	0.04	$5.42 \cdot 10^{-6}$	458	2.15	-5.6	$3.25 \cdot 10^{-4}$	$4.77 \cdot 10^{-5}$	$9.07 \cdot 10^{-4}$	0.33	$5.44 \cdot 10^{-5}$
09051032	269.40	-57.90	11.60	$5.60 \cdot 10^{-7}$	16	2.15	-5.2	$9.17 \cdot 10^{-6}$	$2.48 \cdot 10^{-6}$	$3.77 \cdot 10^{-5}$	8.46	$1.15 \cdot 10^{-5}$
09051391	269.80	-31.60	4.60	$4.94 \cdot 10^{-6}$	44	2.15	-5.4	$1.04 \cdot 10^{-5}$	$2.11 \cdot 10^{-5}$	$2.96 \cdot 10^{-4}$	3.38	$2.97 \cdot 10^{-5}$
09051394	99.10	-72.90	8.80	$1.04 \cdot 10^{-6}$	23	2.15	-5.6	$1.37 \cdot 10^{-5}$	$1.46 \cdot 10^{-6}$	$1.10 \cdot 10^{-5}$	7.29	$1.03 \cdot 10^{-5}$
09051400	12.30	-10.90	4.60	$6.46 \cdot 10^{-6}$	74	2.15	-5.4	$1.46 \cdot 10^{-5}$	$1.91 \cdot 10^{-5}$	$1.03 \cdot 10^{-4}$	3.48	$2.67 \cdot 10^{-5}$
09051472	304.32	-24.40	5.47	$2.25 \cdot 10^{-6}$	8	2.15	-5.8	$1.78 \cdot 10^{-5}$	$2.47 \cdot 10^{-6}$	$6.83 \cdot 10^{-5}$	4.68	$1.11 \cdot 10^{-5}$
09051473	316.03	-43.97	15.17	$9.55 \cdot 10^{-6}$	91	2.15	-5.4	$1.93 \cdot 10^{-5}$	$1.78 \cdot 10^{-6}$	$2.89 \cdot 10^{-5}$	10.93	$1.04 \cdot 10^{-5}$
09051946	105.90	-56.70	3.90	$4.38 \cdot 10^{-6}$	150	2.15	-5.3	$3.24 \cdot 10^{-5}$	$2.24 \cdot 10^{-5}$	$1.07 \cdot 10^{-3}$	2.82	$2.75 \cdot 10^{-5}$
09052085	111.20	-19.70	1.20	$3.32 \cdot 10^{-6}$	10	2.15	-5.7	$7.36 \cdot 10^{-5}$	$3.33 \cdot 10^{-5}$	$1.05 \cdot 10^{-3}$	1.14	$4.09 \cdot 10^{-5}$
09052006	11.61	-8.00	0.05	$3.40 \cdot 10^{-7}$	73	2.15	-5.6	$2.49 \cdot 10^{-4}$	$1.43 \cdot 10^{-5}$	$3.81 \cdot 10^{-4}$	0.40	$2.23 \cdot 10^{-5}$
09053177	252.07	-36.03	$9.44 \cdot 10^{-4}$	$3.18 \cdot 10^{-7}$	132	2.15	-5.4	$2.97 \cdot 10^{-4}$	$3.44 \cdot 10^{-6}$	$4.72 \cdot 10^{-5}$	0.45	$1.23 \cdot 10^{-5}$
09060647	146.94	-70.49	5.55	$9.46 \cdot 10^{-7}$	17	2.15	-5.1	$2.18 \cdot 10^{-5}$	$3.30 \cdot 10^{-6}$	$2.74 \cdot 10^{-5}$	3.80	$1.17 \cdot 10^{-5}$
09060805	100.19	-37.41	4.52	$1.24 \cdot 10^{-6}$	38	2.15	-5.3	$1.14 \cdot 10^{-5}$	$7.04 \cdot 10^{-7}$	$3.47 \cdot 10^{-6}$	3.60	$9.79 \cdot 10^{-6}$
09061072	275.99	-42.09	9.50	$3.96 \cdot 10^{-6}$	236	2.15	-5.0	$2.78 \cdot 10^{-4}$	$7.55 \cdot 10^{-6}$	$3.93 \cdot 10^{-4}$	6.48	$1.07 \cdot 10^{-5}$
09061088	70.37	30.30	8.17	$7.64 \cdot 10^{-7}$	16	2.15	-5.1	$1.38 \cdot 10^{-5}$	$5.16 \cdot 10^{-6}$	$4.11 \cdot 10^{-5}$	5.76	$1.34 \cdot 10^{-5}$
09062618	169.30	-36.05	1.00	$6.30 \cdot 10^{-5}$	82	2.15	-5.4	$2.30 \cdot 10^{-4}$	$5.61 \cdot 10^{-5}$	$1.65 \cdot 10^{-3}$	1.10	$5.47 \cdot 10^{-5}$
09063031	146.55	-46.58	5.80	$1.08 \cdot 10^{-6}$	9	2.15	-5.1	$1.54 \cdot 10^{-5}$	$3.41 \cdot 10^{-6}$	$3.73 \cdot 10^{-5}$	4.13	$1.21 \cdot 10^{-5}$
09070424	208.21	22.79	0.03	$8.48 \cdot 10^{-6}$	116	2.15	-5.5	$2.28 \cdot 10^{-4}$	$5.18 \cdot 10^{-5}$	$6.99 \cdot 10^{-4}$	0.41	$5.73 \cdot 10^{-5}$
09070628	205.07	-47.07	3.01	$7.47 \cdot 10^{-6}$	196	2.15	-5.0	$1.24 \cdot 10^{-4}$	$3.68 \cdot 10^{-6}$	$1.68 \cdot 10^{-5}$	2.40	$1.15 \cdot 10^{-5}$
09071876	274.12	-36.39	1.18	$2.50 \cdot 10^{-5}$	42	2.15	-5.6	$9.88 \cdot 10^{-5}$	$2.93 \cdot 10^{-4}$	$3.74 \cdot 10^{-3}$	1.16	$2.90 \cdot 10^{-4}$
09071906	341.27	-67.86	1.00	$4.68 \cdot 10^{-5}$	22	2.15	-5.7	$7.81 \cdot 10^{-5}$	$2.70 \cdot 10^{-4}$	$1.01 \cdot 10^{-2}$	1.10	$2.65 \cdot 10^{-4}$
09072027	203.68	-10.33	$8.33 \cdot 10^{-4}$	$3.22 \cdot 10^{-6}$	10	2.15	-5.7	$2.84 \cdot 10^{-5}$	$6.76 \cdot 10^{-6}$	$5.87 \cdot 10^{-4}$	0.37	$1.57 \cdot 10^{-5}$
09072071	203.00	-54.80	2.91	$1.42 \cdot 10^{-5}$	21	2.15	-5.5	$2.59 \cdot 10^{-5}$	$1.29 \cdot 10^{-4}$	$1.01 \cdot 10^{-3}$	2.32	$1.30 \cdot 10^{-4}$
09072583	281.88	-69.49	6.60	$2.36 \cdot 10^{-6}$	26	2.15	-5.3	$1.17 \cdot 10^{-5}$	$1.13 \cdot 10^{-5}$	$1.56 \cdot 10^{-34}$	4.40	$1.96 \cdot 10^{-5}$
09080997	95.25	0.16	1.20	$2.16 \cdot 10^{-5}$	22	2.15	-5.6	$6.59 \cdot 10^{-5}$	$1.05 \cdot 10^{-4}$	$2.57 \cdot 10^{-3}$	1.19	$1.09 \cdot 10^{-4}$
09080973	328.68	-0.08	$1.67 \cdot 10^{-4}$	$3.65 \cdot 10^{-7}$	14	2.74	-5.7	$1.91 \cdot 10^{-4}$	$1.55 \cdot 10^{-5}$	$5.39 \cdot 10^{-5}$	0.46	$2.34 \cdot 10^{-5}$
09081065	168.93	-76.40	5.53	$9.89 \cdot 10^{-6}$	202	2.15	-5.0	$6.44 \cdot 10^{-5}$	$3.37 \cdot 10^{-5}$	$3.47 \cdot 10^{-4}$	3.79	$2.71 \cdot 10^{-5}$
09081078	116.43	-17.48	2.77	$5.15 \cdot 10^{-6}$	105	2.15	-5.3	$8.45 \cdot 10^{-5}$	$1.66 \cdot 10^{-5}$	$3.01 \cdot 10^{-4}$	2.13	$2.22 \cdot 10^{-5}$
09082050	318.26	-18.58	9.64	$1.34 \cdot 10^{-6}$	28	2.15	-5.0	$3.70 \cdot 10^{-5}$	$1.01 \cdot 10^{-6}$	$9.82 \cdot 10^{-6}$	6.65	$9.64 \cdot 10^{-6}$
09082809	124.38	-26.14	1.21	$2.37 \cdot 10^{-5}$	113	2.15	-5.4	$1.34 \cdot 10^{-4}$	$1.25 \cdot 10^{-4}$	$1.16 \cdot 10^{-3}$	1.18	$1.23 \cdot 10^{-4}$
09082967	329.23	-34.19	1.00	$7.66 \cdot 10^{-5}$	112	2.15	-5.4	$1.70 \cdot 10^{-4}$	$3.92 \cdot 10^{-4}$	$5.70 \cdot 10^{-3}$	1.02	$3.67 \cdot 10^{-4}$
09082970	354.99	-9.36	3.24	$4.81 \cdot 10^{-6}$	167	2.15	-5.1	$7.89 \cdot 10^{-5}$	$2.08 \cdot 10^{-5}$	$4.79 \cdot 10^{-4}$	2.38	$2.44 \cdot 10^{-5}$
09083189	108.29	-25.12	$5.00 \cdot 10^{-4}$	$3.81 \cdot 10^{-7}$	85	2.15	-5.5	$2.77 \cdot 10^{-4}$	$1.10 \cdot 10^{-6}$	$1.60 \cdot 10^{-5}$	0.28	$1.01 \cdot 10^{-5}$
09090701	86.33	-38.85	2.11	$4.54 \cdot 10^{-6}$	67	2.15	-5.2	$1.10 \cdot 10^{-4}$	$2.58 \cdot 10^{-5}$	$8.46 \cdot 10^{-4}$	1.71	$3.00 \cdot 10^{-5}$
09092003	299.73	-52.19	5.65	$3.74 \cdot 10^{-6}$	47	2.15	-5.2	$4.28 \cdot 10^{-5}$	$1.89 \cdot 10^{-5}$	$1.89 \cdot 10^{-34}$	3.99	$2.09 \cdot 10^{-5}$
09092864	103.91	-43.53	8.91	$1.95 \cdot 10^{-6}$	29	2.15	-5.0	$1.33 \cdot 10^{-5}$	$1.55 \cdot 10^{-6}$	$4.87 \cdot 10^{-5}$	6.06	$1.04 \cdot 10^{-5}$
09100268	41.92	-14.01	4.15	$3.37 \cdot 10^{-7}$	8	2.15	-5.2	$1.67 \cdot 10^{-5}$	$1.15 \cdot 10^{-6}$	$9.41 \cdot 10^{-6}$	3.09	$1.02 \cdot 10^{-5}$
09100319	251.52	36.62	$4.72 \cdot 10^{-4}$	$2.33 \cdot 10^{-5}$	36	2.15	-5.6	$2.47 \cdot 10^{-4}$	$2.37 \cdot 10^{-4}$	$2.82 \cdot 10^{-3}$	0.43	$2.28 \cdot 10^{-4}$
09100567	43.14	12.12	5.14	$1.40 \cdot 10^{-6}$	15	2.15	-5.2	$1.82 \cdot 10^{-5}$	$7.93 \cdot 10^{-6}$	$7.69 \cdot 10^{-5}$	3.75	$1.58 \cdot 10^{-5}$
09101011	298.67	-22.52	$5.28 \cdot 10^{-4}$	$9.96 \cdot 10^{-6}$	14	2.15	-5.7	$8.39 \cdot 10^{-5}$	$3.35 \cdot 10^{-5}$	$7.53 \cdot 10^{-4}$	0.45	$4.12 \cdot 10^{-5}$
09101512	316.09	-49.50	12.65	$1.59 \cdot 10^{-6}$	10	2.15	-5.0	$1.38 \cdot 10^{-5}$	$1.81 \cdot 10^{-6}$	$1.68 \cdot 10^{-4}$	8.82	$1.06 \cdot 10^{-5}$
09101786	210.80	25.49	8.54	$4.50 \cdot 10^{-7}$	8	2.15	-5.4	$1.14 \cdot 10^{-5}$	$3.77 \cdot 10^{-6}$	$2.62 \cdot 10^{-5}$	5.89	$1.25 \cdot 10^{-5}$
09101798	214.40	-64.74	1.71	$2.15 \cdot 10^{-6}$	76	2.15	-5.4	$1.12 \cdot 10^{-4}$	$2.18 \cdot 10^{-6}$	$1.46 \cdot 10^{-5}$	1.66	$1.10 \cdot 10^{-5}$
09101886	32.19	-57.55	$1.69 \cdot 10^{-4}$	$1.43 \cdot 10^{-6}$	12	0.97	-5.7	$9.69 \cdot 10^{-5}$	$1.15 \cdot 10^{-5}$	$5.66 \cdot 10^{-5}$	0.48	$1.99 \cdot 10^{-5}$
09102097	187.80	-13.40	2.17	$1.07 \cdot 10^{-5}$	64	2.15	-5.3	$7.92 \cdot 10^{-5}$	$2.93 \cdot 10^{-5}$	$5.59 \cdot 10^{-4}$	1.80	$3.48 \cdot 10^{-5}$
09102302	215.42	25.95	7.23	$5.34 \cdot 10^{-7}$	14	2.15	-5.0	$1.38 \cdot 10^{-5}$	$2.87 \cdot 10^{-6}$	$1.94 \cdot 10^{-5}$	4.93	$1.15 \cdot 10^{-5}$
09102648	137.08	-23.65	8.15	$5.67 \cdot 10^{-7}$	9	2.15	-5.2	$1.26 \cdot 10^{-5}$	$4.17 \cdot 10^{-6}$	$3.56 \cdot 10^{-5}$	5.54	$1.28 \cdot 10^{-5}$
09102655	276.57	-86.11	$5.28 \cdot 10^{-4}$	$1.38 \cdot 10^{-6}$	18	2.15	-5.6	$8.47 \cdot 10^{-5}$	$5.51 \cdot 10^{-6}$	$4.23 \cdot 10^{-5}$	0.43	$1.43 \cdot 10^{-5}$
09102916	60.18	-55.96	$1.53 \cdot 10^{-4}$	$2.41 \cdot 10^{-6}$	66	2.75	-5.6	$1.69 \cdot 10^{-4}$	$2.98 \cdot 10^{-5}$	$2.90 \cdot 10^{-4}$	0.42	$3.76 \cdot 10^{-5}$
09103150	70.58	-59.08	1.03	$1.53 \cdot 10^{-5}$	58	2.15	-5.5	$9.81 \cdot 10^{-5}$	$1.61 \cdot 10^{-5}$	$5.08 \cdot 10^{-4}$	1.11	$2.39 \cdot 10^{-5}$
09110114	29.80	-33.68	2.20	$7.84 \cdot 10^{-6}$	21	2.15	-5.5	$4.47 \cdot 10^{-5}$	$6.59 \cdot 10^{-5}$	$1.51 \cdot 10^{-3}$	1.79	$7.08 \cdot 10^{-5}$
09110391	170.60	11.30	2.40	$5.60 \cdot 10^{-6}$	26	2.15	-5.4	$5.24 \cdot 10^{-5}$	$2.74 \cdot 10^{-5}$	$4.19 \cdot 10^{-4}$	1.98	$3.39 \cdot 10^{-5}$
09121523	283.25	17.55	9.83	$9.87 \cdot 10^{-7}$	11	2.15	-5.3	$9.82 \cdot 10^{-6}$	$1.08 \cdot 10^{-5}$	$7.68 \cdot 10^{-5}$	6.70	$1.96 \cdot 10^{-5}$
09123026	101.53	0.68	17.97	$1.95 \cdot 10^{-6}$	105	2.15	-5.1	$9.48 \cdot 10^{-5}$	$9.47 \cdot 10^{-6}$	$8.89 \cdot 10^{-5}$	11.89	$1.20 \cdot 10^{-5}$
09123120	199.36	-60.70	1.74	$9.76 \cdot 10^{-6}$	72	2.15	-5.1	$1.42 \cdot 10^{-4}$	$6.97 \cdot 10^{-5}$	$2.35 \cdot 10^{-3}$	1.30	$7.42 \cdot 10^{-5}$
10010373	112.37	-34.49	$4.72 \cdot 10^{-4}$	$1.20 \cdot 10^{-5}$	45	2.15	-5.5	$1.99 \cdot 10^{-4}$	$7.78 \cdot 10^{-5}$	$1.39 \cdot 10^{-3}$	0.42	$8.10 \cdot 10^{-5}$
10011241	240.14	-75.10	14.84	$1.05 \cdot 10^{-6}$	41	2.15	-5.0	$6.58 \cdot 10^{-5}$	$2.74 \cdot 10^{-6}$	$2.18 \cdot 10^{-5}$	9.83	$1.01 \cdot 10^{-5}$
10011689	305.02	14.45	0.30	$3.34 \cdot 10^{-5}$	168	2.15	-5.3	$4.78 \cdot 10^{-4}$	$2.36 \cdot 10^{-4}$	$3.06 \cdot 10^{-3}$	0.49	$2.22 \cdot 10^{-4}$
10011810	9.26	-37.37	5.87	$1.44 \cdot 10^{-6}$	19	2.15	-5.0	$3.77 \cdot 10^{-5}$	$2.66 \cdot 10^{-6}$	$2.97 \cdot 10^{-4}$	4.33	$1.08 \cdot 10^{-5}$
10011976	299.31	-53.15	0.02	$1.40 \cdot 10^{-5}$	45	2.15	-5.5	$1.97 \cdot 10^{-4}$	$2.36 \cdot 10^{-4}$	$5.54 \cdot 10^{-3}$	0.40	$2.28 \cdot 10^{-4}$

TABLE C.1.: Optimization results for all gamma-ray bursts selected from late-2007 to 2011 (cont.)

GRB	RA (°)	δ (°)	Δ_{err} (°)	$\mathcal{F}_\gamma$ (erg cm^{-2})	T_{search} (s)	z	Λ_{cut}	μ_{b}	$\mu_{\text{s}}^{\text{NeuCosmA}}$	$\mu_{\text{s}}^{\text{Guetta}}$	$m(\alpha)$ (°)	$\mathcal{MDP}_i^{296}$
10012261	79.20	-2.71	1.32	$1.20 \cdot 10^{-5}$	40	2.15	-5.3	$1.09 \cdot 10^{-4}$	$2.98 \cdot 10^{-4}$	$2.37 \cdot 10^{-3}$	1.16	$2.88 \cdot 10^{-4}$
10020456	273.07	-52.78	5.69	$3.77 \cdot 10^{-6}$	56	2.15	-5.0	$3.62 \cdot 10^{-5}$	$1.65 \cdot 10^{-5}$	$3.00 \cdot 10^{-4}$	3.87	$2.03 \cdot 10^{-5}$
10020549	133.92	-23.02	8.17	$1.36 \cdot 10^{-6}$	28	2.15	-5.4	$9.23 \cdot 10^{-5}$	$9.40 \cdot 10^{-7}$	$1.52 \cdot 10^{-4}$	6.49	$9.44 \cdot 10^{-6}$
10020766	307.86	-27.73	4.66	$2.08 \cdot 10^{-6}$	29	2.15	-5.2	$2.84 \cdot 10^{-5}$	$1.47 \cdot 10^{-5}$	$7.07 \cdot 10^{-4}$	3.25	$2.07 \cdot 10^{-5}$
10020772	321.78	-15.78	1.00	$4.34 \cdot 10^{-7}$	32	2.15	-5.4	$9.46 \cdot 10^{-5}$	$6.86 \cdot 10^{-6}$	$5.85 \cdot 10^{-5}$	0.99	$1.56 \cdot 10^{-5}$
10021144	132.25	29.49	2.46	$1.52 \cdot 10^{-5}$	38	2.15	-5.4	$8.74 \cdot 10^{-5}$	$1.35 \cdot 10^{-4}$	$3.29 \cdot 10^{-3}$	1.89	$1.24 \cdot 10^{-4}$
10021255	134.27	32.22	1.38	$3.60 \cdot 10^{-6}$	10	2.15	-5.6	$5.90 \cdot 10^{-5}$	$3.64 \cdot 10^{-5}$	$5.99 \cdot 10^{-4}$	1.29	$4.44 \cdot 10^{-5}$
10021902	330.93	37.79	2.93	$3.48 \cdot 10^{-6}$	100	2.15	-5.2	$7.34 \cdot 10^{-5}$	$2.56 \cdot 10^{-5}$	$5.53 \cdot 10^{-4}$	2.07	$3.01 \cdot 10^{-5}$
10021963	154.20	-12.57	$2.78 \cdot 10^{-4}$	$3.70 \cdot 10^{-7}$	30	4.67	-5.5	$1.20 \cdot 10^{-4}$	$1.56 \cdot 10^{-5}$	$5.08 \cdot 10^{-5}$	0.44	$2.38 \cdot 10^{-5}$
10022136	27.12	-17.41	7.99	$1.83 \cdot 10^{-6}$	42	2.15	-5.1	$2.61 \cdot 10^{-5}$	$9.43 \cdot 10^{-6}$	$2.28 \cdot 10^{-4}$	5.39	$1.52 \cdot 10^{-5}$
10022511	310.30	-59.40	0.90	$5.85 \cdot 10^{-6}$	25	2.15	-5.5	$9.28 \cdot 10^{-5}$	$1.92 \cdot 10^{-5}$	$9.25 \cdot 10^{-4}$	0.95	$2.73 \cdot 10^{-5}$
10022854	199.83	15.62	9.29	$2.77 \cdot 10^{-6}$	111	2.15	-5.2	$1.42 \cdot 10^{-4}$	$2.26 \cdot 10^{-5}$	$1.87 \cdot 10^{-34}$	6.28	$1.57 \cdot 10^{-5}$
10030453	260.14	-21.92	2.52	$4.90 \cdot 10^{-6}$	34	2.15	-5.3	$4.44 \cdot 10^{-5}$	$6.16 \cdot 10^{-5}$	$2.58 \cdot 10^{-34}$	2.03	$6.56 \cdot 10^{-5}$
10031328	172.71	-52.58	2.89	$4.40 \cdot 10^{-6}$	25	2.15	-5.5	$1.58 \cdot 10^{-5}$	$1.26 \cdot 10^{-5}$	$9.87 \cdot 10^{-4}$	2.43	$2.14 \cdot 10^{-5}$
10033030	202.08	-0.90	2.52	$4.30 \cdot 10^{-6}$	20	2.15	-5.3	$3.09 \cdot 10^{-5}$	$5.27 \cdot 10^{-5}$	$6.13 \cdot 10^{-4}$	1.95	$5.91 \cdot 10^{-5}$
10033085	326.38	-6.97	7.68	$6.20 \cdot 10^{-7}$	12	2.15	-5.4	$2.92 \cdot 10^{-5}$	$1.13 \cdot 10^{-6}$	$7.72 \cdot 10^{-6}$	5.44	$9.84 \cdot 10^{-6}$
10041373	266.22	15.83	$5.00 \cdot 10^{-4}$	$1.05 \cdot 10^{-5}$	291	3.90	-5.4	$4.45 \cdot 10^{-4}$	$1.15 \cdot 10^{-4}$	$6.43 \cdot 10^{-4}$	0.34	$1.16 \cdot 10^{-4}$
10041778	295.81	9.84	9.41	$1.36 \cdot 10^{-6}$	88	2.15	-5.7	$1.53 \cdot 10^{-5}$	$2.72 \cdot 10^{-6}$	$2.74 \cdot 10^{-5}$	6.74	$1.12 \cdot 10^{-5}$
10061901	84.62	-27.01	$4.17 \cdot 10^{-4}$	$1.13 \cdot 10^{-5}$	158	2.15	-5.6	$2.86 \cdot 10^{-4}$	$8.11 \cdot 10^{-6}$	$1.44 \cdot 10^{-4}$	0.31	$1.63 \cdot 10^{-5}$
10062011	80.10	-51.68	1.46	$3.72 \cdot 10^{-6}$	87	2.15	-5.5	$7.29 \cdot 10^{-5}$	$1.16 \cdot 10^{-5}$	$1.20 \cdot 10^{-4}$	1.28	$1.99 \cdot 10^{-5}$
10062112	315.30	-51.11	$4.72 \cdot 10^{-4}$	$2.10 \cdot 10^{-5}$	214	0.54	-5.6	$3.94 \cdot 10^{-4}$	$4.25 \cdot 10^{-5}$	$9.55 \cdot 10^{-5}$	0.33	$4.90 \cdot 10^{-5}$
10070414	133.64	-24.20	$4.72 \cdot 10^{-4}$	$1.04 \cdot 10^{-5}$	347	3.60	-5.5	$3.52 \cdot 10^{-4}$	$3.68 \cdot 10^{-5}$	$5.82 \cdot 10^{-4}$	0.34	$4.25 \cdot 10^{-5}$
10071398	82.06	13.00	3.74	$3.05 \cdot 10^{-6}$	16	2.15	-5.3	$1.58 \cdot 10^{-5}$	$1.66 \cdot 10^{-5}$	$3.71 \cdot 10^{-4}$	2.82	$2.47 \cdot 10^{-5}$
10071547	299.27	-54.71	9.32	$2.55 \cdot 10^{-6}$	28	2.15	-5.3	$1.25 \cdot 10^{-5}$	$1.63 \cdot 10^{-6}$	$4.63 \cdot 10^{-5}$	7.02	$1.05 \cdot 10^{-5}$
10071737	287.06	-0.66	8.84	$4.26 \cdot 10^{-7}$	14	2.15	-5.7	$1.02 \cdot 10^{-5}$	$1.10 \cdot 10^{-6}$	$2.56 \cdot 10^{-5}$	7.28	$1.01 \cdot 10^{-5}$
10071744	304.31	19.53	9.19	$3.33 \cdot 10^{-7}$	8	2.15	-5.8	$1.52 \cdot 10^{-5}$	$6.73 \cdot 10^{-7}$	$1.36 \cdot 10^{-5}$	6.45	$9.61 \cdot 10^{-6}$
10071816	121.83	-46.18	5.93	$2.75 \cdot 10^{-6}$	56	2.15	-5.3	$1.09 \cdot 10^{-5}$	$6.10 \cdot 10^{-6}$	$1.47 \cdot 10^{-4}$	4.26	$1.49 \cdot 10^{-5}$
10071914	112.32	-5.86	0.04	$5.30 \cdot 10^{-7}$	43	2.15	-5.5	$9.92 \cdot 10^{-5}$	$1.02 \cdot 10^{-5}$	$7.20 \cdot 10^{-5}$	0.46	$1.88 \cdot 10^{-5}$
10072809	88.76	-15.26	$3.89 \cdot 10^{-4}$	$1.28 \cdot 10^{-4}$	269	2.15	-5.6	$1.61 \cdot 10^{-4}$	$9.65 \cdot 10^{-4}$	$1.39 \cdot 10^{-2}$	0.49	$9.11 \cdot 10^{-4}$
10073046	339.79	-22.23	5.40	$6.06 \cdot 10^{-6}$	106	2.15	-5.2	$4.51 \cdot 10^{-5}$	$1.52 \cdot 10^{-5}$	$3.76 \cdot 10^{-4}$	3.88	$1.85 \cdot 10^{-5}$
10080584	112.72	-35.93	3.75	$1.06 \cdot 10^{-5}$	97	2.15	-5.1	$2.98 \cdot 10^{-5}$	$1.13 \cdot 10^{-5}$	$3.08 \cdot 10^{-4}$	2.58	$1.85 \cdot 10^{-5}$
10081004	124.77	-1.61	5.65	$3.94 \cdot 10^{-7}$	8	2.15	-5.8	$1.22 \cdot 10^{-5}$	$3.89 \cdot 10^{-7}$	$8.59 \cdot 10^{-6}$	6.29	$9.41 \cdot 10^{-6}$
10081600	102.12	-26.66	1.06	$2.53 \cdot 10^{-5}$	104	2.15	-5.3	$1.56 \cdot 10^{-4}$	$9.67 \cdot 10^{-5}$	$2.37 \cdot 10^{-3}$	0.96	$9.97 \cdot 10^{-5}$
10081949	279.60	-50.04	3.86	$3.32 \cdot 10^{-6}$	24	2.15	-5.2	$2.64 \cdot 10^{-5}$	$9.43 \cdot 10^{-6}$	$2.37 \cdot 10^{-4}$	2.83	$1.71 \cdot 10^{-5}$
10082037	258.79	-18.51	2.14	$2.99 \cdot 10^{-6}$	18	2.15	-5.4	$4.06 \cdot 10^{-5}$	$8.89 \cdot 10^{-6}$	$2.26 \cdot 10^{-4}$	1.84	$1.75 \cdot 10^{-5}$
10082372	20.70	5.84	$2.50 \cdot 10^{-4}$	$4.10 \cdot 10^{-7}$	23	2.15	-5.6	$6.77 \cdot 10^{-5}$	$6.85 \cdot 10^{-6}$	$2.50 \cdot 10^{-5}$	0.41	$1.57 \cdot 10^{-5}$
10082528	253.44	-56.57	6.34	$1.38 \cdot 10^{-6}$	9	2.15	-5.5	$9.56 \cdot 10^{-6}$	$1.26 \cdot 10^{-6}$	$3.49 \cdot 10^{-5}$	5.31	$1.03 \cdot 10^{-5}$
10082987	90.41	30.31	0.16	$1.50 \cdot 10^{-5}$	18	2.15	-5.6	$1.08 \cdot 10^{-4}$	$1.49 \cdot 10^{-4}$	$2.90 \cdot 10^{-3}$	0.40	$1.53 \cdot 10^{-4}$
10090156	27.26	22.76	$2.25 \cdot 10^{-4}$	$2.10 \cdot 10^{-6}$	478	1.41	-5.5	$1.28 \cdot 10^{-3}$	$4.99 \cdot 10^{-7}$	$8.71 \cdot 10^{-7}$	0.31	$9.54 \cdot 10^{-6}$
10090281	48.63	30.98	$4.17 \cdot 10^{-4}$	$3.20 \cdot 10^{-6}$	463	4.50	-5.4	$1.11 \cdot 10^{-3}$	$1.51 \cdot 10^{-4}$	$1.74 \cdot 10^{-4}$	0.35	$1.39 \cdot 10^{-4}$
10090406	172.91	-16.18	0.03	$1.30 \cdot 10^{-6}$	42	2.15	-5.6	$1.00 \cdot 10^{-4}$	$4.51 \cdot 10^{-6}$	$3.42 \cdot 10^{-5}$	0.30	$1.34 \cdot 10^{-5}$
10090563	31.55	14.93	$4.44 \cdot 10^{-4}$	$1.70 \cdot 10^{-7}$	8	2.15	-5.9	$7.98 \cdot 10^{-5}$	$3.15 \cdot 10^{-6}$	$6.13 \cdot 10^{-5}$	0.39	$1.21 \cdot 10^{-5}$
10090775	177.29	-40.63	6.90	$7.33 \cdot 10^{-7}$	13	2.15	-5.4	$1.05 \cdot 10^{-5}$	$3.81 \cdot 10^{-6}$	$8.19 \cdot 10^{-5}$	4.99	$1.26 \cdot 10^{-5}$
10091081	238.10	-34.62	1.02	$1.65 \cdot 10^{-5}$	27	2.15	-5.5	$1.16 \cdot 10^{-4}$	$2.83 \cdot 10^{-4}$	$3.41 \cdot 10^{-3}$	0.97	$2.79 \cdot 10^{-4}$
10091677	151.96	-59.38	3.48	$1.78 \cdot 10^{-6}$	24	2.15	-5.2	$2.51 \cdot 10^{-5}$	$4.21 \cdot 10^{-6}$	$1.07 \cdot 10^{-4}$	2.63	$1.29 \cdot 10^{-5}$
10091988	163.24	6.02	1.81	$5.76 \cdot 10^{-6}$	83	2.15	-5.3	$6.76 \cdot 10^{-5}$	$2.09 \cdot 10^{-5}$	$4.89 \cdot 10^{-4}$	1.44	$2.89 \cdot 10^{-5}$
10092262	356.98	-25.19	15.03	$4.25 \cdot 10^{-7}$	11	2.15	-5.3	$9.77 \cdot 10^{-6}$	$7.59 \cdot 10^{-7}$	$1.77 \cdot 10^{-5}$	10.63	$9.80 \cdot 10^{-6}$
10092384	106.12	39.60	5.35	$3.92 \cdot 10^{-6}$	87	2.15	-5.1	$3.95 \cdot 10^{-5}$	$3.17 \cdot 10^{-5}$	$5.86 \cdot 10^{-4}$	3.73	$3.11 \cdot 10^{-5}$
10092659	222.75	-72.35	3.81	$6.97 \cdot 10^{-6}$	56	2.15	-5.1	$5.84 \cdot 10^{-5}$	$3.65 \cdot 10^{-5}$	$7.86 \cdot 10^{-4}$	2.72	$3.45 \cdot 10^{-5}$
10092669	43.58	-11.10	12.00	$1.37 \cdot 10^{-6}$	65	2.15	-5.0	$5.96 \cdot 10^{-5}$	$2.18 \cdot 10^{-6}$	$5.53 \cdot 10^{-5}$	8.47	$9.96 \cdot 10^{-6}$
10100227	323.35	-27.47	16.36	$4.40 \cdot 10^{-7}$	15	2.15	-5.0	$1.14 \cdot 10^{-5}$	$2.32 \cdot 10^{-7}$	$6.40 \cdot 10^{-6}$	11.66	$9.33 \cdot 10^{-6}$
10100442	232.22	-43.99	7.29	$9.03 \cdot 10^{-6}$	262	2.15	-5.1	$1.44 \cdot 10^{-4}$	$4.64 \cdot 10^{-5}$	$9.08 \cdot 10^{-4}$	5.01	$2.38 \cdot 10^{-5}$
10101170	48.29	-65.98	$3.06 \cdot 10^{-4}$	$2.71 \cdot 10^{-6}$	62	2.15	-5.5	$1.80 \cdot 10^{-4}$	$8.83 \cdot 10^{-6}$	$1.10 \cdot 10^{-4}$	0.32	$1.74 \cdot 10^{-5}$
10101341	292.08	-49.64	1.60	$6.41 \cdot 10^{-6}$	29	2.15	-5.4	$4.74 \cdot 10^{-5}$	$2.22 \cdot 10^{-5}$	$5.43 \cdot 10^{-4}$	1.40	$3.03 \cdot 10^{-5}$
10101417	26.94	-51.07	1.00	$2.01 \cdot 10^{-4}$	723	2.15	-5.1	$4.06 \cdot 10^{-4}$	$1.18 \cdot 10^{-3}$	$1.75 \cdot 10^{-2}$	0.89	$1.01 \cdot 10^{-3}$
10101555	73.16	15.46	5.94	$3.74 \cdot 10^{-5}$	805	2.15	-5.1	$2.85 \cdot 10^{-4}$	$1.39 \cdot 10^{-4}$	$3.09 \cdot 10^{-3}$	4.10	$4.20 \cdot 10^{-5}$
10101761	27.47	-26.55	4.92	$1.78 \cdot 10^{-6}$	81	2.15	-5.1	$1.78 \cdot 10^{-5}$	$4.03 \cdot 10^{-6}$	$9.83 \cdot 10^{-5}$	3.56	$1.26 \cdot 10^{-5}$
10101743	291.39	-35.14	$2.00 \cdot 10^{-4}$	$1.80 \cdot 10^{-5}$	115	2.15	-5.5	$1.39 \cdot 10^{-4}$	$2.26 \cdot 10^{-4}$	$2.37 \cdot 10^{-3}$	0.44	$2.24 \cdot 10^{-4}$
10102098	189.61	23.13	0.06	$2.60 \cdot 10^{-6}$	213	2.15	-5.4	$4.97 \cdot 10^{-4}$	$6.30 \cdot 10^{-5}$	$2.74 \cdot 10^{-4}$	0.35	$6.71 \cdot 10^{-5}$
10102395	317.96	-65.39	$1.67 \cdot 10^{-4}$	$6.37 \cdot 10^{-5}$	127	2.15	-5.5	$3.61 \cdot 10^{-4}$	$3.25 \cdot 10^{-4}$	$4.89 \cdot 10^{-3}$	0.39	$3.07 \cdot 10^{-4}$
10102448	66.51	-77.27	$1.78 \cdot 10^{-4}$	$4.21 \cdot 10^{-6}$	43	2.15	-5.6	$1.73 \cdot 10^{-4}$	$1.20 \cdot 10^{-5}$	$2.20 \cdot 10^{-4}$	0.33	$2.03 \cdot 10^{-5}$
10102514	240.19	-8.49	24.35	$2.79 \cdot 10^{-7}$	27	2.15	-5.0	$1.58 \cdot 10^{-5}$	$1.31 \cdot 10^{-7}$	$2.76 \cdot 10^{-6}$	16.76	$9.22 \cdot 10^{-6}$
10111348	29.08	0.21	2.67	$3.06 \cdot 10^{-6}$	24	2.15	-5.3	$8.20 \cdot 10^{-5}$	$1.54 \cdot 10^{-5}$	$3.73 \cdot 10^{-4}$	2.09	$2.16 \cdot 10^{-5}$
10111402	303.21	14.03	$7.78 \cdot 10^{-4}$	$8.00 \cdot 10^{-7}$	20	2.15	-5.6	$2.26 \cdot 10^{-4}$	$2.97 \cdot 10^{-5}$	$3.58 \cdot 10^{-4}$	0.35	$3.72 \cdot 10^{-5}$
10111780	173.00	-72.66	$1.19 \cdot 10^{-4}$	$1.10 \cdot 10^{-6}$	13	2.15	-5.7	$6.21 \cdot 10^{-5}$	$4.69 \cdot 10^{-6}$	$4.67 \cdot 10^{-5}$	0.29	$1.36 \cdot 10^{-5}$
10112709	290.31	7.89	23.17	$6.96 \cdot 10^{-7}$	51	2.15	-5.0	$9.90 \cdot 10^{-5}$	$1.08 \cdot 10^{-6}$	$2.67 \cdot 10^{-5}$	15.97	$9.41 \cdot 10^{-6}$
10113007	274.61	26.62	23.61	$2.34 \cdot 10^{-7}$	12	2.15	-5.3	$2.76 \cdot 10^{-5}$	$7.62 \cdot 10^{-7}$	$1.51 \cdot 10^{-5}$	15.16	$9.53 \cdot 10^{-6}$
10120141	1.97	-16.19	$5.28 \cdot 10^{-4}$	$2.37 \cdot 10^{-5}$	184	2.15	-5.4	$7.40 \cdot 10^{-4}$	$1.04 \cdot 10^{-4}$	$1.02 \cdot 10^{-3}$	0.30	$1.00 \cdot 10^{-4}$
10120499	167.54	-20.42	$1.67 \cdot 10^{-4}$	$1.20 \cdot 10^{-6}$	14	2.15	-5.6	$1.96 \cdot 10^{-4}$	$4.34 \cdot 10^{-5}$	$5.18 \cdot 10^{-4}$	0.35	$5.04 \cdot 10^{-5}$
10120530	322.10	-39.10	11.10	$3.90 \cdot 10^{-7}$	17	2.15	-5.1	$4.84 \cdot 10^{-5}$	$8.52 \cdot 10^{-7}$	$2.11 \cdot 10^{-5}$	7.44	$9.51 \cdot 10^{-6}$
10120603	164.08	-38.11	3.50	$5.84 \cdot 10^{-6}$	60	2.15	-5.1	$9.54 \cdot 10^{-5}$	$5.44 \cdot 10^{-5}$	$1.09 \cdot 10^{-3}$	2.53	$4.42 \cdot 10^{-5}$
10120753	175.75	8.72	3.73	$6.65 \cdot 10^{-6}$	102	2.15	-5.0	$8.19 \cdot 10^{-5}$	$8.33 \cdot 10^{-5}$	$1.51 \cdot 10^{-3}$	2.49	$6.18 \cdot 10^{-5}$
10120849	280.94	-59.02	1.41	$3.84 \cdot 10^{-6}$	7	2.15	-5.5	$4.09 \cdot 10^{-5}$	$4.69 \cdot 10^{-5}$	$9.30 \cdot 10^{-4}$	1.24	$5.50 \cdot 10^{-5}$
10121148	31.84	10.06	11.25	$1.63 \cdot 10^{-6}$	26	2.15	-5.0	$2.51 \cdot 10^{-5}$	$7.12 \cdot 10^{-6}$	$1.52 \cdot 10^{-4}$	7.70	$1.37 \cdot 10^{-5}$
10121384	260.99	-64.51	7.06	$1.35 \cdot 10^{-6}$	15	2.15	-5.0	$3.12 \cdot 10^{-5}$	$3.40 \cdot 10^{-6}$	$8.72 \cdot 10^{-5}$	4.92	$1.13 \cdot 10^{-5}$
10121499	181.13	-31.06	5.73	$1.09 \cdot 10^{-6}$	22	2.15	-5.2	$3.91 \cdot 10^{-5}$	$7.75 \cdot 10^{-6}$	$1.70 \cdot 10^{-4}$	3.89	$1.41 \cdot 10^{-5}$
10122499	325.17	-38.66	8.29	$1.36 \cdot 10^{-6}$	34	2.15	-5.0	$4.04 \cdot 10^{-5}$	$3.23 \cdot 10^{-6}$	$8.33 \cdot 10^{-5}$	5.87	$1.08 \cdot 10^{-5}$
10122537	60.68	32.77	1.81	$2.02 \cdot 10^{-5}$	134	2.15	-5.3	$1.29 \cdot 10^{-4}$	$2.02 \cdot 10^{-4}$	$4.06 \cdot 10^{-3}$	1.38	$1.85 \cdot 10^{-4}$

TABLE C.1.: Optimization results for all gamma-ray bursts selected from late-2007 to 2011 (cont.)

GRB	RA (°)	δ (°)	Δ_{err} (°)	$\mathcal{F}_\gamma$ (erg cm^{-2})	T_{search} (s)	z	Λ_{cut}	μ_{b}	$\mu_{\text{s}}^{\text{NeuCosmA}}$	$\mu_{\text{s}}^{\text{Guetta}}$	$m(\alpha)$ (°)	$\mathcal{MDP}_i^{296}$
10122719	186.79	-83.55	7.16	$3.43 \cdot 10^{-6}$	157	2.15	-5.2	$9.71 \cdot 10^{-5}$	$1.34 \cdot 10^{-5}$	$3.17 \cdot 10^{-4}$	4.73	$1.47 \cdot 10^{-5}$
10122753	150.87	-49.44	2.59	$6.44 \cdot 10^{-6}$	50	2.15	-5.3	$5.72 \cdot 10^{-5}$	$1.12 \cdot 10^{-5}$	$3.08 \cdot 10^{-4}$	2.03	$1.87 \cdot 10^{-5}$
11010150	105.50	34.58	16.49	$6.63 \cdot 10^{-6}$	381	2.15	-5.0	$4.05 \cdot 10^{-4}$	$2.64 \cdot 10^{-5}$	$5.33 \cdot 10^{-4}$	11.18	$1.29 \cdot 10^{-5}$
11010278	245.88	7.61	$1.39 \cdot 10^{-4}$	$3.72 \cdot 10^{-5}$	410	2.15	-5.3	$9.45 \cdot 10^{-4}$	$2.63 \cdot 10^{-4}$	$2.18 \cdot 10^{-3}$	0.29	$2.42 \cdot 10^{-4}$
11010897	11.62	-9.64	2.67	$2.51 \cdot 10^{-6}$	86	2.15	-5.2	$7.37 \cdot 10^{-5}$	$2.71 \cdot 10^{-5}$	$5.24 \cdot 10^{-4}$	1.94	$3.16 \cdot 10^{-5}$
11011762	129.51	-12.88	3.57	$3.03 \cdot 10^{-6}$	73	2.15	-5.1	$1.69 \cdot 10^{-4}$	$1.29 \cdot 10^{-5}$	$3.15 \cdot 10^{-4}$	2.59	$1.57 \cdot 10^{-5}$
11011885	226.57	-39.55	4.07	$2.97 \cdot 10^{-6}$	59	2.15	-5.1	$1.47 \cdot 10^{-4}$	$4.02 \cdot 10^{-6}$	$1.13 \cdot 10^{-4}$	3.07	$1.11 \cdot 10^{-5}$
11011993	348.59	5.99	$1.69 \cdot 10^{-4}$	$1.01 \cdot 10^{-5}$	333	2.15	-5.4	$1.29 \cdot 10^{-3}$	$1.38 \cdot 10^{-4}$	$1.38 \cdot 10^{-3}$	0.32	$1.26 \cdot 10^{-4}$
11012380	246.97	28.03	1.16	$1.90 \cdot 10^{-5}$	33	2.15	-5.4	$9.60 \cdot 10^{-5}$	$2.01 \cdot 10^{-4}$	$4.93 \cdot 10^{-3}$	1.04	$2.01 \cdot 10^{-4}$
11012589	331.35	-46.21	5.76	$8.63 \cdot 10^{-7}$	12	2.15	-5.3	$3.06 \cdot 10^{-5}$	$3.29 \cdot 10^{-6}$	$1.69 \cdot 10^{-5}$	4.16	$1.14 \cdot 10^{-5}$
11020558	312.69	-55.85	10.12	$4.21 \cdot 10^{-6}$	258	2.15	-5.0	$2.93 \cdot 10^{-4}$	$2.31 \cdot 10^{-5}$	$4.61 \cdot 10^{-4}$	6.98	$1.36 \cdot 10^{-5}$
11020620	333.70	1.61	15.47	$7.90 \cdot 10^{-7}$	24	2.15	-5.0	$3.84 \cdot 10^{-5}$	$2.77 \cdot 10^{-6}$	$5.85 \cdot 10^{-5}$	10.48	$1.05 \cdot 10^{-5}$
11020795	179.00	-58.43	9.03	$3.42 \cdot 10^{-7}$	16	2.15	-5.1	$2.72 \cdot 10^{-5}$	$2.04 \cdot 10^{-6}$	$4.28 \cdot 10^{-5}$	6.13	$1.04 \cdot 10^{-5}$
11022742	232.73	-9.94	4.99	$2.42 \cdot 10^{-6}$	45	2.15	-5.3	$8.84 \cdot 10^{-6}$	$2.65 \cdot 10^{-5}$	$4.31 \cdot 10^{-4}$	3.68	$3.51 \cdot 10^{-5}$
11022879	245.09	16.41	4.74	$9.60 \cdot 10^{-7}$	31	2.15	-5.4	$1.15 \cdot 10^{-5}$	$5.41 \cdot 10^{-6}$	$1.17 \cdot 10^{-4}$	3.49	$1.43 \cdot 10^{-5}$
11030407	322.93	33.27	4.23	$3.46 \cdot 10^{-6}$	35	2.15	-5.2	$5.16 \cdot 10^{-5}$	$4.95 \cdot 10^{-5}$	$8.78 \cdot 10^{-4}$	3.02	$4.27 \cdot 10^{-5}$
11031864	211.68	-51.58	$5.00 \cdot 10^{-4}$	$2.90 \cdot 10^{-7}$	9	2.15	-5.7	$1.57 \cdot 10^{-5}$	$1.20 \cdot 10^{-6}$	$2.78 \cdot 10^{-5}$	0.32	$1.03 \cdot 10^{-5}$
11031962	207.96	-51.58	4.94	$1.56 \cdot 10^{-6}$	29	2.15	-5.2	$1.30 \cdot 10^{-5}$	$1.62 \cdot 10^{-6}$	$4.45 \cdot 10^{-5}$	3.65	$1.06 \cdot 10^{-5}$
11031981	326.09	-56.78	$6.67 \cdot 10^{-4}$	$2.49 \cdot 10^{-6}$	54	2.15	-5.8	$8.91 \cdot 10^{-5}$	$3.62 \cdot 10^{-6}$	$3.32 \cdot 10^{-5}$	0.33	$1.25 \cdot 10^{-5}$
11031909	356.50	-66.01	$1.22 \cdot 10^{-4}$	$1.40 \cdot 10^{-6}$	36	2.15	-5.7	$2.26 \cdot 10^{-4}$	$5.83 \cdot 10^{-6}$	$1.27 \cdot 10^{-4}$	0.30	$1.45 \cdot 10^{-5}$
11032255	99.04	-48.90	4.72	$3.56 \cdot 10^{-6}$	62	2.15	-5.2	$1.33 \cdot 10^{-4}$	$2.86 \cdot 10^{-5}$	$6.12 \cdot 10^{-4}$	3.35	$2.16 \cdot 10^{-5}$
11040799	97.41	-11.95	1.00	$2.64 \cdot 10^{-5}$	18	2.15	-5.9	$3.38 \cdot 10^{-5}$	$1.89 \cdot 10^{-4}$	$3.70 \cdot 10^{-3}$	1.04	$1.94 \cdot 10^{-4}$
11040758	186.03	15.71	$4.72 \cdot 10^{-4}$	$1.70 \cdot 10^{-6}$	166	2.15	-5.6	$2.24 \cdot 10^{-4}$	$4.79 \cdot 10^{-5}$	$2.78 \cdot 10^{-3}$	0.34	$5.43 \cdot 10^{-5}$
11041013	30.94	-15.95	3.67	$6.41 \cdot 10^{-6}$	103	2.15	-5.0	$1.61 \cdot 10^{-4}$	$2.35 \cdot 10^{-5}$	$5.75 \cdot 10^{-4}$	2.57	$2.11 \cdot 10^{-5}$
11041077	337.17	-21.96	17.39	$9.52 \cdot 10^{-7}$	17	2.15	-5.2	$2.84 \cdot 10^{-5}$	$1.41 \cdot 10^{-6}$	$3.49 \cdot 10^{-5}$	11.68	$9.84 \cdot 10^{-6}$
11041231	133.49	13.49	0.03	$2.55 \cdot 10^{-6}$	37	2.15	-5.5	$1.84 \cdot 10^{-4}$	$1.73 \cdot 10^{-5}$	$1.53 \cdot 10^{-4}$	0.34	$2.57 \cdot 10^{-5}$
11050914	180.81	-34.00	4.60	$3.76 \cdot 10^{-6}$	114	2.15	-5.3	$2.62 \cdot 10^{-5}$	$1.80 \cdot 10^{-5}$	$4.05 \cdot 10^{-4}$	3.21	$2.35 \cdot 10^{-5}$
11051161	214.10	-45.42	10.62	$4.89 \cdot 10^{-7}$	13	2.15	-5.2	$1.18 \cdot 10^{-5}$	$1.23 \cdot 10^{-6}$	$2.92 \cdot 10^{-5}$	7.33	$1.02 \cdot 10^{-5}$
11051757	190.15	6.29	2.11	$8.74 \cdot 10^{-6}$	41	2.15	-5.4	$3.80 \cdot 10^{-5}$	$1.07 \cdot 10^{-4}$	$1.93 \cdot 10^{-3}$	1.62	$1.14 \cdot 10^{-4}$
11052030	71.01	-85.93	12.41	$1.04 \cdot 10^{-6}$	24	2.15	-5.0	$3.24 \cdot 10^{-5}$	$2.41 \cdot 10^{-6}$	$5.69 \cdot 10^{-5}$	8.35	$1.04 \cdot 10^{-5}$
11052147	57.54	-62.34	1.31	$3.61 \cdot 10^{-6}$	14	2.15	-5.5	$7.29 \cdot 10^{-5}$	$4.10 \cdot 10^{-5}$	$8.17 \cdot 10^{-4}$	1.18	$4.85 \cdot 10^{-5}$
11052263	180.57	-26.81	12.50	$3.04 \cdot 10^{-6}$	97	2.15	-5.1	$1.97 \cdot 10^{-5}$	$4.11 \cdot 10^{-6}$	$7.07 \cdot 10^{-5}$	8.05	$1.21 \cdot 10^{-5}$
11052926	172.60	8.79	2.10	$6.78 \cdot 10^{-6}$	77	2.15	-5.2	$1.86 \cdot 10^{-4}$	$3.67 \cdot 10^{-5}$	$8.78 \cdot 10^{-4}$	1.64	$3.66 \cdot 10^{-5}$
11052981	340.62	1.86	4.82	$3.33 \cdot 10^{-6}$	60	2.15	-5.1	$1.12 \cdot 10^{-4}$	$1.44 \cdot 10^{-5}$	$3.46 \cdot 10^{-4}$	3.50	$1.57 \cdot 10^{-5}$
11053144	190.51	11.85	11.06	$2.29 \cdot 10^{-6}$	66	2.15	-5.0	$3.11 \cdot 10^{-5}$	$8.81 \cdot 10^{-6}$	$1.90 \cdot 10^{-4}$	7.55	$1.40 \cdot 10^{-5}$
11060168	310.71	11.48	3.00	$1.24 \cdot 10^{-5}$	88	2.15	-5.3	$6.21 \cdot 10^{-5}$	$6.22 \cdot 10^{-5}$	$1.44 \cdot 10^{-3}$	2.19	$5.97 \cdot 10^{-5}$
11060461	270.86	18.40	$6.67 \cdot 10^{-4}$	$3.10 \cdot 10^{-5}$	41	2.15	-5.7	$6.16 \cdot 10^{-5}$	$2.62 \cdot 10^{-4}$	$2.64 \cdot 10^{-3}$	0.39	$2.63 \cdot 10^{-4}$
11061363	336.86	-3.47	2.79	$3.26 \cdot 10^{-6}$	68	2.15	-5.3	$4.62 \cdot 10^{-5}$	$1.25 \cdot 10^{-5}$	$3.08 \cdot 10^{-4}$	2.11	$2.04 \cdot 10^{-5}$
11061664	274.45	-34.02	11.96	$1.29 \cdot 10^{-6}$	24	2.15	-5.0	$1.22 \cdot 10^{-5}$	$2.37 \cdot 10^{-6}$	$5.96 \cdot 10^{-5}$	8.13	$1.11 \cdot 10^{-5}$
11062215	133.96	19.46	1.79	$5.43 \cdot 10^{-5}$	117	2.15	-5.4	$1.70 \cdot 10^{-4}$	$4.31 \cdot 10^{-4}$	$9.49 \cdot 10^{-3}$	1.42	$3.65 \cdot 10^{-4}$
11062490	65.02	-15.95	17.34	$2.78 \cdot 10^{-7}$	10	2.15	-5.7	$1.93 \cdot 10^{-5}$	$2.27 \cdot 10^{-7}$	$6.48 \cdot 10^{-6}$	14.80	$9.20 \cdot 10^{-6}$
11062557	315.33	-39.44	4.60	$3.52 \cdot 10^{-6}$	61	2.15	-5.3	$2.18 \cdot 10^{-5}$	$3.11 \cdot 10^{-6}$	$8.86 \cdot 10^{-5}$	3.54	$1.16 \cdot 10^{-5}$
11070620	100.08	6.14	8.03	$3.27 \cdot 10^{-6}$	23	2.15	-5.2	$1.28 \cdot 10^{-5}$	$3.54 \cdot 10^{-5}$	$6.15 \cdot 10^{-4}$	5.38	$4.02 \cdot 10^{-5}$
11070647	94.15	-50.77	2.04	$6.72 \cdot 10^{-6}$	121	2.15	-5.3	$1.27 \cdot 10^{-4}$	$9.12 \cdot 10^{-5}$	$1.63 \cdot 10^{-3}$	1.56	$8.89 \cdot 10^{-5}$
11070672	9.06	31.73	4.11	$2.34 \cdot 10^{-6}$	31	2.15	-5.2	$2.10 \cdot 10^{-5}$	$2.21 \cdot 10^{-5}$	$4.46 \cdot 10^{-4}$	2.79	$2.87 \cdot 10^{-5}$
11070986	156.21	-41.79	10.84	$7.97 \cdot 10^{-7}$	13	2.15	-5.1	$1.13 \cdot 10^{-5}$	$3.42 \cdot 10^{-6}$	$7.55 \cdot 10^{-5}$	7.55	$1.22 \cdot 10^{-5}$
11071555	237.68	-46.24	$1.56 \cdot 10^{-4}$	$1.18 \cdot 10^{-5}$	25	0.82	-5.6	$1.96 \cdot 10^{-4}$	$3.66 \cdot 10^{-5}$	$6.03 \cdot 10^{-4}$	0.33	$4.36 \cdot 10^{-5}$
11071601	329.68	-76.98	3.86	$1.35 \cdot 10^{-6}$	15	2.15	-5.3	$3.31 \cdot 10^{-5}$	$8.53 \cdot 10^{-6}$	$1.95 \cdot 10^{-4}$	2.82	$1.60 \cdot 10^{-5}$
11080693	112.04	2.38	2.42	$7.19 \cdot 10^{-6}$	49	2.15	-5.2	$7.65 \cdot 10^{-5}$	$3.07 \cdot 10^{-5}$	$7.55 \cdot 10^{-4}$	1.83	$3.61 \cdot 10^{-5}$
11081289	77.76	1.71	2.49	$1.17 \cdot 10^{-6}$	22	2.15	-5.6	$2.44 \cdot 10^{-5}$	$5.73 \cdot 10^{-6}$	$1.34 \cdot 10^{-4}$	2.03	$1.46 \cdot 10^{-5}$
11081719	336.04	-45.84	1.54	$1.19 \cdot 10^{-5}$	14	2.15	-5.7	$2.16 \cdot 10^{-5}$	$1.11 \cdot 10^{-4}$	$2.17 \cdot 10^{-3}$	1.41	$1.19 \cdot 10^{-4}$
11081886	317.34	-63.98	$3.89 \cdot 10^{-4}$	$5.15 \cdot 10^{-6}$	111	3.36	-5.6	$3.56 \cdot 10^{-4}$	$1.07 \cdot 10^{-4}$	$5.34 \cdot 10^{-4}$	0.37	$1.08 \cdot 10^{-4}$
11081966	139.49	-76.64	3.19	$3.04 \cdot 10^{-6}$	30	2.15	-5.3	$3.13 \cdot 10^{-5}$	$1.54 \cdot 10^{-5}$	$3.68 \cdot 10^{-4}$	2.28	$2.30 \cdot 10^{-5}$
11082857	110.58	-23.81	1.04	$2.72 \cdot 10^{-6}$	75	2.15	-5.5	$9.45 \cdot 10^{-5}$	$2.91 \cdot 10^{-5}$	$5.35 \cdot 10^{-4}$	0.95	$3.74 \cdot 10^{-5}$
11090300	164.21	42.08	1.18	$1.52 \cdot 10^{-5}$	50	2.15	-5.4	$1.48 \cdot 10^{-4}$	$2.28 \cdot 10^{-4}$	$4.16 \cdot 10^{-3}$	1.02	$2.23 \cdot 10^{-4}$
11090416	190.40	-28.85	6.11	$3.46 \cdot 10^{-6}$	86	2.15	-5.1	$1.13 \cdot 10^{-4}$	$8.81 \cdot 10^{-6}$	$2.30 \cdot 10^{-4}$	4.29	$1.26 \cdot 10^{-5}$
11090453	323.74	23.94	1.68	$3.81 \cdot 10^{-6}$	37	2.15	-5.4	$8.53 \cdot 10^{-5}$	$4.20 \cdot 10^{-5}$	$8.50 \cdot 10^{-4}$	1.40	$4.75 \cdot 10^{-5}$
11091107	258.58	-66.98	50.00	$5.94 \cdot 10^{-7}$	18	2.15	-5.2	$1.65 \cdot 10^{-5}$	$3.12 \cdot 10^{-7}$	$8.39 \cdot 10^{-6}$	34.87	$9.34 \cdot 10^{-6}$
11091889	32.54	-27.11	$1.53 \cdot 10^{-4}$	$7.50 \cdot 10^{-4}$	73	0.98	-5.5	$3.74 \cdot 10^{-4}$	$3.49 \cdot 10^{-2}$	$1.66 \cdot 10^{-1}$	0.32	$3.25 \cdot 10^{-2}$
11092144	6.09	-5.83	7.31	$5.90 \cdot 10^{-6}$	243	2.15	-5.0	$2.67 \cdot 10^{-4}$	$1.66 \cdot 10^{-5}$	$4.14 \cdot 10^{-4}$	4.95	$1.29 \cdot 10^{-5}$
11092807	257.73	36.54	$6.11 \cdot 10^{-4}$	$6.90 \cdot 10^{-7}$	32	2.15	-5.6	$2.67 \cdot 10^{-4}$	$4.06 \cdot 10^{-5}$	$6.22 \cdot 10^{-4}$	0.34	$4.68 \cdot 10^{-5}$
11092918	288.19	-62.21	4.03	$2.20 \cdot 10^{-6}$	12	2.15	-5.2	$2.04 \cdot 10^{-5}$	$3.81 \cdot 10^{-6}$	$1.04 \cdot 10^{-4}$	2.90	$1.24 \cdot 10^{-5}$
11100346	276.76	-62.32	1.11	$2.10 \cdot 10^{-5}$	31	2.15	-5.5	$1.12 \cdot 10^{-4}$	$1.00 \cdot 10^{-4}$	$3.22 \cdot 10^{-3}$	1.04	$1.05 \cdot 10^{-4}$
11100533	223.31	-19.72	0.04	$6.20 \cdot 10^{-7}$	32	2.15	-5.5	$2.25 \cdot 10^{-4}$	$3.60 \cdot 10^{-5}$	$1.37 \cdot 10^{-4}$	0.31	$4.39 \cdot 10^{-5}$
11100899	220.75	-5.67	4.34	$3.03 \cdot 10^{-6}$	72	2.15	-5.2	$8.49 \cdot 10^{-5}$	$1.14 \cdot 10^{-5}$	$2.80 \cdot 10^{-4}$	3.12	$1.55 \cdot 10^{-5}$
11100892	60.45	-32.71	$4.72 \cdot 10^{-4}$	$5.30 \cdot 10^{-6}$	75	4.99	-5.5	$3.62 \cdot 10^{-4}$	$2.16 \cdot 10^{-3}$	$2.61 \cdot 10^{-3}$	0.35	$2.04 \cdot 10^{-3}$
11100928	183.04	-56.82	1.08	$1.20 \cdot 10^{-5}$	37	2.15	-5.5	$8.11 \cdot 10^{-5}$	$1.09 \cdot 10^{-4}$	$2.29 \cdot 10^{-3}$	0.99	$1.14 \cdot 10^{-4}$
11101066	183.54	-31.70	7.08	$8.71 \cdot 10^{-7}$	18	2.15	-5.4	$8.76 \cdot 10^{-6}$	$6.57 \cdot 10^{-6}$	$1.28 \cdot 10^{-4}$	4.98	$1.56 \cdot 10^{-5}$
11101070	69.80	41.88	1.67	$1.26 \cdot 10^{-5}$	89	2.15	-5.4	$5.56 \cdot 10^{-5}$	$1.84 \cdot 10^{-4}$	$3.11 \cdot 10^{-3}$	1.34	$1.91 \cdot 10^{-4}$
11101089	77.02	-14.96	7.68	$9.59 \cdot 10^{-7}$	34	2.15	-5.1	$9.32 \cdot 10^{-6}$	$6.24 \cdot 10^{-6}$	$1.21 \cdot 10^{-4}$	5.18	$1.53 \cdot 10^{-5}$
11101542	220.65	-58.41	1.96	$2.42 \cdot 10^{-5}$	152	2.15	-5.2	$7.65 \cdot 10^{-5}$	$2.27 \cdot 10^{-4}$	$4.63 \cdot 10^{-3}$	1.50	$2.21 \cdot 10^{-4}$
11101677	153.83	27.46	$4.17 \cdot 10^{-4}$	$4.00 \cdot 10^{-6}$	583	2.15	-5.3	$1.26 \cdot 10^{-3}$	$1.28 \cdot 10^{-4}$	$6.03 \cdot 10^{-4}$	0.30	$1.19 \cdot 10^{-4}$
11101765	8.10	-7.01	1.00	$2.07 \cdot 10^{-5}$	22	2.15	-5.5	$1.12 \cdot 10^{-4}$	$2.19 \cdot 10^{-4}$	$2.23 \cdot 10^{-3}$	0.97	$2.18 \cdot 10^{-4}$
11102472	162.74	-44.94	2.57	$1.58 \cdot 10^{-5}$	114	2.15	-5.0	$1.67 \cdot 10^{-4}$	$3.59 \cdot 10^{-5}$	$9.50 \cdot 10^{-4}$	1.87	$3.51 \cdot 10^{-5}$
11102507	325.62	-35.52	2.73	$2.98 \cdot 10^{-6}$	87	2.15	-5.2	$1.58 \cdot 10^{-4}$	$1.81 \cdot 10^{-5}$	$4.14 \cdot 10^{-4}$	2.04	$2.20 \cdot 10^{-5}$
11110703	129.48	-66.52	$1.81 \cdot 10^{-4}$	$9.07 \cdot 10^{-7}$	23	2.89	-5.6	$1.37 \cdot 10^{-4}$	$9.33 \cdot 10^{-6}$	$5.27 \cdot 10^{-5}$	0.37	$1.80 \cdot 10^{-5}$
11110707	315.46	-38.53	3.53	$1.04 \cdot 10^{-5}$	127	2.15	-5.0	$1.13 \cdot 10^{-4}$	$3.45 \cdot 10^{-5}$	$8.55 \cdot 10^{-4}$	2.45	$3.07 \cdot 10^{-5}$
11110945	133.73	-33.35	7.38	$3.05 \cdot 10^{-7}$	12	2.15	-5.2	$1.75 \cdot 10^{-5}$	$2.26 \cdot 10^{-6}$	$4.71 \cdot 10^{-5}$	5.16	$1.09 \cdot 10^{-5}$

TABLE C.1.: Optimization results for all gamma-ray bursts selected from late-2007 to 2011 (cont.)

GRB	RA (°)	δ (°)	Δ_{err} (°)	$\mathcal{F}_\gamma$ (erg cm^{-2})	T_{search} (s)	z	Λ_{cut}	μ_{b}	$\mu_{\mathrm{s}}^{\mathrm{NeuCosmA}}$	$\mu_{\mathrm{s}}^{\mathrm{Guetta}}$	$m(\alpha)$ (°)	$\mathcal{MDP}_i^{296}$
11111341	4.32	-7.52	3.96	$3.10 \cdot 10^{-6}$	29	2.15	-5.1	$4.35 \cdot 10^{-5}$	$1.13 \cdot 10^{-5}$	$2.82 \cdot 10^{-4}$	2.86	$1.75 \cdot 10^{-5}$
11111423	268.08	-20.01	5.72	$1.11 \cdot 10^{-6}$	39	2.15	-5.0	$4.94 \cdot 10^{-5}$	$4.43 \cdot 10^{-6}$	$1.04 \cdot 10^{-4}$	4.05	$1.17 \cdot 10^{-5}$
11111752	27.16	-16.11	6.22	$1.42 \cdot 10^{-6}$	42	2.15	-5.0	$7.48 \cdot 10^{-5}$	$5.08 \cdot 10^{-6}$	$1.24 \cdot 10^{-4}$	4.37	$1.15 \cdot 10^{-5}$
11112055	344.60	-37.34	5.17	$6.73 \cdot 10^{-6}$	162	2.15	-5.1	$2.01 \cdot 10^{-4}$	$5.47 \cdot 10^{-5}$	$1.14 \cdot 10^{-3}$	3.61	$2.76 \cdot 10^{-5}$
11112168	154.76	-46.67	$5.00 \cdot 10^{-4}$	$2.20 \cdot 10^{-6}$	145	2.15	-5.4	$4.42 \cdot 10^{-4}$	$4.13 \cdot 10^{-6}$	$3.07 \cdot 10^{-5}$	0.23	$1.28 \cdot 10^{-5}$
11112375	154.85	-20.64	$4.72 \cdot 10^{-4}$	$7.30 \cdot 10^{-6}$	494	2.15	-5.4	$1.19 \cdot 10^{-3}$	$1.80 \cdot 10^{-5}$	$1.30 \cdot 10^{-4}$	0.24	$2.45 \cdot 10^{-5}$
11112781	103.70	3.50	2.09	$8.64 \cdot 10^{-6}$	34	2.15	-5.3	$5.02 \cdot 10^{-5}$	$1.20 \cdot 10^{-4}$	$2.16 \cdot 10^{-3}$	1.56	$1.25 \cdot 10^{-4}$
11112967	307.43	-52.71	$1.50 \cdot 10^{-4}$	$1.80 \cdot 10^{-7}$	13	2.15	-5.7	$1.20 \cdot 10^{-4}$	$2.99 \cdot 10^{-5}$	$5.70 \cdot 10^{-5}$	0.35	$3.81 \cdot 10^{-5}$
11120554	134.68	-31.94	$1.19 \cdot 10^{-3}$	$1.70 \cdot 10^{-4}$	84	2.15	-5.6	$2.05 \cdot 10^{-4}$	$2.28 \cdot 10^{-4}$	$4.07 \cdot 10^{-3}$	0.30	$2.20 \cdot 10^{-4}$
11121060	191.48	-7.17	$5.83 \cdot 10^{-4}$	$1.60 \cdot 10^{-7}$	7	2.15	-5.7	$7.41 \cdot 10^{-5}$	$4.31 \cdot 10^{-6}$	$5.51 \cdot 10^{-5}$	0.36	$1.33 \cdot 10^{-5}$
11121239	310.43	-68.61	$4.17 \cdot 10^{-4}$	$1.40 \cdot 10^{-6}$	73	2.15	-5.4	$2.51 \cdot 10^{-4}$	$1.66 \cdot 10^{-5}$	$1.26 \cdot 10^{-4}$	0.31	$2.48 \cdot 10^{-5}$
11122048	267.60	-56.05	1.39	$5.36 \cdot 10^{-5}$	66	2.15	-5.2	$1.43 \cdot 10^{-4}$	$6.15 \cdot 10^{-4}$	$1.19 \cdot 10^{-2}$	1.13	$5.84 \cdot 10^{-4}$
11122865	150.07	18.30	$2.08 \cdot 10^{-4}$	$1.81 \cdot 10^{-5}$	164	0.71	-5.5	$5.33 \cdot 10^{-4}$	$7.43 \cdot 10^{-6}$	$8.16 \cdot 10^{-6}$	0.33	$1.59 \cdot 10^{-5}$
11122994	76.29	-84.71	$1.53 \cdot 10^{-4}$	$3.40 \cdot 10^{-7}$	31	1.38	-5.5	$8.59 \cdot 10^{-5}$	$8.82 \cdot 10^{-8}$	$9.00 \cdot 10^{-8}$	0.31	$9.20 \cdot 10^{-6}$
11123068	150.19	33.43	2.78	$2.90 \cdot 10^{-6}$	49	2.15	-5.2	$5.04 \cdot 10^{-5}$	$3.02 \cdot 10^{-5}$	$5.87 \cdot 10^{-4}$	2.03	$3.65 \cdot 10^{-5}$
11123081	242.61	-22.12	2.02	$3.51 \cdot 10^{-6}$	24	2.15	-5.4	$5.21 \cdot 10^{-5}$	$7.27 \cdot 10^{-6}$	$1.97 \cdot 10^{-4}$	1.68	$1.59 \cdot 10^{-5}$
mean	180.01	-22.81	3.80	$1.10 \cdot 10^{-5}$	80.4	2.38	-5.35	$1.69 \cdot 10^{-4}$	$2.05 \cdot 10^{-4}$	$1.63 \cdot 10^{-3}$	2.85	$1.97 \cdot 10^{-4}$
sum				$3.25 \cdot 10^{-3}$	$2.38 \cdot 10^{4}$			$5.01 \cdot 10^{-2}$	$6.07 \cdot 10^{-2}$	$4.83 \cdot 10^{-1}$		
$\mathcal{MDP}(296)$												$5.72 \cdot 10^{-2}$

ACKNOWLEDGMENTS

This work would not be the same without the help and support of many people, to whom I owe my deepest gratitude. First of all, I am indebted to my thesis adviser Gisela Anton, for giving me the opportunity to work on this very interesting topic and for always supporting me.

I would like to thank the group around Walter Winter in Würzburg (now Zeuthen) for their fruitful collaboration and providing their NeuCosmA code. Thanks in particular to Philipp Baerwald and Mauricio Bustamante.

I want to thank Colas Rivière, with whom I worked closely together for the GRB analysis from December 2007 to 2011. Thank you, Bruny Baret, for the fast detector calibration and Monte Carlo simulations of GRB130427A, and for the fruitful discussions on the time independent search. I am grateful to a lot of people within the ANTARES collaboration for their support and comments. In particular, I would like to mention Dorothea Samtleben and Heide Costantini, for refereeing the GRB analysis from late-2007 to 2011 and the time independent analysis, respectively. Thank you for your time and your constructive remarks.

Let me also express my gratitude to Clancy James, who helped me a lot with the publication, and Thomas Eberl and Alexander Kappes for helpful discussions. Moreover, I want to thank all people at the Erlangen Centre for Astroparticle Physics (ECAP) for a great time I spent there. Thanks especially to the people I shared office with, for a very nice working atmosphere, refreshing conversations, coffee breaks and a lot of sweets: Stefan, Jannik, Tamás and Kerstin. Thank you, Bruny, Clancy, Thomas, Kay, Robert, Oli, José, Stefan, Roland, and dad, for taking the time to read parts of this thesis.

I gratefully acknowledge the financial support by the Studienstiftung des deutschen Volkes. Furthermore, I would like to thank the Elite Netzwerk Bayern and its coordinator Klaus Mecke for the opportunity to profit from the Physics Advanced study program.

Last but not least, I owe my deepest thanks to my parents for their encouragement, patience and uncompromising support throughout.

Für meine Großeltern.